Interlayer excitons and polaritons in atomically thin van der Waals heterostructures

Charalambos Louca

Department of Physics and Astronomy

University of Sheffield

This thesis is submitted for the degree of

Doctor of Philosophy

April 2023

This thesis is dedicated to the memory of Alessandro Catanzaro (1989-2020).

DECLARATION

I hereby declare that except where specific reference is made to the work of others, the contents of this dissertation are original and have not been submitted in whole or in part for consideration for any other degree or qualification in this, or any other university. This dissertation is my own work and contains nothing which is the outcome of work done in collaboration with others, except as specified in the text. This dissertation contains fewer than 65,000 words including appendices, bibliography, footnotes, tables and equations and has fewer than 150 figures.

Charalambos Louca

April 2023

ACKNOWLEDGEMENTS

Over the duration of this PhD, I was extremely lucky to interact daily with amazing individuals both in and out of the workplace. All of these people have shaped my experience in Sheffield for the better.

I cannot thank enough a particular man. Armando Genco, you have been a great mentor, colleague and friend. I really believe you are a rare person. Even after the countless hours we spent in the lab, I had fun working with you and will continue to do so.

We have also spent together a great deal of time in the lab with the person this thesis is dedicated to, who has left us prematurely. Alessandro has taught me everything about fabrication, introduced me to optics and believed in me from the start. This thesis would be impossible without you, my friend. In your thesis you said "I am sure that you will reach results that I could not even imagine now". I wish you were here to see them and discuss them over a beer (even if you probably could imagine).

Special thanks, also, goes to the massive help and great fun of the person behind the curtain, Tom Lyons. Thanks for doing a great job at introducing me to the dark side of D54 and the open cavity set-up, which has been a pivotal moment for success. I also owe a lot to Luca for showing me the way he works, the many discussions and the many beers. Another great person is Panaiot. Until this day he is the person who is always willing to help in and out work and the person to go to when you want to get creatively distracted with stimulating conversations on future projects. Thanks to Dan for helping me and teaching me the cooldown of our precious magnet and the many conversations over food. I would wish to Oscar and Sam who have 1-3 years left for the end of their PhD good luck. Thanks for the drinks and barbecues in the park and I hope in the next few months I can help you as much

as the people before me helped me. I would also like to welcome and wish good luck to the newest members of the group Yadong, Xuerong, Alex and Paul. Toby I thank you for the fun times in the lab and the gatherings after we were allowed during the pandemic with Tom, Panaiot and Gaby. Of course, you had an excellent host. My partner, Eirini, has been the person who has seen me go through all the emotions from stress and absent-mindedness to joy in the last few years. Thank you deeply for the massive patience and support you have shown to my quirks until this day.

I would like to thank our collaborators Johanna and Alexey (University of Manchester), Chiara , Stefano and Giulio (Politecnico di Milano) Salvatore and Sasha (University of Exeter) for the fruitful collaborations and for hosting me in their facilities during my visit there. In addition, Peter, Rahul, Kyriacos and Kirsty from David Lidzey's group for the supply of mirrors and the fun conversations in and out of the Austin room.

Of course, I would like to thank my supervisor Prof. Sasha Tartakovskii for allowing me to grow so much in his group and giving me the freedom to take initiatives and express my thoughts freely.

Last but definitely not least, the biggest thank you goes to my family. Your unconditional support and love since I can remember myself has shaped who I am and has made this thesis possible.

ABSTRACT

In two dimensional materials, arbitrary combinations of stacks are possible where each layer constitutes an atomically thin building block to engineer unprecedented properties. In monolayer form, 2D semiconductors show outstanding light-matter interactions, stemming from the confined nature of Coulomb-bound complexes known as excitons. When two Transition Metal Dichalcogenide (TMD) layers are brought together, new excitonic species of interlayer excitons (IXs) can be formed. Their properties can, hence, be engineered with material choice and stacking order. In Chapter 4, we stack pure monolayers of $MoSe_2$ to single-layer $Mo_xW_{1-x}Se_2$ alloys, which allows a continuous tuning of the IX energy by more than 50 meV introducing a chemical degree of freedom. Profound modifications of the electronic band structure occur when the alloy composition become increasingly similar to the adjacent pure TMD. In addition, we are able to observe optical signatures of interlayer exciton hybridisation and moiré superlattice potentials. We therefore expand the design possibilities for atomically thin devices. In the next chapters, we employ encapsulated homobilayers of MoS_2 to observe hybridised interlayer excitons (hIX) that uniquely combine high oscillator strength and promise for increased nonlinear interactions. Compared to excitons in MoS_2 monolayers, hIX exhibit ≈ 8 times higher nonlinearity, which is further strongly enhanced when hIX and intralayer excitons, sharing the same valence band, are excited simultaneously. This provides access to an unprecedented highly nonlinear regime which, through collaborative work, we describe theoretically by introducing the concept of hole crowding. In Chapter 6, the aforementioned system is embedded in energy-tunable optical microcavities, in which the TMD excitons strongly couple to photonic modes, forming composite exciton-polaritons. This allows the realisation of dipolar polaritons (dipolaritons).

We find dipolaritons to be an order of magnitude more nonlinear than monolayer polaritons, showing a rapid quenching of the Rabi splitting with increased density. The presented insight into many-body interactions can provide new avenues for accessing sought-after few-polariton quantum correlations.

List of publications

- T.P. Lyons, D.J. Gillard, C. Leblanc, J. Puebla, D.D. Solynshkov, L. Klompmaker, I.A. Akimov, **C. Louca**, P. Muduli, A. Genco, Y. Otani, G. Malpuech, and A.I. Tartakovskii "Giant effective Zeeman splitting in a monolayer semiconductor realized by spin-selective strong light–matter coupling." *Nature Photonics*, 1-5, 2022. (*Published*)

- **C. Louca**, A. Genco, S. Chiavazzo, T.P. Lyons et al "Nonlinear interactions of dipolar excitons and polaritons in MoS_2 bilayers". *arXiv preprint arXiv:2204.00485.*, 2022. (*Under Review*)

- A. Genco, C. Trovatello, **C. Louca**, A. I. Tartakovskii, G. Cerullo, S. Dal Conte" Ultrafast Exciton and Trion Dynamics in High-Quality Encapsulated MoS_2 Monolayers"(*Under Review*)

- A. Catanzaro, A. Genco, A. Kozikov, L. Sortino, **C. Louca**, D. Gillard, E. Alexeev, K. S. Novoselov, A. I. Tartakovskii "Resonant electronic and excitonic hybridisation in transition metal dichalcogenides alloys heterobilayers" (*Under preparation*)

- P. G. Zotev, Y Wang, D.A Penares, T.S Millard, S. Randerson, X. Hu, L. Sortino, **C. Louca**, M.B-Gisbert, T. Huq, R. Sapienza, T. F Krauss, B. Gerardot, A. I. Tartakovskii "Van der Waals materials for applications in nanophotonics." *arXiv preprint arXiv:2208.06249*, 2022 (*Under Submission*).

- **C. Louca**, N. Mullin, T.S. Millard, P. Zotev, A. Genco and A.I. Tartakovskii "UV/O_3 treatment of PDMS for heterostructure fabrication"(*Under preparation*)

Conference contributions

- "*Band-structure engineering in alloy-based TMD van der Waals heterobilayers*", **Poster**, Lord Porter Laser Laboratory 1st Annual Symposium, June 2019
- "*Band-structure engineering in $Mo_xW_{1-x}Se_2/MoSe_2$ TMD van der Waals heterobilayers*", **Poster**, UK Semiconductors, July 2019
- "*Band-structure engineering in alloy-based TMD van der Waals heterobilayers*", **Poster**, Nanophotonics Winter School , January 2020
- "*Band-structure engineering in alloy-based TMD van der Waals heterobilayers*", **Poster**, Graphene2020 Virtual conference , October 2020. (Best PhD student posters award)
- "*Nonlinear interactions of dipolar excitons and polaritons in MoS_2 bilayers*", **Oral**, Graphene Flagship Meeting, March 2022
- "*Nonlinear interactions of dipolar excitons and polaritons in MoS_2 bilayers*", **Poster**, Graphene 2022, July 2022
- "*Nonlinear interactions of dipolar excitons and polaritons in MoS_2 bilayers*", **Oral**, UK Semiconductors, July 2022
- "*Nonlinear interactions of dipolar excitons and polaritons in MoS_2 bilayers*", **Oral**, Photon 2022, September 2022
- "*Nonlinear interactions of dipolar excitons and polaritons in MoS_2 bilayers*", **Oral**, Graphene Week 2022, September 2022
- "*Nonlinear interactions of dipolar excitons and polaritons in MoS_2 bilayers*", **Oral**, Programme Grant Away Day, September 2022

TABLE OF CONTENTS

LIST OF FIGURES

CHAPTER 1

INTRODUCTION

1.1 Introduction to 2D Materials

"What could we do with layered structures with just the right layers? What would the properties of materials be if we could really arrange the atoms the way we want them? They would be very interesting to investigate theoretically. I can't see exactly what would happen, but I can hardly doubt that when we have some control of the arrangement of things on a small scale we will get an enormously greater range of possible properties that substances can have, and of different things that we can do" [1]

Richard Feynman has wondered in 1959, envisioning that "There is plenty of room at the bottom". Despite early theoretical work suggesting otherwise [2, 3], today we can routinely isolate atomically thin layers after the experimental realisation of graphene in 2004 [4]. This fact, combined with the numerous impressive properties of graphene, has led to the award of the Nobel Prize to AK Geim and K.S Novoselov in 2010. Ever since, the family of two dimensional crystals keeps increasing rapidly, with properties ranging from metallic to insulating, magnetic and semiconducting [5–7]. Two dimensional materials are layered crystals in their bulk form with each layer being weakly held to the next via van der Waals (vdW) forces. In contrast, strong covalent bonds hold the atoms within the plane of each layer. This interplay of forces, enables high quality single layers to be isolated by simply repetitively cleaving a bulk crystal using adhesive blue tape in a process called mechanical

exfoliation. Therefore, one can use these methods to gain access to fields spanning virtually all of the material sciences in a new condensed matter world, bypassing expensive epitaxial deposition methods and demanding controlled nanofabrication cleanroom environments. The reduced dimensionality, increased surface to volume ratio and quantum confinement allows single layers to combine unique electrical and optical properties with outstanding mechanical capabilities. The latter allow them to be integrated into practically any substrate regardless of whether is flat, structured, metallic, dielectric or biological. Impressively, their

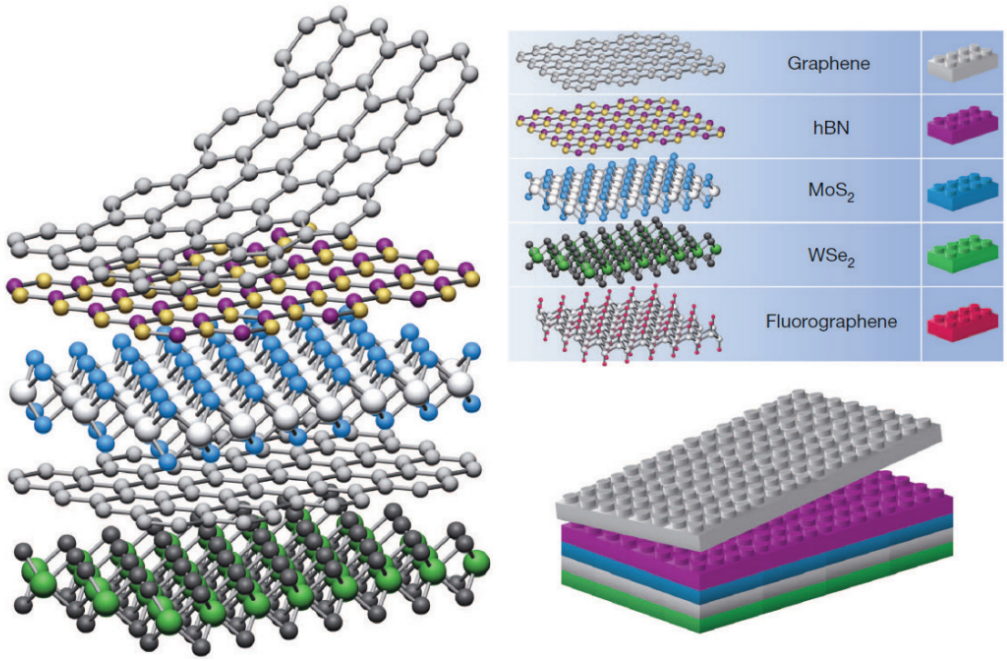

Fig. 1.1 **Analogy to Lego © bricks.** Van der Waals heterostructure stacking of a variety of layers with different properties as an analogy to Lego © bricks . Adopted from [8]

weak interlayer versus strong intralayer bonds make it possible to stack any combination 2D layers together to create vdW devices with new unprecedented properties, much like the aforementioned envision of Feynman. This process does not require to meet any conditions of lattice matching and bonding and was parallelised with stacking Lego © blocks in any order to make new structures, as shown in Fig 1.1. With advances in scalability and fundamental research on the special properties offered by the vdW capability, 2D materials may one day restructure science and technology.

1.2 Motivation

One of the advantages of confinement is the efficient interaction of light with electronic excitations in semiconductors, called excitons (electron-hole pairs), as explained in Chapter 2. Upon the addition of another layer on top, charges can transfer such that apart from excitons confined within each layer, new exciton species arise that have an electron in one material (layer) and the hole in the other. The resulting properties of this excitons, called interlayer excitons, dependent strongly on the choice of materials and have additional degrees of freedom that are specific to the arbitrary choices one can make at the stacking process. Interlayer exciton properties and their versatility is, hence, a direct consequence of choosing "just the right layers" and having "some control of the arrangement of things". In this thesis we would therefore like to explore this choices and study the tunability of interlayer excitons.

As mentioned earlier, the true 2D nature of atomically thin semiconductors makes them couple to light strongly, even at ambient temperatures. They are therefore a very good platform for observing coherent superposition of light and matter. Upon careful experimental design one can hybridise excitons and photons into new quasiparticles called exciton-polaritons that inherit properties of both. After the first observation of 2D material based exciton polaritons, a great interest has followed on addressing peculiarities of 2D excitons in the strong coupling regime, such as the spin valley locking. This has led to valley-addressable exciton polaritons and valley-hall effect with long range propagations.

The community is now moving into non-linear interaction induced effects such as Bose Einstein condensation and superfluidity, which has been observed in other systems and the quest towards polariton blockade. Polaritons inherit a low effective mass through their photonic component. At the same time they allow for effective photon-photon interactions induced through their excitonic component. It is therefore apparent, that using an excitonic system with increased non-linear interactions is of central importance for the observation of these effects. In this thesis, we approach this by employing interlayer excitons in the strong-coupling regime to realise dipolar polaritons(dipolaritons).

1.3 Thesis Outline

At the start of this thesis, we review the literature on the fundamental properties of the widely used 2D semiconductors, transition metal dichalcogenides (TMDs) . We focus on crystal, band structure, and valley degree of freedom and how these influence the excitonic properties. In particular how these influences their optical signatures. We then move on to explore excitons in vdW heterostructures and introduce interlayer excitons and the main features that affect/determine their spectral footprints. Later on we introduce optical microcavity structures, exciton-polaritons and the TMDs in the strong coupling regime.

The next chapter discusses the experimental methods employed for carrying out the studies shown in this thesis. We describe the components involved for high spacial resolution optical emission and absorption spectroscopy. We then, introduce tunable cavity set-ups that allow for clear observations of strong coupling. Then we move on to explain the Fourier-plane imaging spectroscopy used to characterise non-tunable microcavites. The second part of this chapter is on 2D material specific fabrication methods. We discussed mechanical exfoliation and monolayer identification techniques. We then proceed to describe several fabrication methods for monolayer and heterostructure fabrication, with the latter requiring specialised procedures. In the last part of this chapter, the author presents new approaches to heterostructure fabrication that have been developed during the course of this PhD.

Chapter 4 is concerned with tuning IX properties in vdW heterostructures. We show the approach of using alloys of TMDs as one of the constituent layers to achieve a non-monotonic tuning of IX emission energy resulting from fundamental changes in the heterostructure bandstructure with alloy concentration. We then proceed to the observation of hybridised interlayer excitons, modified by a moire potential snd note the complex nature of the origin of these excitonic species.

In the next chapter, we study the excitonic configurations in encapsulated homobilayers of $MoS_2$and observe hybridised interlayer excitons in as exfoliated 2H pristine samples. Next, we proceed to study their density dependent behaviour and observe enhancement and changes

in non-linear behaviour with different illumination regimes. With theoretical support from collaborators we discuss the origin of this effects and name distinct non-linear mechanisms.

In Chapter 6 we carefully design optical microcavites and mirror configurations that allow us to strongly couples the hybridised interlayer excitonic species discussed in the previous chapter. With the use of tunable optical microcavities we present the realisation of dipolar polaritons in homobilayers. Later on, the polariton density is increased to observe the non-linear effects being transferred to the strong-coupling regime.

The thesis is concluded with a brief summary and an outlook into potential future studies.

CHAPTER 2

2D SEMICONDUCTORS: TRANSITION METAL DICHALCOGENIDES

Since the isolation of graphene and the realisation of its attractive properties, the quest for atomically thin layers in the true 2D limit has sparked a 'chain reaction' of scientific activity. Unsurprisingly, a large part of this activity is on semiconducting 2D materials since semiconductors are everywhere in our everyday lives. Specifically, the group IV Transition Metal Dichalcogenides (TMDs), monolayers of which have shown exceptional optoelectronic properties. The latter are summarised and discussed in the below section.

2.1 Crystal Structure

Bulk TMDs are layered crystals. In the plane of each layer atoms are held together by strong covalent bonds. In contrast, each layer is held to the next by weak out-of-plane van der Waals attraction which consequently enables their mechanical exfoliation down to single layer(monolayer). TMD monolayers consist of series of transition metal atoms, like Molybdenum (Mo) or Tungsten (W), sandwiched between two series of chalcogen atoms, like Sulphur (S) or Selenium (Se). In their most stable phase of 2H, the atoms are arranged in a trigonal prismatic structure with each transition metal atom coordinated to 6 chalcogen atoms , as shown in Fig 2.1b. The multi-layer stacking in the 2H phase is in the A-B-A-B order. Two adjacent monolayers are 180 °in-plane rotations of one another, such that the

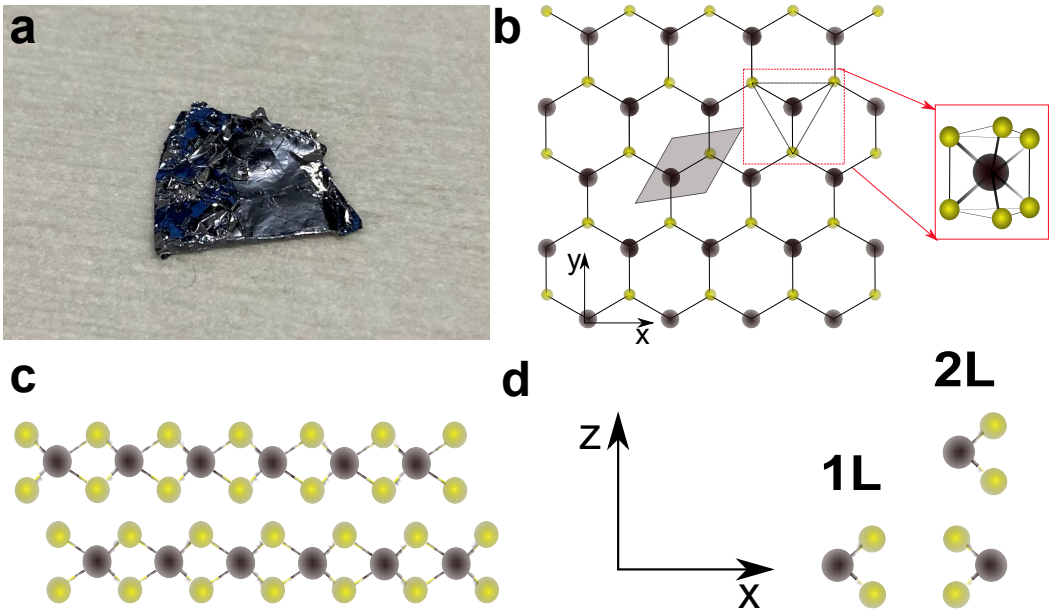

Fig. 2.1 **Van der Waals Crystal. a** Photograph of a crystal.**b** Top view of monolayer TMD lattice. The grey area is the primitive unit cell which is shown in 3 dimensions on the right corner. **c** Side view illustration of a 2H bilayer. In the plane of each layer covalent bonds are marked with solid lines while the empty space between layers signifies they are only held together by van der Waals forces. **d** Side view of monolayer primitive cell. In the bilayer we see that the 2H configuration corresponds to 180 °rotation with the chalcogen atoms (yellow) coinciding with the metal atoms(black).

metal atoms coincide with the chalcogen atoms of the other layer, as shown in the side views of Fig 2.1c,d. Hence, the 2H bilayer configuration creates an axis over which inversion symmetry is maintained. This inversion symmetry is broken in the monolayer limit.

2.2 Electronic bandstructure

Bulk TMDs are indirect band gap semiconductors. However, in their monolayer form they were found to undergo a transition to direct band gap changing significantly their optical response [10–12]. To understand this dramatic change, the atomic orbital contributions to the electronic bandstructure need to be considered.

As seen in Fig 2.1b, the hexagonal lattice of TMDs is composed of nonequivalent lattice sites since each site can be either a transition metal or a chalcogen atom. This leads to a mixed contribution of transition metal *d*-orbitals and chalcogen *p*-orbital to the band-structure, with

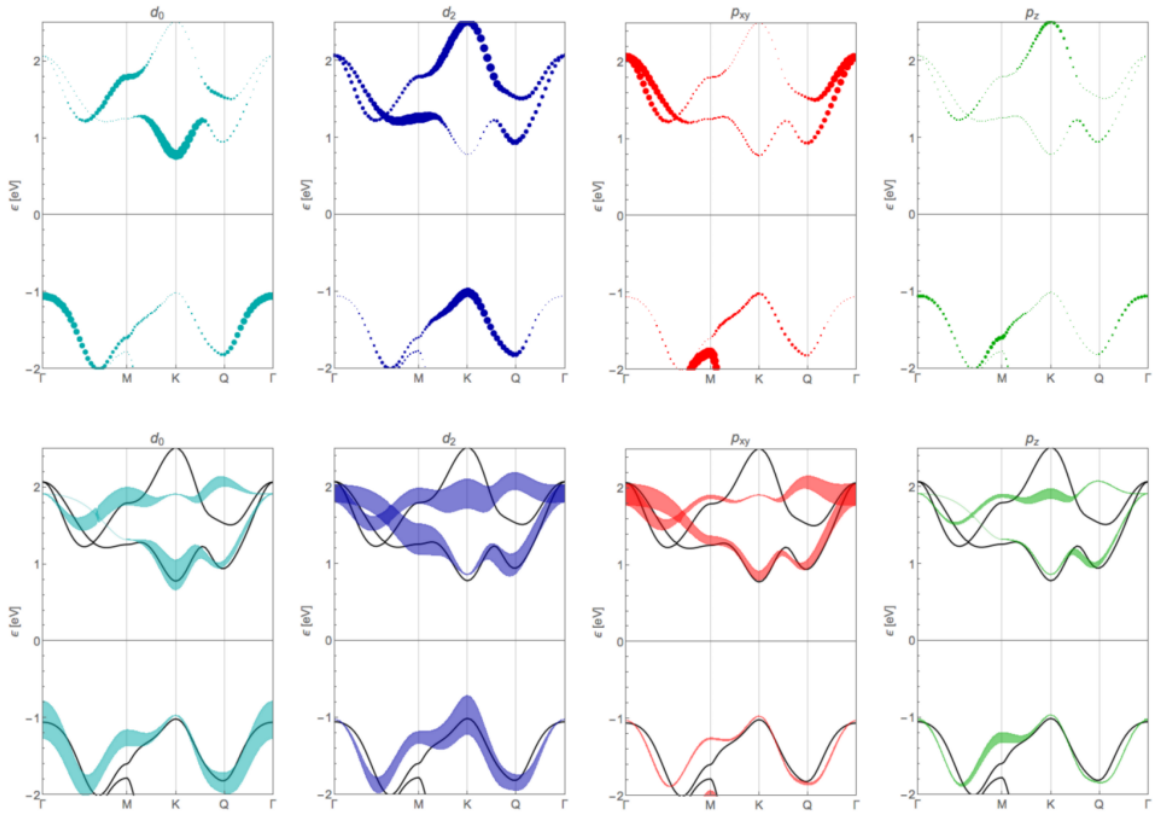

Fig. 2.2 **Orbitals in momentum space**. Orbital contributions across the Brillouin Zone for MoS_2. Adapted from Ref [9]

varying proportions at different points in momentum space. Taking the example of MoS_2, the orbital contributions along the first Brillouin zone are shown in Fig 2.2. Specifically, molybdenum atoms are responsible for the d^0 (or d_{z^2}) which are oriented out of plane and d^2 (or d_{xy},$d_{x^2-y^2}$) which are oriented in plane. Sulphur atoms exhibit p_{xy} and p_z orbitals oriented parallel and perpendicular to the TMD plane, respectively. At the K-point, the conduction band is composed of d^0 orbitals while the valence band is made of d^2 orbitals, with negligible contribution from Sulphur p orbitals[13, 9, 14]. Hence electronic states at the K -point are confined near the transition metal atoms, situated in the inner plane of the monolayer. The Γ-point valence band has primary contributions from out of plane orbitals, both d^0 and p_z. The Q point conduction band has significant contributions from both molybdenum and sulphur in plane orbitals. Considering placement of the chaclogen atoms, p orbitals located in the edges of each layer are influenced significantly in the presence of another layer. In

addition, out of plane orbital contributions are largely affected with the addition of atoms from other layers. Its is, hence, easy to see why the valence band is largely affected at the Γ-point and not at the K-point, which is the primary reason for the transition from indirect to direct bandgap from bilayer to monolayer. In addition, for structures greater then 4 layers, the non negligible orbital *p* contribution becomes dominant and moves the conduction band minimum to the Q point (Fig2.3). Light-matter interaction of direct band gap monolayer TMDs is much more efficient than the indirect bulk. In direct band gap transitions, the electron absorbing a photon is excited to the conduction band, leaving behind it a hole of effective charge +1 in the valence band and can easy recombine. If the VBM and CBM have a large momentum mismatch (i.e indirect), momentum conservation requires a compensation through interactions with phonons, decreasing significantly the recombination efficiency. Hence monolayer TMDs process a large quantum yield, since no phonon mediated excitations are required for recombination[12]. This makes the photoluminescene (PL) intensity of monolayers strikingly larger.

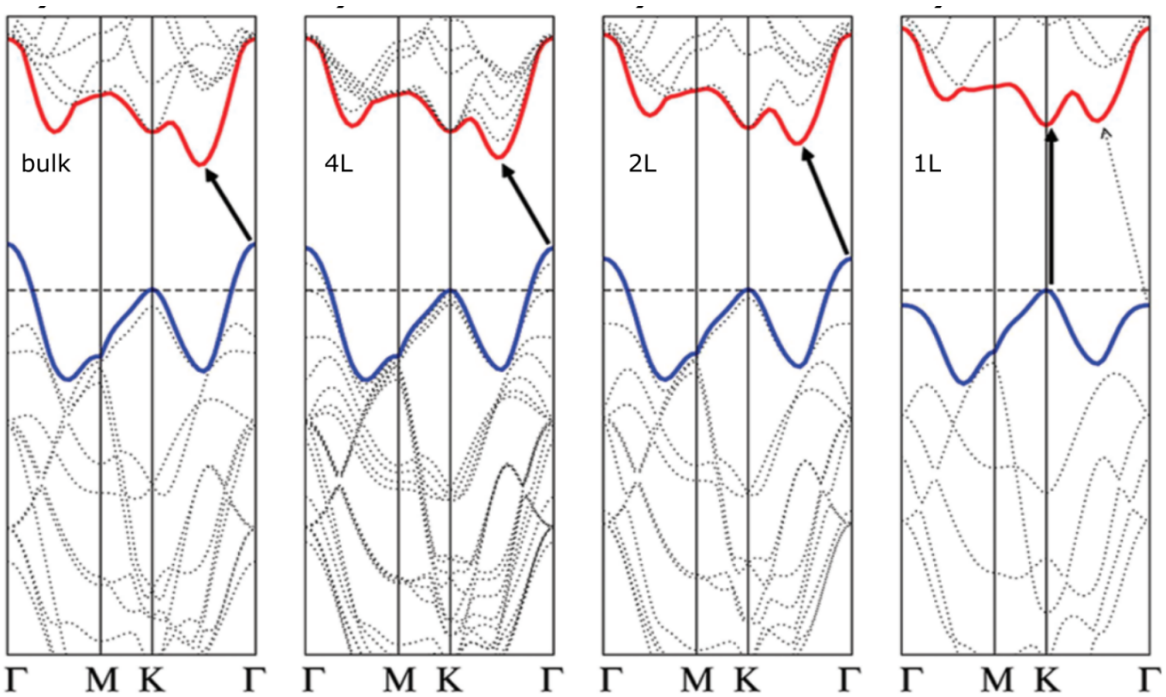

Fig. 2.3 **Bulk to Monolayer Brillouin zone**. Bandstructure changes at different points of k-space due to vertical atomic overlap from Bulk to Monolayer

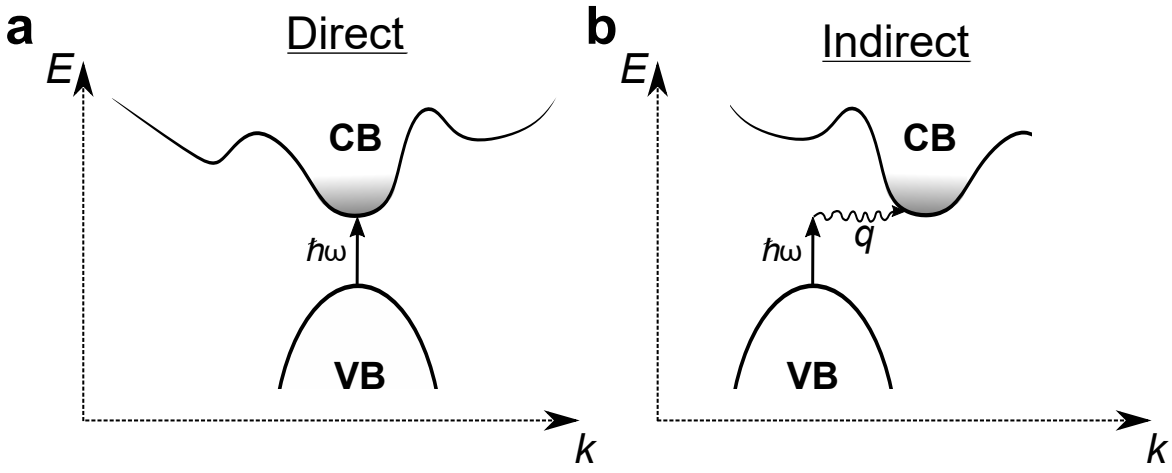

Fig. 2.4 **Two kinds of optical transitions**. Direct optical transition (**a**) vs indirect(**b**) where a phonon mediation is needed for momentum conservation. Adapted from [15]

2.3 Spin-orbit splitting and Valley Pseudospin

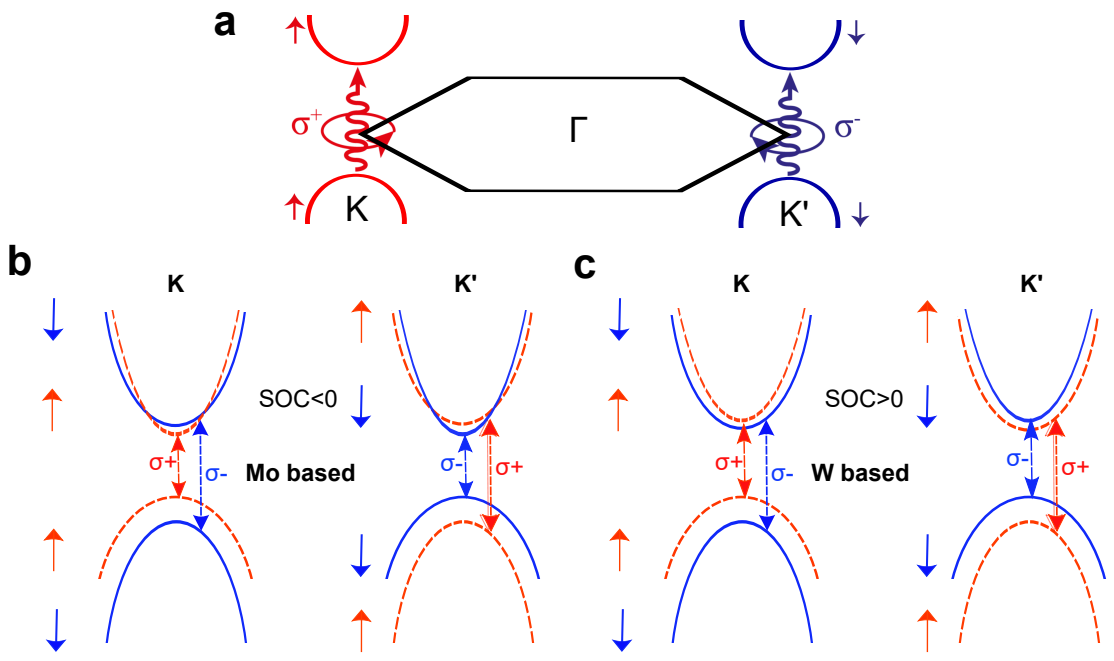

Fig. 2.5 **Valley pseudospin**. **a**Schematic of the spin-valley locking with the K and K' carrying a valley pseudospin. Optical selection rules lead to left and right handed circular (σ^+, σ^-) polarisation addressing K,K' valleys respectively. There are opposite spin-orbit coupling values in the conduction band of Mo ,**b**, and W, **c**, based TMDs. This leads to spin-allowed transitions being the lowest in Mo based and the second lowest in W based

The nonequivalent atoms on the hexagonal lattice sites lead to antisymmetric K-points (hosting the CBM and VBM) of the first Brillouin zone in TMD monolayers, since the rotational symmetry is reduced to 3-fold. Through the d orbitals of heavy transition metals, the confinement to single layer induces a giant spin-orbit coupling which introduces a splitting in energy bands. This splitting is opposite for opposite directions in the BZ giving an opposite spin to the conduction and valence band edges of adjacent K-points, refereed to as K and K' valleys. There is, therefore, a one to one correspondence between spin and valley known as a valley pseudospin. The splitting in valence band maximum bands is of the order of a few hundred meV[17–19], leading to two valence sub-bands of opposite spins. In the conduction band of the k-points the sub-band splitting is only of the order of a few tenths of meV, partially compensated by the contributions of π and d states. Interestingly, the balance of contributions is such that the overall spin splitting in the conduction band of W based TMDs is opposite to that of the Mo-based ones, leading to the CBM being of opposite spin for a given valley in the two monolayers. The above is illustrated in Figure 2.5. The conduction bands carry a principal quantum number of $m_{\pm} = \pm 1$ while the valence bands have $m_{\pm} = \pm 0$. Considering the selection rules of $\delta m_{\pm} = \pm 1$, we can see that for a given material monolayer, absorption of σ^{+}/σ^{-} couples the induced interband transition to a K/K' valley index. This spin-valley locking is a distinct peculiarity of TMD systems, allowing for increased degrees of freedom and the observation of effects of interest to both fundamental and technological application such as the valley spin-hall effect.

2.4 Excitons in TMDs

Upon absorption of photons, electrons acquire energy to transition to available states in the conduction band. For each promoted electron (of charge -1), this creates a vacancy in the valence band which acquires an effective charge of +1. This vacancy is called a hole. Oppositely charged electron and holes can interact through attractive electrostatic Coulomb forces[16]. Similar to hydrogen atoms, this attraction can form electron-hole bound pairs to

make a composite quasiparticle called exciton. Here we discuss excitons in two-dimensional TMD semiconductors and their peculiarities

2.4.1 Binding energy

Research in conventional semiconductors has classified excitons in two main categories. First the excitons found in typical inorganic semiconductors are called Wannier-Mott excitons. Their size is larger than one unit cell and are, therefore, not fixed within one atomic site. In contrast, Frenkel excitons in organic semiconductors are strongly localised to one molecular cite with their size being very small. Each exciton type has their advantages and disadvantages, with Frenkel excitons being robust and strongly coupling to light while Wannier-Mott type excitons interacting more due their larger size. Excitons in TMDs combine properties of both types. They are small in size but are still free to move through the crystal in different atomic sites. Therefore, they are suitably approximated to fall in the lower limit of Wannier-Mott excitons.

The energy that holds together or the energy required to dissociate the bound pair is called binding energy, E_B. For an exciton to exist this energy must withstand thermal fluctuations and collisions with thermally activated phonons. Hence, a stable exciton is the one that its binding energy exceeds the thermal energy in the system, k_bT, where k_b is the Boltzmann constant and T is temperature. The value of binding energy can be approximated using the Bohr model considering the Coulomb interaction. Namely:

$$E_b = \frac{\mu}{m_0}\frac{1}{\varepsilon_r^2}\frac{R_H}{n^2} \tag{2.1}$$

where m_0 is the electron rest mass, ε_r^2 is the dielectric constant of the medium, R_H is the hydrogen Rydberg constant and μ is the exciton effective mass calculated considering the electron and hole effective masses from their band curvature.

By analogy to the derivation of Bohr radius of hydrogen which is proportional to $\frac{\varepsilon_r}{\mu}$, we can see that excitonic Bohr radius, a_x, is related to the binding energy with an inverse proportion, $E_b \propto \frac{1}{a_x}$. It can hence be deduced that excitons with higher principal quantum

number have lower binding energy and are of larger size. The excitons within 2D TMD

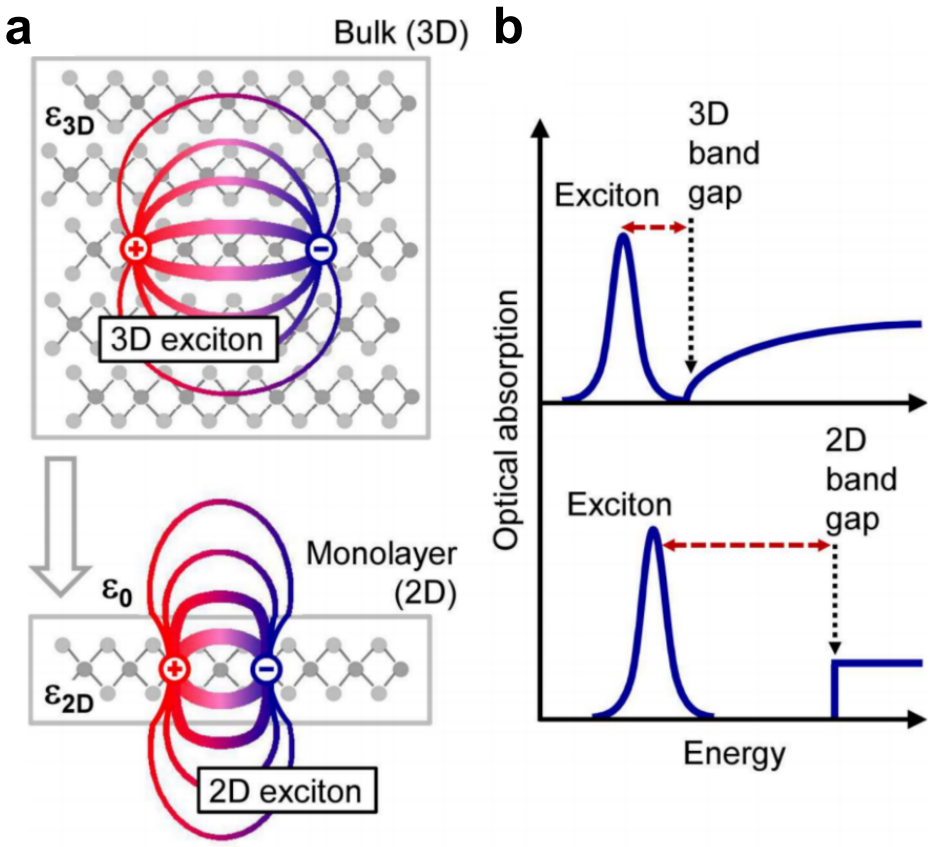

Fig. 2.6 **Environment and binding energy**. Exciton dielectric screening in bulk TMD ε_{3D} vs monolayer TMD ε_{3D}. In 3D we have neighbouring layers inducing screening in the excitonic dipole. This is reduced in the true 2D limit, resulting in excitons of larger binding energies and smaller Bohr radii. The larger biding energy is also shown spectrally as a larger separation of the excitonic peak from the absorption edge band gap (red arrow). Adopted from [20]

monolayers are small due to their strong confinement. In addition, excitons in the true monolayer limit do not have any surrounding material of a finite dielectric constant, inducing dielectric screening to the electron-hole interaction. Thus, excitons in TMDs have a large binding energies (500 meV) and small Bohr radii of about 1 nm [16, 21–23], as shown in Fig 2.6. From this simple argument one can understand the sensitivity of 2D semiconductor excitons to their environment. TMD excitons can interact strongly with light. Due to this absorption measurements can show signatures of Rydberg excitons up to n=5, as shown in

Fig 2.7. One can note also the deviation of the n=1 and n=2 excitons from the hydrogenic Rydberg series owing to the reduced dielectric screening aforementioned[20].

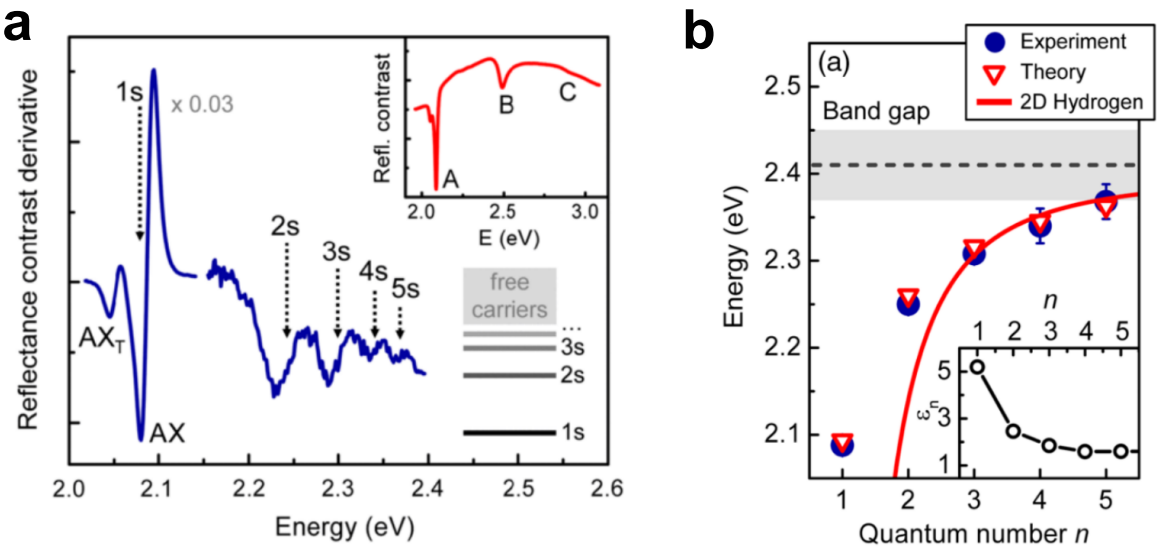

Fig. 2.7 **Rydberg series of TMD excitons a**First derivative of the reflectance contrast spectrum shows the Rydberg series of ground and higher excited exctions in WS_2.**b** Fitting this transitions(circles) and comparing with the hyrdogenic Rydberg Model(line) we see that there is a deviation in the low quantum numbers n=1 and n=2 coming from the reduced dielectric screening. Theory confirms the aforementioned (triangles) Adopted from [20]

2.4.2 Optical signatures of intralayer excitons

The spin-split subbands of CBM and VBM in TMDs with been introduced in the previous sections. Optical selection rules are such that the spin is conserved, with a one to one correspondence of light circular polarisation and the valley of excitons. Considering the simple band diagram of a Mo based TMD, illustrated in Fig 2.8a, we can see that the optically favourable excitonic transitions within each valley result in two non-degenerate excitons. The lower energy A exciton, X_A, which hosts a hole in the maximum subband of the valence band and an electron in the minimum sub-band of the conduction band. The spin split second lowest(highest) conduction(valence) bands can form the B-series exciton in an arrangement illustrated in the Figure2.8. Absorption spectra reveal the distinct energies of these excitons,

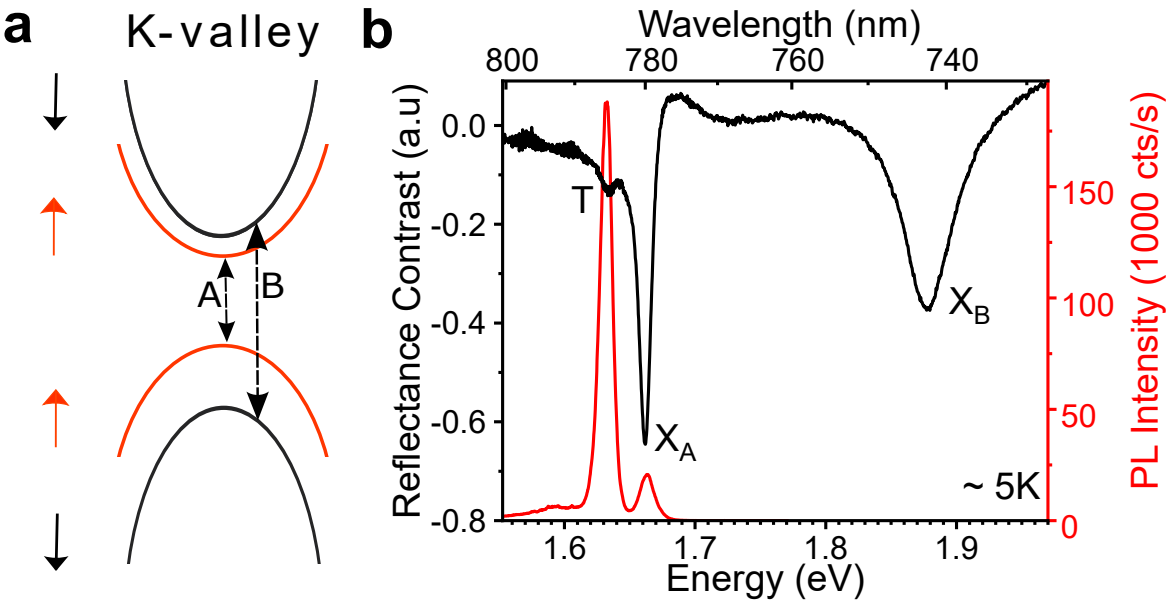

Fig. 2.8 **Excitonic optical signatures a** Simplified schematic of the band edges at the K point of a Mo-based monolayer. Orange bands indicate spin up and black bands indicate spin down. Dashed lines indicate the A and B series excitons and the bands that they involve. **b** Reflectance contrast (black) and PL spectra (red) of $MoSe_2$. The A and B series excitonic resonances are shown as dips in RC. In PL two transitions are apparent. The higher energy peak is due to the A series neutral exciton X_A, while at 30 meV lower in energy we can see the trion A series exciton (T) emission.

with their separation stemming from the spin splitting of the bands. These excitons are called neutral excitons and absorb light efficiently.

Excitonic species in the system can also be accessed through photoluminescence (PL) spectroscopy. Under non resonant illumination, high energy transitions are excited. These can decay to lower transitions and later recombine radiatively, resulting in the emission of photons of lower energy. Therefore although related, unlike reflectance contrast, PL intensity does not directly correspond to the oscillator strength. Rather, it depends on the efficiency of decay of carriers and the selection rules for the lowest bright state. Fig 2.8b shows a low temperature PL spectrum of $MoSe_2$. Here one notices the emergence of another excitonic species, 30 meV lower to the neutral A-series excitons. These excitons are called trions [24–26]. In the low density limit, they can be thought to consist of a bound state of two electron and one hole (-1 charge) or two holes and one electron (+1 charge). Their redshift from the neutral exciton stems from the additional binding energy acquired from the extra

charge carrier while their relative intensity to the neutral exciton are a measure of the doping level of the sample. Recently it was found that trions in the high doping regime are better described as Fermi-polarons. These consist of an exciton interacting in with a charged Fermi-sea, resulting in an attractive polaron (previously known as trion) and a repulsive polaron previously known as excitons [27–29]. However, the trion picture holds well for any reference mentioned in this thesis.

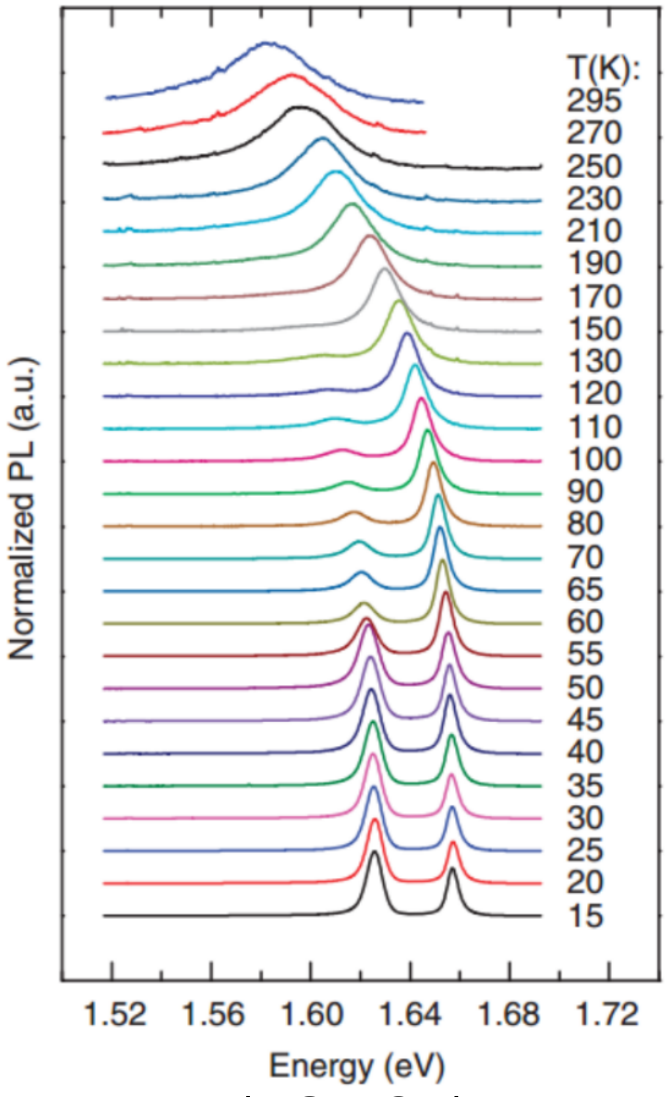

Fig. 2.9 **TMD excitons at elevated temperatures**. Temperature dependent PL spectra of $MoSe_2$ from 15K to room temperature. Adopted from [24]

Upon elevated temperature, excitons redshift due to a renormalisation while line broadening is observed due to thermal dephasing as shown in Fig 2.9. Trion emission does not exist at temperatures greater than 100 K owing to the additional charge escaping the bound state leaving behind a neutral exciton. Neutral excitons in TMDs due to their high binding energies are stable up to room temperature, which is a major attraction for future technological applications[30]. Interestingly at room temperature PL intensity of W based monolayers is very high compare to molybdenum based layers while the opposite holds true for low temperatures. This can be explained by the opposite conduction sub-band configuration stated in previous sections. In WSe_2 based materials the most favourable state allowed by optical selection rules does not stem from the conduction band minimum lowest sub-band. Hence with temperature, the emission intensity is greatly enhance due a thermally promoted spin-flipping mechanism enabling radiative recombination though relaxation to the lowest energy sub-band. At low-temperature this mechanism is not available, prohibiting radiative recombination.[31, 32] In the previous sections we have seen the symmetry dictated opposite spin splitting in opposite directions in the K-space , which in combination with selection rules gives inter-band transitions a valley pseudospin. This valley pseudospin is shown in the optical signatures of excitons. Through the choice of polarisation we can selectively excite one of the valleys with circular right or left handed helicity polarisation. In addition, linearly polarised excitation can generate a coherent superposition of K and -K valley states. This is called valley coherence and its optical signatures are manifested as a linearly polarised light emission from excitons, in the same polarisation axis as the excitation. The valley pseudospin can therefore be described in the Bloch sphere formalism, where it can be represented as a vector pointing from the origin to the surface of the sphere. As shown in figure 2.10, a vector pointing north(south) corresponds to $|K\rangle(|-K\rangle)$ and is addressed by circularly polarised $\sigma^+(\sigma^-)$ light. A valley coherent state is denoted as a vector pointing in any direction in the equator plane and is addressed by the corresponding linear polarisation. In principle, elliptical polarisation would therefore correspond to vectors pointing at any point in the Bloch sphere surface which is not at the equator or poles.

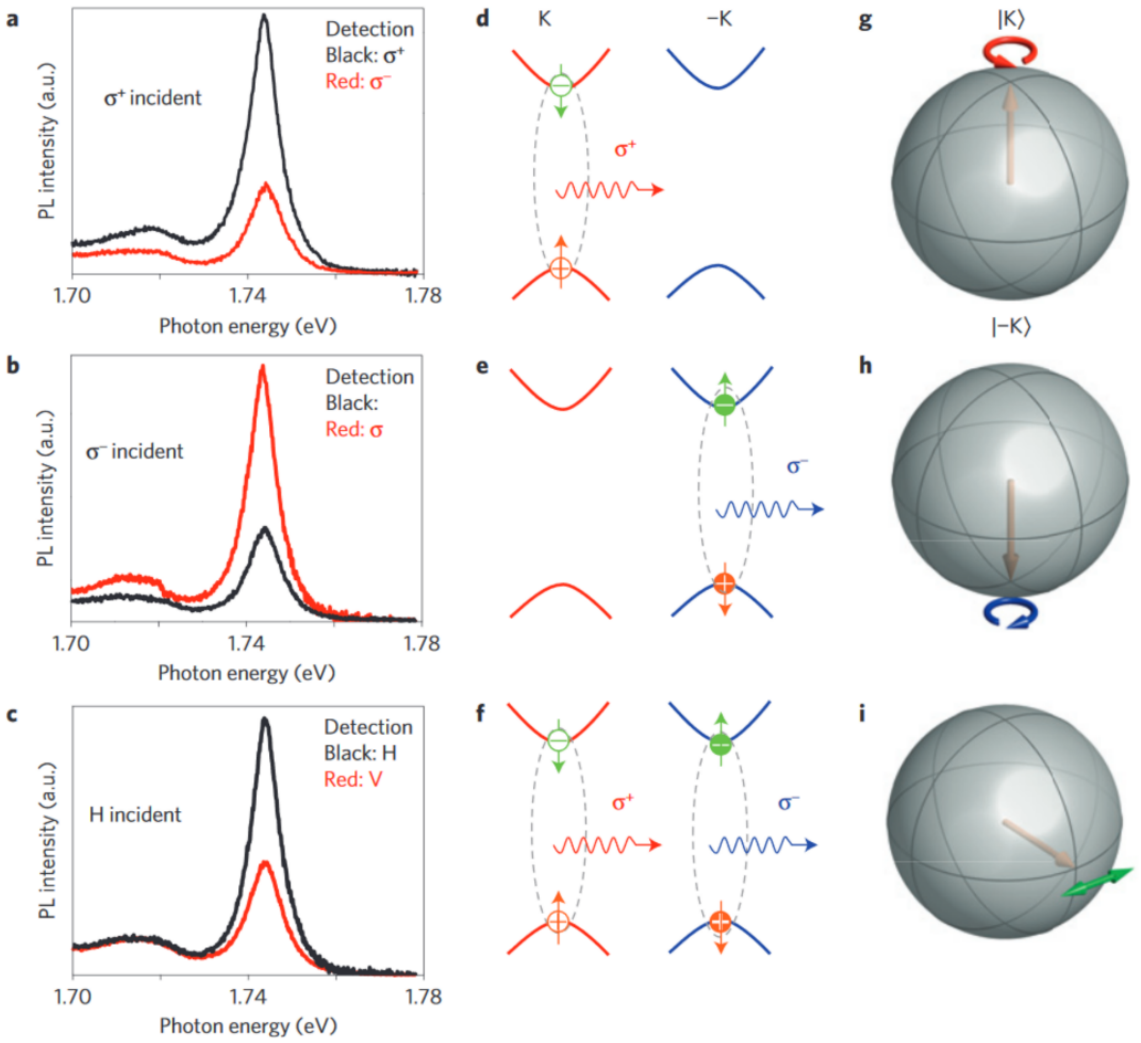

Fig. 2.10 **Optical signatures of valley coherence and Bloch sphere vector notation**. **a,b,c** Polarisation resolved PL spectra for WSe_2 monolayer. The incident and collection polarisation is stated in the legend of each panel. 50% retention of circular polarisation is observed. **d,e,f** Band edge schematics at the K,-K valleys of WSe_2. Arrows here show each individual particle spin(with the valence band arrow corresponding to the hole spin, unlike the other band diagrams shown in this thesis)**g,h,i** Valley states illustrated in the Bloch sphere vector notation. Adopted from [33]

Under the influence of external magnetic fields the valley degeneracy can be lifted. The valley pseudospin carries with it a magnetic moment (called valley magnetic moment) which accompanied by the magnetic moments arising from conventional electron spin and the transition metal d- orbtals in the valence and conduction band edges. Under magnetic field, each subband will shift in energy in accordance to the sum of these three moments [34–36].

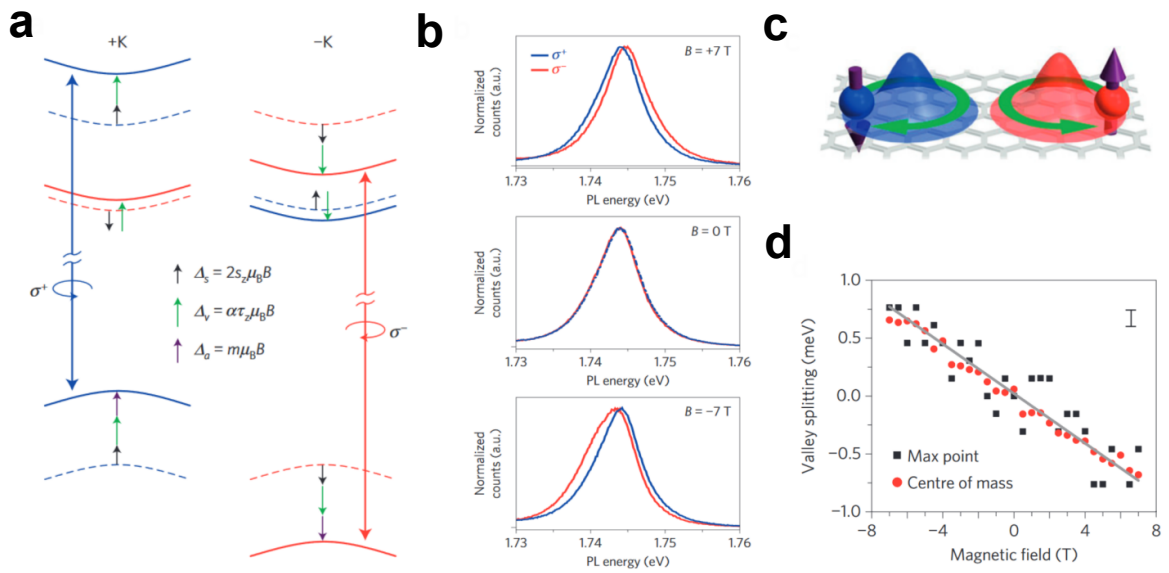

Fig. 2.11 **Optical signatures of Valley Zeeman splitting a** Band edges and the magnetic moments of spin Δ_s, valley Δ_v and atomic orbital angular momentum Δ_a that cause the bands to shift in the presence of a magnetic field. **b** Polarisation resolved PL spectra to measure the valley Zeeman spliting of WSe_2 monolayer neutral exciton under mangetic field **c**Illustration of valley contrasting magnetic moment given in green arrows. The purple arrows indicate the atomic orbital magnetic moment. Adopted from [34]

The difference in shifts of the involved valence and conduction bands will dictate the energy of the exciton signatures in absorption or emission spectra. The cumulative effect of the valley and orbital magnetic moments aforementioned, causes intralayer excitons in different valleys to shift in energy in opposite directions. This leads to an energy splitting between the oppositely polarised excitons, which is called the Zeeman splitting. Optical signatures of Zeeman splitting are shown in Fig. 2.11

2.5 Excitons in vdW Hetrostructures

2.5.1 hBN encapsulation

One of the most fundamental heterostacks is the encapsulation of a monolayer TMD in hexagonal Boron Nitride (h-BN). hBN is an atomically flat layered insulator with a large band-gap of 9 eV. Its has similar hexagonal lattice structure and stacking to graphene, but

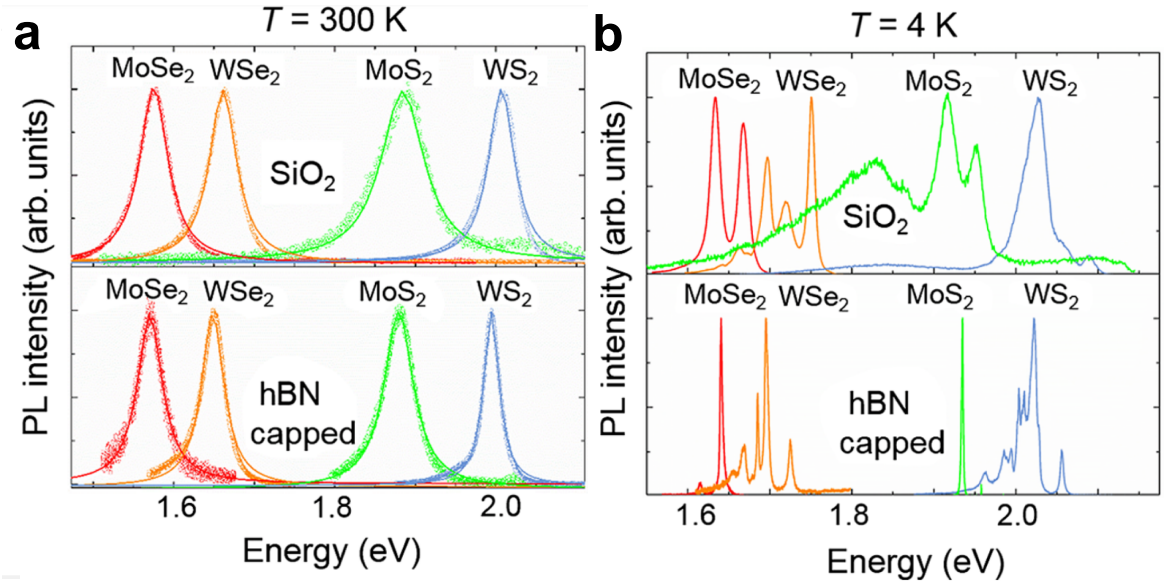

Fig. 2.12 **hBN capping for linewidth narrowing**. Influence of encapsulation of TMDs on their PL spectrum at room temperature, **a**, and low temperature **b**.

within a layer there are alternating Boron and Nitrogen atoms. Its vdW, flat and insulating nature make it a good material to be stacked either side of TMDs. As seen in previous sections, excitons in TMDs have large sensitivity to their environment. If a monolayer sits on a substrate, such as SiO_2. the bottom neighbouring medium will have a dielectric constant of ≈ 1.5 were as the top medium will be air of dielectric constant 1. These therefore creates ensembles of excitons of slightly different binding energies, manifested in the spectra as broad peaks. Encapsulation in h-BN enables a uniform and symmetric environment. This, along with the insulation of the active TMD from charge disorder within a given substrate, allows for more coherent excitonic resonances, reaching the homogeneous limit [37, 38]. The effects of encapsulation are shown in Figure 2.12 where PL spectra of hBN capped vs non-encapsulated TMDs are shown. In addition, studies have shown that, apart from reducing disorder, hBN of carefully chosen thickness can be used to induce weak cavity effects and impact exciton photon coupling through Purcell effect. This allows to control radiative recombination lifetimes and reduce linewidths further [39]. More recently, hBN encapsulation of homobilayers has allowed to clearly resolve new excitonic species, that are mainly discussed in chapters 5,6

2.5.2 Interlayer excitons in heterobilayers

The unique excitonic properties of TMD monolayers can be further enriched with placing one monolayer in direct contact to another of a different semiconductor to construct vdW heterobilayers. The band edge alignment of two different TMD monolayers are in a staggered configuration such that the CBM is in one layer and the VBM is in the other layer, as shown in Fig 2.13. Subject to orbital and symmetry conditions discussed below, electrons/holes from one layer can transfer to the other layer. This can in turn form bound electron-hole pairs called interlayer excitons (IX). IX are spatially separated with their constituents in different layers and their dipole moment aligned out of the plane, as shown in Fig 2.13.

We hence have a new excitonic species with numerous degrees of freedom such as arbitrary material choice and stacking twist angle, with high electrical tunability and a large promise for increased interaction. It is these excitonic species that are the focus of this thesis. Details for the formation, the degrees of freedom and the optical characteristics of these excitons are introduced below.

Band alignment and orbital hybridisation and optical signatures

The relative band alignment is a decisive factor for the formation and properties of interlayer excitons. In conventional semiconductor heterostructures there are three typical types of band alignments (straddling/type-I, staggered/type-II, and broken/type-III) , with their formation being generally explained by Anderson's rule [40]. Most of TMD heterostructures have a Type-II band edge alignment which has been confirmed by both theoretical and experimental studies [41–45]. The crucial parameter of the band offset can then be choosen with the use of different material combinations. For example VB and CB edges in different heterobilayer configurations have been measured to range from 0.3 eV to 0.9 eV.[46–48].

Apart from the band offset, the coupling strength between monolayers causes interlayer hybridisation or interlayer hopping of charges. This depends on the atomic orbital overlap at each point on the bandstructure upon the proximity of two TMDs layers. The new heterobilayer bandstructure therefore has contributions arising from the balance of the

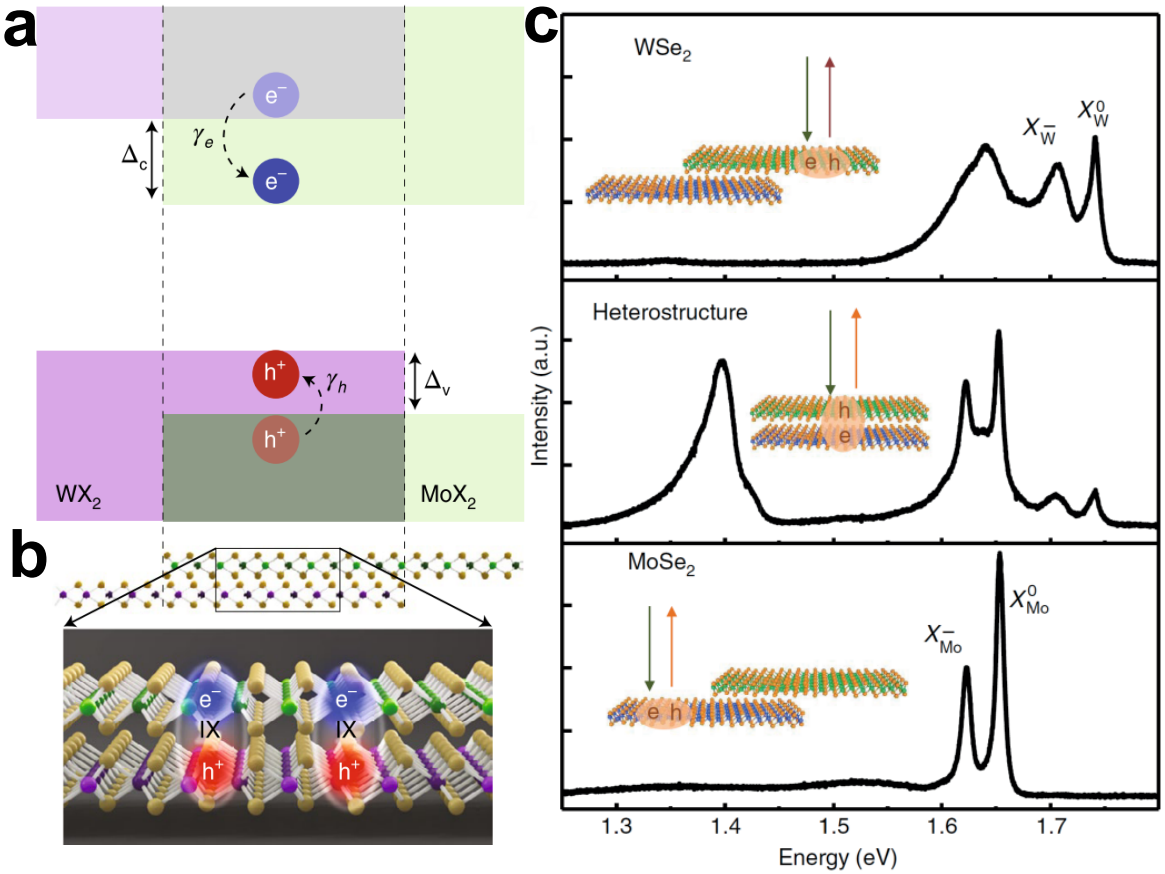

Fig. 2.13 **Type II band alignment and interlayer excitons a** Illustration of the heterobilayers type-II band alignment. This allows ultrafast charge transfer of electrons, γ_e, and holes, γ_h from one layer to the other for the formation onf interlayer excitons. The energy and charge transfer efficiency are dictated by the band offsets Δ_c , Δ_v for conduction and valence bands respectively. **b** Schematic representation of interlayer excitons with the electron in one layer and the hole in the other, aligned out of plane. **c** PL spectra on each monolayer (top, bottom panel) and the heterostructure regin in the middle panel. The formation of low energy interlayer excitons is observed

different types of orbitals in each constituent layer. Interlayer excitons were observed in many heterobilayers, such as $MoSe_2/WSe_2$ [50, 46, 51–54] , MoS_2/WS_2[55, 56], $MoSe_2/WS_2$ [57, 58], MoS_2/WSe_2[59, 60], $MoSe_2/MoS_2$ [61, 62] and WS_2/WS_2 [63]. Here, let us take the well studied example of $MoSe_2/WSe_2$. In this structures, the K points were found to be composed of mainly in plane orbitals as shown in Fig 2.14 [49]. Therefore, the heterobilayer stacking does not shift the band configuration at the K points of the Brillouin Zone. However, a larger out-of plane orbital contribution was found around Γ and Λ or Q

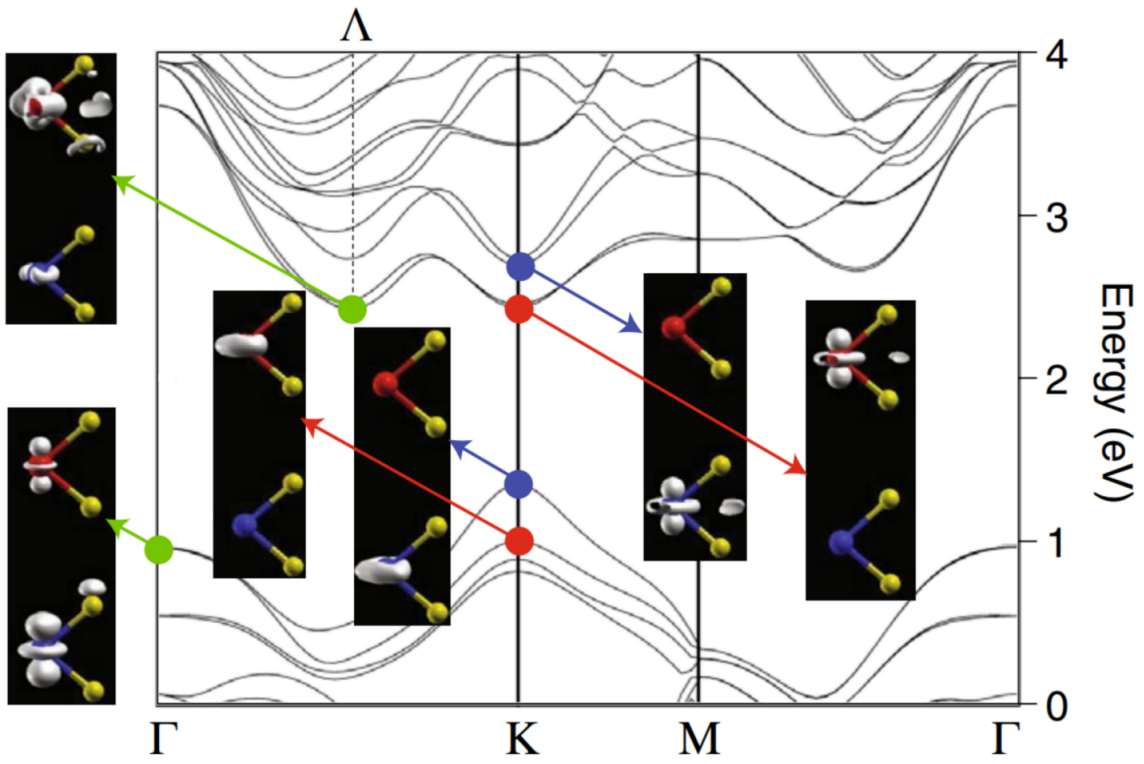

Fig. 2.14 **Bandstructure of $MoSe_2$/WSe_2 with the orbital contributions and their shapes at band edges**. Blue and Red spots show predominant contribution from the W and Mo layer respectively. The points with green spot signify the wavefunction to be distributed over both layers. Adopted from [49]

points. This makes them more sensitive to interlayer distance and stacking manner allowing for substantial modification of the nature of the interlayer optical transition. In some material combinations the direct nature is retained while some other show a transition to indirect. IX are usually the lowest energy transitions. Hence, their optical signatures are easily probed in photoluminescence spectroscopy. Examples of such spectra can be seen in Fig 2.13 where the overlapped regions show a strong low energy peak. This is attributed to IX and is absent in the spectra of monolayer regions. The aforementioned degrees of freedom of interlayer distance and twist angle have been observed experimentally as shown in Fig 2.15 and 2.16, respectively. Specifically, by placing a spacer layer of hBN between monolayers, their interlayer distance can be increased. These separates the out-of plane orbitals reducing their overlap, hence, affecting the band structure edges, the formation of interlayer excitons

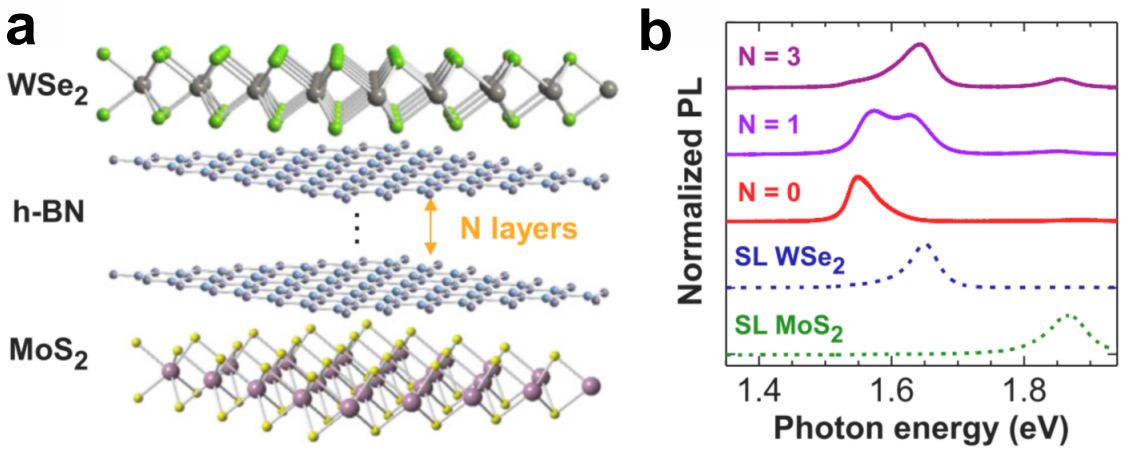

Fig. 2.15 **Effect of spacer on PL spectra**. Heterobilayers with N layers of hBN as a spacer as illustrated in **a**. The PL spectra in **b** show the implications on the emission up to N=3. [59]

and their radiative recombination rates. The emission of IX is therefore suppressed with increasing hBN spacer layers, N, returning to the monolayer emission spectra after N = 3. In addition the exact position and shape of IX peaks is modified. Similar effects can be observed as a function of twist angle. Fig 2.16 shows the hexagonal BZ of the two monolayers. Assembling a structure with a finite twist angle, θ, introduces a momentum mismatch between the K points of the two monolayers. The more the twist angle is increased, the less efficient radiative recombination becomes since a larger compensation of the momentum shift is needed. This eventually leads to a quenching the emission of IX in large twist angles. The intensity of IX PL peak recovers close to 60 °due to the crystal rotational symmetry.

Dipole moment and long lifetimes

The electron hole separation with each charge residing in two vertically adjacent layers results in an out of plane component of the dipole moment, in similar ways to conventional semiconductor double quantum wells [66–68]. This has enabled the experimental observation of large stark shifts several tenths of meV in TMD bilayers [69, 70]. Such observations require the fabrication of high-quality dual-gate devices to dissosiate carrier doping from electrical field effects [71]. In addition, the orientation of dipoles and the component of the out-of plane dipole moment can be controlled with the application of vertical electric field.

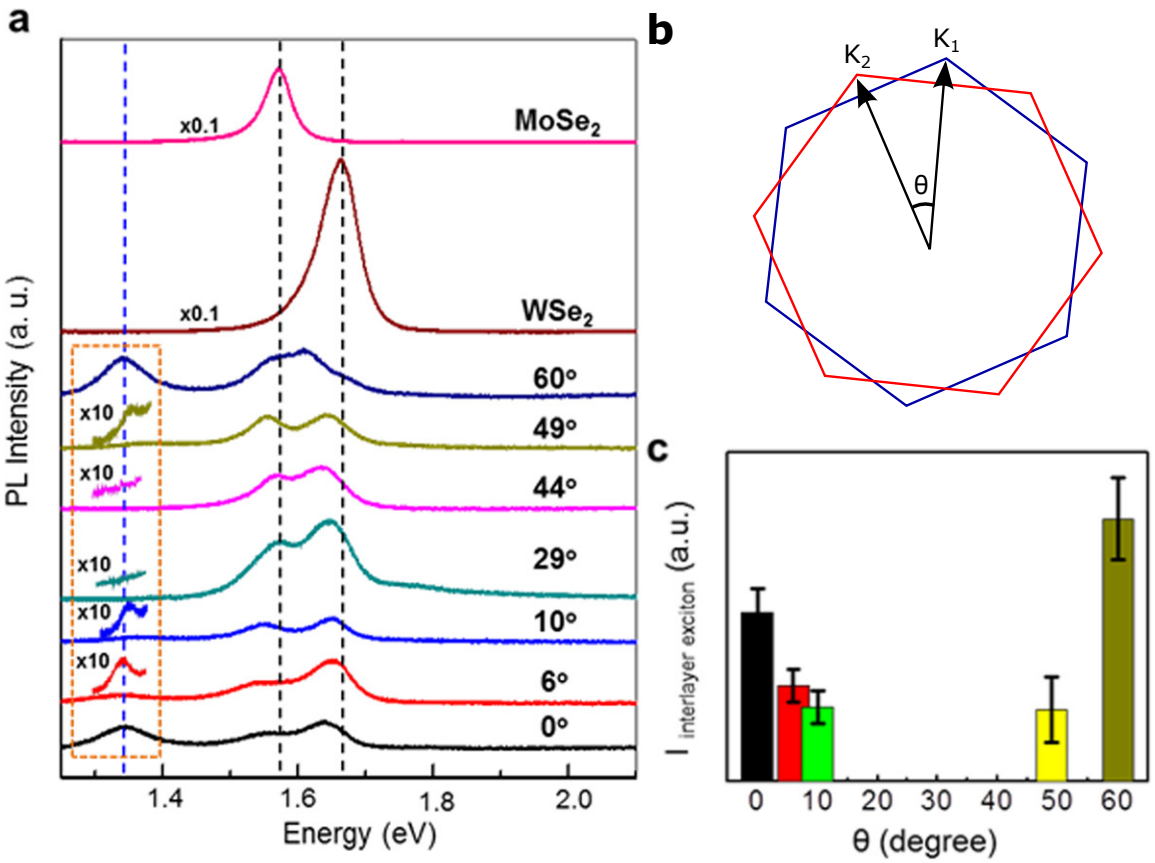

Fig. 2.16 **Twist angle dependence of IX PL. a** PL spectra as function of layer twist angle for a $WSe_2/MoSe_2$ structure. **b** Momentum mismatch of Brillouin Zones of two layers with twist angle θ. [53]

The spatial separation of the excitonic constituents, results in a reduced electron-hole wavefunction overlap. This causes significant reduction of the oscillator strength of pure interlayer excitons down to about 50 times smaller of that of interlayer excitons. However, the reduced overlap and the fact that IX are the lowest energy transitions result in long radiative lifetimes of the order of a few to hundreds of nanoseconds [50, 49, 52]

In addition the out-of plane dipole moment causes the alignment of neighbouring excitons in the vertical direction , as shown in Figure 2.17b. This is contrast in contrast to intralayer excitons, 2.17a, that their alignment is free in any direction within the plane of the monolayer and their interactions only arises upon excitonic wavefunction overlap in high densities. The out of plane orientation, combined with the significantly increased lifetime allows for

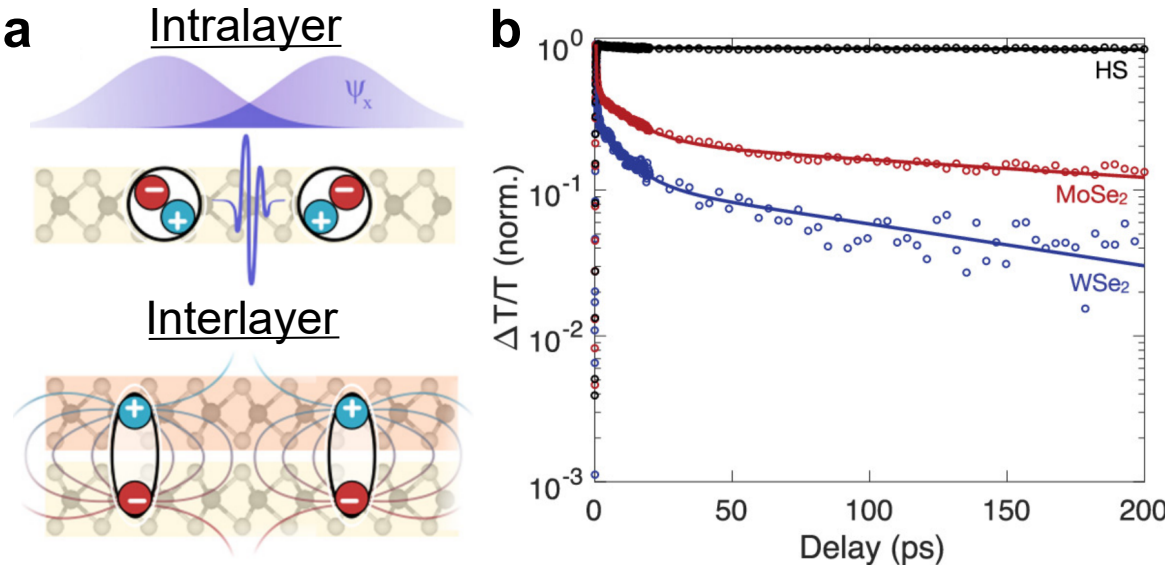

Fig. 2.17 **Dipole moment and long IX lifetime.** **a** Intralayer (top) vs Interlayer(bottom) exciton configuration. The alignment of out of plane dipoles of IX allows for coulomb interactions illustrated as overlapping field lines. Adapted from [64] **b** $\Delta T/T$ delay dynamics on the heterostructure (HS) vs monolayer regions (WSe_2, $MoSe_2$). Unlike monolayers, HS signal does not decay significantly within the timescales measured, showing the much slower recombination rates of IX compared to intralayer excitons. Adopted from [65]

enhanced interactions causing nonlinear coulomb repulsion and exciton-exciton annihilation [64].

Moire periodicity

When two monolayers of different lattice constant or different orientation are overlapped, a new larger scale periodicity emerges refereed to as moiré pattern. This pattern is a result of the different vertical alignment of atoms in top and bottom layers, which causes a periodic potential variation across the unit cell. Excitons feel this moiré potential. The superlattice periodicity of a TMD heterobilayers, l, can be expressed as $l = \frac{a_o}{\sqrt{\delta^2+\theta^2}}$, where $\delta = |a_0' - a_0|/a_0$, a_0 and a_0' are the lattice constants of the the two layers and θ is the twist angle between them[49, 74, 73]. How the latter can minimise the periodicity of the moié pattern is illustrated in Fig 2.18a. The positions of maxima and minima of these potentials are shown schematically in Fig2.18, located at points A, B and C and their magnitude can be as large as hundreds of electronvolts[75–77, 74, 78–83]. The exciton potential energy

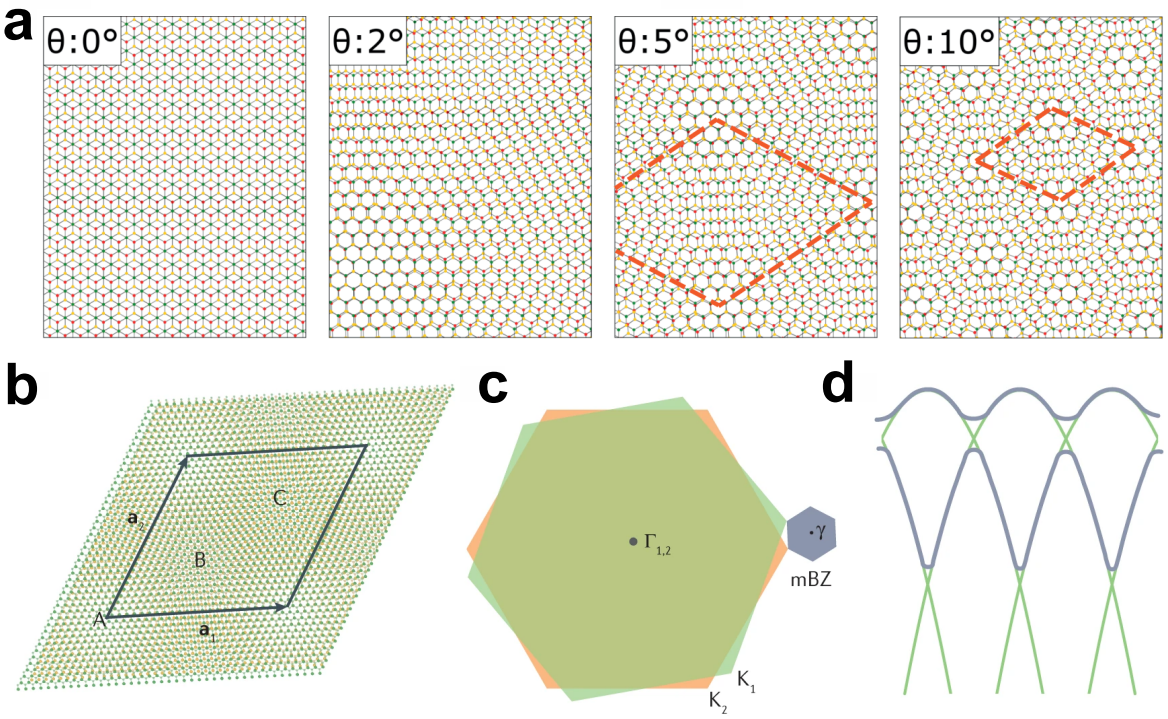

Fig. 2.18 **Moiré superlattices.** Illustrations of moiré in real and reciprocal space. **a** Emerging real space moire pattern with decreasing period size as a function of angle. Adopted from [72] **b** real space moir/'e superlattice whith the vectors a_1 and a_2 forming the superlattice unit cell. High symmetry points with the atomic configuration having 3-fold rotational symmetry are indicated as A,B,C. **c** Brilloun Zone schematic for each layer. The superlattice forms a mini Brilouin Zone mBZ with a wavefector that corresponds to the difference of K1 and K2. **d** At the edges of the mBZ, the moiré periodic potential opens up band-gaps. Adopted from [73]

can, therefore, be expressed as $\delta(r) = E_g(d(r) - \langle E_g \rangle)$ where d(r) is the interlayer distance at the position vector r and E_g is the interlayer exciton band gap. The depth of these moiré potentials, also, varies with twist angle with 0 and 60 ° being largely inequivalent. Hybridisation of the electronic structure can introduce further modification of the electronic structure of the superlattice. [73]

As depicted in Fig 2.18c,d the large scale periodic potential depth of the moiré superlattice can be approximated to generate a small reciprocal-space periodicity around the K and K' valleys referred to as the moiré mini Brillouin zone. This causes a mini band folding in the first Brillouin Zone, opening band gaps near the mBZ boundaries. These manifest themselves as additional peaks in the PL and RC spectra that are thought to originate from

mixed excitonic states separated by the moiré reciprocal lattice vectors or formerly dark states brightening through umklapp scattering leading to complex absorption and emission resonances of mixed excitonic species[73, 84, 85].

The different atomic stacking configurations across the moiré lattice leads to a position-dependent interlayer stacking energy. Therefore some areas in the lattice are more energetically favourable than the others. In reality, the superlattice can relax and twist to maximise the most favourable stacking areas and minimise the overall lattice energy. This is called lattice reconstruction[73]. There is, therefore, a large deviation from the ideal moiré lattice. The magnitude of this deviation varies for parallel an antiparallel layer stacking as has been theoretically studied and experimentally directly imaged[86, 87]. The implication of this on the optical spectra has been largely unexplored, complicating further the effort to decipher the exact origin of excitonic resonances.

Hybridised interlayer excitons

Under the right conditions tunnelling of charges can cause interlayer excitons (IX) to hybridise with intralayer excitons(DX). This could be mediated through a combination of small band offsets (leading to nearly resonant IX and DX) and favourable out of plane orbital contribution in the involved subbands, like in homobilayers [88, 89]. If these conditions are met and subbands of the same spin are involved, spin-conserving resonant tunnelling is possible in heterobilayers as well. These can be further modified by the aforementioned moire lattice periodic potential leading to optical resonances due to hybridised moire interlayer excitons with promise for increased correlation and sizeable oscillator strength[84]. The realisation of the collection of these effects is shown in Fig 2.19

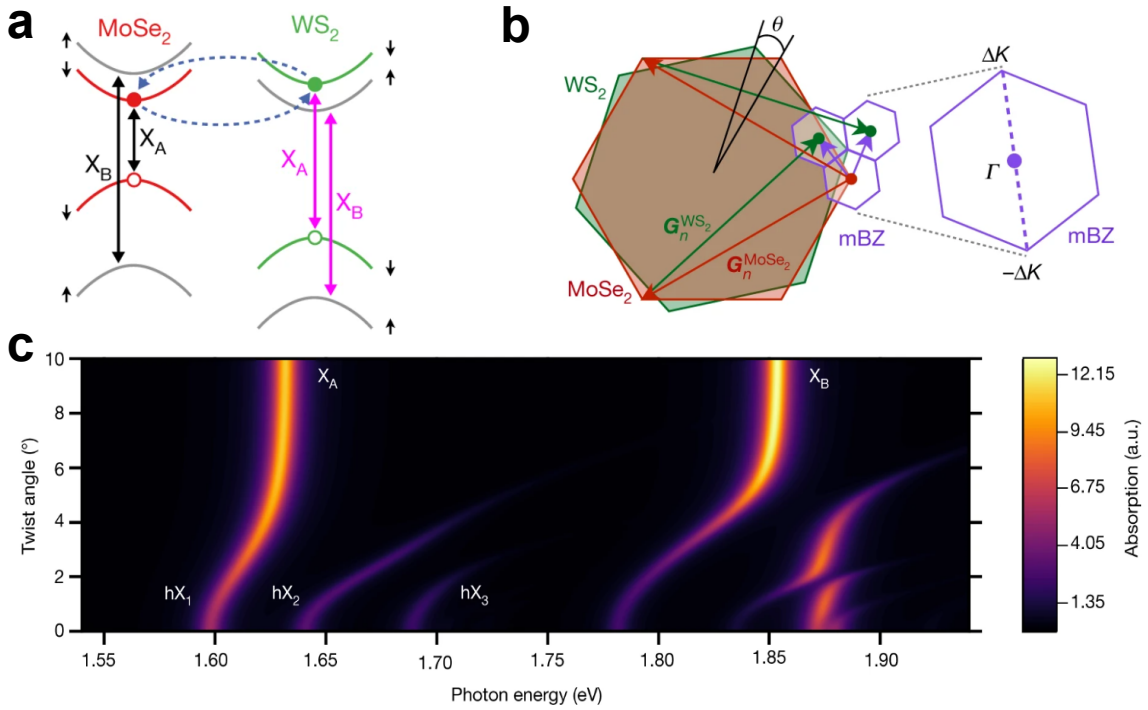

Fig. 2.19
Resonantly hybridised moiré interlayer excitons in $MoSe_2/WS_2$ heterobilayers. **a** Schematic of band edges of each layer. The conduction bands are nearly degenerate which enables charge tunnelling shown as dotted curves. This enables resonantly hybridised interlayer excitons. **b** Illustration of the moiré periodicity Bragg vectors in the mini Brillouin zone (mBZ,purple) defined as $b_n = G_n^{WS_2} - G_n^{MoSe_2}$. **c** Absorption of $MoSe_2/WS_2$ as a function of twist angle. At small twist angles hybridised excitons $hX_{1,2,3}$ arise near X_A of $MoSe_2$;analogous features in the range of XB are not labelled. Adopted from [84]

2.6 Exciton-polaritons

2.6.1 Optical Microcavities

When light is confined between two mirrors of high reflectivity, in the length scale of the wavelength of interest (visible), an optical microcavity is formed. Interference effects cause light confined in the cavity to form a standing wave, the wavelength and distribution of which is dependent on the specific distance between the mirrors and their design. Microcavities that cause a standing wave in the volume between two parallel planar mirrors are called Fabry-Perot cavities.

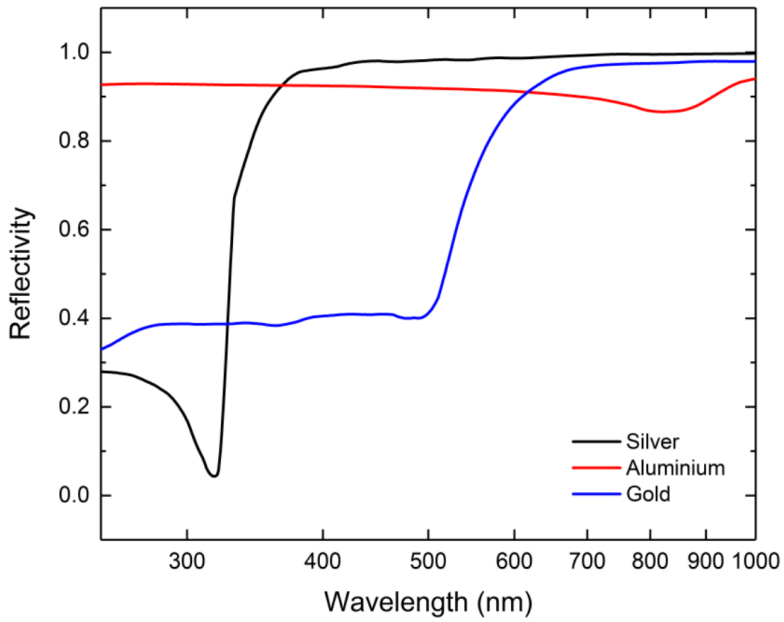

Fig. 2.20 **Metallic mirrors**. Reflectivity of Silver (Black), gold(blue) and aluminium (red). Adopted from [90]

One design is through the use of metallic planar mirror. These have high reflectivity on a broad wavelength range, due to their metalic nature. The onset of this reflectivity depends on the specific metal used. Reflectivity spectra of widely used metallic mirror materials are shown in Fig 2.20. The thickness of the mirrors can be chosen to tune the amount of light that enters and escapes the cavity. However, metallic cavities are often prone to optical dissipation leading to often broad cavity mode linewidth.

One of the most widely used planar mirrors are distributed Bragg Reflectors (DBR), due to their very high reflectivity. A typical electric field distribution and reflectivity of a DBR cavity is shown in Fig2.21. Each DBRs consists of alternating layers of high and low reflective index dielectrics n_H and n_L. At the interface between each layer we define the reflectivity, r, to be [91]:

$$r = \frac{n_L - n_H}{n_L + n_H} \tag{2.2}$$

The thickness of each layer can be chosen to cause constructive interference to determine the wavelength of light that is confined in the cavity. Each interface of DBR layer introduces

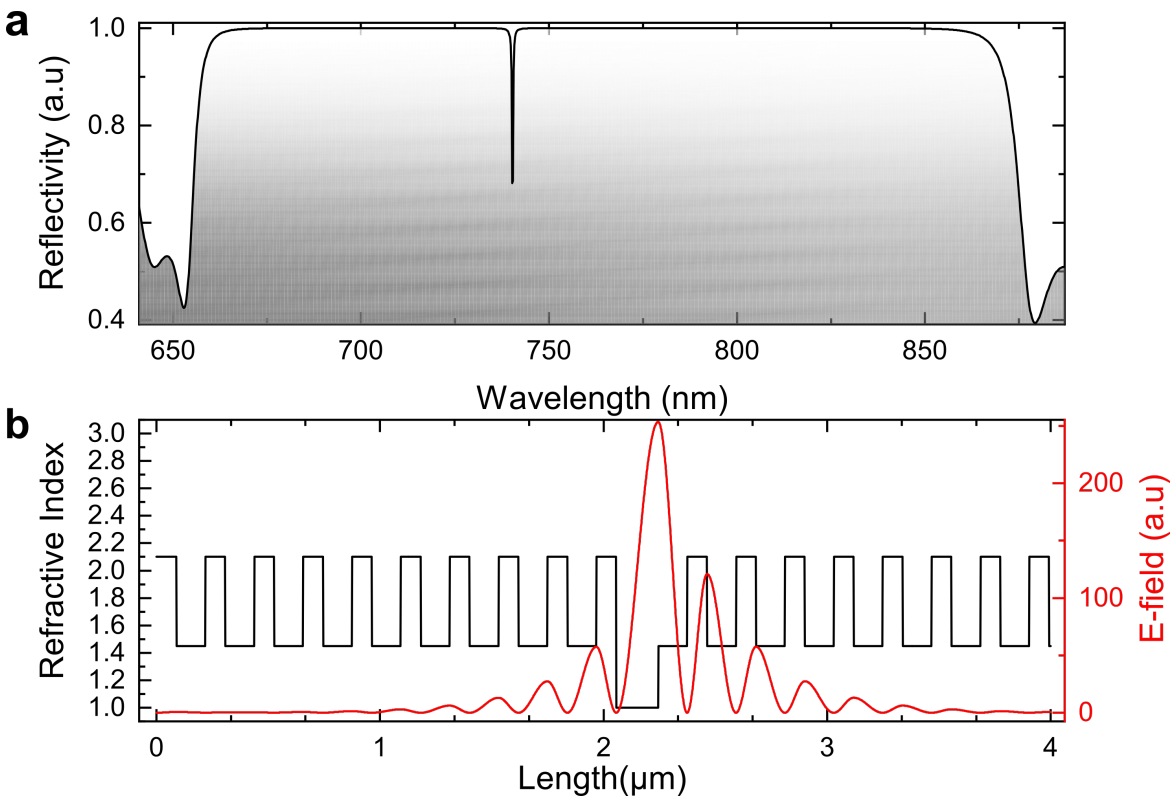

Fig. 2.21 **Distributed Bragg reflectors microcavity**. Transfer Matrix Method simulated Reflectivity (**a**) and Electric-filed distribution (**b**) of a microcavity composed of two Distributed Bragg reflectors.

a phase shift,$\delta\phi_r$, that can be defined as: [91, 92]

$$\delta\phi_r = \frac{4\pi}{\lambda} d_{H,L} n_{H,L}. \tag{2.3}$$

where λ is the desired wavelength and $d_{H,L}$ is the thickness of the low and high refractive index layers, respectively. To form constructive interference and a standing wave, the cavity should be designed such that the above equation is equal to π. Therefore we can calculate the thickness needed for each layer as:

$$d_{H,L} = \frac{\lambda}{4 n_{H,L}} \tag{2.4}$$

Accounting for the number of high low index pairs, N, on can calculate the total reflectivity, R, of the mirror to be[91]:

$$R = \left(\frac{1 - \frac{n_1}{n_2} \left(\frac{n_L}{n_H} \right)^{2N}}{1 + \frac{n_1}{n_2} \left(\frac{n_L}{n_H} \right)^{2N}} \right)^2 \tag{2.5}$$

where n_1 and n_2 are the refractive indices of the neighbouring media either-side of the DBRs. It is also easy to see that the larger the contrast (ratio) in of high and low refractive index layer and the more the number of pairs the higher the reflectivity of the mirror. In addition the difference between the two refractive indices that constitute each DBR pair determines the spectral width, Δ_{sb}, of the photonic band gap, called the stopband, such that:[91]

$$\Delta_{sb} = \frac{\lambda \Delta_n}{\pi n_{eff}} \tag{2.6}$$

where $\Delta n = n_H - n_L$ is the DBR refractive index contrast and $n_{eff} = \left(\frac{1}{n_H} + \frac{1}{n_L} \right)^{-1}$ is the effective refractive index of the entire DBR structure.

2.6.2 Strong exciton-photon coupling regime

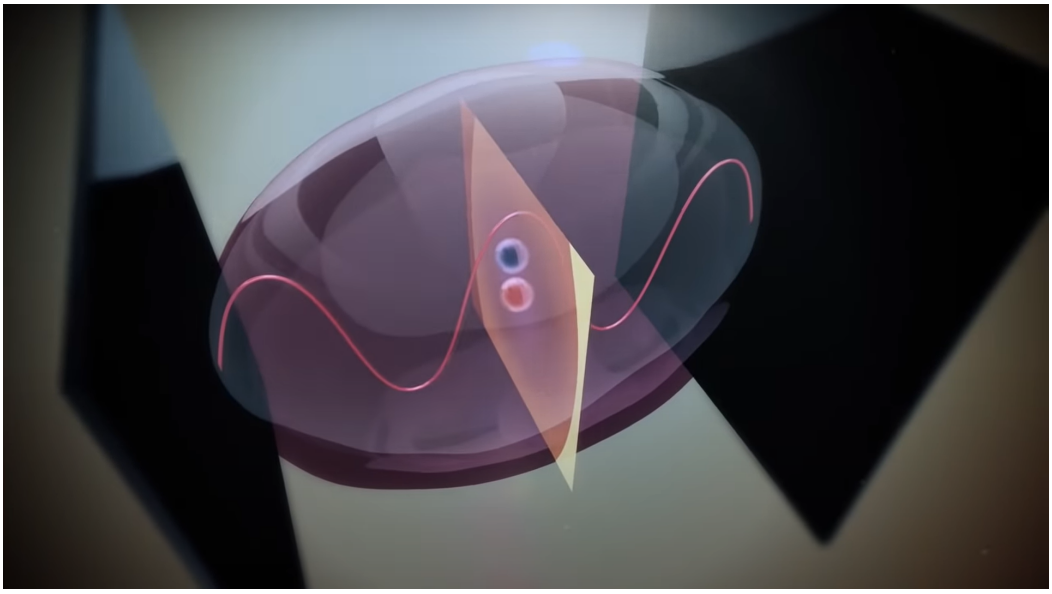

Fig. 2.22 **Exciton-Polariton illustration**. Graphical illustration of cavity light and excitons hybridising to form a new quasiparticle; exciton-polariton (shown as a purple ellipsoid) [93]

By placing an exciton-hosting semiconductor between two mirrors, light and matter can interact given that the semiconductor excitonic transition is in resonance with the wavelength of the confined photons. In thin 2D semiconducting systems the configuration must be designed such that the excitonic 2D plane coincides with the antinode of the electric field in the cavity. The strength of light-matter interaction is, broadly, classified into two regimes. The weak coupling regime and the strong coupling regime. To determine the aforementioned, one need to consider the following three parameters. The first two are related to the losses are in the system. Namely: (i) the rate at which photons are lost by escaping the cavity mirrors ,κ, (ii) the dephasing rate of excitons in the semiconductor, γ. The third parameter opposes the previous two and is the exciton-photon coupling constant, g. If g is much smaller than the maximum values of κ and γ we are in the weak coupling regime, where the effect of the cavity is small and therefore the system can be well described by perturbation theory of light matter interaction. The effect of the cavity is only limited to increasing the photonic density of states where spontaneous emission can happen in an irreversible process, referred to as Purcell effect [15].

When the rate of losses in the system (κ and γ) are minimised and the coupling between light and matter, g, is maximised such that it is much greater , we can access the strong coupling regime. In this regime the emission of a photon by a decaying exciton becomes a reversible process and leads to oscillatory exchange of energy between excitons and photons. The frequency of this exchange of energy is proportional to the light-matter coupling strength. When the system is in such a regime, excitons and photons cannot be classified as individual particles interacting pertubatively. Instead, they hybridise to form new bosonic quasipartcles called exciton-polaritons. These are a linear superposition of the photonic and excitonic components and inherit properties of both. The weight of each component is determined by the detuning of the two and described by the so called Hopefield coefficients. [94–97]

Even though this cyclic energy exchange is quantum mechanical in nature, it can be accurately described with a classical 2-level coupled oscillator model, just like two pendulums connected with a spring as shown in Fig 2.23. The oscillators in our case are the electric field in the cavity, **E**, and the polarisation of dipole in the semiconductor, **P**. Their uncoupled

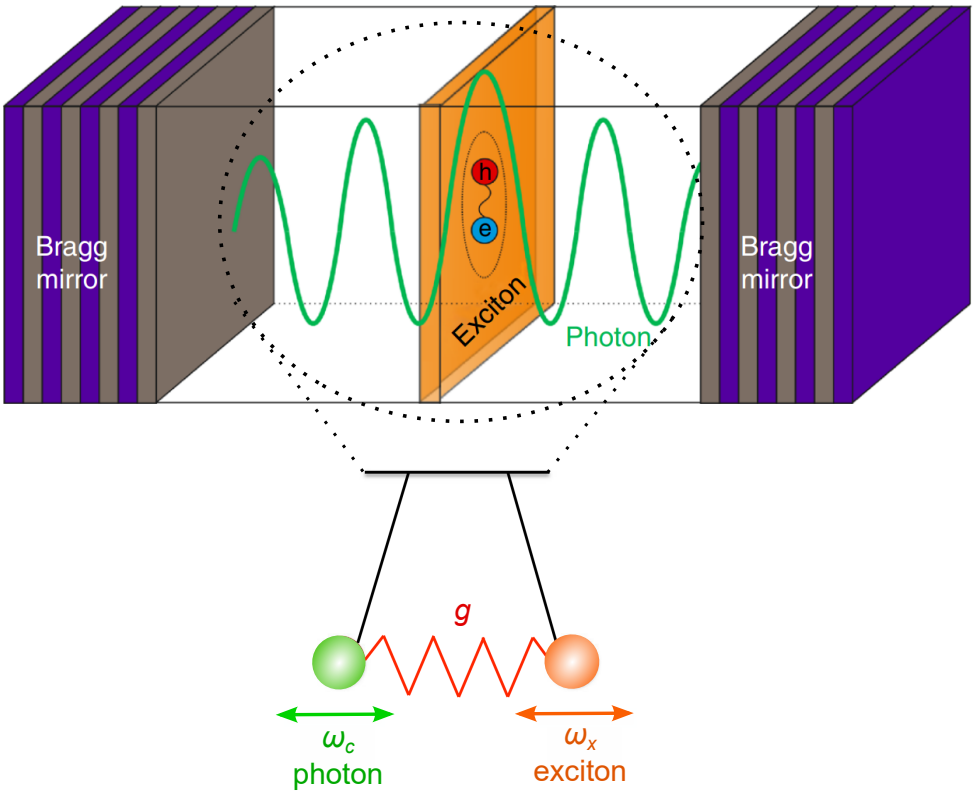

Fig. 2.23 **Coupled oscillators**. Schematic of polaritons modelled as two coupled oscillators. Green represents the photon oscillator, orange the exciton and the red zigzag line illustrates the coupling strength g. Adapted from [98]

frequencies are ω_c and ω_x, respectively and interact through the coupling term g. The magnitude of g in planar microcavities may be roughly approximated as $g \propto \sqrt{\omega_c \Gamma_0}$ where Γ_0 is the exciton radiative decay rate in vacumm and the proportionality constants dependent on the specifics of the design of the mirrors. The role of the damping terms are played by κ and γ which in experiment correspond to the linewidth of the cavity mode and the excitonic absorption peak, respectively. The equation of motion of the oscillators can then be expressed as: [94, 99, 98]

$$i\frac{d\mathbf{P}}{dt} = (\omega_x - i\gamma)\mathbf{P} + g\mathbf{E}, \tag{2.7}$$

$$i\frac{d\mathbf{E}}{dt} = (\omega_c - i\kappa)\mathbf{E} + g\mathbf{P}. \tag{2.8}$$

Solving the above equations and following from the harmonic time-dependence of the oscilators $\mathbf{P},\mathbf{E} \propto \exp^{-i\omega t}$, the eigenfrquencies of the system can be found in the following quaratic equation :

$$(\omega - \omega_x + i\gamma)(\omega - \omega_c + i\kappa) = g^2, \tag{2.9}$$

In the case of resonance ω_0 the detuning is zero and ω_c=ω_x. The solutions of equation 2.9 can therefore be expressed as:

$$\omega_\pm = \omega_0 - i\frac{\gamma+\kappa}{2} \pm \frac{\sqrt{4g^2-(\gamma-\kappa)^2}}{2} \tag{2.10}$$

Evidently, if $2g < |\gamma - \kappa|$ the final term becomes imaginary and the eigenfrequencies of the oscillators are indistinguishable at ω_0. On the contrary if $2g > |\gamma - \kappa|$ the oscillators enter the strong coupling regime. The last term of equation 2.10 is real and the non-degenerate solutions of the system, $\omega_\pm$ correspond to the upper and lower polariton branches. The splitting between them at resonance is the experimental analogous to the coupling strength as is given by $\hbar\Omega_R = \sqrt{4g^2-(\gamma-\kappa)^2}$. Therefore, one can see that it is difficult to distinguish between strongly and weekly coupled systems if the polariton branch linewidths are comparable to the Rabi splitting, $\hbar\Omega_R$.

2.6.3 Exciton polaritons in TMDs

As seen in section 2.4 excitons in TMDs have a large binding energy and oscillator strength, owing to their true two dimensional nature and decreased dielectric screening from neighbouring atoms. This makes them an attractive platform to introduce as an active layer in the optical microcavities, aforementioned, to achieve strong light-matter coupling. In this section, the first experimental efforts for the realisation of exciton-polaritons in TMD monolayers are described while the main methods to experimentally observe strong coupling are demonstrated. Early signatures of strong-coupling were shown at room temperature by embedding a monolayer of a Chemical Vapour Deposition(CVD) grown MoS_2 in a dielectric DBR cavity[100]. Here the authors have resolved the momentum dispersion of the confined photons in the cavity, observing polaritons at the anticrossing. This is done by Fourier

spectroscopy 3.4, to resolve the angles of light illuminated/collected to/from the microcavity sample. Since the anticrossing in this study was not fully mapped out, groups continued to study the details and the coupling strength of TMD in cavities. Very shortly after, an unambiguous demonstration of strong coupling in single and double monolayers of $MoSe_2$ followed [99]. In this study, the distance between the mirrors was controlled to change the wavelength of light that is confined in the cavity. RC and PL spectra were taken to monitor the coupling at low angles as a function of detuning. Tuning the cavity mode through the exciton resonance energy allows clear mapping of the coupling. These two observations are shown in Fig 2.24 and while demonstrating strong-coupling also serve as a means to see the two main means of experimental methods to observe exciton polaritons in microcavities. Later, several observations in the strong coupling were performed for all of the four main TMDs. [98]

In previous sections we have discussed the valley degree of freedom of excitons in TMDs and the degree of circular polarisaion that they inherit from it. While the degrees of polarisation are observed routinely for WS_2, WSe_2 and MoS_2, $MoSe_2$ monolayers show only 5 % of circular polarisation, owing to their fast depolarisation dynamics [101] compared to the exciton radiative lifetime. By strongly coupling the monolayer to a cavity mode, these dynamics can be tailored making the polarisation timescales one order of magnitude slower[102]. This enables the observation of valley addressable exciton polaritons in $MoSe_2$ which is the cleanest spectrally out of the TMDs. Investigations have also found spin-valley locking in the strong coupling regime to persist up to ambient conditions for monolayers of MoS_2 and WS_2[103–105]. The valley tagged excitons in TMDs can therefore be combined with the ultra-fast propagation [106] and low power switching the polaritons can offer from their photonic component, making TMDs and their peculiarities an interesting system to strongly couple to photons.

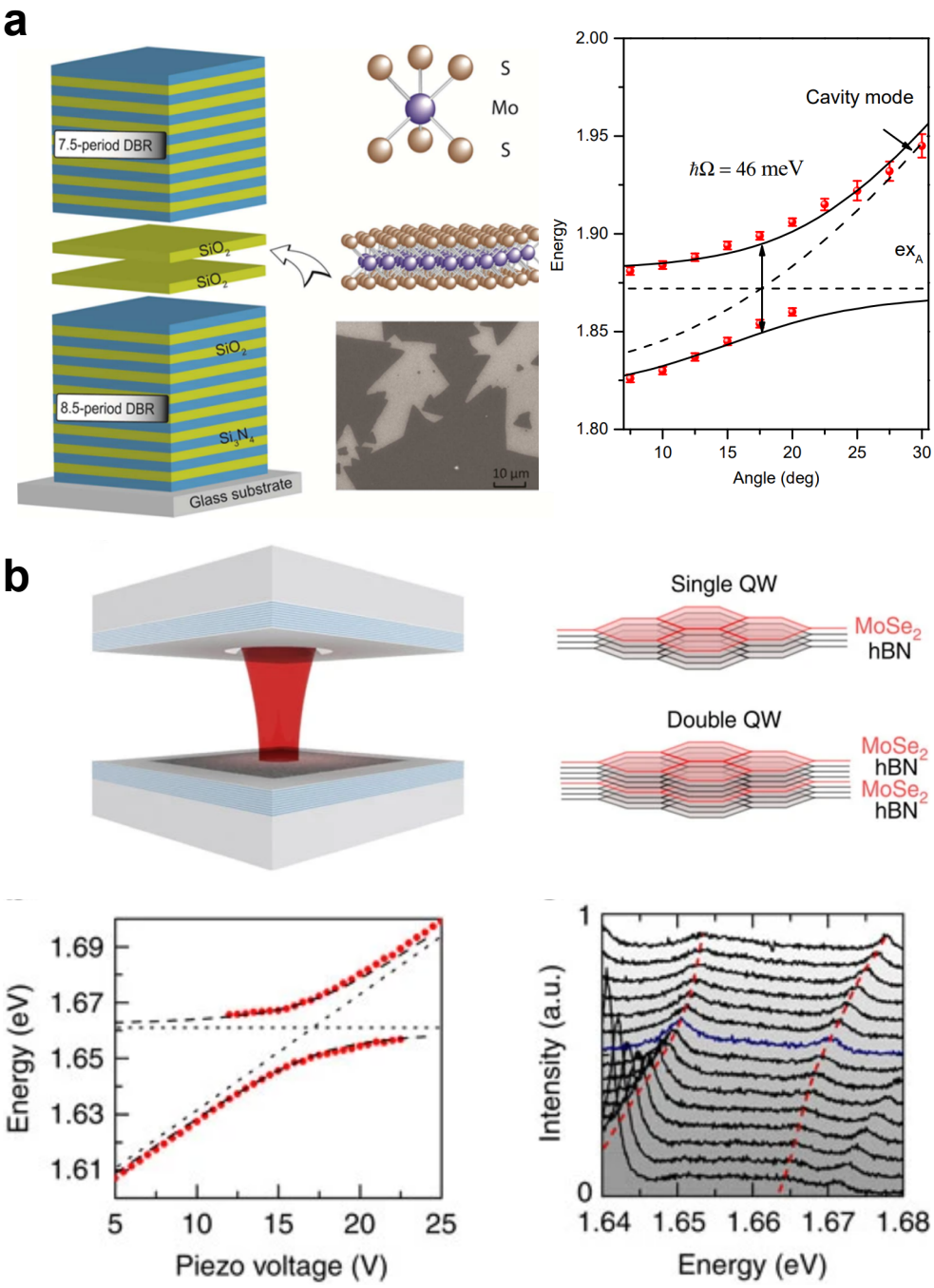

Fig. 2.24 **First Observations of strong-coupling in TMDs.** **a** MoS_2 in a monolithic DBR cavity strong coupling at room temperature. Map of the polariton dispersion with datapoints(diots) fitted to the coupled oscillator model with the cavity mode and exciton energy shown as dotted lines. The eigenvalues of the coupled oscillators are shown in solid curves, referred to as upper and lower polariton branches(UPB, LPB). Adopted from [100] **b** Unambiguous observation of strong coupling in in $MoSe_2$ single and double monolayers. Top left panel show the tunable cavity system. On the bottom left a clear map of the anticrossing is shown. The cavity mode is represented as a straight line as the x-axis now is the piezo voltage, used to detune the cavity photons. Adopted from [99]

CHAPTER 3

EXPERIMENTAL METHODS

3.1 Micro-Photoluminescence spectroscopy

Here the setup used to implement micro-Photoluminescence μ-PL spectrocopy is described. In all of the works described in this thesis the set-ups work in reflection geometry. First the laser light source need to be directed on the sample through a series of mirrors, filters and the objective lens, which is needed to obtain the micron scale resolution required. Subsequently, only the reflected emission is collected, directed and focused on diffraction grating spectrometer with a high resolution charge coupled device (CCD). The specifics of the set-ups used, which allow for valley polarisation resolution are illustrated in Fig 3.1.

The laser source is fiber-coupled to a single mode fiber. This is convenient for the set-up placement on the optical board and simultaneously helps in getting less distorted and highly symmetrical tightly focused spots on the sample. The fiber is outcoupled on the optics board the setup is located on and is collimated by an aspheric lens. A short pass filter (SP) is used to clean the excitation path from any high wavelength light coming from a possible low energy laser tail or elsewhere. The beam can be directed in the centre of the objective and fully aligned by the use of two adjustable mirrors. Between the two mirrors we place a Glan-Thompson prism linear polariser (LP) followed by a half-wave plate ($\lambda/2$) allowing us to rotate the linear polarisation of the laser beam relative the sample. Then, a beam splitter (BS) splits the beam in transmitted and reflected parts in 50:50 ratio. The reflected part goes

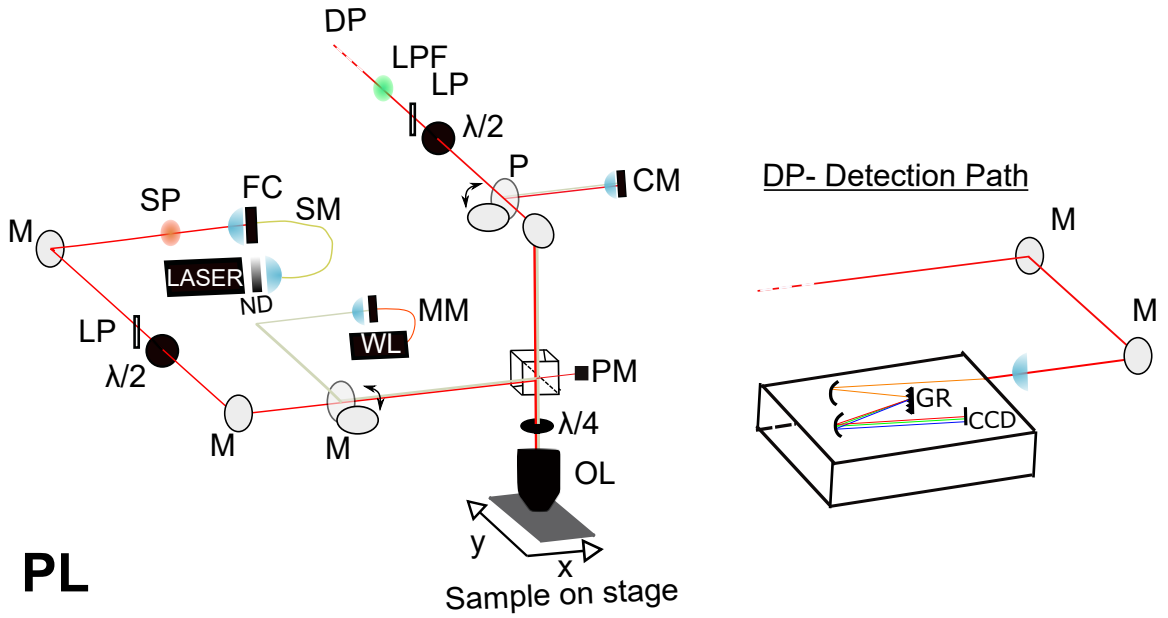

Fig. 3.1
Micro-Photoluminescence spectroscopy setup. Schematic diagram of the optics arrangement in the PL set-up used for high spatial and spectral resolution.

through the objective focusing into the cryostat where the sample is located. The transmitted part is used to monitor the power via a power meter (PM). Just before the objective a $\lambda/4$ quarter waveplate is placed. This allows to convert from linearly polarised light to circularly polarised light and vise versa. Specifically, one can chose to excite the sample with $\sigma^{\pm}$ by rotating the $\lambda/4$ waveplate optical axis to be $\pm 45^0$ from the linear polarisation plane, respectively. If one places the quarter waveplate's optical axis in parallel to the linear polarisation of the laser, the light will pass through unmodified. Hence one can chose to pump the sample isometrically in both valleys, if needed. Let s take the example of the σ^+ illumination. The emission from the sample will be made of σ^+ or σ^- components. This will pass through the $\lambda/4$ waveplate that will then convert it to two orthogonal linear polarisations corresponding to opposite helicity. The light then is transmitter though the beam splitter and directed towards another set of $\lambda/2$ and LP which enable us to selectively probe each one of the polarisations by rotating the $\lambda/2$ waveplate. Therefore one can perform co and cross polarised PL measurements in linear and circular polarisation. If no polarisation resolved measurements are needed, only the linear polariser in the excitation part is used

while the rest of the waveleplates are can be flipped out of the optical path. Then the long pass filter(LPF) is used to filter out the laser and the sample signal is directed in the detection path (DP), either through free space or another single mode fiber. The detection path consists of a series of mirrors and a lens that focuses the beam onto a spectrometer split of with 50 or 100 μm. The spectrometer uses two concave mirrors and a 300 groove/mm diffraction grating (GR) to focus single wavelength light onto pixels from a charged coupled device (CCD) array. The CCD has an array of 1340 x 100 pixels of pixel size 20 μm.

As shown in Fig 3.1, we can selectively introduce a white light halogen lamp (WL) in the excitation path coupled with a multi-mode fiber. When combined with a 10 per cent reflective Pellicle Beam Splitter on a flip mount and a small CMOS camera(CM) it allows for real time-imaging of the sample and the laser spot, such that their relative position, alignment and focus can be monitored.

Another fundamental optical characterisation method we use is the reflectance contrast (RC). When the sample is placed on a reflective substrate with no absorption and negligible transmission in the wavelength range of interest, one can use RC to study the light absorbed by the sample. This is done by taking a spectrum of the reflected light on a point on the sample and comparing it to the spectrum of reflected light from the substrate, taken under the same illumination conditions and integrated over the same exposure time. Reflectance contrast is then given by the difference between these two spectra, normalised by the spectrum on the substrate.

The setup configuration that allows μRC spectroscopy is illustrated in Fig 3.2. Here a broad band laser source is used that will cover the band width required for the experiment. This is introduced in the path either with a suitable SM fiber or free-space if short pulses and high powers are needed (such as the non-linear measurements in chapters 5 and 6). As can be seen the spectral filters are removed, where as the waveplate configuration has changed. As before, if no polarisation resolved spectroscopy is needed the waveplates and polarisers are on flip mounts so that they can be taken out of the path. However, for magneto-optical measurements discussed in chapters 5 and 6, we have used the illustrated polariser configuration. In comparison to PL the setup, the quarter waveplate has now changed position

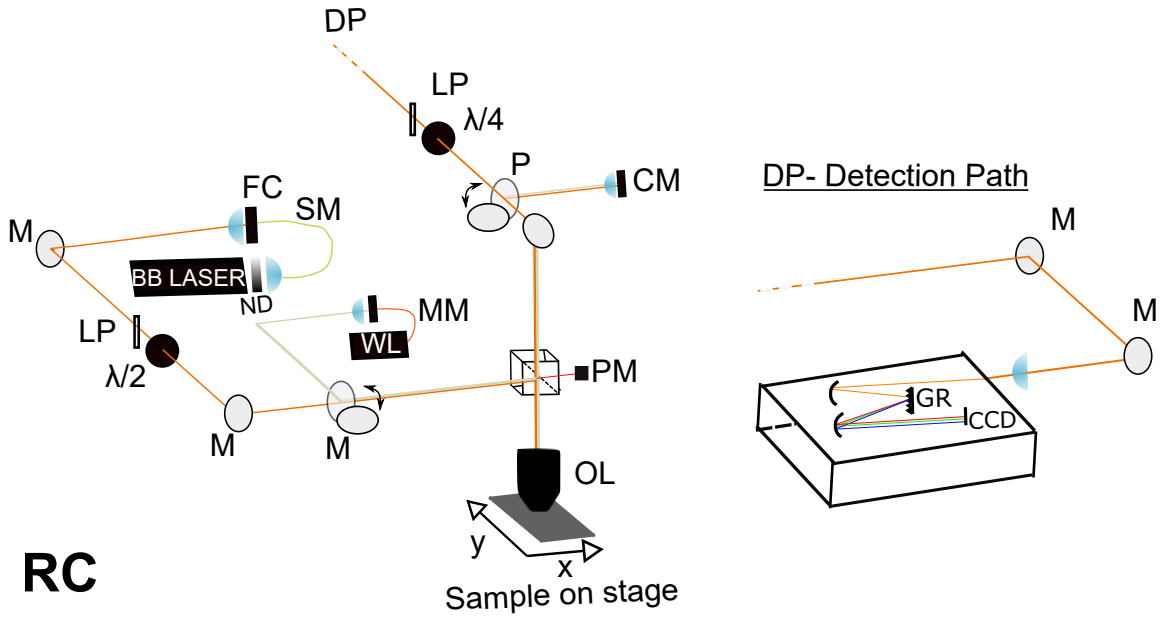

Fig. 3.2 **Micro-Reflectance Contrast spectroscopy setup**. Schematic diagram of the RC set-up used and the optics used for high spatial and spectral resolution.

to after the beam splitter in the collection path just before the linear polariser. In addition the $\lambda/2$ in the collection side is removed. In this configuration we can excite with linear polarisation so that the valleys are isometrically pumped and detect the $\sigma^{\pm}$ absorption by rotating $\lambda/4$ waveplate optical axis to be $\pm 45^0$ from the plane of the linear polariser, which is aligned with the optical axis of the laser polarisation. This is done in the presence of a magnetic field in the setup mentioned in section 3.2 of this chapter.

The laser sources of choice in Chapter 4 were a 532 and a 680 nm CW diode laser for PL investigations For the investigations of Chapters 5, 6 is a NKT SuperK Extreme supercontinuum picosecond pulsed laser of repetition rate down to 150 kHZ and a Coherent Libra Ti:Sapphire laser of 100 fs pulses and a repetition rate of 2kHz for the non-linear measurements.

3.2 Low temperature Tunable microcavity setup

For experiments in Chapter 6 we have used a tunable open-access microcavity system where the top and bottom mirror of the cavity can be controlled independently. The setup allows

for low temperature measurements (4.2K) as the mirrors are mounted inside a 2-inch bore insert of a helium bath cryostat. On top of the insert sits an optical board where the optics for the μPL/μRC reflection geometry setup are located. Access to the laser source and the detection path is achieved with single mode fibers, that allow for clean excitation/collection spots of symmetric Gaussian distributions. A schematic of the arrangement of the board and the optical access to the cavity system in the bath cryostat is shown in Fig 3.3a.

Fig 3.3b shows the area of the cavity mirrors and the nanopositioner stacks that are used for their control. The top mirror is attached to an arm which is in turn connected to a stack of three nanopositioners, each one with independent motion along one axis resulting in the XYZ control. This allows to bring the mirror in and out of the optical path/focus. The bottom mirror sits on a stack of 5 nanopositioners. Three of them are are also for XYZ control. The other two (which sit directly below the bottom DBR) are responsible for controlling the tilt of the mirror. Tilt control is needed in order to ensure the two mirrors are parallel to each other and perpendicular to the optical path, making a uniform cavity length along the collection spot diameter. This can be checked using broad band illumination by imaging the periodicity of interference fringes on the camera to achieve maximum period. The the laser is focus on the surface of the top planar mirror. The alignment is fine tuned by connecting the collection side of the setup with a laser source of a similar wavelength to the one used in the excitation. Hence, one can align the spot from the collection path to coincide to the spot from the excitation path. The collection fiber is then connected back to the detection path and the beam is aligned to the spectrometer slit. Once the set-up is ready, the bottom mirror can be carefully moved up to touch the top mirror. Once there, the cavity length is decreased in very small incremental steps by applying DC voltage to the bottom Z nanopositioner. Between each step a new spectrum is taken, until the scan is complete. The decrease in cavity mode, increases the confined photon cavity mode energy. Hence within a scan once can tune through the energy of the exciton, to go from photonic to 50 per cent excitonic and back to photonic again, when the scan is terminated.

Our setup combines the above capabilities with magneto-optical measurements. This is done by mounting superconducting coils around the sample space. By appropriate ramping

of current. One can increase a magnetic field of up to 9 Tesla in either direction out-of-plane (Faraday geometry.). When the target magnetic field is achieved the user can select a persistent mode. During this mode a superconducting element short-circuits the coils creating an infinite current loop of effectively no resistance. Therefore, a stable high magnetic field can be achieved over several hours.

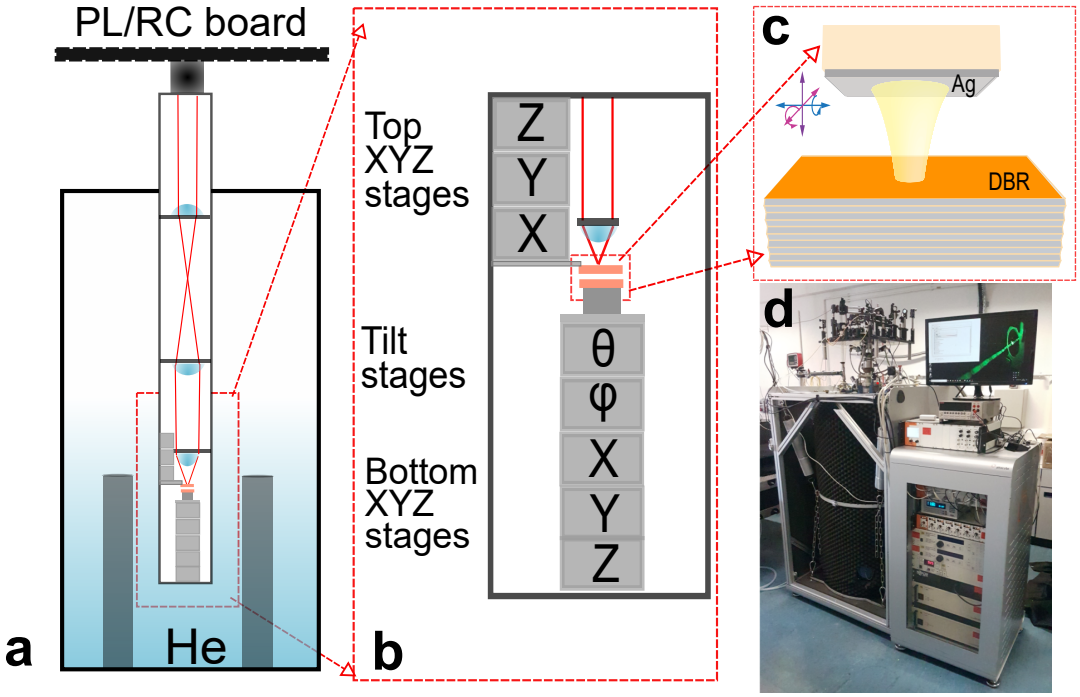

Fig. 3.3 **Low temperature tunable cavity system a** Schematic diagram of the helium bath cryostat and optics setup used. On the top of the cryostat sits a board with the PL/RC optics mentioned in previous figures. Windows and lenses provide optical access to the tunable cavity system and the sample, which sit on the bottommost half of the cryostat. The grey rods either side of the sample area represent the magnet superconducting coils. **b** Schematic of the tunable cavity system. An objective lens focuses the spot on the top mirror. Nanopiezos control an arm where the top mirror sits which allows 3-axis motion. The bottom mirror has two additional nanopiezos for the tilt control. **c** Schematic diagram of the top(Ag) and bottom mirrors(DBR) used for the experiments in this thesis. **d** Photograph of the cryostat/magnet in the lab(left) with the optical board on top. On the right the controls for the nanopiezos, magnet and temperature are depicted.

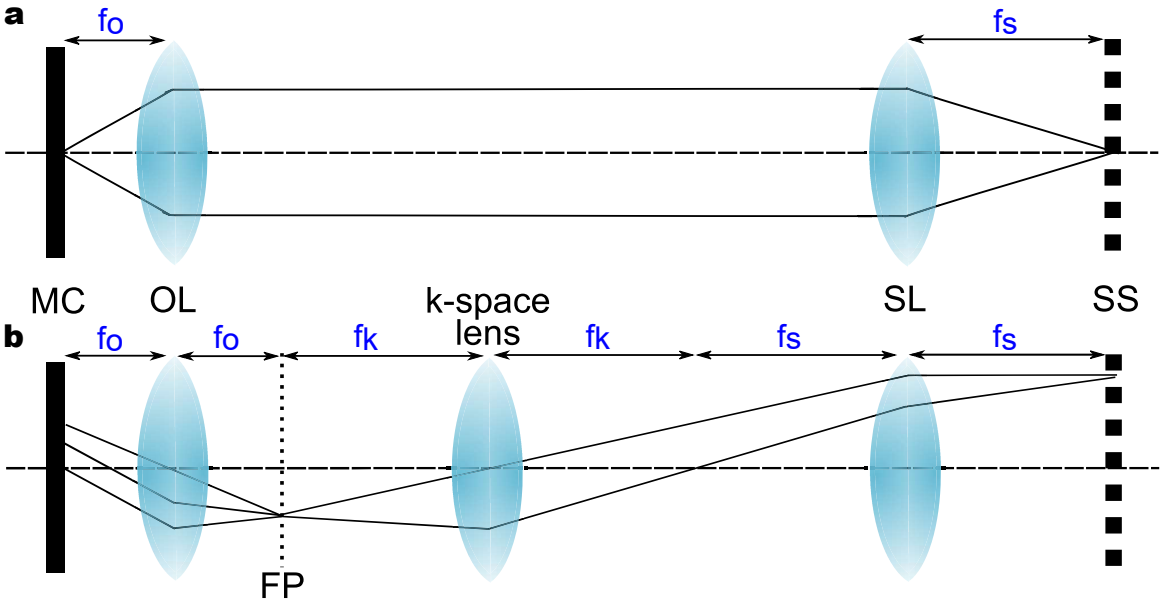

Fig. 3.4 **k-space imaging setup in the collection and detection path** Lens configuration for real space(a) and k-space (b) imaging. The relative position of the lenses (OL,K-space,SL)to the sample (MC) and the spectrometer split (SS).

3.3 K-space Imaging Spectroscopy

The observation of non-linear exciton-polaritons in chapter 6 was performed in fixed-length monolithic cavity samples (MC), as access to the tunable cavity system was not possible. MC are measured by resolving the angular dispersion of the cavity mode energy, which due to the photonic nature is parabolic in the range of angles we can image. This is done by measuring the momentum-space (k-space) energy distribution, which are a Fourier transform of the real space spectra. In optics, each lens can be thought to perform a Fourier transform of the light beam. Hence, by modifying the combination of lenses in the collection side of the RC setups described above, one can direct the k-space image in the spectrometer and CCD array. Therefore, angular resolution of RC is achieved, over the angles the sample is illuminated. The angular range is defined by the numerical aperture of the objective lens

while the resolution depends on the number of rows in the CCD array in relation to the size of the image.

Specifically, k-space imaging works by the introduction of one lens (k-space lens) in the correct position, such that one can image the back focal plane (FP) of the objective lens(OL), as illustrated in the bottom panel Fig3.4. Therefore one has to think of focal length of OL (f_O) and the k-space lens (f_K) in relation to each other's position. In addition, the lens (SL) before the spectrometer slit(SS) has to be considered. The relation of focal lengths the k space lens and SL (f_K,f_S) defines the magnification of the image and therefore the angular resolution of the energy dispersion. Considering the total path length of the collection and detection sides, one can therefore choose appropriate lenses such that the k-space lens can be flipped in and out of the beam path. One can, then, switch from k-space Fig3.4(b) to real space Fig3.4(a) imaging and vice versa.

For measurement preparation one can, therefore, first ensure alignment by imaging the real space spot on the CCD while switching to image its Fourier transform by flipping the k-space lens in. If the SS width is set to maximum, one should see a concentric circle of significantly larger radius(equal in k_X and k_Y directions) and well defined edges. Narrow parabolic dispersion spectral images can then be achieved by closing the slits to select a narrow slice of k_Y near k_X=0 and then putting the grating in the path to disperse the image.

3.4 Mechanical exfoliation and Flake Identification

For fabrication of monolayers, mechanical exfoliation was the method of choice for all the studies included in this theses as it yields the highest optical quality of samples. In this top down approach, commercially available TMD bulk crystals, grown using Chemical Vapour Transport, are placed between blue tape (Nitto BT-130E-SL water soluble tape). The first step is to place the bulk crystal between two pieces of the tape. By gently applying pressure, using the thumbs, to the crystal-tape sandwich one can leave imprints of the crystal on the tape. This is repeated 3 times, trying not to overlap the previous imprint. Once enough amount of

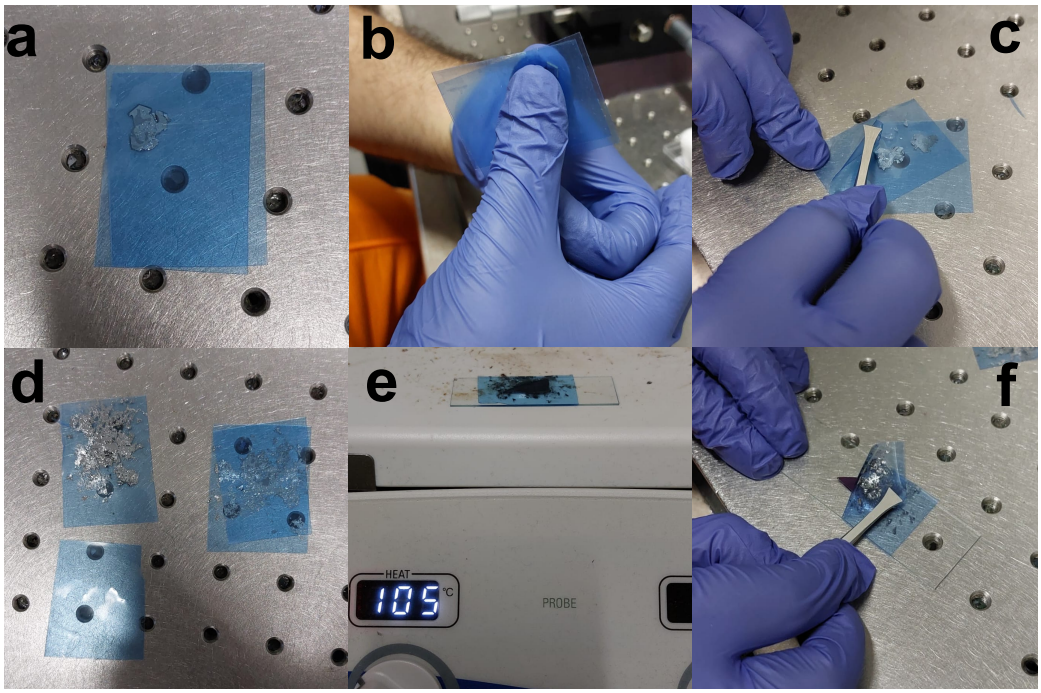

Fig. 3.5 **Photographs of the followed procedure for exfoliation of TMDs on Si/SiO_2 a** The bulk crystal is put in between two adhesive tapes. **b** Gentle pressure is applied and the tapes are separated using tweezers, **c**, to leave an imprint in both tapes. Once 3 imprints are left and density is spread two clean tapes are brought in contact to the imprinted ones, **d**, and are separated to make a total of four tapes. **e** Each tape is attached to Si/SiO_2 and annealed to 105 °C. **f** Once the wafer returns to room temperature the tapes as slowly released to exfoliate the crystal on the SiO_2 surface.

the crystal is on the tape, the next step is to create density. Creating enough density increases the probability of finding a monolayer within a finite surface area of a given substrate. This can be done by rotating the tapes with respect to each other, overlap the imprints with the empty areas to 'fill in the gaps' and then carefully peel them off, avoiding any wrinkles or folds on the tape. The latter step should be repeated by up to four times. Care should be taken not to exceed this number since it was found that too many peels can break the crystal on the tape ultimately resulting in smaller monolayers. The last step is to take two clean pieces of tape, overlap them with the two already made and carefully peel off again to thin down the remaining crystals. Therefore one ends up with four tapes with crystal imprints that can be used to exfoliate on four substrates. The above procedure is a series of steps that

were found to work best after recent independent studies [107] and several trials that I have preformed throughout the duration of this PhD that are in agreement.

The actions in the next step are decisive as this the point where the exfoliation down to monolayer happens. This is the step when the crystal is exfoliated on a useful substrate. The mechanical response of the substrate needs to be taken into account for this step of the process. The two main substrates used are Si/SiO_2 and PDMS, which we will take here as good examples on how to treat mechanically hard and soft substrates, respectively.

Si/SiO_2: This substrate is a hard wafer with relatively low adhesion to the TMD crystals. Therefore during the exfoliation process, crystals are more likely to break laterally, reducing greatly the size of the flakes that exfoliate down to single layer. It is therefore necessary for the user to execute a series of actions that will minimise this effect. The first is to prepare the substrate accordingly, such that there are no contaminants between the top surface of the substrate and the bottom surface of the crystals on the tape. The substrate is cleaned in ultrasonic bath for 10 minutes in acetone IPA and DI water. Once off the bath the substrate is blown with a nitrogen gun to avoid residues of the solvent. The next step is to place the substrate for 7 minutes under Ultraviolet/Ozone (UV/O_3) treatment to eliminate any remain organic residues. The substrates are then taken out of the UV/O_3 machine, placed on a clean glass slide. As soon as possible the tapes with the prepared crystal should be placed on top of the Si/SiO_2 followed by a gentle roll with a cotton bud if air bubbles are visible. Subsequently the substrate is heated to 105 ^{0}C for 30-45 seconds until the tape becomes visibly softer. This enables uniform contact of the interface between crystal and substrate and enhances adhesion between the two. The glass slides are, then, taken off of the hotplate and placed for one minute in a metal optical board until they reach room temperature. Here, it is believed that we make use of the difference in the thermal expansion coefficients of the tape, crystal and substrate, promoting the peeling off of the layers of the vdW crystal. Lastly, the tape is retracted from the substrate in a very slow and uniform speed to avoid breaking of the crystals in contact with the hard substrate. For reference, we use an approximate speed of 10 seconds per cm of the substrate for the motion of the interface of the retracted tape.

Polydimethylsiloxane (PDMS): PDMS is a viscoelastic polymer film. This means its mechanical response is more liquid-like under forces over longer timescales and more solid-like under forces over very short timescales. If the retraction of the tape is made as slow as its done on Si/SiO_2 the liquid like behaviour promotes the crystal to detach from the PDMS and stick to the tape. Therefore a high speed of retraction is needed to retain contact with the crystal and promote exfoliation [108]. Here we use the rule of 1s/cm of substrate as an estimate for a quantified reference. Due to the soft polymer the crystals are less likely to break at the interface of exfoliation. Hence the probability of finding large flakes is significantly larger on PDMS than Si/SiO_2. We also find that in the case the substrate does not have any monolayers after the first exfoliation, it is particularly successful to use a clean tape to re-peel off the bulk crystals from the surface of PDMS hoping that they will exfoliate a single layer on the surface of PDMS. For this a slightly slower peel of 2-3 seconds per centimetre works best.

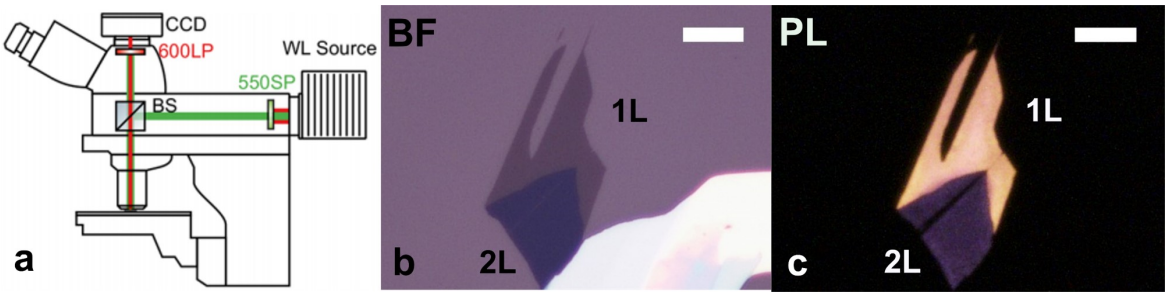

Fig. 3.6 **Flake identification a** Schematic diagram of the microscope based PL set-up used. With the appropriate long pass (LP), short pass(SP) filters and beam splitters (BS) used. Adopted from [57] **b** Optical microscope bright field image of WSe_2 exfoliated on SiO_2. Monolayer (1L) and Bilayer(2L) areas are indicated, showing different optical contrast. The white scale bar is equivalent of 10 µm **c** PL image of the same area, with the same magnification. 1L is bright and yellow and 2L is a dimmer purple.

After exfoliation, the monolayers need to be identified and located. To do this we use a high quality microscope in reflection geometry with a white light halogen lamp source and a series of high quality objectives of magnifications of x5, x10, x20 and x50. The x10 or x20 magnification objectives are used while the XY manipulators of the sample stage are turned to sequentially scan the surface of the substrate. We call this 'flake search'. The BF field mode, where the spectral filters illustrated in Fig3.6 are not present, is sufficient to recognise

the monolayers by their optical contrast to the substrate. Optimisation of the contrast can be achieved by the choice of the substrate on which the flakes are exfoliated. For this we chose a Si/SiO_2 with 90 nm SiO_2 layer thickness to exfoliate the flake onto. For final verification and distinction of monolayers to bilayers photoluminescence microscopy is used in the same set-up. As shown in Fig 3.6 (a) a short pass filter and a beam splitter are used for excitation of the sample at the higher energy end of the visible spectrum. Subsequently, the emission of the sample is collected with the use of a long pass filter before the CCD of the camera. This results in an image where the monolayers are much brighter(and different colour) than the bilayers, since they are direct band gap semiconductors, as in Fig 3.6(c).

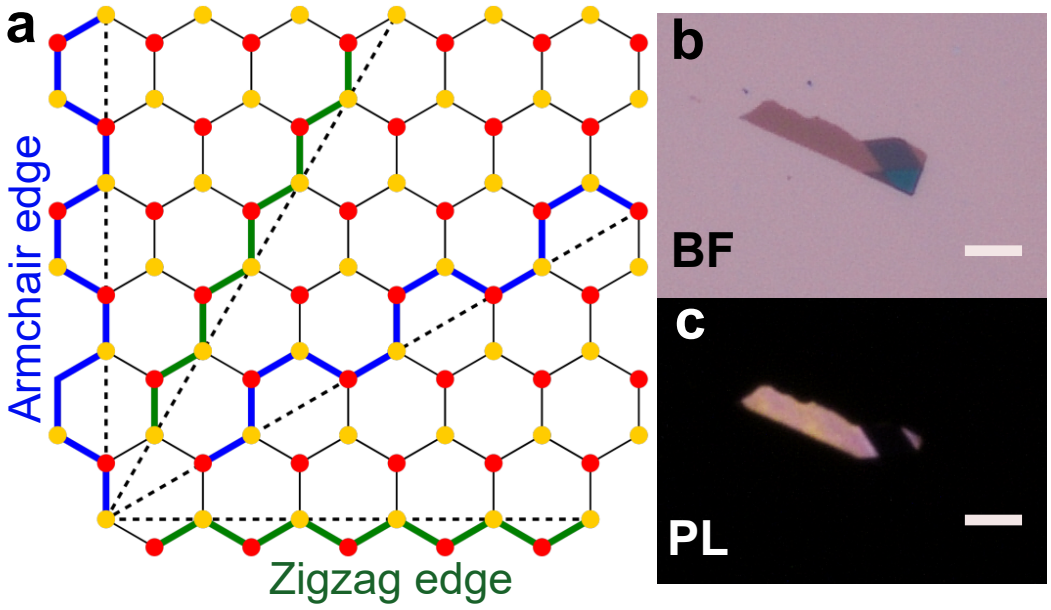

Fig. 3.7 **Flake requirements for heterostructure stacks a** Top view of a TMD honeycomb lattice. The zigzag and armchair crystal axis and their symmetry can be seen with dotted lines. The transition metal and chalcogen atoms are represented with red and yellow colour respectively. **b,c** BF and PL images of a $MoSe_2$ monolayer on Si/SiO_2 suitable for heterostructure fabrication. The white sclae bar corresponds to 10 µm

For the fabrication of aligned heterobilayers discussed in chapter 4, the requirements on the identification of suitable flakes are stricter than in applications where single-layer structures are needed. The prerequisites we are looking for are listed in below:

- **Well isolated flakes :** Since the layers will be stacked together, any thick flakes (>30 nm) attached to the monolayer of interest will constitude a problem, since they will obscure good contact and allow air gaps to propagate during the stacking process.

- **Recognisable crystal axis :** For deterministic stacking with a particular twist angle, the crystal axis of each monolayer needs to be indentified first. TMDs structure makes for a hexagonal lattice, as shown in Fig 3.7 a. This lattice has two crystal axis, which are called zigzag and armchair (Fig 3.7). They are separated by 30 degrees and each axis is repeated with a symmetry of 60 degrees. TMD layers, often, break along these axis. However, due to the fragile atomically thin nature of few layer flakes, this is not always the case. When a monolayer exhibits long straight edges, these are very likely one of the crystal axis. To confirm this is the case, the other edges orientation with respect to the long straight edge is examined. If the other edges are oriented in an angle of 30 or 60 degrees (or their multiples) from the long straight edge identified we can conclude that we have recognised the crystal axis. Unfortunately this is a large constraint as most of the monolayers found do not exhibit clear recognisable crystal axis on multiple edges, especially when exfoliating on hard substrates.

- **Lateral size** The final assembled heterostructure will consist of areas where monolayers overlap, but also of areas of each monolayer alone (encapsulated in hBN) for reference. The laser spot total diameter is 2-3 μ m. Hence, the dimensions of each monolayer should be big enough to allow for multiple laser spots in each of these areas considering the constraints imposed on overlap by orientation considerations.

- **No cracks/strain** The monolayers chosen for heterostructure assembly should be able to provide as spacially uniform interlayer inteface as possible. Hence, the user checks for any cracks or, folds or areas of strain in the BF and PL images .

An example of a flake which was identified to meet the above conditions is shown in Fig 3.7b in both BF and PL images.

3.5 Transfer Processes and their Advances

3.5.1 Transfer Setup and Heterostructure Assembly

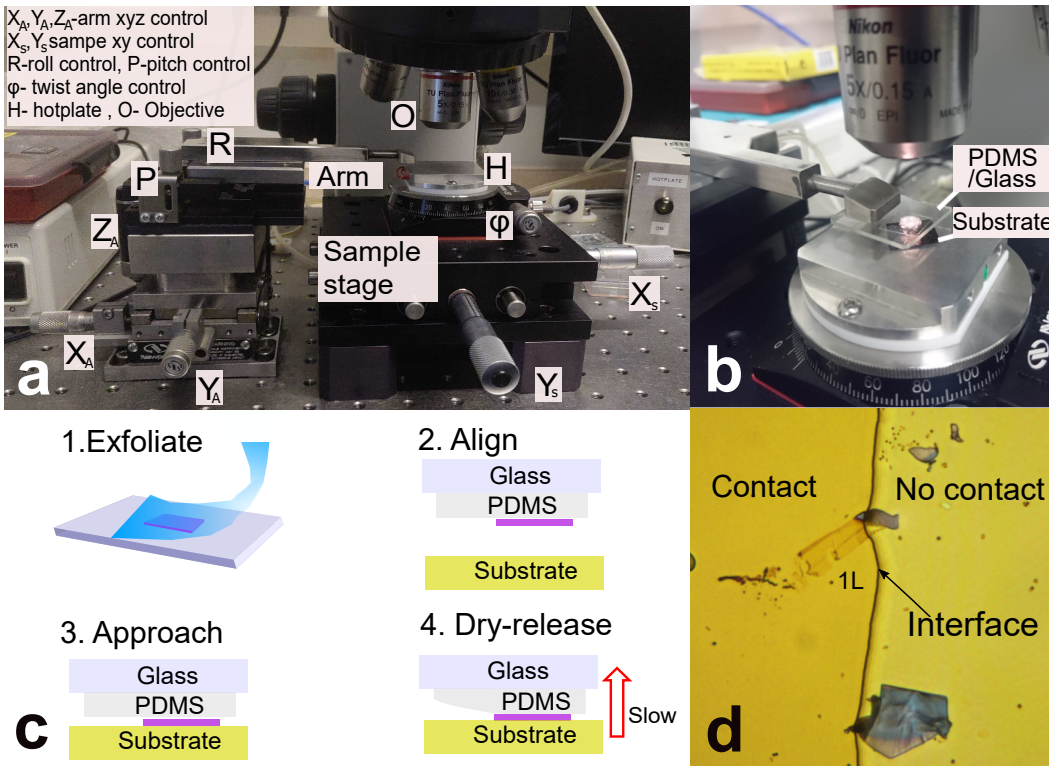

Fig. 3.8 **Transfer Set-up and PDMS dry release a** Transfer setup use. This includes a microscope, a sample stage(rigt) and arm stage (left). The top left legend shows the controls of the setup. **b,c** Close-up photograph during transfer. The arm hold a glass with a transparent polymer membrane (PDMS) where the monolayer to be transferred sits. The target substrate sits on the sample stage directly below. **c** Process for PDMS dry-release transfer. 1. Exfoliate the flake on the PDMS. 2. Mount on the arm and align with the target position on the substrate. 3 Carefully approach the target substrate and ensure good contact 4. Retract very slowly to transfer the flake on the substrate. **d** Contrast difference of contact vs non contact area and the air/PDMS interface that is controlled during the transfer.

Once the flakes are identified, the next step is their deterministic transfer with a specific placement on a required surface or substrate. This is done using the setup shown in Fig 3.8a. This consists of a microscope with long working distance objectives (O) in order to allow enough distance for safely handling the membrane, where the exfoliated flake sits. The membrane is in the optical path, between the objective and the target substrate, which sits

on the sample stage (see Fig 3.8b). The relative position of the flake to the target substrate is controlled by independent XY manipulators for the arm and sample stage, controlled by micrometer screws. The sample stage is equipped with a 5x5cm hotplate with a thermocouple that can reach up to 170 °C. The sample hotplate stage can be rotated at any arbitrary angle, ϕ within the horizontal plane. The rotation is controlled with another micrometer screw with a precision of ± 0.5 °. The tilt between the membrane and the target substrate can be altered by the user with the use of two separate micromanipulators for the roll and the pitch. The precise control of the vertical separation of the membrane and the substrate is of fundamental importance to successful transfer. Therefore for the Z-axis control of the arm, we add a nano-piezo actuator(Newport PZA12) to ensure precision down to 30 nm while still having the necessary range of motion of 13 mm for safe handling. To enhance visibility the camera image can be digitally controlled to apply colour filters for enhanced contrast.

PDMS: Dry release

As mentioned in the previous section, PDMS is a viscoelastic polymer, with a solid like behaviour under short timescale and a liquid like behaviour under large timescale. This is a particularly useful property, that has enabled PDMS to be one of the most convenient and widely used transfer methods. An overview of a PDMS transfer is illustrated schematically in Fig 3.8c. Once the flake is exfoliated, th PDMS on glass substrate with the flake of interest is placed upside down hold by vacuum on the arm of the transfer set-up. Note here the use of transparent glass and transparent polymer films to allow for the identification of the monolayer in this configuration. An outline of the flake is annotated using the microscope software and then the focus of the microscope is moved on the plane of the substrate. Here the XY and ϕ positioners on the sample stage can be moved/rotated such that the flake will be positioned and aligned as required on the substrate. The focus is then moved on a focal plane slightly lower than the sample. The arm is then moved down with the use of the z nanopositioner until it reaches the focal plane the microscope is imaging. The focus is then moved back to the substrate plane and the procedure is repeated to ensure safe approach contact of the monolayer to the substrate. When contact is close, the user

can utilise interference fringes and the air/PDMS (shown in Fig 3.8d interface image at low magnifications to ensure slow and controlled contact of approach of the flake to the substrate. This is important for the reduction of strain and contaminants on the flake. [108]. Once the interface passes the flake we continue for at least 30 μm further and wait for 1 minute to ensure good contact of the flake with the substrate. Lastly, the interface is retracted very slowly to enable the liquid-like response of the polymer, such that the flake detaches from the PDMS and attaches to the substrate. PDMS advantages lie on the ease of the all-dry process, the nearly 100 percent rate of success and on the large flakes that one can produce using this method. It has helped the immense growth of activity in the field by various groups that study atomically thin monolayers. Unfortunately, the properties that cause the advantages also cause the main disadvantage of PDMS method, which is a layer of PDMS contaminants on the surface of the flake. This would therefore significantly reduce interlayer coupling of heterobilayers in the case of sequential dry release transfer from the lower to the upper layer [57].

PC: Pick-up

To avoid the aforementioned problems stemming from polymer contact to each layer, pick-up methods have been developed. In these methods, each of the layers is exfoliated on Si/SiO_2 and sequentially picked up by a membrane, starting from the top layer and ending with the bottom. For successful pick-up a mechanically stiff polymer with sufficient adhesion is needed. One of the methods used in this work is the polycabonate (PC)[109]. The membrane is made of PC solution(6 % dissolved in chloroform mixed at HQ Graphene). The films are prepared from the solution and secured with a double sided tape on a glass slide, with the PC membrane sitting on small piece of PDMS. The latter acts as a cushion and allows reproducible pick-up with low strain. A schematic of a membrane is shown in Fig 3.9. In the top view schematic, a small cut on the double sided tape is illustrated. This is to allow for an air channel. Enabling hot air to escape during the fabrication process prevents the detachment of the PC membrane from the PDMS, increasing the reproducibility of the method. Once the membrane is prepared, the first layer can be picked up. Just before approach the temperature

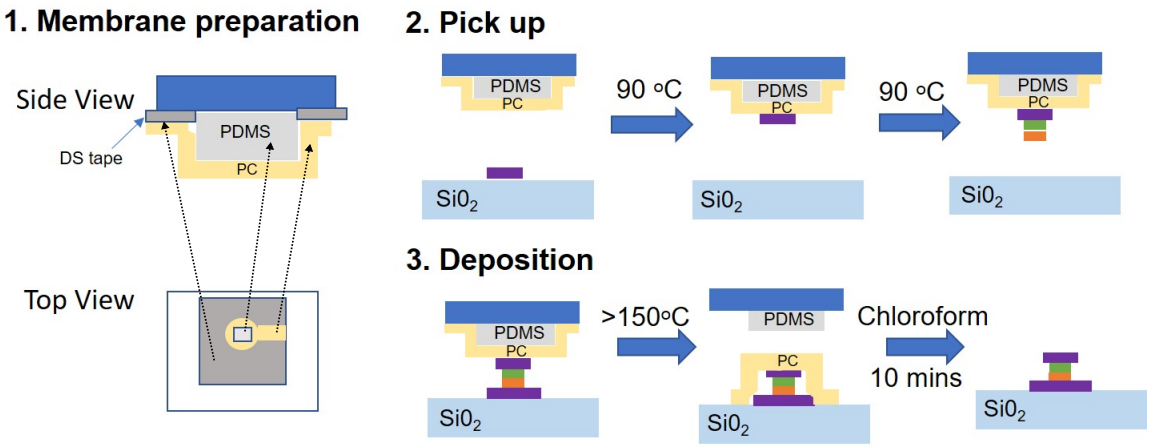

Fig. 3.9 **Polycarbonate (PC) pick-up method for heterostructure fabrication**: 1. Membrane preparation. Sideview of glass, double sided (DS) tape holding the PC membrane on the glass. In between PC and glass is a PDMS cushion. Below is the topview of a prepared membrane. One the right we can see a channel is cut in the DStape to allow hot air to escape. 2. Pick-up process. Raise the temperature to 90 °C approach and retract to pick up. Repeat for each flake. 3. Once structure is complete approach the stack on the target substrate. Raise the temperature to above 150 °C to leave the PC membrane on the substrate. The membrane is subsequently dissolved in chloroform.

is raised to 90 °C. Then, a careful approach and retraction are enough to pick up any flake in contact with the membrane from Si/SiO_2 , due to the high adhesion of PC. The process is repeater untill the stack is complete. For the final step, the stack is deposited on the substrate with the membrane on top, by heating the membrane above its glass transition. To this the temperature is raised to $\geq$ 150°C before contact. Temperatures above 150°C increase the success rate of this last step, but are only recommended in inert or vacuum environments. Later on, the membrane needs to be dissolved in chloroform for at least 10 minutes. To clean the residues, baths in iso-propanol and deionised water follow.

PMMA/PDMS: pick-up and dry release

The following section is a description of the widely used PMMA method with some refinements.

Polymethyl methacrylate (PMMA) has long been used as a polymer for atomically thin material transfer. Its is a much softer polymer than PC but not as viscoelastic as PDMS. To

exfoliate on it one spin coats a sacrificial layer, like PMGI Polydimethylglutarimide (PMGI SF-8) on Si and then PMMA(950 A3.5) follows. Thereup, the procedure for exfoliation on Si/SiO_2 is followed to identify the first layer of the structure. The wider area around the layer is scratched, enabling access for the developer (MF-319) to dissolve the sacrificial PMGI. The PMMA with the monolayer is then retrieved from DI water to make a membrane. In the initial form of this method, the above procedure was repeated for every layer, and dry release was performed sequentially starting from the bottom layer, given that each successive layer's lateral dimensions were smaller than the previous one. Despite PMMA leaving less residues than PDMS, the problem of interlayer contaminants was present also in this method. After that, groups were able to use the same membrane to pick up. The below section shows modifications and refinements performed to the old method, resulting from a combination of our trials and recent studies [110] to enable reproducible pick-up from Si/SiO_2, followed by dry release on an exfoliated hBN flake of larger dimensions than the heterostructure. Fig 3.10 illustrates the three main steps in this method. Firstly the membrane is prepared in the conventional PMMA method where the sacrificial layer is dissolved. Then the PDMS was secured on a ring membrane holder with the help of a double sided tape with a hole to ensure PDMS does not detach at any point of the fabrication from the ring holder. This is used to retrieve the membrane from the water's surface and let to dry for a minimum of 30 minutes at 60 degrees Celsius to accelerate the process. Subsequently, the structure was assembled by picking up the next layers from Si/SiO_2 (90nm). To pick-up, the temperature is raised to 75 ^{0}C before approach. Later, the membrane is slowly brought in contact with the substrate after orienting and overlapping the required flakes. After one minute, the temperature is lowered to 55 ^{0}C. The aforementioned change in lower temperatures promotes a more solid-like behaviour of the membrane system to enable pick-up. We have, also, noticed that such behaviour can also be promoted by increasing the speed of retraction, compared to the very slow speeds used in most of the conventional methods. However, a great speed can lead to tearing of the flakes to be picked up. Therefore, moderate speeds were used to pick up. Once the structure is complete, one normally can slowly dry release the structure on an large hBN. However in applications were the complete structure needs to be deposited on a bare

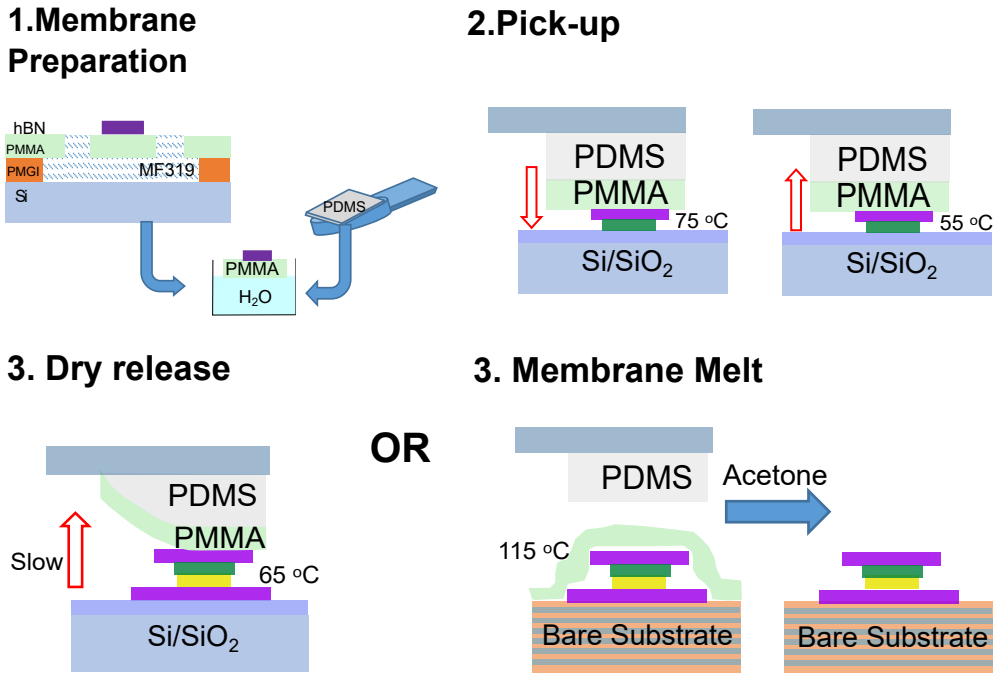

Fig. 3.10 **PMMA pick-up/dry release method for heterostructure fabrication**: 1. Membrane preparation. Sideview of exfoliated hBN on PMMA/PMGI/Si wafer. The PMGI is dissolved with MF319 and the membrane is then allowed to float in deionised water. A metallic loop with PDMS attached is used to retrieve the membrane and let to dry 2. Pick-up process. To pick-up align the flake with the hBN and approach slowly at a temperature of 75 °C. Once good contact is ensured, the temperature is dropped to 55 °C and the membrane is retracted. This process is repeated for consecutive layers 3. Deposition: This method allows to dry release if the substrate is another 2D material, such as hBN, at a temperature of 65 °C and a slow retraction. Alternatively, for deposition on bare substrates the membrane is heated to 115 °C to be left with the stack on the substrate and then dissolved in acetone.

substrate, dry-release is not possible since the imbalance of adhesive forces on the flake from the PMMA and the substrate is too large. Hence, heating the PMMA at a temperature above the glass transition is required, along with dissolving in acetone. To clean the residues, baths in iso-propanol and deionised water follow.

3.5.2 UV/O_3 treatment of PDMS for heterostructure fabrication

The following section is a report of the effort for the development of new fabrication processes in the duration of my PhD which has enabled easier transfer on substrates of interest for the studies shown in the following chapters

The deposition of van der Waals (vdW) heterostructures with minimal interlayer polymer residue on low adhesion substrates, often requires complications such as organics solvents and metal contacts. In this work, the surface stiffness and adhesive properties of Polydimethylsiloxane(PDMS) is altered with exposure to Ultraviolet/Ozone (UV/O_3). This serves as an pick-up membrane to ultimately demonstrate dry release of stacks on very low adhesion substrates, such as dielectric Distributed Bragg Reflectrors (DBRs). The effect of UV/O_3 exposure is further investigated with the use of Atomic Force Microscope (AFM) nanoindentation and the fabricated structures are characterised with optical imaging studies.

Introduction

As seen is previous sections 2D materials and their vdW heterostructures are mainly transferred by two methods: dry release[108, 111, 112] and pick-up[113, 109, 114]. In dry release methods the structure is build starting from the bottom-most layer successively depositing each layer until the structure is complete to the top. However, as each layer is in contact with the polymer, dry release methods result in a significant amount of interlayer contaminants [115, 116]casing a weakened interlayer coupling [57, 117], To reduce this problem, pick up methods have been developed, where the structure is build starting from the top-most layer while pick up each subsequent layer from a non-polymer substrate. With the refinement of some techniques (Section3.5.1),[110], the stack can be dry released to the bottom-most layer, like hBN, if the latter can be exfoliated on the substrate of interest. However, some of the great advantages of PDMS is lost. For example, the flexibility to transfer to any bare substrate of interest of virtually any roughness. In addition the ease of all-dry membrane, with no required steps for membrane preparation. Deposition of stacked structures on bare substrates, such as Distributed Bragg Reflectors (DBRs) often requires the polymer membrane to be brought in contact with the target substrate and is then melted. It subsequently needs to be dissolved in organic solvents. Exposure to solvents and high temperatures compromise the optical quality of of atomically thin semiconductors or, in some cases, induces a risk in losing the structure.

One approach to overcome this limitations is to utilise thermoplasticity of the membrane to promote a more solid like behaviour for the pick up and a more liquid like behaviour with temperature for the dry release of the structure[118].

Our approach is to selectively tune the surface properties of PDMS, arguably the most widely used polymers in the community, by the use of ultraviolet Ozone (UV/O_3) treatment. By carefully choosing the exposure time one can modify the polymers surface, to enable pick-up, while not destroying the overall bulk viscoelastic behaviour of PDMS the enables dry release transfer on bare substrates.

Effect of UV/O_3 treatment on PDMS

In the following section the effect of $UV/0_3$ on the structure and mechanical behaviour of the PDMS film is discussed and supported by AFM investigations performed by collaborators within our department. PDMS exposure to UV/O_3 causes an abstraction of hydrogen. Then a Methylene radical (CH_2) reacts with oxygen to give a peroxy radical (HO_2) which, then, rearranges to a silanol group (Si-OH). This causes a condensation reaction of silanol groups forming a SiO_2 layer on the surface of the film, while further in methyl side groups are retained as shown in Fig 3.11 a . [119, 120] Systematic nanoindentation AFM studies were carried out to confirm this effect on the PDMS films used in our method. A silicon nitride tip was approached and force distance curves were taken for films with UV/O_3 exposure times ranging from 0 minutes to 105 minutes of exposure in 15 minute increments. A grid of 64x64 curves over a 30 μm^2 area on each film was taken. As expected, the indentation data taken, shown in Fig b, reveal a clear effect of the exposure on the surface hardness. In particular, after 60 minutes the surface is significantly stiffer as seen in the slopes of in the inset of Fig b. This surface stiffness allows a more solid-like membrane with an adhesion that is slightly higher than that of SiO_2. Hence, the treated membrane can act as an acceptor or pick-up membrane flakes from softer polymers.

Despite the surface modification, it was found that the dry transfer of flakes or stacks from the $UV/0_3$ treated PDMS to the low adhesiion substrate is still possible . The SiO_2 layer is only formed a few nanometers[119, 120] on the surface, while the rest of the film

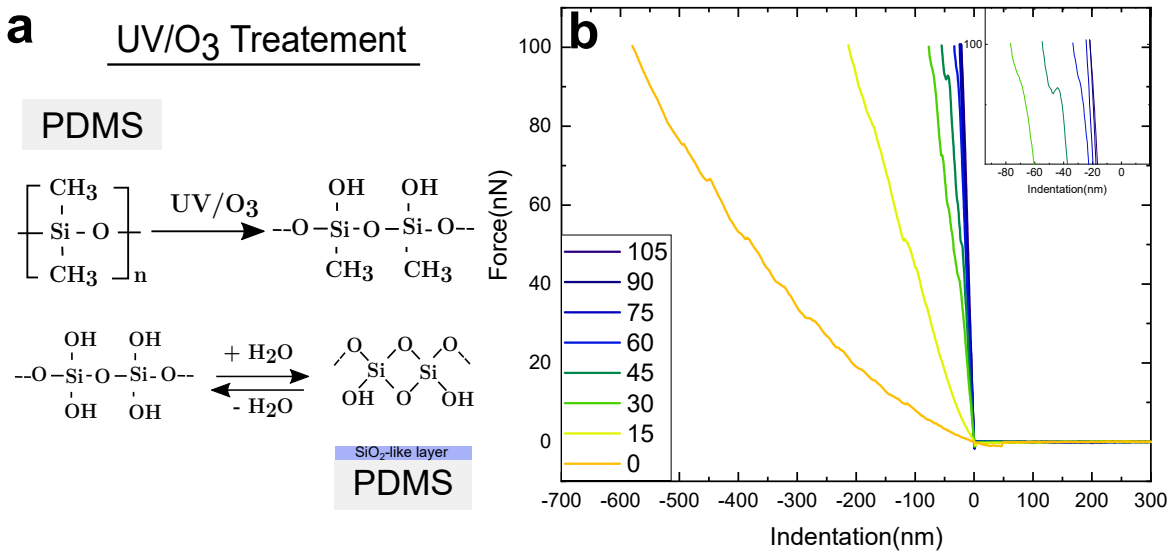

Fig. 3.11 **PDMS surface hardening upon UV/0_3 treatment.** **a** Schematic of structural change of PDMS surface under treatment. A SiO_2-like layer is formed on the top surface **b** Nanoindentation measurements from 0 to 105 minutes of exposure indicating a change of surface

remains unchanged. Hence, the bulk viscoelastic properties of the PDMS are unaffected. This is also supported by a study on similar PDMS films [120], where the storage modulus of PDMS stays within the same order of magnitude, in contrast to other polymers. We found a dry-release success rate of about 75 per cent, with a significantly increased rate of success with structure of total thickness over 30 nm. Also, cleaning the substrate with the appropriate organic solvent baths followed by 5 minutes of exposure to UV/O_3 was found to increase the rate of success

AFM adhesion measurements were also carried out, as a function of exposure time in a similar arrangement to the nanoidentation measurements, but with smaller force of 2 nN for the indentation. When the tip was retracted, an adhesion pull-off force was measured. As shown in Fig. 3.12 a decay of the adhesion force was observed, asymptotically approaching a minimum value after 30 mins. The adhesion force measured may be attributed to the rapid decrease of the vdW forces due to the formation of the SiO_2 like layer.

The effect of UV/O_3 treatment is further investigated in terms of roughness, another interrelated parameter that may dictate successful dry release transfer of two dimensional

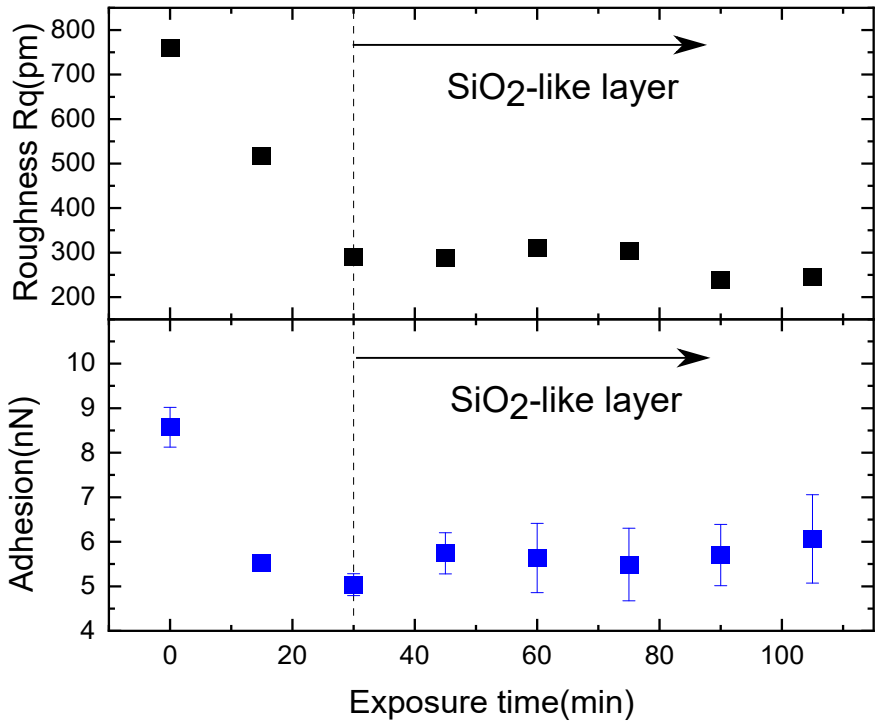

Fig. 3.12 **Further changes on surface properties upon UV/O_3 treatment.** Surface roughness **a** and adhesion **b** from 0 to 105 minutes of exposure. The approach to constant values for both variables after 30 mins indicates the creation of SiO_2.

materials. Images of length scales of $\approx$ 200 nm were taken and the images were analysed to find the root-mean-square roughness .As shown in figure 3.12 the roughness of the PDMS decreases steeply with exposure for the first 30 minutes and then levels plateaus at around 300pm. This is another consequence of the SiO_2-like layer formation. We therefore present the capability to tune the roughness of the membrane in accordance to the required target substrate of the specific application. Our target substrate is a DBR, which we have measured to have a roughness of 292 pm, matching the roughness of UV treated PDMS.

Proposed uses UV/O_3 treated PDMS for heterostructure assembly

After presenting the tunability of the properties of UV/O_3 treated PDMS we proceed to suggest their use for van der walls assembly techniques. This can be particularly advantageous for applications were larger samples than the ones obtains from SiO_2 are needed with clean encapsulated interfaces. The relative surface rigidity offered by the formation of SiO_2 layer

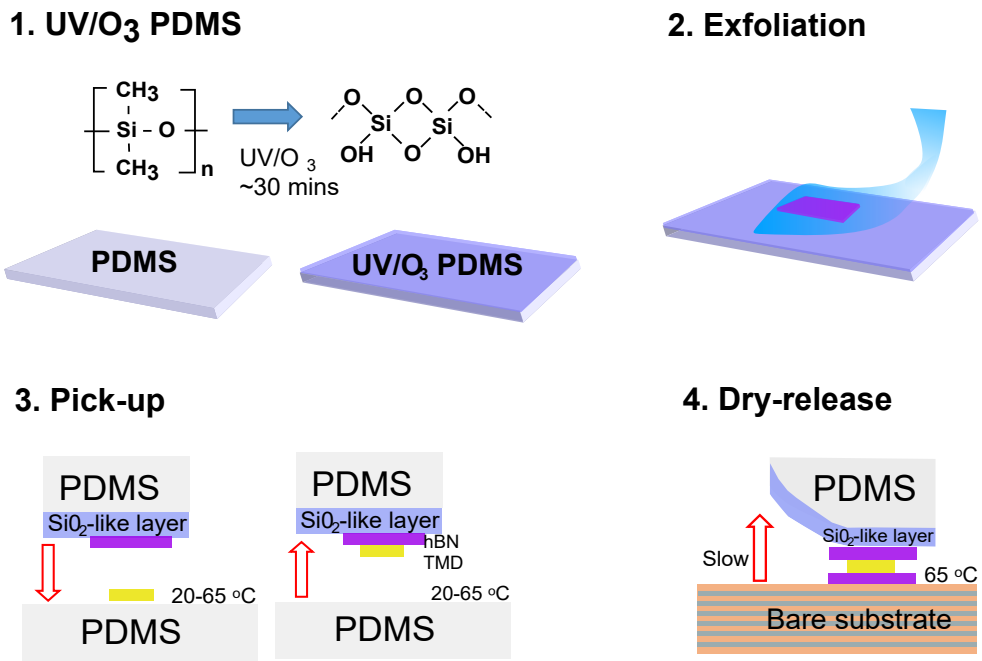

Fig. 3.13 **UV/O_3 treated PDMS for heterostructure fabrication** 1. PDMS is exposed in UV/O_3 for at least 30 mins 2. Exfoliation of the top layer (hBN) on the treated PDMS 3.Pick up from untreated PDMS from room temperature to 65 °C. 4. The stack can be dry released on a bare low adhesion substrate with a very slow retraction of the treated membrane

allows to pick up flakes exfoliated on softer polymers. In Fig3.13 we illustrate the process we used to pick up flakes exfoliated on untreated PDMS, but we note the possibility to pick up from other soft polymers, like PMMA and hot PPC. Firstly, a PDMS substrate is treated. We find that any time greater or equal to 30 minutes works for the purposes of this method, consistent with the adhesion and roughness measurements aforementioned. A few minutes after the treatment we proceed with the exfoliation of the top layer of the structure, like hBN, which will be used to pick up other flakes. As mentioned in Section 3.5 mechanical exfoliation on softer substrates is done fast, where as on hard rigid substrates the peel is executed as slowly as possible. Our membranes have bulk viscoelasticity but a more rigid surface. Therefore we find a more medium speed (of about 3s per cm of PDMS/tape interface) to work best. Once the required top hBN flake is identified one can proceed with the pick up step of the process. To do this the the membrane with hBN is carefully positioned and aligned with the target flake on the untreated PDMS. Similar to other methods, we find that a slow speed of approach is crucial to achieve clean interfaces, as one needs to allow time for

contaminants to escape the surface of the flakes. To pick up we wait for 1 min to ensure good contact and then the membrane is carefully retracted, attaching to the hBN on the UV/O_3 treated PDMS. We find that without the use of temperature, only the parts that are in contract with the hBN re picked-up. We, also, find that increasing the temperature to 65 ° C before approaching, increases the chances of picking up areas that are not in contact with hBN which may be desirable for partially encapsulated structures. We attribute this to increased adhesion to the SiO_2 layer at high temperatures. The pick up step is repeated for the number of layers desired to be stacked.

Once this is done the final step is to dry release the stack to the desired bare substrate. In our case, we release the structure on DBRs, but we note the possibility to deposit the stack on a clean substrate of exfoliated hBN on Si/SiO_2 as done in other aforementioned methods(3.5.1). To perform the dry release, we note that the speed of retraction should be as slow as possible, even slower than what is required for untreated PDMS transfer. During the transfer we also increase the temperature to 65 ° C before contact to promote adhesion to the substrate. Figure3.14b shows a structure fabricated with the above method. The dark field

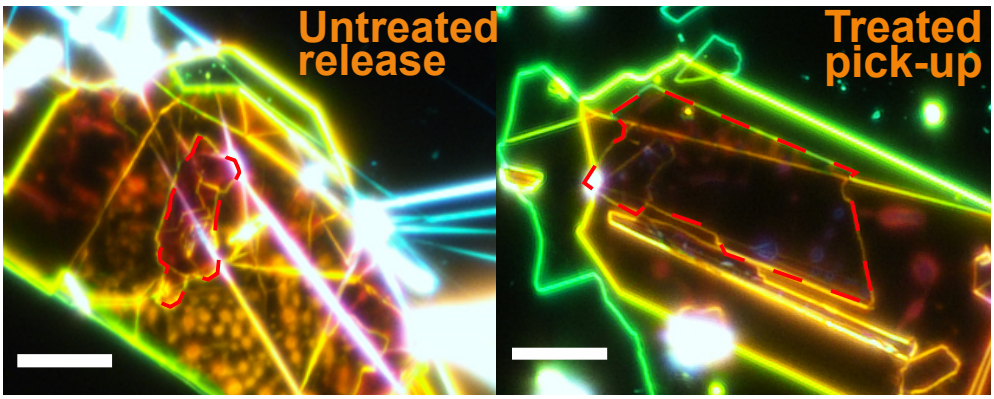

Fig. 3.14 **Untreated vs treated PDMS heterostructures**(left) Dark Field (DF) image of an encapsulated bilayer fabricated by sequential dry release of untreated PDMS (b) DF image of the same exposure time of an encapsulated bilayer fabricated with the proposed UV/0_3 treated pick-up method.

images show clean interfaces without any bubble formation from interlayer contaminants. In contrast, the dark field image of a structure fabricated with sequential PDMS release transfer(see Fig 3.14a) shows a large amount of interlayer contaminants. Hence we see that,

despite the exfoliation on PDMS, our method allows for relatively clean interfaces. We believe that the formation of oxide on the membrane surface acts as a protective layer for contamination during the pick up. Our finding and interpretation may also support the results of a recent study were they found that dry released monolayers from UV/0_3 treated PDMS with vacuum annealing resulted in significantly less contamination [121]. In addition, in the case of the encapsulated bilayer shown above only the interface of the flake with the bottom hBN was in contact with the untreated polymer, which could also greatly reduce the contaminants trapped in the structure. We also note that all the structures are fabricated in ambient air. We anticipate that this method can yield even cleaner heterostructures when applied to an inert environment, due to the absence of hydrocarbons [122] along with the possibility to be combined with vacuum annealing [121].

In addition UV/O_3 treated PDMS may be used as an intermediate step to enable dry release to substrates, where other polymer membranes (like PMMA) cannot due to the large imbalance of adhesive forces on the flake from the membrane and the substrate. This allows to avoid complications like melting the membrane,clamping and exposing the structure to solvents. The more solid-like behaviour of the treated PDMS surface and the higher adhesion to the SiO_2 -like layer allow a release from the PMMA membrane to the treated PDMS by a slow retraction at 65^0C. Finally, the structure can then be dry transferred on the low adhesion substrate by repeating a very slow retraction at elevated temperature. It is noted that at this point the structure is vertically flipped. Therefore, the first layer that was used to pick up the rest will end to the bottom of the structure, which should be taken into account before starting the fabrication process. In addition, we found that a treatment time of 60 to 75 mins is needed, as it relies highly on the larger Young's modulus of the surface. This method is dependent on a fine balance of forces and hence we introduce this intermediate step as a last resort for cases that dry transfer on the bare substrate is not possible. Successful completion of this method combines no polymer contact with no exposure to solvents or high temperature. Hence the structures produced are of high quality, as we have observed in the the encapsulated monolayer of MoS_2 assembled. Fig 3.15 shows the structure deposited on a DBR.Fig 3.15 (a,b) show optical BF and PL images of the monolayer. To examine the homogeneity, we

have also taken AFM height (c) and phase (d) images that show the uniformity of the sample. Low temperature PL of a fully encapsulated MoS_2 structure is shown in Fig. 3.15e . The narrow linewidth of 7.7 meV of the neutral exciton at 1.94 meV and the suppression of the low energy defect related emission [37] (despite the low thickness of top hBN (5nm) and without the use of glovebox environment or vacuum annealing) confirm the high optical quality of structures by the use of this fabrication method.

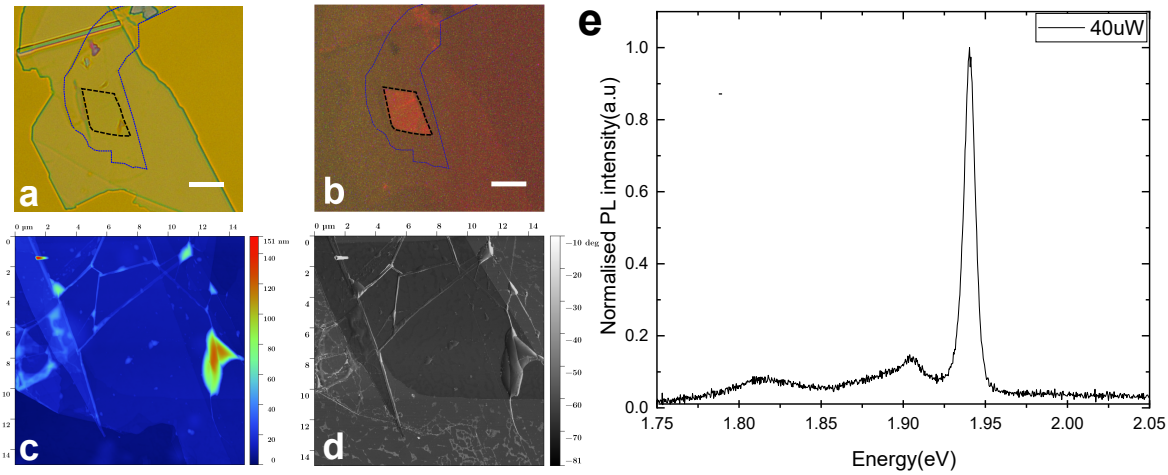

Fig. 3.15 **Characterisation of a fabricated structure with UV/0_3 PDMS as intermediate step a** Bright Field image of encapsulated monolayer MoS_2 on DBR. Top hBN (5 nm) in blue silhouette and MoS_2 (ML) in black silhouette. Bottom hBN is 45 nm. White bar is 10 µm. **b** PL image of the structure. Brighter region is the emission of the monolayer. White bar is 10 μm. **c** AFM height image of the heterostructure. Structure is clean without any vacuum annealing or AFM cleaning **d** AFM phase image of the heterostructure. MoS_2 region is shown as a darker phase. **e** Low temperature (5K) PL spectrum showing narrow linewidth and reduced low energy defect states

To summarise, the concept of using UV/O_3 treatment for altering the mechanical behaviour of widely used elastomers, like PDMS, is introduced to 2D heterostructure fabrication to enable dry transfer of high quality structures on low adhesion substrates. Treated PDMS of stiff surface, soft bulk and similar adhesion levels to untreated can be used in combination with other pick-up methods such as PMMA or PPC to pick up flakes from silicon and then dry transfer on low adhesion substrates, such as DBRs. This tuning of the mechanical properties of the surface of polymers, allows pick up and dry release methods to meet and ,hence,

enable dry transfer on substrates that were not able before without the use of solvents and high temperature.

CHAPTER 4

INTERLAYER EXCITON ENGINEERING IN TMD ALLOYS HETEROBILAYERS

4.1 Introduction

Arguably the greatest promise of atomically thin two dimensional semiconductors is the ability to vertically stack an arbitrary choice of constituent layers of van der Waals(vdW) heterostructures. Their properties make an ideal platform to develop novel ultra-flexible devices with widely tunable properties[8, 123] as well as gain new insights in the physics of excitons[42, 41] and emergent quantum phenomena in moiré superlattices[85, 124, 125]. More specifically, as mentioned in section 2, type-II band alignment and charge transfer allows for the formation of new excitonic species of interlayer excitons (IX). One therefore has an unprecedented amount of tunability of energy of IX through the arbitrary choice of materials and stacking angles.

However, at the moment, air stable TMD monolayers with well known bandstructures hosting excitons in the visible range are mainly limited to MoS_2, WS_2, $MoSe_2$ and WSe_2. Here we employ the approach of continuous tuning of the semiconductor structure properties by the use of alloyed materials, which has been successfully applied in numerous applications from lasers to few-nm-sized transistors in more traditional III-V, II-VI and group IV semiconductors[126]. This approach allows gradual tuning of bandgaps as well as the whole band-structure, allowing to control carrier confinement and thus influence their transport

and optical properties. Numerous semiconducting alloys of layered materials have been demonstrated in the monolayer form achieved both by direct synthesis and exfoliation from bulk[127]. One example is $Mo_xW_{1-x}Se_2$, where alloying was used to control the valley polarisation properties[128]. More recently, alloying was employed to tune the energy of interlayer excitons[129] in $WS_{2(1-x)}Se_{2x}/WSe_2$. In our work, we employ alloying to tune the energy of IX in $Mo_xW_{1-x}Se_2/MoSe_2$ heterostructures for a variety of composition x, in a similar way to recent studies of $WS_{2(1-x)}Se_{2x}/WSe_2$[129]. We demonstrate significant tuning of IX energy, as well as unusual asymptotic dependence of its energy around the x composition near the homobilayer case.

This work is part of a large study including both $Mo_xW_{1-x}Se_2/MoSe_2$ and $Mo_xW_{1-x}Se_2/WSe_2$ heterostructures which is about to be submitted. The author of this thesis was the main contributor for the $Mo_xW_{1-x}Se_2/MoSe_2$ structures and was also involved in the fabrication and measurements of some of the $Mo_xW_{1-x}Se_2/WSe_2$ heterostructures. Hence, the results presented are mainly on the Molybdenum based heterobilayers. When judged instructive, $Mo_xW_{1-x}Se_2/WSe_2$ data are presented alongside the $Mo_xW_{1-x}Se_2/MoSe_2$, or referred to in Appendix A

4.2 Alloy Heterostructure Optical characterisation

The TMD heterobilayers (HBLs) were fabricated by assembling mechanically exfoliated monolayers from bulk crystals of pure $MoSe_2$ and alloyed $Mo_xW_{1-x}Se_2$. Using fabrication techniques mentioned in section 3 the monolayers were assembled together as nearly aligned as possible (with either near 0° or 60° degree crystal axis rotation) and encapsulated in hBN of thicknesses of the order of 30 and 10 nm for bottom and top, respectively. A range of heterostructures were made with varying alloying concentrations. With increasing molybdenum concentration, x, we expect the IX energy to be tuned towards the blue, due to the type-II band alignment, as illustrated in Fig 4.1. Their excitonic transitions were studied using photoluminescence (PL) and reflectance contrast (RC), the latter defined as $RC(\lambda) = (R(\lambda)$ -

R0(λ))/(R0(λ)), where R (R0) is the intensity of light reflected by the sample (substrate). This section demonstrates the characterisation carried out in our structures, through the example of a high quality structure of $Mo_{0.21}W_{0.79}Se_2/MoSe_2$.

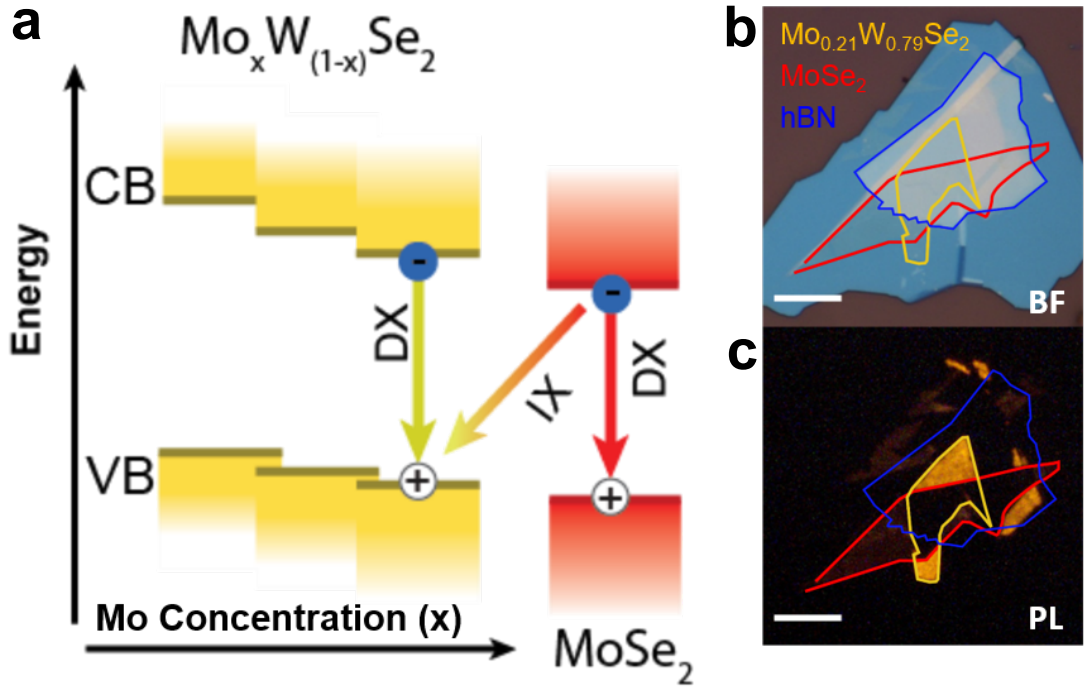

Fig. 4.1 **Alloy heterostructure band edge configuration a** Band alignment configuration at the k-point. Both Conduction and Valence Bands (CB and VB) of alloyed monolayers redshift with concentration,x. This cause the IX excitons to increase in energy. **b,c** Bright Field (BF,b) and PL(c) optical microscope image of the heterostructure. The $Mo_{0.21}W_{0.79}Se_2$ monolayer, $MoSe_2$ monolayer and top hBN flakes are marked with yellow green and blue silhouettes, respectively.

Fig 4.1c shows a room temperature PL microscope image of one of the structures fabricated for this study. The alloy monolayer outline is highlighted with yellow lines, while the edges the $MoSe_2$ flake are shown in red. The bright regions correspond to the area of only monolayers encapsulated in hBN with luminescence from the intralayer excitons. As expected the alloy monolayer area is brighter, due to the higher concentration of W atoms, since W based TMDs emit significatly brighter than Mo based TMDs at room temperature. Notably lower PL intensity is observed in the heterobilayer region where the two monolayers overlap. This arises from the quenching of the intralayer exciton PL due to the efficient

charge transfer between the layers. It shows efficient interlayer coupling and confirms the formation of a type-II heterostructure[57, 130, 50].

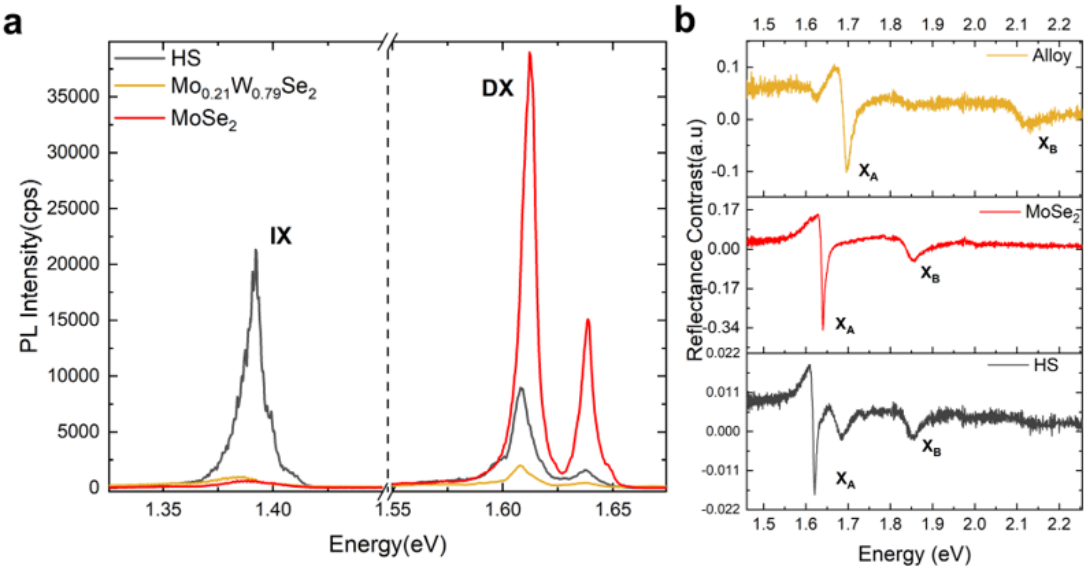

Fig. 4.2 **Optical characterisation at cryogenic temperature (10K)**. Photoluminescence(a) and RC (b) specta of the structure shown for the heterostruture(HS) region in black. The spectra of monolayer regions are shown in red for $MoSe_2$ and gold for the alloy

Optical spectroscopy was also performed at cryogenic temperatures of 10 K. Fig 4.2a shows an example of the PL spectrum of the $Mo_{0.21}W_{0.79}Se_2/MoSe_2$ in the area where the two monolayers overlap (HS) with spectra of areas of just monolayers for comparison. The high energy features of HS spectrum are a combination of the alloy and $MoSe_2$ intralayer exciton (DX) spectra. At the low energy side, the strong emission peak originates from the interlayer exciton(IX). It is worth noting that at this particular structure the relative intensity of IX compared to DX was particularly strong throughout the sample's area, due to the good coupling of the layers and the relatively uniformly clean interface between the TMDs. It can be seen that the high energy spectral region of the HBL area has much lower counts than the monolayer regions for the same exposure time, due to the efficient interlayer coupling. However, we note that the relative intensity of IX to DX in the hererostructure region strongly depends on the quality of the sample and the nature of IX involved. In RC, Fig Fig 4.2b, the region of overlap of the HBL is a superposition of the intralayer exciton absorption peaks

observed in the constituents monolayers. As expected no clear signature of IX is observed, as their oscillator strength is small, due to their out of plane dipole moment orientation and reduced electron-hole wavefunction overlap.

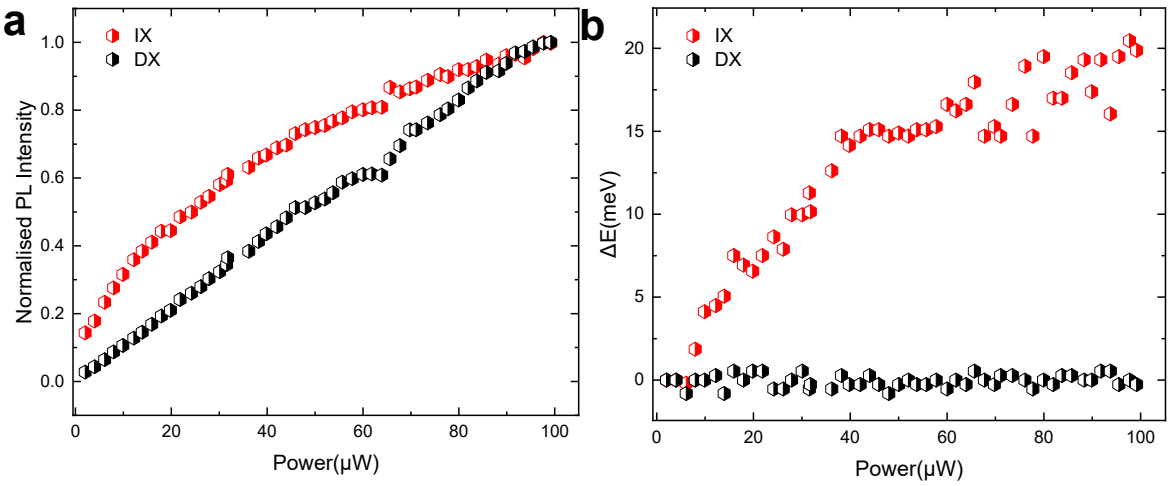

Fig. 4.3 **Power dependent PL of IX vs DX.** PL peak integrated intensity(a) and energy shift (b) of IX vs DX as a function of excitation power

Their dipolar nature is also evident in the power dependent PL measurements. Using continuous wave (CW) excitation the power was tuned from 2 to 100 μW and the integrated intensity of the IX PL region of the spectrum was measured, shown in Fig 4.3a. For comparison the same is shown for intralayer excitons (DX) of monolayer $MoSe_2$ in the same structure. As can be seen the latter follow a linear dependence of intensity as the number of excitons in the system increase with power. However, for IX the PL intensity saturates above a certain excitation power. In addition a strong blueshift of IX energy is apparent, 4.3b, in contrast to DX. The interlayer excitons possess permanent dipole moments aligned along the direction normal to the plane of the device, resulting in enhanced repulsive dipolar exciton-exciton interactions[71, 64] of coulomb nature. This gives rise to a blue-shift of the PL peak energy at sufficiently high excitation density. Above a certain excitation power threshold both the blue-shift and the PL intensity saturate, due to exciton-exciton annihilation processes[131].

Here we note that, apart from the enhanced Coulomb interactions, we believe the observed blueshift to be also a result of the significantly longer lifetimes of IX compared to DX. This

is true since the excitation is achieved through a CW pump, continuously exciting new carriers. We hence believe to reach higher IX concentrations under the same incident fluence, inducing an ambiguity on the exact quantification of the interaction enhancement. One way to overcome this, is to pump with a low repetition rate laser with femtosecond pulse duration such that the carriers do not decay within the duration of the pulse, while the population goes to zero until the other pump pulse arrives. The above is employed in Chapters 5 and 6 in single pulse RC experiments. However, the CW excitation allows for significantly more counts in PL, which is appropriate for the study of this chapter.

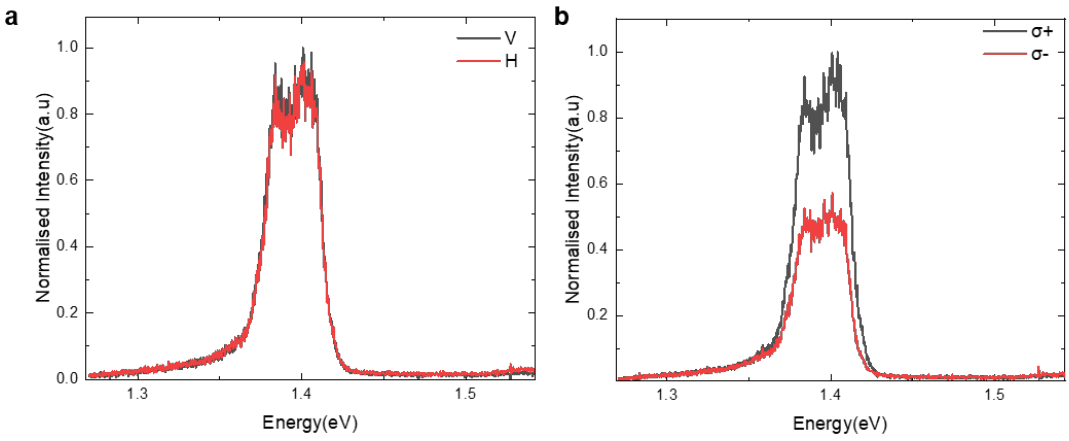

Fig. 4.4 **Polarisation resolved PL of IX**(a) A linearly polarised excitation to the vertical direction. The black spectrum is taken with a co-linear polarisaer in the detection whereas the red spectrum is taken detecting a cross polarised light to the vertical. The spectra are normalised to the maximum of the co-polarised configuration. (b) Circularly polarised excitation with σ^+. Detection is with σ^+(black) and σ^-(red). Spectra are normilsed to the maximum of the σ^+ spectrum

PL of IX was also studied in linear and circular polarisation as a probe of the valley physics. Namely, to study the degree of circular polarisation the sample was excited using a 780nm CW laser with σ^+ while a detection of σ^+ and σ^- polarised light was carried out. In addition, the sample was also excited with linearly polarised light and co/cross linear polarisation configuration was collected. In Fig. 4.4a, 50 per cent circular polarisation retention was observed, whereas PL did not show linear polarisation dependence Fig 4.4 b. The high degree of circular polarisation observed, is believed to arise from the suppressed

intervalley exchange pathways due to the electron-hole separation, that prolong the time of depolarisation of IX compared to to their radiative recombination rates[132]. It is worth noting that the degree of circular polarisation (DOCP) was not reproducibly observed as it depends on several factors such as twist angle (0 or 60 degrees), crucially sample quality and the bandstructure of heterobilayers involved. In addition, it depends on the concentration of alloy with monolayers of high W concentration having significantly higher DOCP than $MoSe_2$ like monolayers [128].

Fig 4.5 shows the spatial dependence of low temperature emission of some the structures fabricated. The DX colour maps are spatial maps of PL intensity maxima at the high energy range (1.53-1.65 eV) of the spectrum where as the IX colour maps show the low energy range of the spectrum (1.35-1.50 eV). As expected the IX map show more prominent intensity on the regions where monolayers overlap, where as DX maps show the majority of their PL in the regions of the monolayers, especially $MoSe_2$ which is brighter than alloys at low temperature. Within each IX region the PL is heterogeneous, indicating different interlayer distances throughout the sample. As a general trend these maps indicate that at higher concentrations the relative emission intensity of IX to DX is decreased. The tuning of IX with concentration will be further discussed in the following section

4.3 Tuning of IX with Alloy Concentration

Next we study the tuning of IX as a function of concentration x. Fig 4.6 shows the normalised IX spectra of different structures studied. As expected, the IX PL moves to higher energies with increasing Molybdenum concentration. In HBL with x>0.49, we observe broader multi-peak spectra while at low concentration the IX spectrum is narrower and more intense. To quantify the energy tuning, the highest energy IX peak is taken. The results are shown in Fig 4.6 with the error bars representing the spread of PL within a standard deviation of the position of the peak averaged through 20-30 points across each HBL. We observe a tuning of the IX energy by approximately 60 meV with the energy reaching a plateau at about 1.45 eV approaching then the energy of the homobilayer MoS_2 PL. It is worth noting that the error

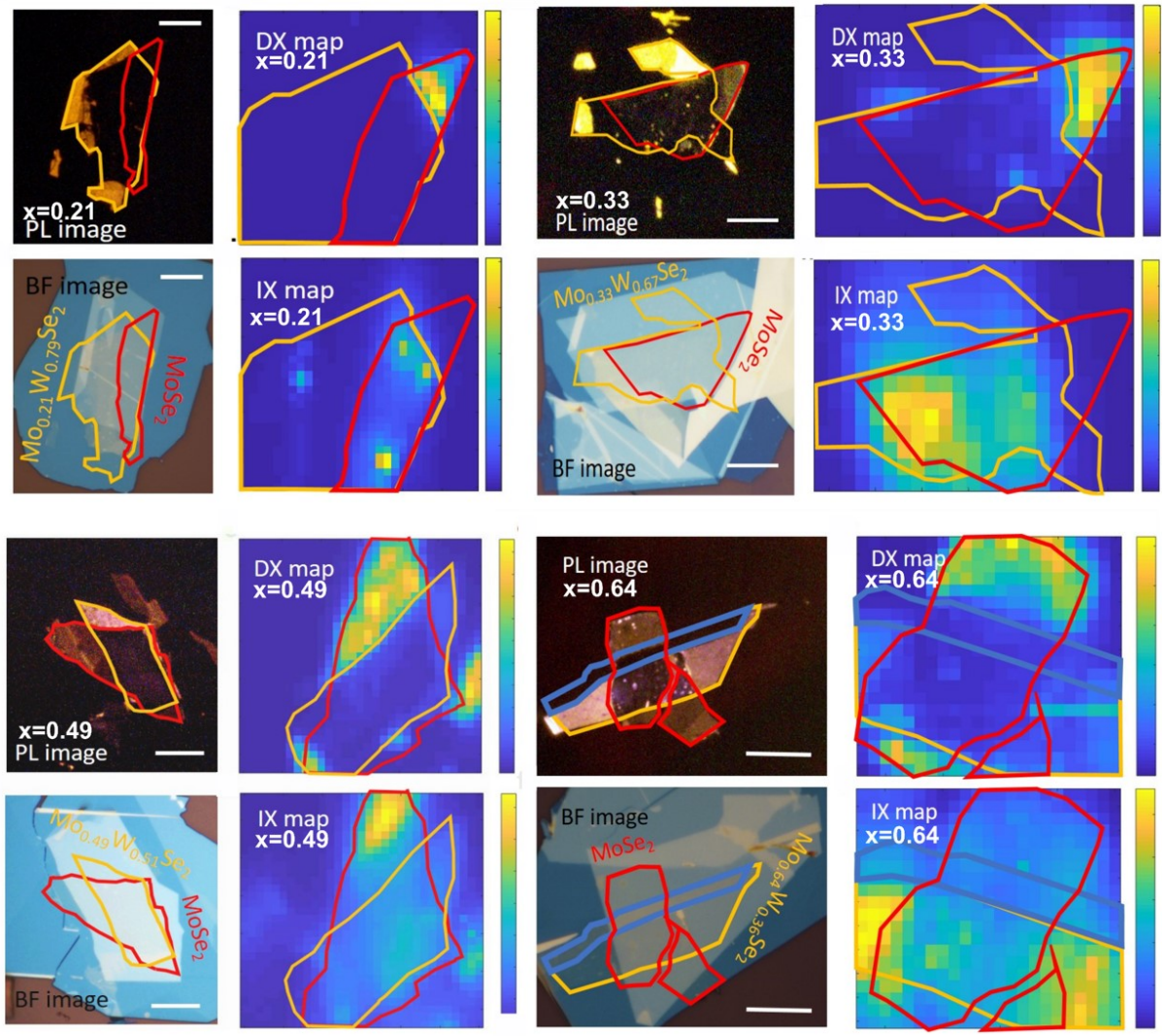

Fig. 4.5 **PL maps $Mo_xW_{(1-x)}Se_2/MoSe_2$ heterostructures.** PL maps of the structures ranging from x=0.21 to x=0.64. For each structure we show the room temperature PL and BF microscope images (left) where the constituents alloy and $MoSe_2$ monolayers are marked with yellow and red silhouettes respectively. Next to the images (right) the low temperature (10K) PL maps are shown. The spacial distribution of the energies of the DX regions and IX regions are shown in separate maps for the same structure, showing the IX on the region of overlap.

associated with the energy positions compared to the energy steps in this set of structures is significant. However, the same trend was confirmed with the more clear observations we have carried out on WSe_2 /alloy based heterobilayers, that can be found in Appendix A.2.1.

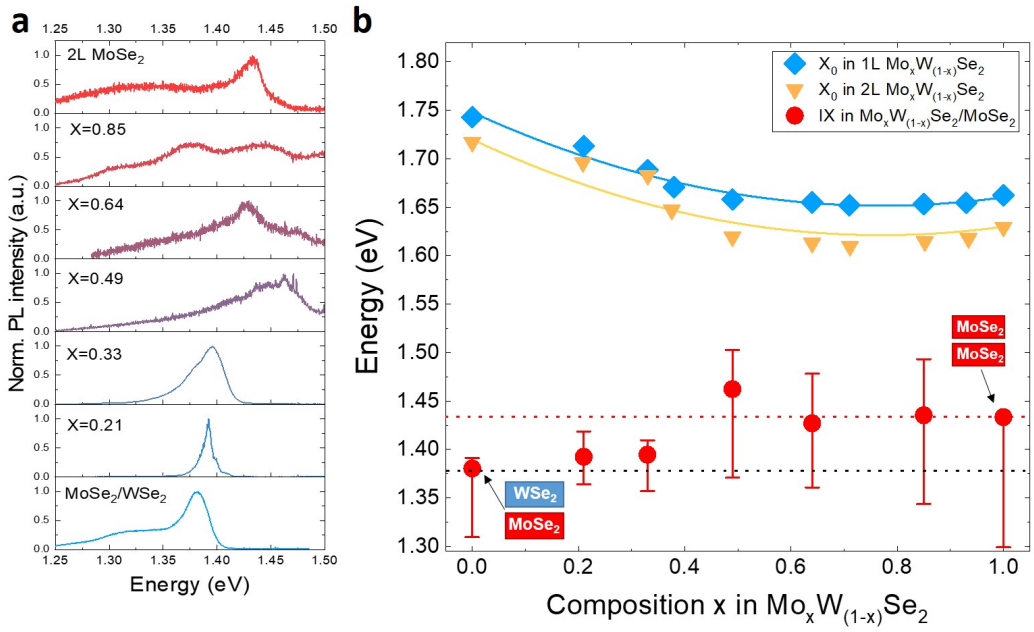

Fig. 4.6 **IX emission spectra for $Mo_xW_{(1-x)}Se_2/MoSe_2$ heterostructures. a** Normalized PL spectra of the $Mo_xW_{(1-x)}Se_2/MoSe_2$ heterostructures measured at 4K for different alloys compositions. **b** Peak position of the highest energy IX peak in the alloy/$MoSe_2$ (red circles) HBLs as a function of Mo composition x in the alloy layer, together with the neutral exciton peak position of the alloy monolayers (sky blue diamonds) and bilayers (yellow triangles). The error bars depict the spread in energy of multiple indirect transitions peaks, calculated as the standard deviation from the average PL wavelength. Sky blue and orange solid lines are parabolic fits of the DX peak energy in isolated alloy monolayers and bilayer respectively. The dashed black (red) horizontal line refers to the IX energy in $MoSe_2/WSe_2$ HBLs ($MoSe_2$ homobilayers).

In addition, IX power dependence changes as a function of concentration. IX energy and PL intensity have a non-linear dependence. As discussed in the previous section this is due to the aligned out of plane dipole moment causing direct coulomb interactions and IX-IX annihilation and the high densities achieved in these long living excitons. For increased statistics , it is instructive to look on both sets of $Mo_xW_{1-x}Se_2/MoSe_2$ $Mo_xW_{1-x}Se_2/WSe_2$, which together form coherent conclusions. As can be seen in Fig 4.7a PL saturation progressively decreases with concentration, x. Similarly saturation effects diminish at low x in $Mo_xW_{1-x}Se_2/WSe_2$ datasets, shown in 4.7b. The above results can be interpreted by considering of a more lenient electron and hole localisation in each adjacent layer, with weaker

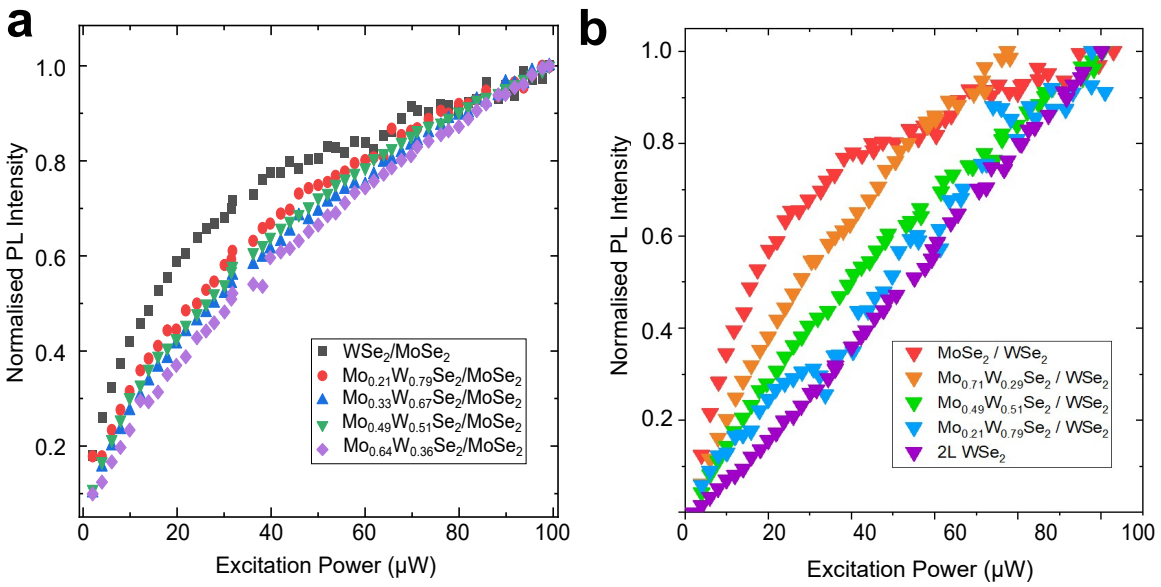

Fig. 4.7 **Power dependent PL intensity with concentration** Normalised integrated intensity of IX region as a function of power at several concentrations of $Mo_xW_{(1-x)}Se_2/MoSe_2$ (a) and $Mo_xW_{(1-x)}Se_2/WSe_2$ structures (b). The PL saturation decreases as the structures approach the homobilayer configuration.

charge separation and less aligned out of plane dipole moment of IX as the heterobilayers become more homobilayer-like. Further confirmation of the above interpretation is found on the time-resolved PL measurements performed on the $Mo_xW_{1-x}Se_2/WSe_2$ heterostructures, shown in Appendix A.2.2, where we observed that the PL decay of the IX shortens significantly, decreasing from tens of nanoseconds in $MoSe_2/WSe_2$ down to hundreds of picoseconds in the $Mo_{0.21}W_{0.79}Se_2/WSe_2$ HBL and bilayer WSe_2, which is the limit of the resolution of the setup. Hence, the lifetime decreases by more than two orders of magnitude. Such a strong lifetime reduction can be explained by the increase of spatial overlap between electron and hole wavefunctions moving towards the homobilayer configuration. A similar effect has been observed in gated bilayer WSe_2[16] where depending on the applied vertical voltage, the increase of the interlayer exciton lifetime was found, directly related to the enhanced spatial confinement of the carriers in the adjacent layers. It is, therefore, evident that interlayer excitons undergo a significant alteration of their nature with concentration.

Even for a non-alloyed $WSe_2/MoSe_2$ HBL, the exact origin of these peaks is still under debate, due to its complex electronic band structure. As clearly pointed out in [133], depend-

ing on the different experiments and theoretical calculations, the main PL features can be attributed to 1) a mix of momentum direct (K→K) and momentum-indirect (K→Q) interlayer excitons, the former being at higher energy, as shown by temperature-dependent behaviour of the exciton lifetimes at the different IX wavelengths; [71, 52] 2) only to momentum-indirect K→Q excitons, with an energy separation due to the spin–orbit splitting of the conduction band valley at the Q point, demonstrated by the observed opposite circular polarisation behaviour;[134] 3) a singlet–triplet pair of momentum-direct excitons at the K and K' points, as shown by the IX PL measurements applying an external magnetic fields;[135–138] and 4) a combination of neutral and charged spatially indirect excitons[139]. Very recently, crucial experiments of differential reflectivity under a modulated electric field unveiled the exact dipole moment and spectral position of the momentum-direct IXs, observed at higher energy compared to the momentum-indirect ones. [140] The latter has been found more visible in the PL spectra at low excitation powers, while the momentum-direct IX states have been efficiently populated by increasing the temperature or the excitation density, corroborating the explanation 1). We believe the above is therefore the most well evidenced proposal. It is consistent with our measurements, which fall in the increased density range, and is the one that can be used as a base for the explanation of our results.

We can now consider the PL data to analyse IX tuning with molybdenum concentration. For each heterostructure we have the energies of the PL of both IX and DX. Considering the Type II band alignment, these are largely related to the valence and conduction band offsets. The inset in Fig. 4.8a shows a schematic of PL peaks for IX in the heterobilayers and DX in $Mo_xW_{1-x}Se_2$ and $MoSe_2$ monolayers, used to extract ΔE1 and ΔE2. These are calculated as the difference between the DX peak energy of $MoSe_2$ ($MoWSe_2$) and the IX one, which become approximate experimental measures of the conduction and valence band offsets between the two materials. Here one assumes that the binding energies of excitons are not strongly dependent on x and that the binding energies of IX and DX are only modestly different. At the K-point band edges, predictions of the dependence of ΔE1 and ΔE2 with the alloy composition, shown with red and black lines in Fig. 4.8a, are obtained assuming a linear

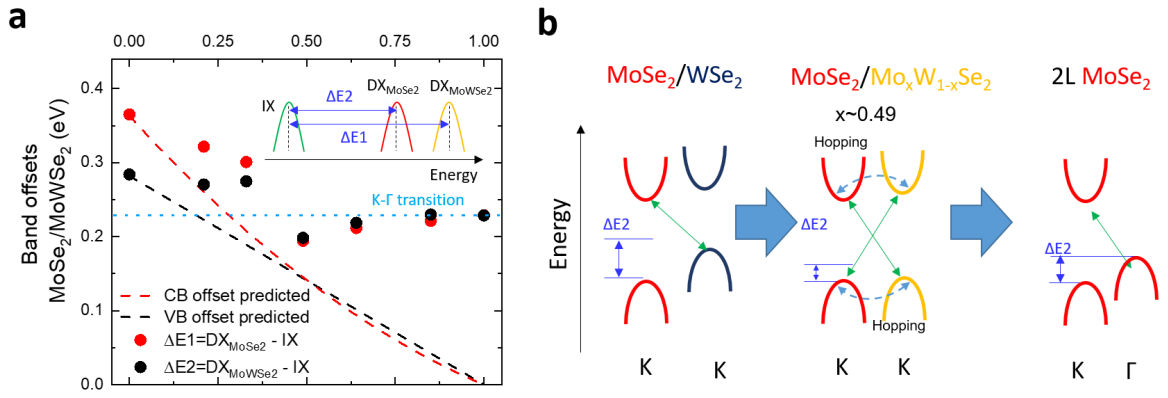

Fig. 4.8 **Band offsets of the $Mo_xW_{(1-x)}Se_2/MoSe_2$ HBLs.** **a,** Band offsets of $Mo_xW_{(1-x)}Se_2/MSe_2$ HBLs as a function of Mo composition x in the alloy monolayers. Red (black) lines indicates the predicted values of conduction (valence) band offsets for direct K-K transitions, without taking into account any band structure hybridisation. The band offsets ΔE1 and ΔE2 extracted from the experimental IX energies are displayed as filled red and black circles respectively **b,** Sketch of the band structure evolution for $Mo_xW_{(1-x)}Se_2/MoSe_2$ HBLs. Starting from the $MoSe_2/WSe_2$ configuration (left panel), the band structure hybridizes (central panel), moving towards the $MoSe_2$ homobilayer one (right panel), where the offset ΔE1 becomes the energy difference between the K and Γ points in the valence band.

change of the valence band energy and a parabolic change of the conduction band energy in the alloy[141], as detailed in Appendix A.2.3. The metal orbitals involved in the valence band edge composition for both WSe_2 and $MoSe_2$ are the same (d_{xy} and $d_{x^2-y^2}$), leading to a uniform shift of the VB energy varying the alloy composition. In contrast, the metal orbitals which contribute to the conduction band edges of the two materials are different, resulting in a non-linear energy shift.[142]. This is also reflected in the parabolic dependence of DX energy in alloy monolayers, shown in Appendix A.1. Comparing the experimental with the predicted band offset estimates, we notice a large deviation. In particular, large concentration heterobilayer move from a decreasing offset trend to increasing and, eventually approach a value just above 200 meV at concentrations close to a homobilayer.

This behaviour can be explained if we consider major modifications of the band-structure. For high concentrations ($\approx$ x$\geq$0.8), the Γ point of the valence band in the HBL becomes higher in energy than the K point, and the momentum indirect transition moves to lower energy than the direct one (Fig. 4.8b, right panel). For high concentrations ΔE1,ΔE2 account for the energy offset between the Γ and K points of the $MoSe_2$ valence band.

This in combination with the PL spectra intensity drop, broadening and lifetime reduction observed in both sets of alloy heterostructures indicate we are moving from a K-K direct to a momentum indirect transition. However, the exact concentration when this becomes dominant is not clearly deduced from our data. We also note that after the intermediate regime of x>0.4 (middle schematic in Fig 4.8b, the band offsets become so small that we expect hybridisation effects to become significant, due to efficient hopping of charge carriers from the valence (conduction) band of one layer to the valence (conduction) band of the other layer. If this happens, the hybridised exciton energy and absorption intensity will be affected. The aforementioned effect is best studied in the RC spectra which we present in the next subsection as a function of concentration.

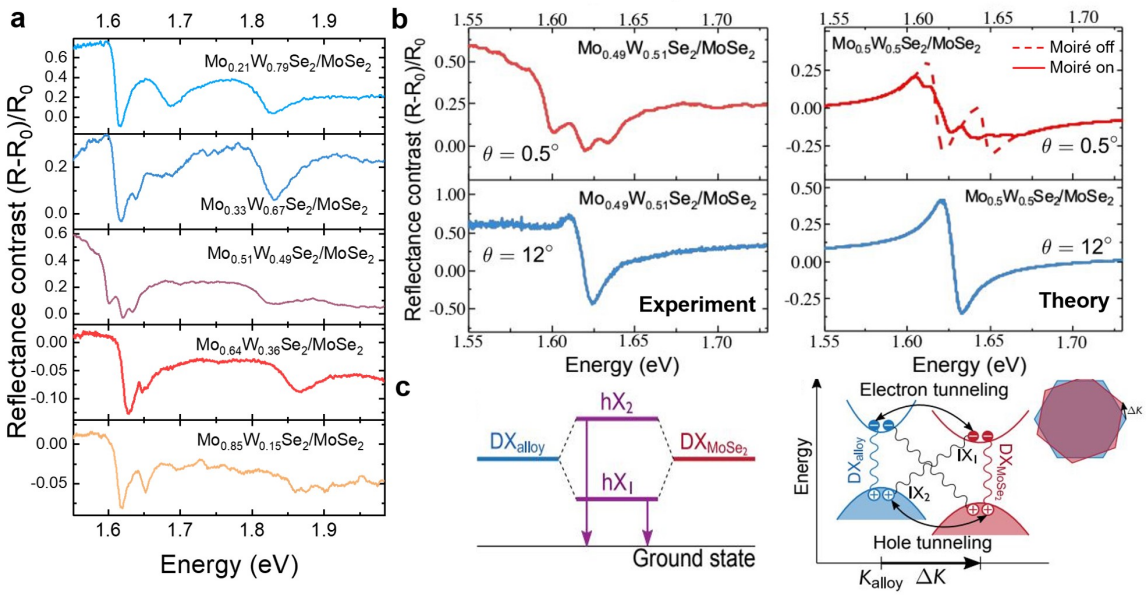

Fig. 4.9 **Hybridized moiré excitons in $Mo_xW_{1-x}Se_2/MoSe_2$.** **a** RC spectra as a function of concentration. From x=0.33 onwards the emergence of additional resonances is apparent. **b** (left) Aligned (top) and strongly misaligned (bottom) heterostructures (twist angles θ = 0.5 °and θ = 12 °, respectively), both with the same alloy concentration x = 0.49. (right) Corresponding theoretical RC curves at concentration x = 0.5, where dashed (solid) lines indicate that moiré mini band folding effects has been neglected (included) in the calculation. The theoretical hybridized moiré exciton spectrum shows the additional transitions observed in experimental. (c) (left)Schematic of the resonant excitons resulting in two hybridised modes. On the right the band schematic shows that this mechanism is mediated through carrier tunnelling forming two hybridised excitons IX1,2. The tunnelling and the moiré periodicity depends on the momentum mismatch ΔK, illustrated in the top right inset.

Fig 4.9 shows the RC of the alloy structures studied in the range of concentrations. At low concentrations x<0.3, the band offset is large. We therefore see only two peaks in the low energy region, coming from the constituent monolayers intralayer excitons. As mentioned before, due to the large bowing parameter of the alloyed layer, the two monolayer excitons become degenerate already at x $\approx$0.49. However this is not enough to explain the multi-peak RC structure seen from already x$\geq$0.3. As shown the theoretical spectra of alighned heterostructures in Fig 4.9b if only resonant hybridisation occurs the calculated spectra (dashed lines) only give two resonances in reflectance contrast. We , therefore, propose the moire pattern periodicity to play a significant role in the measured spectra, in a similar way to the resonantly hybridised moiré excitons in other heterobilayers [124]. This is qualitatively confirmed by theoretical calculations from collaborators (solid line in theory panel of Fig 4.9) In small angle structures, the large moire pattern causes mini-band folding in the first Brillouin Zone as illustrated in Fig 4.9c. As expected, the RC spectrum of a large angle twisted structure with the same composition shows no signs of moiré effects or hybridisation as we observe a broader single peak at the energy of DX (Fig 4.9). However, for a complete explanation of the origins of these transitions, their position and their separation, we expect lattice reconstruction effects to be dominant [143, 86]. Hence, we note that the exact origin of these spectral features is complex subject and calls for a separate investigation outside of the scope of this study.

4.4 Conclusions

To summarise, we study $Mo_xW_{1-x}Se_2$/$MoSe_2$ alloy heterostructures for a variety of composition x using cryogenic temperature (T=10 K) photoluminescence spectroscopy. We present the concept of alloyed monolayers to broaden the variety of atomically thin semiconductors available. This enhances the choice of 2D materials that can be stacked together, increasing further the degrees of freedom offered by two dimensional semiconductor heterostructures for material properties engineering. We observe interlayer exciton species with an out of plane dipole moment and demonstrate significant tuning of their PL energy as a function of

molybdenum concentration. The IX energy shows asymptotic behaviour with a maximum energy for high values of x approaching that of the indirect bandgap in $MoSe_2$ bilayer. Power dependent measurements show a large noninearity of IX which becomes smaller as a function of concentration. This IS also accompanied by a reduction of the lifetime in similar structures that approach the homobilayer configuration.

This behaviour is explained by a momentum direct to indirect transition of the band-structure caused by the replacement of the transition metal atoms in one layer. In addition, we use RC to observe hybridisation effects which are further modified by the moire potential found in nearly aligned HBL. Given the sample non-uniformity and the uncertainty of the origin of of such excitonic species which could be dictated by lattice reconstruction effects, we note capability of future studies on this structures as a systematic platform to observe these effects.

CHAPTER 5

HYBRIDISED INTERLAYER EXCITON IN MoS_2 BILAYERS

5.1 Introduction

Excitons in monolayer semiconductors have attracted great scientific interest. In particular, as explained in Chapter 2 the confinement and decreased dielectric screening of excitons in TMDs give them high oscillator strengths and large binding energies. These, in combination with the valley degree of freedom make them attractive for light matter interaction studies, up to room temperature.

With the advance of heterostructure stacking, studies of interlayer excitons in TMD heterobilayers have revealed some very interesting physics such as moiré superlatices and the interfacial phenomena governing interlayer exciton spectral characteristics. However as seen in the previous section, the interfacial contaminants (which are inevitable with current fabrication processes) and the sensitivity to many effects, such as twist angle and lattice reconstruction, make their subtle spectral characteristics largely non-uniform and of unknown origin.

Despite the scientific communities significant focus on heterobilayers, interlayer excitonic species also exist in homobilayers. Specifically, as-exfoliated $MoSe_2$ and MoS_2 bilayers encapsulated in hBN were recently discovered to host hybridized interlayer excitons (hIX) [88, 89]. hIX in 2H MoS_2 biayers in particular possess a large oscillator strength, comparable to that of the intralayer exciton, arising from interlayer hybridisation of valence band states,

aided by a favourable orbital overlap and a relatively small spin-orbit splitting among semiconducting TMDs [89]. Importantly, these do not suffer from inhomogeneity imposed by artificial stacking, allowing for more conclusive studies. Such hybridized interlayer excitons (hIX) are highly tunable using out-of-plane electric field [70, 144] when their valley degree of freedom persists up to room temperature [145].

The first optical characterisation of monolayer TMDs has been on MoS_2. However, due to the spectrally broad features, the interest was quickly switched to the other TMD semiconductors, such as $MoSe_2$ which has a clean spectrum due to the absence of defect states. Since then, heterostructure stacking has allowed encapsulation of monolayers in hBN. The more symmetric dielectric environment and the suppression of inhomogeneous broadening resulting from atomically flat encapsulation has lead to significant narrowing of each transition [37], allowing to spectrally resolve the excitonic characteristics of originating from different transitions. Encapsulation also makes hIX much more prominent which resulted in their observation

Here we take the approach of encapsulated MoS_2 homobilayers to study hIX dipolar excitonic species, observe their non linear interactions and understand their many body physics.

The results presented in this Chapter are part of preprint [146], which is currently under review. The author of this thesis is the first author of this work. Our results we supported with a theoretical microscopic model from collaborators, which can be found in it's more detailed form in Appendix B

5.2 Hybridised interlayer exciton in MoS_2 homobilayers

Figure 5.1 a,b shows the fabricated heterostructures encapsulated bilayer MoS_2 in an optical microscope image and a schematic of the cross section, respectively. Fig. 5.1a shows a bright field microscope image of the encapsulated BL MoS_2. A sketch of the side view of the device is displayed in Fig. 5.1b. To probe the optical response of the excitonic species present in this material reflectance contrast (RC) spectra were undertaken at 4K, displayed in Fig. 5.2. This

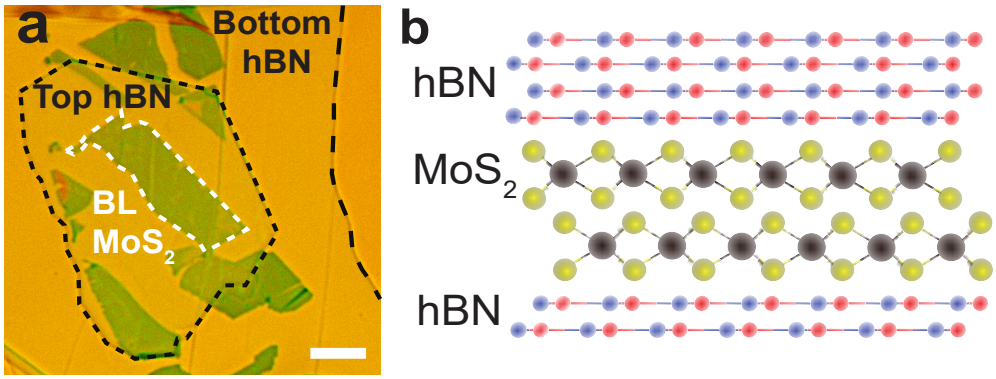

Fig. 5.1 **Homobilayer MoS_2 encapsulated sample a,** Bright field microscope image of an encapsulated BL MoS_2 transferred on top of a DBR. Scale bar: 10 μm. **b,** Schematic side-view of the fabricated heterostructure comprising a BL MoS_2 sandwiched between few-layer hBN.

shows three distinct absorption features at 1.937 eV, 2.004 eV and 2.113 eV for XA, hIX and hXB , respectively. The measured linewidths are 20, 23 and 64 meV, respectively. This is unlike the well reported monolayer spectra where two peaks are observed, attributed to the neutral intralayer A and B series excitons. In the bilayer these are associated with transitions at 1.937 eV (see Fig. 5.2) and 2.113 eV, respectively. The additional peak observed has been recently attributed to the hybridised interlayer excitons[89]. For charges to delocalise over both layers, two conditions have to be met. Firstly, the charge hoping should be allowed by orbital symmetry. The second condition that affects charge tunnelling from one layer to the other, is the band splitting between the second lowest and lowest bands of the two layers, where the charge will tunnel to. The configuration specific to bilayer MoS_2, is depicted by the schematic shown in Fig 5.3a, where the K point in the bilayer momentum space is shown at Layer 1 and Layer 2 of the structure. Orbital symmetry allows for hole delocalisation over both layers. Specifically, holes from the second lowest valence band tunnel to the lowest band of the other layer. As MoS_2 has the smallest valence band splitting out of the TMDs, this effect is particularly prominent for this material. However, this is not allowed for the electrons in the conduction band. It can therefore be inferred that the interlayer exciton is hybridised with the B-series intralayer exciton. The ratio of the integrated intensities of X_A and hIX is 4.5, showing an unusually large oscillator strength compared to interlayer excitons in most heterobilayers, due to their hybridisation with intralayer excitons. Based

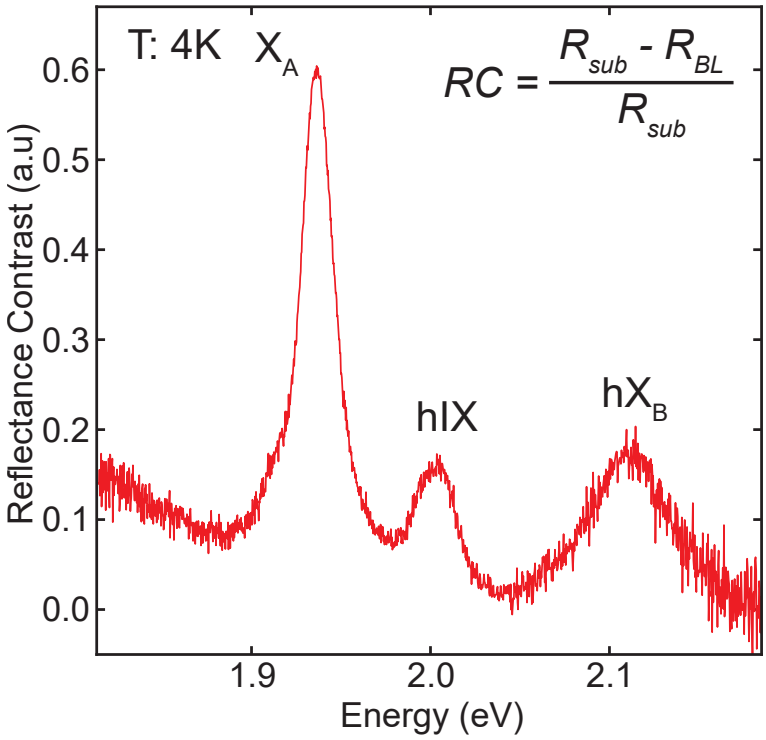

Fig. 5.2 **Homobilayer MoS_2 Reflectance contrast (RC) spectrum** RC spectrum of the sample measured at low temperature (4 K) showing three distinct absorption features at 1.937 eV, 2.004 eV and 2.113 eV for X_A, hIX and hX_B, respectively. RC is calculated using the formula in the top-right corner of the graph.

on these data, our collaborators from the University of Exeter estimate the electron-hole separation $d = 0.55$ nm (see details in Appendix B.2) in agreement with previous studies [145]. Recently, the application of out-of plane electric fields where the anticrossing observed at the B exciton energy and the giant stark splitting of hIX has confirmed both its hybridised nature and the large out-of plane dipole moment [70, 144].

The interlayer nature of hIX is further confirmed by its response under a magnetic field of 8T in Faraday configuration, where the spin degeneracy is lifted. Using opposite circularly polarised detection, the chiral properties of this system were probed in RC at 4 K (Fig. 5.3b). A Zeeman splitting of 1.5 meV was observed for X_A. Interestingly, the hIX shows an opposite energy shift and a larger Zeeman splitting of -3.5 meV. Recent studies reporting similar behaviour have suggested that this effect comes from the holes residing in the opposite layer[144], leading to an additional valley and orbital contribution in the

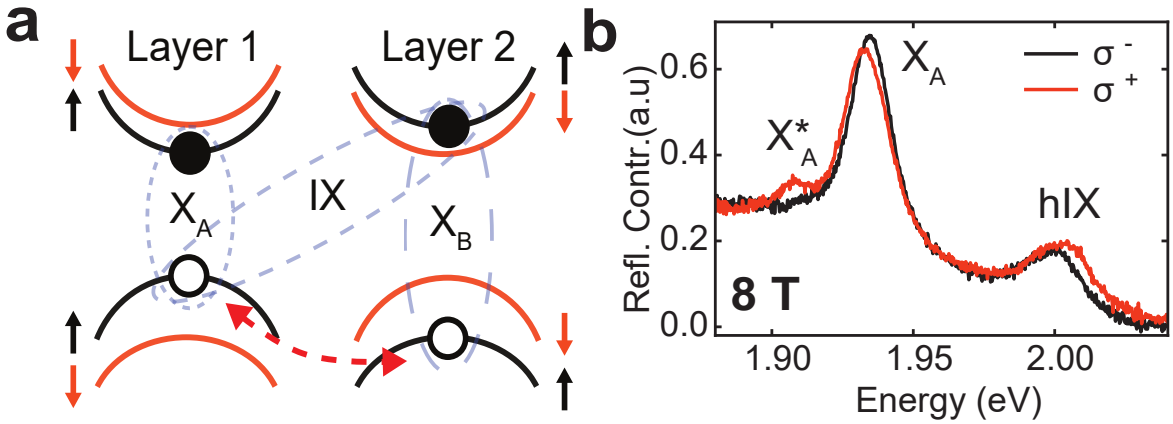

Fig. 5.3 **Band edges and Zeeman splitting a,**Sketch of the conduction and valence bands in two adjacent layers of MoS_2, displaying the allowed optical transitions of A and B direct intralayer excitons (X_A and X_B) and interlayer excitons (IX) for spin-up states (black lines) at the K point in the bilayer momentum space. IX hybridizes with X_B through the hole tunnelling between the two layers (red dashed arrow). At the K' point of the bilayer Brillouin zone, the same configuration applies for the states with the opposite spins. **b,** RC spectra of excitons in BL MoS_2 detected in two circular polarizations in an out-of-plane magnetic field of 8 T at T=4 K.

opposite direction. In addition, a signal from intralayer trions (X^*_A) is observed only in σ^+ polarisation, suggesting the presence of fully spin-polarised charge carriers, similarly to monolayer MoS_2 under high magnetic fields [147].

5.3 Non-linear behaviour: NB vs BB illumination

5.3.1 Experimental Observations

Now the origin of the spectrum and resonances in this platform are understood, we investigate the non linear responce of BL excitons as a function of the laser power using resonant narrow band (NB, full-width at half maximum, FWHM=28nm) illumination. For comparison, we also perform the same measurement on a fully encapsulated monolayer at the neutral intralayer exciton energy.

As can be seen in Fig. 5.4, when subjected to increased fluence, the response from ML excitons is significantly different to that of BL excitons. It is evident from the RC spectral shapes, shown in Fig. 5.4 a,b,c, that the broadening and saturation (bleaching) in the BL

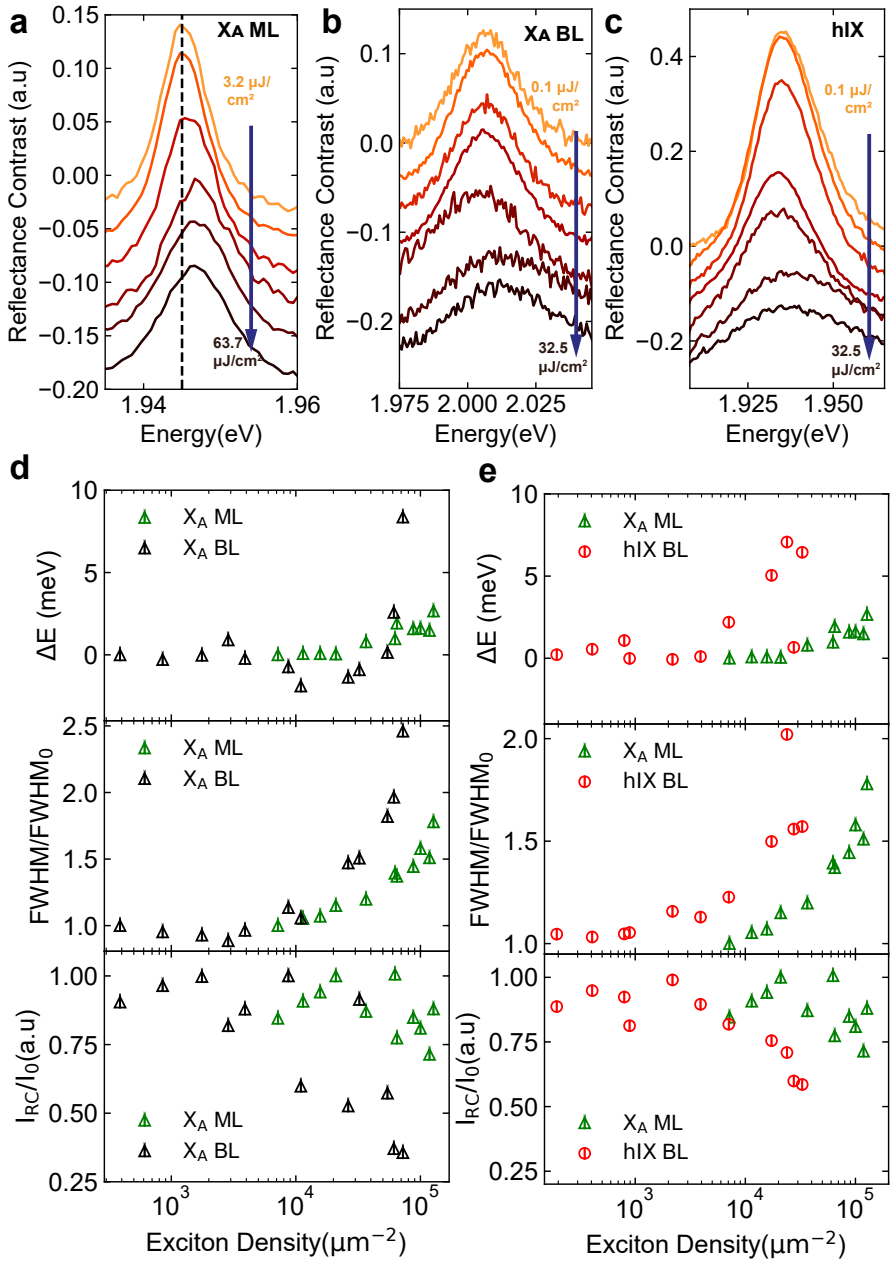

Fig. 5.4 **Exciton nonlinearity in MoS_2 bilayer vs monolayer. a, b, c,** RC spectra measured with the NB (FWHM=28nm) excitation for the X_A in monolayer (**a**), X_A in bilayer(**b**) and hIX (**c**).**d, e,** Comparison of bilayer excitons to monolayer X_A energy shift ΔE (top), linewidth variation ΔFWHM (middle) and normalized integrated intensity (bottom) as a function of the exciton density for the intalayer excitons (**d**) and hIX (**e**). Solid (open) symbols show the results for the BB (NB) excitation. For the normalized intensity we divide the intergrated intensity at each laser power by that at the maximum intensity.

excitons is significantly more prominent. However, the blueshift observed is common to all the three exciton species shown here. Fitting the spectra to lorenzians, the energy position, linewidth and integrated intensity was extracted.

How the above quantities change with exciton density (calculated following [148] with the procedure shown in Appendix B.1) is illustrated in Figures 5.4 d,e. Specifically, we see that BL X_A reaches same normalised broadening and saturation values, at 3 times lower densities(Fig 5.4d). The blueshift also indicates an enhanced non-linearity, but the low number of points after threshold does not allow for conclusive comparisons.

A much clearer blueshift can be seen when the hIX in BL is compared to conventional monolayer intralayer excitons. The broadening and bleaching values are also significantly more prominent. In particular, we can see that the same non-linear saturation is observed at ≈ 8 times lower densities for hIX.

To understand the results of intralayer excitons, the sensitivity of monolayer TMDs to their environment (mentioned in 2.4) needs to be considered. Due to close proximity of another layer of high dielectric constant, an increased screening is induced. Hence, the excitonic binding energy is reduced, creating larger electron-hole pairs. Owing to the increased excitonic Bohr radius, the onset of the nonlinear behaviour for X_A in bilayers occurs at a lower exciton density than for X_A in monolayers. Regarding non-linearity of hIX, we attribute this to the increases dipole moment arising from the larger spatial separation of these interlayer species. Combined to the aforementioned screening effect in bilayers, the result clear enhancement of non-linearity compare to X_A in monolayers, observed in Fig 5.4

Interestingly, as shown in Fig 5.5 our observations differ under simultaneous pumping of intralayer and hIX excitons. More specifically, the bleaching of hIX is significantly faster while a redshift is observed. In contrast, X_A behaviour does not seem to be qualitatively different under the two illumination regimes. Fig. 5.6a quantifies the trends observed in Figs. 5.5 showing for the BB excitation an abrupt bleaching of the hIX peak above the hIX density 5×10^3 μm^{-2} accompanied by a redshift of ≈ 4 meV and a 12 meV broadening. For the NB case, a similar decrease in peak intensity is observed only around 4×10^4 μm^{-2}, accompanied with a peak blueshift of ≈ 7 meV and a broadening exceeding 15 meV. In

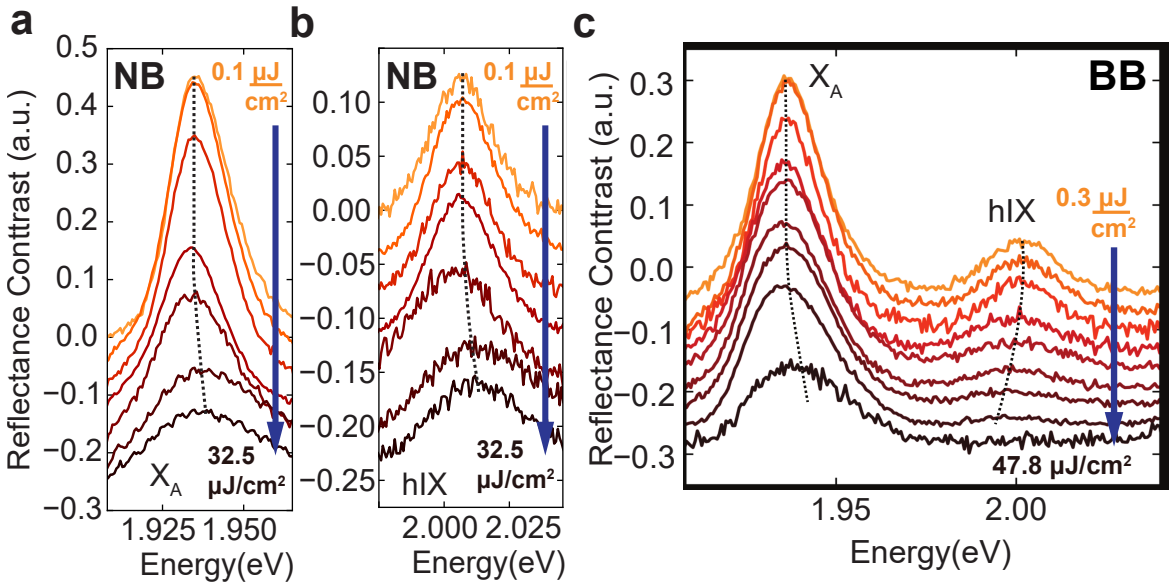

Fig. 5.5 **Fluence dependence in MoS_2 bilayer spectra. a, b, c,** RC spectra measured with the NB (FWHM=28nm) excitation for the X_A (**a**) and hIX (**b**), and with the BB (FWHM=50nm) excitation (**c**) at different fluences. The dashed curves are guide for the eye.

contrast, Fig. 5.6b, shows that for X_A a similar blueshift, broadening and saturation are observed under the two excitation regimes and at slightly higher densities compared to the hIX under the NB excitation.

5.3.2 Discussion: Nonlinear Interactions Interpretation

To further understand the non-linear processes governing exciton-exciton interactions, we collaborated with theoretical physicists from the Univeristy of Exeter, where microscopic model to describe the contrasting phenomena under the NB and BB excitation was developed. The details of the mathematical model can be found in Appendix B. Here we present the main points the aforementioned model alongside our intuitive interpretation of the non-linear mechanisms.

Under the NB excitation, either X_A or hIX excitons are created. In this case, nonlinearity arises from Coulomb exciton-exciton interactions causing blueshift and dephasing [64]. This Coulomb potential, V_{Coul} consists of exchange and direct terms. As in monolayers[64, 149], the bilayer intralayer excitons are dominated by exhange interaction processes. In contrast,

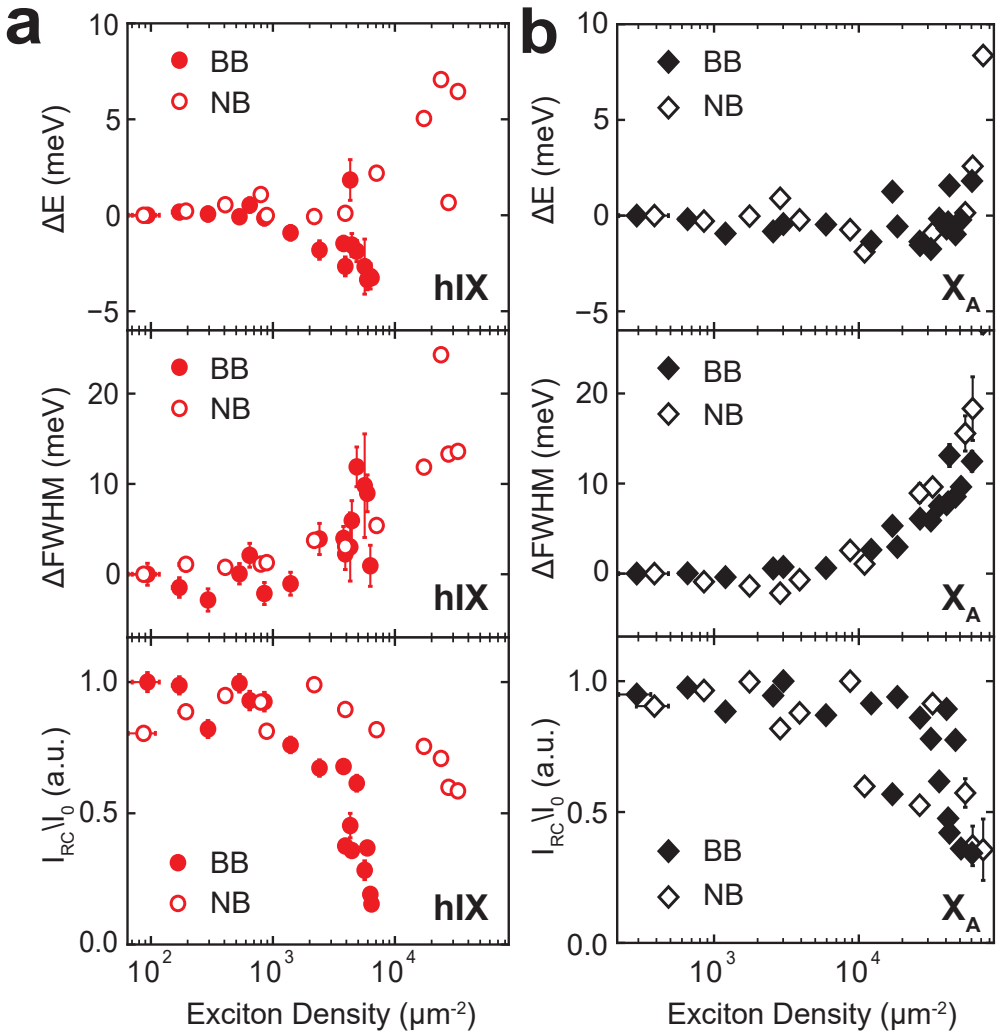

Fig. 5.6 **Exciton nonlinearity from RC in MoS_2 bilayer under two illumination regimes .a, b** The energy shift ΔE (top), linewidth variation ΔFWHM (middle) and normalized integrated intensity (bottom) as a function of the exciton density for the hIX (a) and X_A (b). Solid (open) symbols show the results for the BB (NB) excitation. For the normalized intensity we divide the intergrated intensity at each laser power by that at the maximum intensity.

in interlayer hIX, due to their larger size and partially out-of plane dipole moment, the direct Coulomb (dipole-dipole) interaction is the main mechanism of hIX-hIX scattering[150]. From the energy separation of hIX from the intralayer exciton energies, an interlayer distance of $d = 0.55$ nm can be implied (see Appendix B.2). Considering this out-of plane dipole moment V_{Coul} is overall 2.3 times stronger for hIX compared with X_A, which agrees with the experimental observations.

The shapes of the NB reflectance contrast spectra can also be analysed to probe the interactions present, as they depend on the rates of radiative (Γ_R) and non-radiative (Γ_{NR}) processes. Namely, the area under RC curves is described by the ratio $\Gamma_R/(\Gamma_R+\Gamma_{NR})$. Under increased excitation, the scattering induced non-radiative processes change this ratio. More specifically, non radiative processes scale as $\Gamma_{NR} \propto |V_{Coul}|^2 n$, since they depend on the combined matrix elements for the Coulomb interactions and the exciton density n. [64]. With this process the RC can be reproduced to follow the bleaching. In addition it explains stronger nonlinearity for X_A in bilayers compared to monolayers, $X_A^{(ml)}$, owing to the larger Bohr radius($V_{Coul} \propto \alpha$) in bilayers due to enhanced screening .

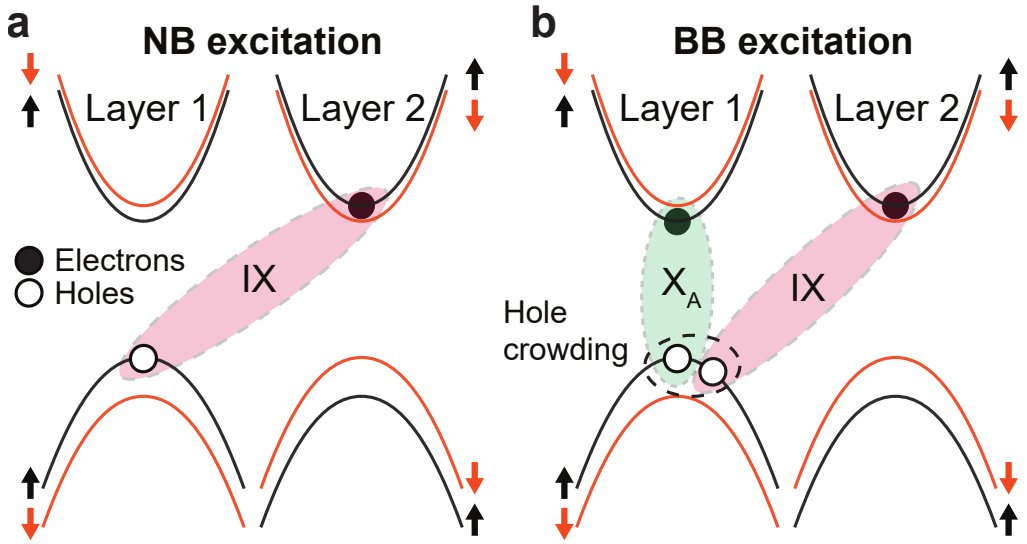

Fig. 5.7 **Band schematics and hole crowding in MoS_2 bilayers.** Schematic diagram showing exciton generation under the NB, **a**, and BB, **b**, excitation

In the BB case, both X_A and hIX excitons are generated simultaneously, and together with intraspecies scattering (X_A-X_A and hIX-hIX), interspecies scattering (X_A-hIX) occurs, similarly to the direct-indirect exciton Coulomb scattering in double quantum wells [151]. Since X_A and hIX are formed by the holes from the same valence band (Fig. 5.7a), an additional contribution arises from the phase space filling, i.e. the commutation relations for the excitons (composite bosons) start to deviate from the ideal weak-density limit once more particles are created [152]. For particles of the same flavour, the phase space filling enables nonlinear saturation effects , similar to polariton saturation observed in [153]. However, in

the presence of several exciton species, we reveal a distinct phase space filling mechanism which we term the *hole crowding*. Crucially, we observe that the commutator of the X_A annihilation operator ($\hat{X}$) and hIX creation operator ($\hat{I}^\dagger$) is non-zero, $[\hat{X}(\mathbf{p}),\hat{I}^\dagger(\mathbf{q})] = -\hat{B}_{\mathbf{p},\mathbf{q}}$. Here $\mathbf{p}$, $\mathbf{q}$ are exciton momenta and $\hat{B}_{\mathbf{p},\mathbf{q}}$ is an operator denoting the deviation from the ideal commuting case ($\hat{B}_{\mathbf{p},\mathbf{q}} = 0$) of distinct bosons where holes do not compete for the valence band space. This statistical property of modes that share a hole has profound consequences for the nonlinear response. Namely, the total energy is evaluated as an expectation value over a many-body state with both X_A and hIX excitons, $|N_\mathrm{X}, N_\mathrm{hIX}\rangle := (\prod_\mathbf{p}^{N_\mathrm{X}} \hat{X}^\dagger)(\prod_\mathbf{q}^{N_\mathrm{hIX}} \hat{I}^\dagger)|\Omega_{max}\rangle$, where N_X and N_hIX particles are created from the ground state $|\Omega_{max}\rangle$. If the excitonic modes are independent, the contributions from X_A and hIX simply add up. However, the hole coexistence in the valence band induces the excitonic interspecies scattering. The phase space filling combined with the Coulomb energy correction leads to a negative nonlinear energy contribution. This nonlinear term scales as $\Delta E_\mathrm{hIX} = -\eta\sqrt{n_\mathrm{X} n_\mathrm{hIX}}$, where $\eta > 0$ is a coefficient defined by the Coulomb energy and Bohr radii and $n_\mathrm{X,hIX}$ are the exciton densities (see Appendix B.4). This nonlinearity also modifies the non-radiative processes leading to substantial broadening for the hIX states. Using the estimated nonlinear coefficients caused by the hole crowding, we model the RC in the BB regime and qualitatively reproduce the strong bleaching and redshift for hIX at the increased density, as shown in Fig 5.8c.

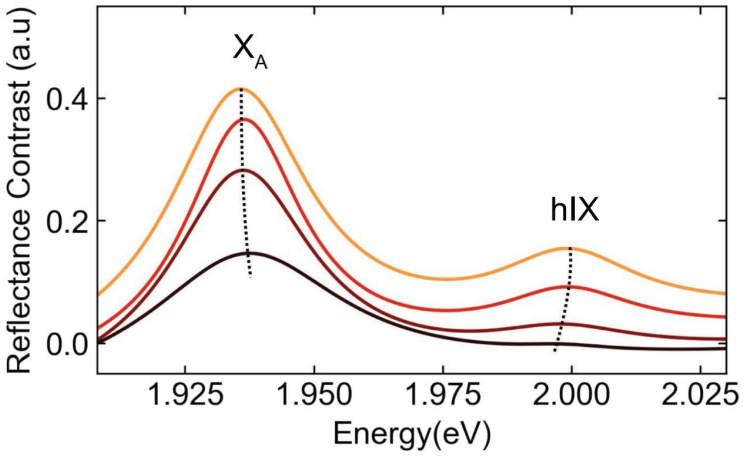

Fig. 5.8 **Theoretical reproduction of nonlinear optical response in MoS_2 bilayers** Theoretically calculated absorption spectra for the BB excitation case (see Appendix B), providing qualitative agreement with the experiment. The dashed black curves are guides for the eye.

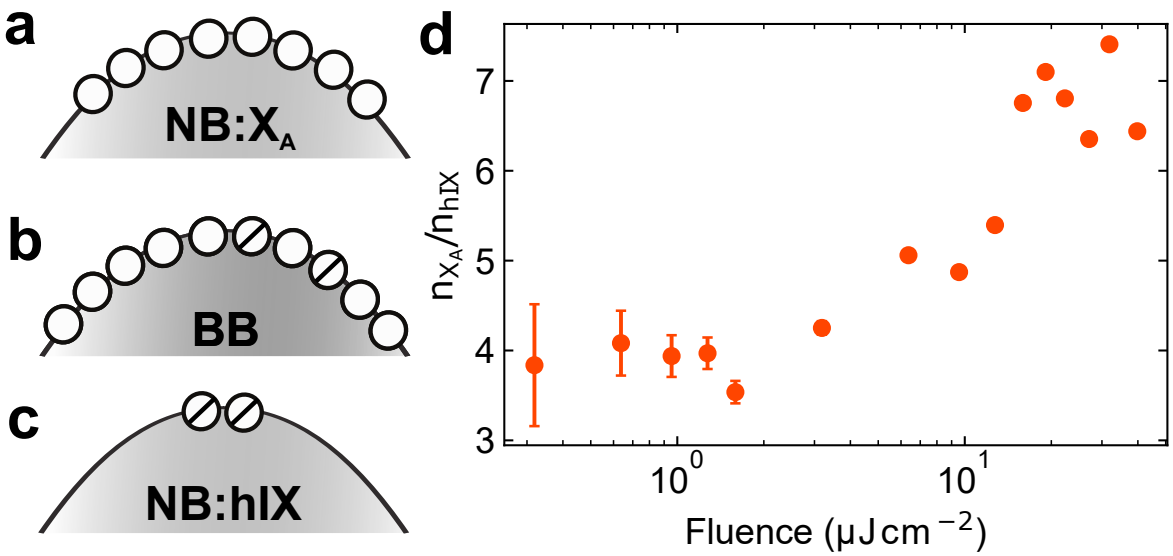

Fig. 5.9 **Illustration of hole crowding self-amplification a, b,c** Schematic diagram of the valence band hole occupation under three illumination configurations for a given power. Namely the X_A holes under NB illumination, (b) simultaneous BB illumination an (c) NB illumination at the energy of hIX. Even though holes are indistinguishable, a proportion of the population is statistically ascribed to each exciton. Empty circles signify holes ascribed to X_A and slashed circles to hIX. **d** Ratio of experimental X_A to hIX exciton density as a function of fluence.

Merging the mathematical model with the intuitive band diagram considerations of Fig 5.7a,b, we deduce there is large co-dependence of the two excitonic species upon simultaneous pumping. This is induced by a coexistence of their holes in the same valence band causing phase-space filling, which apart from enhanced optical saturation uniquely results in attractive coulomb scattering. The magnitude of this effect depends on the relative number of excitons in each species $n_{\mathrm{X,hIX}}$. According to this analysis, the effect of the BB excitation should be most pronounced for hIX as the stronger X_A absorption leads to enhanced Pauli-blocking. In simple terms, let us consider the hole configurations in the valence band for each illumination case at a given power, illustrated in Fig 5.9. For X_A if we compare Fig 5.9a with 5.9b we see that the excess number of holes due to BB illumination is very small. However, for hIX comparing Fig 5.9b and 5.9c one can see that BB illumination introduces a large number of excess holes. Hence, hole crowding bleaching and scattering effects are felt more for hIX. When the illumination power is increased, the hIX fast saturation

further grows this hole population imbalance, as shown in Fig 5.9d, enhancing the effective nonlinearity on the low population species. Through this process the hole crowding effect on hIX, therefore, becomes a self-amplifying mechanism. In contrast, the more the fluence the less apparent the effect of hole crowding on X_A. Therefore, other non-linear mechanisms become dominant and its behaviour remains unaffected by the illumination regime. To the best of our knowledge this is the only semiconducting system that showcases this collective series of interspecies saturation, attraction and self-amplification effects that lead to our observations.

5.4 Conclusions

To summarise, we encapsulated 2H bilayers of MoS_2 to study the linear and non-linear of new interlayer excitonic species. This species uniquely combine an out plane dipole moment with a significant oscillator originating from their hybridised nature with intralayer excitons. Under a magnetic filed we observe an opposite Zeeman splitting to neutral intralayer excitons due to the exciton constituents residing in adjacent layers, giving this system a layer pseudospin. Then the many body interactions of excitons in this system are studied under single pulses at increasing fluence. In particular we find that hIX is about 8 times more non-linear than monolayer neutral excitons due to their larger size and out of plane dipole moment. In fact, we observe that intralayer excitons of bilayers are as well more interacting than in monolayers, due to the increased screening induced by the adjacent layer. We support the previous conclusions with theoretical models developed by collaborators for this work.

Interestingly, we find that in the case of simultaneous pumping of intralayer and interlayer excitons a new type of non-linearity arises. Namely, for hIX the previously observed blueshift becomes a redshift while the non-linear behaviours happens at up to a further order of magnitude lower densities. hIX excitons hence posses up to a total of two orders of magnitude more non-linear interactions than monolayer intralayer excitons. The aforementioned enhancement under simultaneous excitation is a consequence of the fact that holes of the two excitonic species reside in the same valence band. It is hence a type of phase space filling

which induces interspeces scattering. The aforementined is confirmed by microscopic theory calculations of the system. We call this new mechanism hole crowding and we note this is special to the conditions of TMD bilayers. Additionally worth-note is the binary selection to reverse non-linear shift, offered through hole crowding, in the same sample platform over a uniform area which may be of interest for logic gate devices of the future.

Hence we have excitons of high oscillator strength, chiral degrees of freedom and high non-linnearity in prestine atomically thin samples. the unique combination of oscillator strength and interacting properties in these new excitonic species are particularly attractive for coupling quantum tunnelling to cavity photons, in order to realise dipolar polaritons. The latter will be the topic of the next chapter.

CHAPTER 6

DIPOLAR INTERLAYER POLARITONS

6.1 Introduction

Coherent superposition of light and matter enables for the creation of hybrid quasiparticles called polaritons. Excitons in two-dimensional transition metal dichalcogenides (TMDs) have large oscillator strengths and binding energies [16], making them attractive as a platform for studies of strong light-matter coupling in optical microcavities [100, 99, 154, 27]. A variety of polaritonic states have been realised using monolayers of MX_2 (M=Mo, W; X=S, Se) embedded in tunable [99] and monolithic microcavities [155, 156, 106]. These include exciton- and trion-polaritons (also described as Fermi-polaron-polaritons [27]), Rydberg polaritons involving excited exciton states [157] and, very recently, moiré polaritons in stacked TMD monolayers forming a van der Waals heterostructure[148]. Polariton states in TMDs inherit the valley pseudo-spin degree of freedom of their excitonic counterparts, and respond sensitively to externally controlled doping (e.g. by using gate voltages) [27, 158, 159], polarization of light [102], exciton hybridization [148] and magnetic field [159].

One of the central research themes in polaritonics is the study of nonlinear interactions that lead to extremely rich phenomena such as Bose-Einstein condensation [160, 161], polariton lasing [162, 163] or optical parametric amplification [164]. Polaritons formed from tightly bound neutral intralayer excitons in TMDs, having both the electron and hole in the same monolayer, are not expected to show strong nonlinearity. However, pronounced

nonlinear behavior was observed for trion [153, 159] and Rydberg polaritons [157], having respectively a more pronounced Fermionic character or a larger size.

In conventional semiconductor systems, one approach to increase polariton interactions was the use of excitons of increased special extend, where electrons and holes are physically separated residing in adjacent quantum wells. Typically, however, interlayer excitons (in double quantum wells also called 'indirect') possess low oscillator strength [132, 165]. Thus, in order to access strong coupling regime, hybridisation with high-oscillator-strength intralayer excitons is required [166, 167, 150]. In conventional double quantum well systems, this was achieved by the application of electric fields. These polaritonic species inherit the enhanced interactions arising from the out of plane excitonic dipole orientation and are therefore called dipolar polaritons or dipolaritons. It is therefore easy to notice that the system studied in Chapter 5.1, would be an ideal canditate for realising dipolaritons if atomically thin heterostructures are embedded in microcavities.

In this work we realise dipolaritons in atomically thin semiconductors in encapsulated homobilayers of MoS_2 in Distributed Bragg Reflectors (DBRs). Recently, similar phenomena were realized using hybridized excitons in $MoSe_2/WS_2$ heterostructures [124], where moire polariton nonlinearities have been reported [148]. The approach of MoS_2 bilayers having naturally occurring 2H stacking [89, 168] allows for a more spatially uniform sample over large scales. They employ straightforward fabrication of high-quality directly exfoliated MoS_2 bilayers encapsulated in hexagonal boron nitride (hBN) resulting in uniform samples suitable for the observation of macroscopic many-body phenomena [169]. As such, the high crystallinity unperturbed by stacking order variation or interlayer contaminants makes MoS_2 bilayers as yet the only platform among TMD systems that can provide dipolar excitons with high oscillator strengths, large binding energies and chirality without compromising the spatial uniformity of the system. We therefore study this sytem linear properties in the strong coupling regime and then proceed to engineer dipolaritons of large non-linearity .

6.2 Microcavity design

To achieve strong exciton photon coupling, the active semiconducting layer must coincide with the antinode of the electric field of the wavelength of resonance confined in the cavity. Therefore, carefull design of the thicknesses and refractive indexes of the microcavity structure is needed. We do this with the use of open source transfer matrix method simulations, which work considering the continuity arising from Maxwells equations to calculate the electric field distribution. We consider the bottom mirror to be a commercially availabe highly reflective DBR of 12 pairs composed of Nb_2O_5 and SiO_2, terminated with the latter with a stopband centred at 625 nm.

First the reflectivity spectrum of the bare heterostructure is taken and lorenzians are fitted to reproduce the spectrum. From the fits and Kramers-Kronig relations the complex and real refractive indices of the MoS_2 bilayer sample can be extracted. Subsequently, the thickness of top and bottom hBN are measured using atomic force microscopy. Taking the refractive indices of the materials involved from literature [170–173] we are then in a position to find the right the cavity length, such that the antinode of the electric field at our desired wavelength, spatially coincides with the bilayer. As mentioned earler in this thesis,there are two types of Fabry Perot cavities that one can experimentally study. For monolithic cavities (fixed length) we choose Polymethyl methacrylate (PMMA) as the spacer layer between the mirrors as we find that hBN has a good adhesion to PMMA which allows for uniformity without airgaps at the interface. In a tunable open cavity system the spacer layer is air.

As 2D materials are more easily transferred on rigid substrates, we work on a $\lambda/4$ configuration. This means that the bottom mirror is terminated with the low index SiO_2 layer, such that the antinode of the elecric field is at its top surface, instead of the middle of the cavity length usually found in conventional semiconductor and organic microcavites. An example of the electric field distribution is shown in Fig 6.1. It can be seen that the configuration of choice is the 3λ / 4 , while the bilayer (high refractive index) coincide the second antinode of the field distribution in the cavity. The first antinode is only a few tenths of nanometers from the top mirror. This cavity length is usually difficult to achieve, either

due to the presence of thicker flakes in a tunable cavity or due to the non- reliable spin coating deposition of the PMMA layer at these thickness.

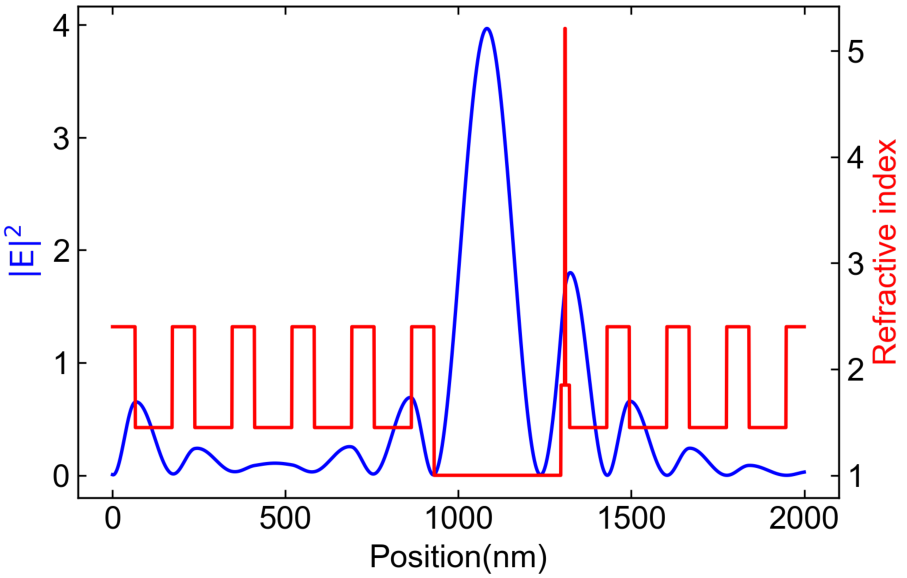

Fig. 6.1 **Electromagnetic Field distribution in DBR cavity**. The x axis is the position on the microcavity along the out of plane direction starting from the top and moving to the bottom. The blue curve is the absolute value of the electric field multiplied by its complex conjugate. With red, the real part of the refractive index is used for each layer of the structure, including the high index MoS_2.

One other factor to consider when designing the cavity is the reflectivity of the top and bottom mirrors, in accordance to the geometry the measurement is done. Since we are working in reflection geometry, it is important for the relative reflectivity of the mirrors to allow the reflected light in the direction of optical access. In addition, as can be seen from if the contrast between the high and low index layers of the DBR or if the number of pairs are too high, the amount of light that gets into or escapes the cavity is very little. On the other hand, the lower the losses from the mirror the higher the quality factor of the cavity, minimising the dissipations of the system resulting in narrow linewidths. The design of each microcavity is therefore a trade-off between these two contrasting outcomes. Figure 6.2 presents a comparison of the simulated spectra at the hIX anticrossing for DBR and Ag top mirrors at different number of pairs or thickness, respectively. One can see how the Rabi splitting changes as a function of pairs/thickness of the top mirror, but also the visibility of

polaritons from the evolution intensity of the peaks. It can be seen that for DBR top mirrors, the Rabi splitting increases but the intensity decreases very rapidly as a function of number of pairs. In contrast, the Ag mirror enables a large Rabi splitting, even at low thickness where the visibility of the peaks are more prominent. It is therefore concluded that a cavity with bottom DBR mirror and a top Ag mirror allows for an easier balance of the trade-offs needed experimental observation of strong coupling.

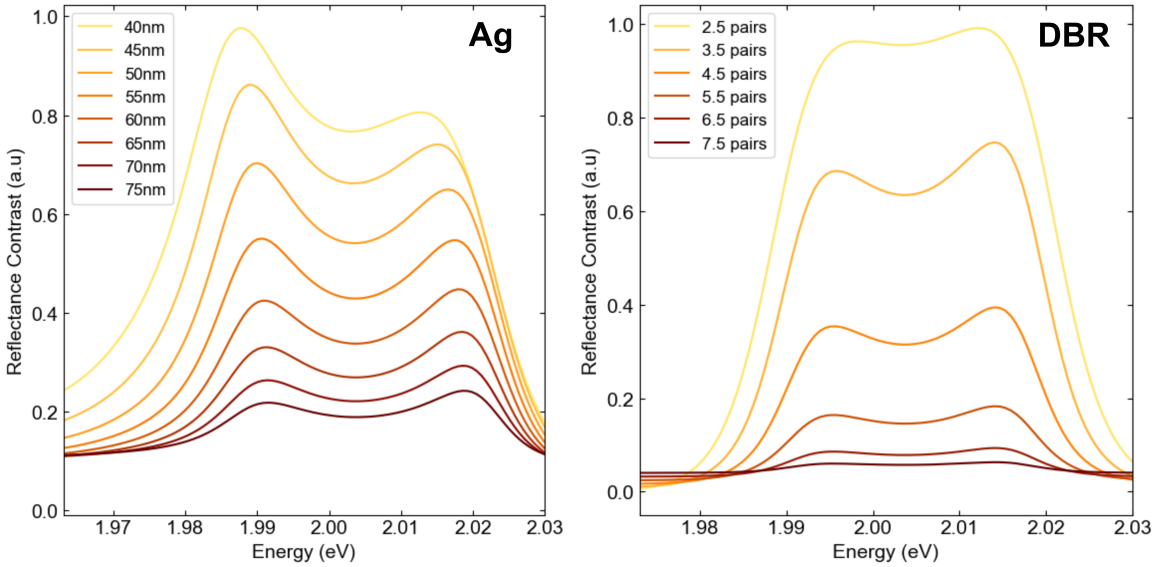

Fig. 6.2 **Simulated spectra at hIX anticrossing. a** For a cavity with a Ag top mirror the evolution of the spectra at different thickness **b** . Simulated spectra at anticrossing for different number of pairs.

The simulations of the resulting dispersions and the electric field distribution is shown in Fig 6.3 a,b respectively. We can see that a Ag-DBR cavity results in well pronounced polariton modes with strong coupling for both the intralayer and hybridised interlayer excitons in simulation. In addition, the magnitude of the electric filed in the cavity is calculated to be higher than the one shown with top/bottom DBR in Fig 6.1. This can be explained by the fact that the metal mirror promotes the localisation of the field, as in similar configurations of Tamm-plasmon polaritons in literature [174, 175]. In contrast to a top DBR which, despite the much higher Q-factors, allows for distribution of the field in the pairs. This would, also, spport why the large splitting in Fig 6.2 is retained at low Ag thickness. By using a Ag top mirror we partly sacrifice the Q factor of the cavity to achieve better field confinement,

hence better coupling, and increase visibility of the polariton peaks. We note that while we believe this is the best choice for experimental observation of interlayer polaritons in bilayer TMDs this may not be case in other systems as it depends heavily on the exciton linewidths, oscillator strength and the collection efficiency of the set-ups involved.

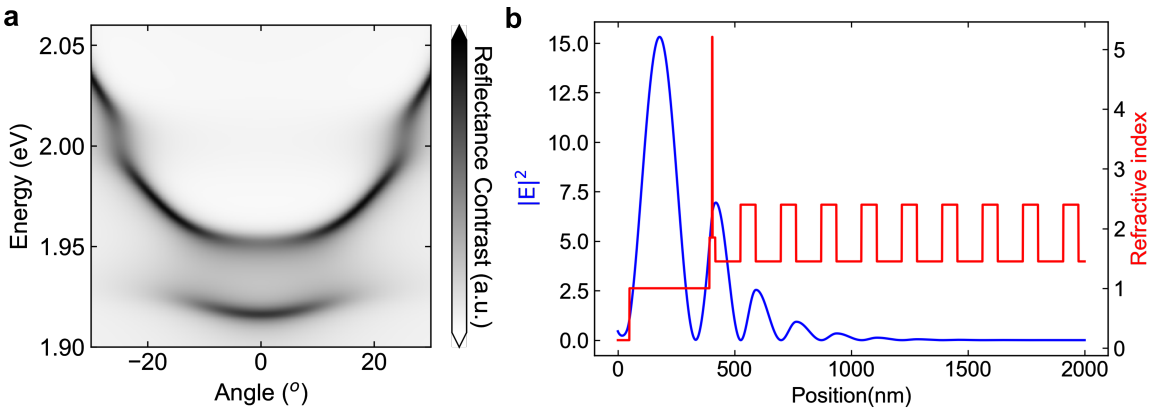

Fig. 6.3 **Simulation for the chosen cavity design a** Dispersion simulation of a cavity dispersion that allows for dipolariton observation . **b** Simulated electric filed distribution (blue) and the refractive index of each layer (red) along the length of the cavity

6.3 Observation of Dipolar polaritons

A tunable planar micro-cavity, illustrated in Figure 6.4a, is formed introducing a silver mirror above the bottom DBR, where our device is placed, inside a 4.2 K helium bath cryostat. Piezo actuators with 5 degrees of freedom are used to translate, align and approach the mirrors. The bottom DBR with the encapsulated MoS_2 BL sits on a set of piezo nanopositioners, allowing precise tuning of the cavity length, ΔL, and cavity mode energy. With optical access from the top of the cavity, RC spectra are taken at each ΔL, collecting only angles within 5 degrees from normal incidence.

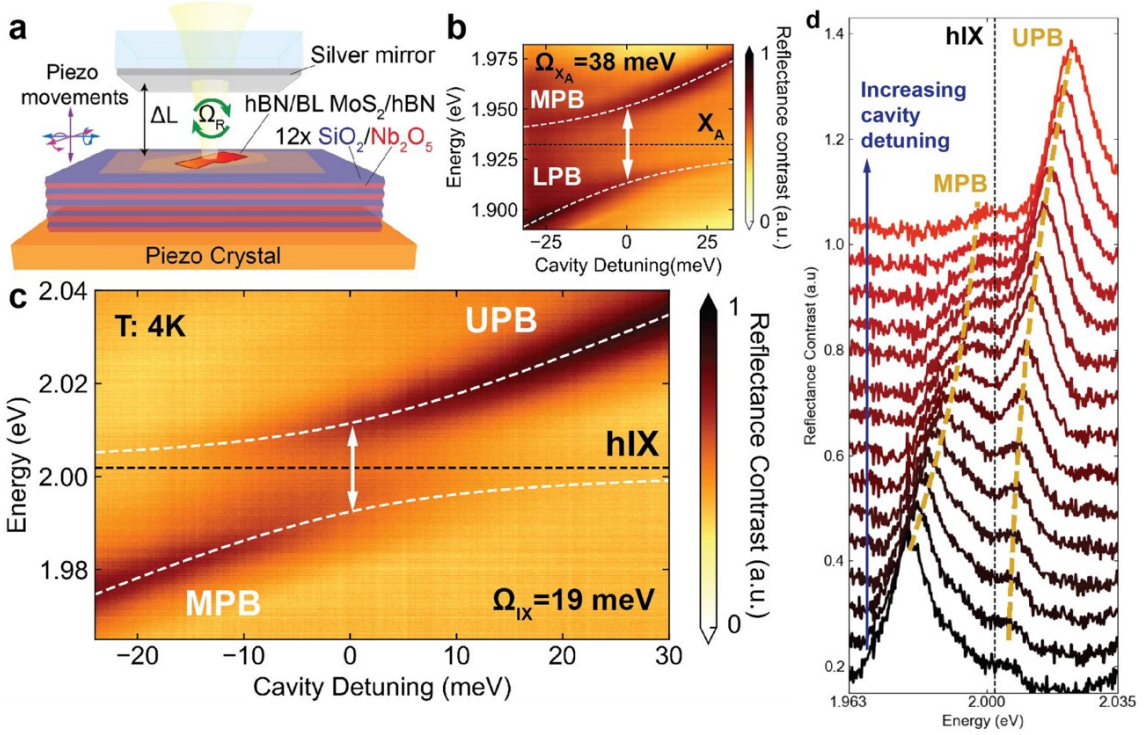

Fig. 6.4 **Strong coupling in homobilayers and hybridised interlayer polaritons. a,** Schematics of the tunable open microcavity system. **b, c,** Low temperature (4K) RC cavity scans across **b** X_A and **c** hIX energies as a function of cavity-exciton detuning ($\Delta = E_{cav} - E_{exc}$). **d,** Cascade plot of the RC spectra extracted from **c** showing unambiguously the UPB and MPB appearing from the anticrossing between hIX and the cavity mode.

RC scans as a function of the cavity detuning $\Delta = E_{cav} - E_{exc}$, where E_{cav} and E_{exc} are the cavity mode and the corresponding exciton energy respectively, are shown in Fig. 6.4 b,c,d. Strong coupling of the cavity mode with X_A and hIX resonances occurs, resulting in two clear splittings and three visible polariton branches. The clear anticrossing observed at hIX energy is a direct consequence of the large oscillator strength acquired after the hybridization of IX with X_B. The extracted Rabi splitting is $\Omega_X = 38$ meV for X_A and $\Omega_{hIX} = 19$ meV for hIX.

The unambiguous observation of strong coupling is also apparent in the clearly resolved peaks of MPB and UPB through the tuning of the cavity, as shown in the spectra in Fig. 6.4d. As expected in strong coupling regime, the visibility of each polariton branch decreases as a function of the excitonic character of the mode, becoming dark at increasingly positive (negative) cavity detunings for the MPB (UPB). The polaritons linewidth increases accordingly,

approaching that of the bare excitons. The larger Rabi splitting of $\Omega_X = 38$ meV observed for X_A, is expected from its stronger absorption relative to hIX in the bare flake. In fact, the polariton coupling strength scales as the square root of the corresponding exciton oscillator strength. Hence, taking the ratio of Rabi splittings $\Omega_{hIX}/\Omega_X = 0.5$, we see a good agreement with out-of-cavity data, which indicate a ratio of about 4 between the oscillator strengths of X_A and hIX.

A full picture of our system, corresponding to MoS_2 homobilayer, has to take into account 4 different modes coupling to each other: only IX and X_B hybridise through a tunneling parameter, while X_A and X_B can couple with the cavity due to their high oscillator strength. We can then simplify this picture by rewriting the IX and X_B states in terms of the new basis of hybridised modes, hIX and hX_B, all of them now capable of a coupling with the cavity mode. The corresponding Hamiltonian reads

$$H = \begin{pmatrix} E_c & \Omega_{X_A} & \Omega_{hIX} & \Omega_{hX_B} \\ \Omega_{X_A} & E_{X_A} & 0 & 0 \\ \Omega_{hIX} & 0 & E_{hIX} & 0 \\ \Omega_{hX_B} & 0 & 0 & E_{hX_B} \end{pmatrix}, \tag{6.1}$$

where E_c in the energy of the cavity mode, and E_{X_A}, E_{hIX}, E_{hX_B} denote energies of the respective excitonic modes. Here, Ω_{X_A}, E_{hIX}, and Ω_{hX_B} are corresponding matrix elements for light-matter coupling (Rabi splittings).

Due to the large energy separation between the resonances, each splitting can be fitted to a two level oscillator model independently. In our case, the spectra from piezo voltages close to resonant anticrossings of X_A and hIX, were fitted to Lorenzian functions. The energies of the polariton branches at each spectrum were then collected to find the best fit respective Hamiltonians of two level coupled oscillators, such that $H_A = \begin{pmatrix} E_c & \Omega_{X_A} \\ \Omega_{X_A} & E_{X_A} \end{pmatrix}$ and $H_{h_{IX}} = \begin{pmatrix} E_c & \Omega_{hIX} \\ \Omega_{hIX} & E_{hIX} \end{pmatrix}$ and the values of Rabi splittings and resonant energies were extracted. The aforementioned is shown in Fig. 6.5. A Lorenzian peak (orange) is fitted to

the data (blue dots) and the linewidth is extracted to be equal to 11 meV, confirming that the condition for strong coupling regime is met, $\Omega^2 > (\gamma_c{}^2 + \gamma_x{}^2)/2$ as stated by [176].

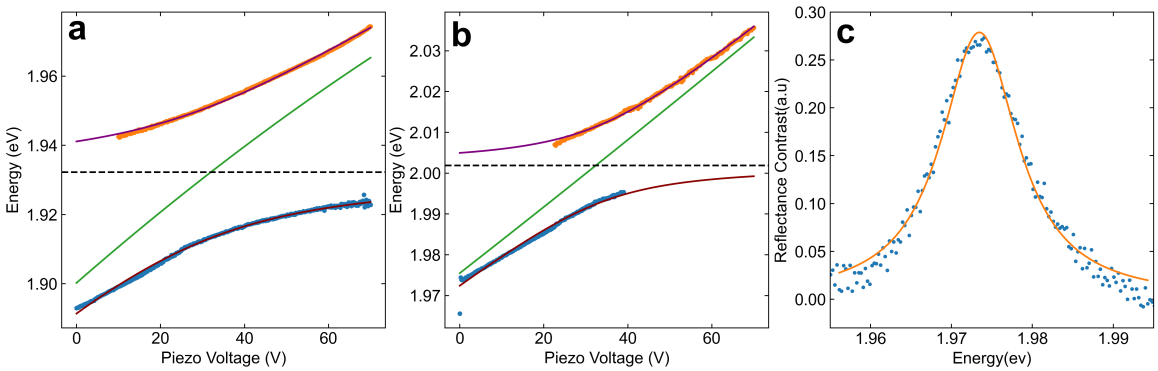

Fig. 6.5 **Coupled oscillator model fits. a), b)** Orange and blue dots represent the extracted peak energies of individual spectra near the a) X_A and b) hIX energies. The solid purple (UPB) and red (LPB) curves are the solutions to the fitted coupled oscillator Hamiltonians, and the green solid line is the extracted cavity mode energy as a function of voltage. **c)** shows a spectrum(dots) and the fit (line) of the uncoupled cavity mode.

By performing polarisation-resolved cavity scans at high magnetic fields of 8T in the Faraday geometry, we show that the layer pseudospin inherited chirality is preserved in the strong light matter coupling regime (Fig. 6.4e,f). A similar behaviour to the uncoupled excitons is observed, with the polariton Zeeman splitting increasing as a function of exciton fraction. Dipolar polaritons show an opposite and larger Zeeman splitting relative to the intralayer polaritons (Figure 6.6). The magneto-optical response of the dipolaritons is in agreement with the bare flake observations. A detailed analysis is outside the scope of this project, and a full study of the interplay of magnetic and electric fields with the exciton pseudospins in this rich polaritonic system will be investigated in a different study. The extracted exciton energy difference (2.8 meV) is comparable with the Zeeman splitting measured on the bare flake, while the Rabi splitting remains equal between the two polarization (23.2 meV). Specifically, the Rabi splitting measured under magnetic field is higher than at 0T. Such effect was previously observed in microcavities of GaAs QWs under high magnetic fields [177], being ascribed to a shrinkage of the exciton wave-function. Here, the opposite Zeeman splitting for X_A and hIX (shown in Fig. 6.6) offers an additional degree of freedom for the tunability of polariton properties. For example since the two anticrosings decrease in

energy separation, the effective mass of the MPB can be further tuned, within a fixed cavity length.

6.4 hIX dipolariton nonlinearity

To investigate the nonlinear properties of strongly-coupled dipolar excitons, a monolithic cavity was fabricated, covering an encapsulated MoS_2 homobilayer placed on a DBR with a PMMA spacer (245 nm) and a silver mirror. The cavity, now with a fixed length, was investigated using a microscopy setup optimized for Fourier-plane imaging. The measured dispersion, shown in Fig.6.7(a) displays the LPB and UPB at the anticrossing between the hIX and cavity resonance, showing a similar value of Rabi splitting compared to the tunable cavity experiment in Fig.6.4. At increased fluence at 58.5 μJcm^{-2}, only a weakly coupled cavity mode is visible, as illustrated in Fig.6.7(b). A cascade plot of the spectra taken at the anticrossing angle ($\sim 6.5°$) for the different fluences is presented in Fig.6.7(c), clearly showing the collapse of the polariton peaks into one weakly coupled cavity mode after a threshold of 25 µJcm^{-2}. The LPB and UPB energies extracted from the coupled oscillator model and the related normalised Rabi splitting (Ω/Ω_0) are shown in Fig.6.7(d,e) as a function of the total polariton density. The normalised Rabi splitting value drops to 0.6, before the collapse of strong coupling regime. As the polariton density is increased, the LPB and UPB approach each other almost symmetrically, converging to the exciton energy. Remarkably, we thus observe a complete density-induced transition of the TMD cavity from strong to weak coupling regime.

In this experiment, the cavity mode at all angles lies at higher energies compared to X_A, which therefore is not coupled to the cavity, being analogous to the case of NB excitation for hIX in Fig.5.5(b). Hence, the extracted Rabi splittings are fitted with a theoretically predicted trend of Ω as a function of polariton density, Rabi splitting at low density Ω_0, Bohr radius α and the nonlinear coefficients taking into account the optical saturation and the exciton spectral broadening calculated for the NB illumination regime B.3. For the fit, Ω_0 and α are left as free parameters giving values of Ω_0 = 20 meV and α = 2.28 nm, in good

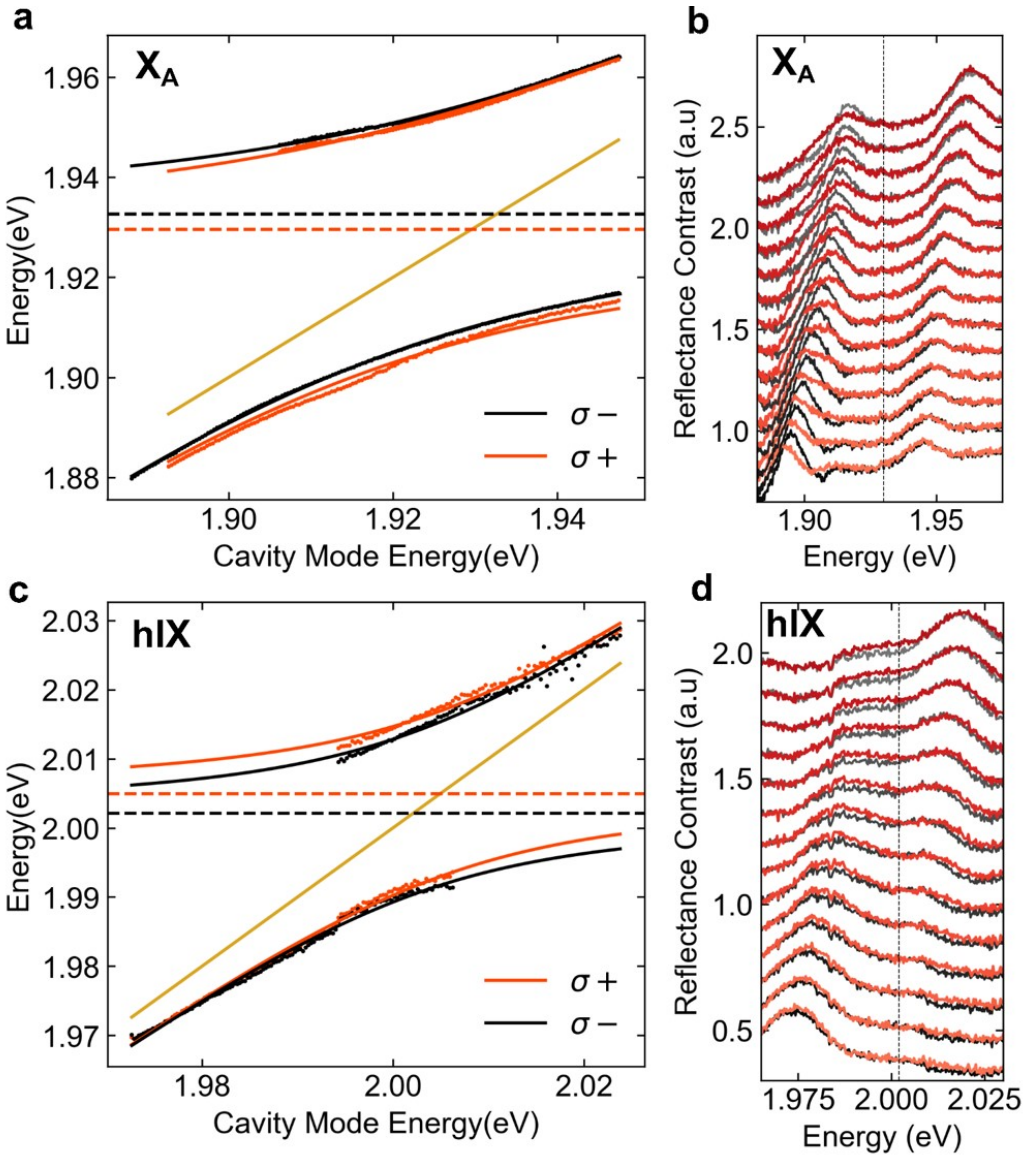

Fig. 6.6 **Polariton Zeeman Splitting** Tunable cavity RC scans near X_A (**a,b**) and hIX (**c,d**) energies under 8 T magnetic field, with a circularly polarised detection. Orange and black colours represent σ^+ and σ^- detection respectively. **a,c** Dots represent the extracted peak energies of individual spectra. The solid orange and black curves are the solutions to the fitted coupled oscillator Hamiltonians and the golden solid line is the extracted cavity mode energy. The extracted exciton energies are shown in as the dashed horizontal lines of the corresponding colour. **b,d** Cascade plot of the spectra near resonance in the two polarisations for each exciton-polariton energy. **a,b**The deviation of the σ^+ LPB datapoints from the coupled oscillator model solution (solid line) is due to the presence of the fully polarised trion at ≈ 1.91 eV. This can be seen as a broadening due to weak coupling of the lower energy peak of the orange (σ^+) spectra in **b)**, where a cascade plot of the spectra near resonance in the two polarizations is shown.

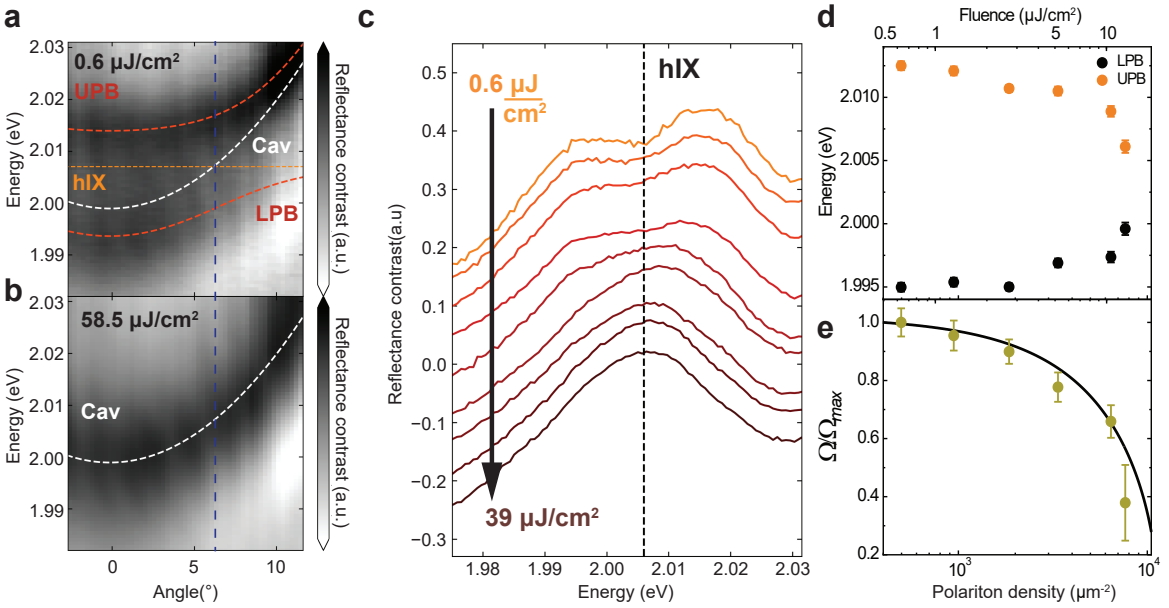

Fig. 6.7 **Dipolariton nonlinear behaviour. a, b** Reflectance contrast maps of the BL MoS_2 monolithic cavity dispersion as a function of the incidence angle measured at different incidence fluence. At a low fluence (0.6 μJcm^{-2})(a) a clear anticrossing is observed at about 6.5°, which can be fitted with a two coupled oscillator model as shown in the figure: the dashed orange lines refers to UPB and LPB, the cavity mode dispersion is depicted by the white dashed line, while the hIX mode is in dark yellow. The vertical blue dashed line shows the anticrossing angle. In (b) the fluence is increased to 58.5 μJcm^{-2}, causing a complete collapse of the strong coupling regime, with the disappearance of the anticrossing in favour of a weakly coupled cavity mode. **c,** Cascade plot of the cavity spectra taken at the cavity-exciton resonance angle with increasing excitation fluence, clearly displaying the collapse of strong coupling regime. **d,** UPB and LPB peak energies at the anticrossing and **e,** Rabi splittings normalised by the Rabi splitting measured at the lowest power(Ω/Ω_0). The above extracted from the coupled oscillator model fit are shown as a function of fluence (top horisontal axis) and total polariton density(bottom horisontal axis). The experimentally deduced values for (Ω/Ω_0) are fitted with our theoretical model (black solid line in (e)).

agreement with the expected values, hence confirming the validity of our results. A nonlinear polariton coefficient $\beta = 0.86\ \mu\text{eV}\mu\text{m}^2$is extracted by differentiating the fitted function with respect to the polariton density. Comparing our results to X_A intralayer exciton polaritons for encapsulated monolayers in similar cavities [148], we observe that the nonlinearity factor in dipolar interlayer polaritons is about an order of magnitude larger. This is in good agreement with the theoretically predicted intrinsic nonlinearity of hybridized interlayer polaritons, and with the experimental comparison of hIX and monolayer X_A outside the cavity. We predict that by tuning the cavity mode at lower energies in order to couple both hIX and X_A, the nonlinear polariton coefficient will be enhanced owing to the inter-exciton saturation of the hole crowding effect, discussed in in their common VB. The foreseen nonlinearity factor can be thus increased further by almost an order of magnitude, reaching values significantly higher than TMD monolayers in strong coupling regime.

6.5 Conclusion

In summary, we report the non-linear exciton-polariton behaviour in MoS_2 homobilayers. The later is unique material platform that provides high oscillator strengths in dipolar excitons, with many degrees of freedom, over a uniform large area. To achieve access to the strong light-matter coupling regime, we embed the active layer in hybrid Ag/DBR microcavities. This leads to the first experimental demonstration of dipolar polaritons in TMD homobilayers. Their chirality is further investigated with the application of an out-of-plane magnetic field, leading to a Zeeman slitting of an opposite direction to intralayer polaritons. By increasing the polariton density, we observe the non-linear behaviour as a quenching of the polariton Rabi-splitting. Analysing the rate of nonlinear changes we extract a nonlinearity factor which is an order of magnitude larger than TMD monolayer polaritons. This is in agreement with the theoretical microscopic model and experimental evidence, previously developed in a collaborative study on the hIX exitons. In fact, this system offers a unique possibility to exploit delocalised holes shared between different intra- and interlayer exciton species in the same sub-band.We expect that in microcavities where the cavity mode is coupled to both

hIX and X_A in MoS_2 bilayers, and the excitation similar to the broad-band regime can thus be realized, the nonlinear polariton coefficient will be dramatically enhanced owing to the hole crowding effect, allowing highly nonlinear polariton system to be realized. We also note the possibility to further increase the nonlinearity with the use of gated bilayers in such cavities. These would allow to independently apply change doping levels while controlling the intra-interlayer component, with the potential for further study and enhance the nonlinear mechanisms. We thus predict that MoS_2 bilayers could be an attractive platform for realization of quantum-correlated polaritons with applications in polariton logic networks [178] and polariton blockade [179, 180].

CHAPTER 7

CONCLUSION

7.1 Summary of findings

To summarise, in Chapter 4 we use alloying of TMD to study the tunability of IX in $Mo_xW_{1-x}Se_2/MoSe_2$ structures. We observe a fine tuning of IX with concentration by more than 50 meV before we approach the energy of homobilayer indirect excitons. It is also apparent from the IX spectral feutures of PL linewidth and intensity that they undergo a substantial change in nature from spacially indirect to momentum indirect. Thisis confirmed by a similar clear trend we observe $Mo_xW_{1-x}Se_2/WSe_2$ structures in a collaborative work for this study which was also supported by lifetime measurements. Power dependencies on both sets of structures show the enhanced exciton-exciton interaction of IX, compared to intralayer excitons, which is also seen to be affected as we approach concentrations where the momentum indirect transition is dominant. Due to the small band offsets achieved by the $Mo_xW_{1-x}Se_2/MoSe_2$, we are able to resolve further changes in IX in medium Molybdenum concentrations, even before reaching the homobilayer configuration. Namely, signatures of hybridised interlayer excitons were observed in RC. Using theory from collaborators in the univerity of manchester, we confirm that the multiple absoption dips apparent in our spectra are induced by the moire periodicity mini band folding. We conlcude that alloying is a good method to increase further the variety of 2D semiconductor that can be stacked together, opening noumerous combinations that can be studied to fine-tune IX nature. However,

more work is needed is scrutinising the exact origin of IX transitions observed, due to their multifaceted depenance on several physical and fabrication-induced parameters.

Instead, Chapter 5 proposes homobilayers as a system that possesses interlayer excitons of equally interesting physics, but more straightforward origin and fabrication processes. We encapsulate as-exfoliated 2H MoS_2 homobilayers in hBN to observe hybridised interlayer excitons (hIX). The combination of atomic orbital symmetry and the fact that the valence band splitting is the smallest in MoS_2 out of the TMDs allows for very efficient delocalisation of holes over both layers, forming an exciton which has both inter and intra-layer components. We measure hIX to have 23 % of the oscillator strength of A series intralayer excitons, which is an unusually large oscillator strength for interlayer excitons. By applying an out of plane magnetic field toe break the spin degeneracy, we observe the opposite Zeeman splitting of hIX compared to intralayer excitons, confirming their interlayer nature. Next, we increase the fluence to observe the denisty dependent behaviour and non-linear interactions of MoS_2 bilayer excitons. We find that both hIX and A series intralayer excitons are more non-linear that intralayer excitons in monolayer, with hIX saturating at 8 times lower densities. From the absorption transitions in this system and the energy separation of hIX to intralayer excitons, our collaborators from the University of Exeter can deduce the dipole moment of this excitons to be accounted into the non-linear interaction mechanisms in play in this system. We attribute the increased interactions to increased coulomb interactions, arising from the larger size of dipolar excitons and the fact that both excitonic species are larger in size than monolayer excitons due to the increased dielectric screening induced by the presence of another layer. Our most striking finding is the significant enhancement of in non-linearity of hIX by an extra order of magnitude and the switching of its density dependent energy shift, upon simultaneous excitation with intralayer excitons. In collaboration with theoretical physicists we analyse microscopically this system. We interpret this non-linearity as a result of the interdependency of excitons caused by the holes of the two excitonic species residing in the same valence subband. Specifically, we find this interdependency to result in a phase space filling effect which causes both enhanced optical saturation and attractive interspecies scattering. To our best of knowledge this is a mechanism unique to 2D bilayers

which we term as hole crowding. The combination of mechanisms described above result in the observation of hIX to interact up to a total of two orders of magnitude more strongly than monolayer excitons.

In Chapter 6 we use the high oscillator strength dipolar hIX studied in the previous chapter, to realise dipolar exciton polaritons. We simulate designs of planar microcavities and find that a hybrid Ag/DBR mirror cavity will work best in our case, due to a combination of increased visibility of the polariton branches and localisation of the electric field. Using tunable open microcavity systems at low temperatures, we tune through the hIX energy and observe distinct hybridised polariton branches, signifying we are well into the strong coupling regime. We, also, observe that the Zeeman splitting is transferred in the strong coupling regime. We later increased the fluence in similar monolithic cavities and observe a fast quenching of the Rabi splitting. Analysing this quenching as a function of polariton density we observe hIX dipolaritons to have an order of magnitude larger non-linear factor than monolayer polaritons.

7.2 Outlook

In this section we discuss promising advances on fabrication and scalability. In addition, we state possible directions for future studies, based on the findings presented in this thesis.

7.2.1 Fabrication and Scalability

While the properties of TMDs have proved them to be a system of great potential and the ability of vdW stacking opens virtually countless avenues, the quality and scalability of their fabrication is what hinders their large scale implementation in everyday life. While exfoliated samples are still believed to give the best optical spectra, there have been some noticeable advances in literature, that may allow for large scale devices, automation and clean interfaces. Namely, studies have demonstrated the exfoliation of centimeter sized monolayers via gold assisted exfoliation immediately after the growth of gold in a variety of 2d materials [181, 182]. Meanwhile, an impressive study on the automation of heterostructure fabrication

has been reported [183]. In this study a fully automated inert environment glovebox system allows for the identification of up to 400 graphene monolayers per hour, doing four stacks per hour and with the capability to stack up to 29 layers. In addition, other studies have managed to fabricate high quality centimetre sized heterostructures of atomically sharp interfaces, by stacking CVD grown samples in vacuum. While still these are not close to conventional systems wafer-scale sizes, the combination of this advances allows to talk about the future of 2D materials.

7.2.2 Future studies

Lattice reconstruction Optical Signatures

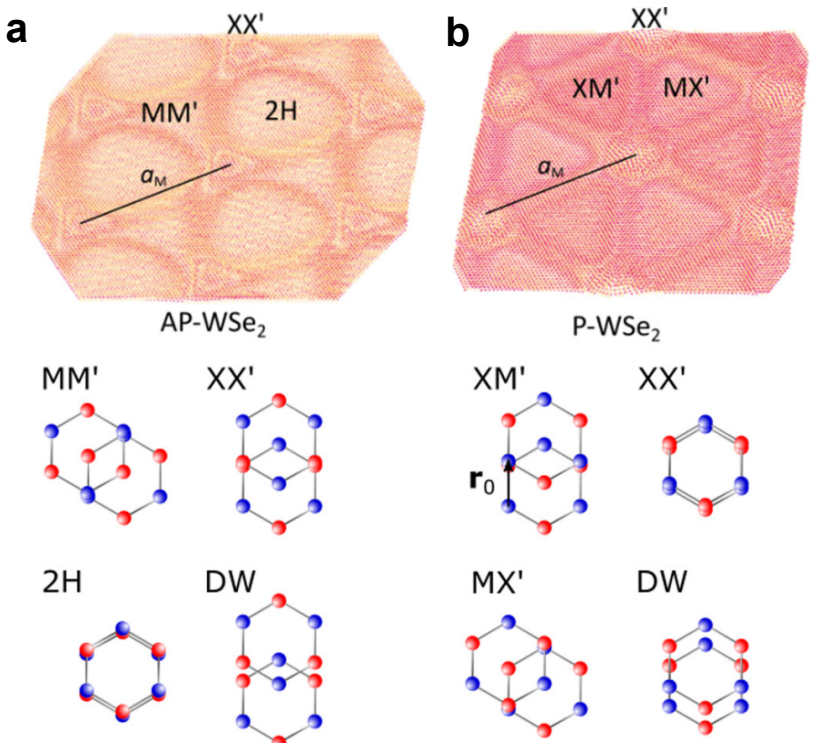

Fig. 7.1 Schematic illustration of lattice reconstruction effect **a** Antiparallel and parallel **b** configuration of WSe_2 bilayers. Bottom panels show the atomic overlap at the different stacking energy regions. [86]

In chapter 4 we have seen moire hybridised interlayer exciton signatures in the RC spectrum. These spectra are believed to be largely influenced by lattice reconstruction ef-

fects deviating from the ideal moire periodicity. Lattice reconstruction effects have been investigated theoretically and observed using SPF and conductive AFM imaging techniques. However, to the best of our knowledge their exact influence on the optical signatures of IX have not been studied. Heterobilayers with one layer for pure TMD stack in parallel alignement with an alloyed TMD would allow for finely tuning the lattice mismatch between each layer, and therefore the severity of lattice reconstruction effects. We propose that our set of $Mo_xW_{1-x}Se_2/MoSe_2$ structures as a good platform to study the influence of lattice reconstruction on the optical spectra of TMD heterostructures. This may be investigated with both μPL but also s-SNOM PL to compare and contrast localised over collective effects.

Gate tunable MoS_2 bilayers

The non-linearity of hIX in homobilayers of MoS_2 may be further explored, tuned and even enhanced further through the use of gated structures. Below we present a list of anticipated studies and results with the application of electrical field in this system:

- With the use of a vertical electrical field, one should be able to fine tune the interlayer vs intralayer component. We expect the coulomb interactions arising from the out-of plane dipole moment to increase significantly, since that would align the dipoles in the same vertical direction. Hence, the nonlinearity can be potentially increased and balanced according to the application or up to the point that the oscillator strength is still enough to couple to a cavity.

- With fabrication capabilities of clean interfaces and multilayer stacking, one can make a gated device with the two layers having antiparallel orientation and also introduce one or few layers of hBN as a spacer between the layers. The spacer layer should not exceed few layers since that woud hinder strongly the hole delocalisation. Upon application of a vertical field, interlayer coupling will be activated to form new hIX of much larger size and vertical dipole moment, enabling for strongly interacting species in direct analogy to InGaAs double quantum wells [166].

- A vertical electric field would create dipoles facing in one direction. These would allow to couple the layer pseudospin to the valley pseudospin securing the one-one correspondence of valley and selection rules. Combining the large nonlinearity of dipolar polaritons with the valley addressable of TMD polaritons can be of great scientific and technological interest.

- In addition, with the contacted gates one may study the doping effects in this system. It was, recently, found that high doping of trions can increase their nonlinearity [159]. An interesting future direction would be to investigate the effects of positive doping on the hole-crowding effect and the dependence of the resulting non-linearity on the valence band Fermi level.

Hole crowding in the strong coupling regime

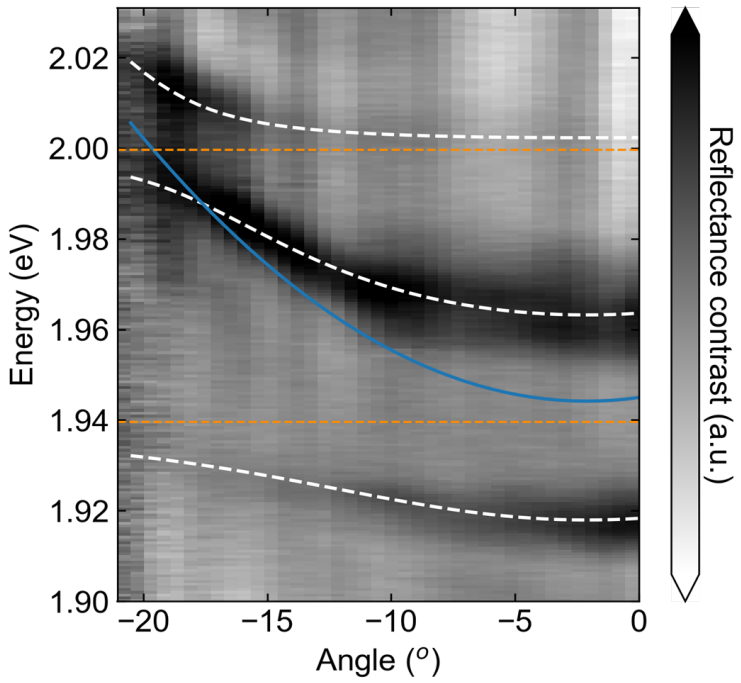

Fig. 7.2 Cavity coupling to both hIX and X_A. The blue solid line is the cavity mode and the orange dashed lines are the X_A and hIX energies. The white dashed lines are the coupled oscillator model fitted polariton branches

In Chapter 6, we study the interlayer exciton polariton non-linearity in a cavity that couples to only the hIX. That may be considered as being analogous to the NB illumination scheme of excitons in Chapter 5. Very recently, a cavity that couples to both X_A and hIX was fabricated, shown in Fig 7.2. A future direction would be to study the hole crowding effect in the strong coupling regime in such cavities, analogous to the broadband scheme. Since the excitons would couple to the same cavity mode, one can expect intracavity polariton correlations mediated through hole crowding effect in the exciton reservoirs. Scrutinising this effect in different illumination regimes (NB vs BB) can help us learn more about intracavity and hole crowding mechanisms. In addition, detuning dependent studies can add another degree of freedom to enhance the tunability of the hole crowding mechanism and control on the interdependence of hIX to X_A polaritons through their relative hopefield coefficients.

REFERENCES

[1] Richard P Feynman. Plenty of room at the bottom. In *APS annual meeting*, 1959.

[2] Rudolf Peierls. Quelques propriétés typiques des corps solides. In *Annales de l'institut Henri Poincaré*, volume 5, pages 177–222, 1935.

[3] Lev Davidovich Landau. Zur theorie der phasenumwandlungen ii. *Phys. Z. Sowjetunion*, 11(545):26–35, 1937.

[4] Kostya S Novoselov, Andre K Geim, Sergei V Morozov, De-eng Jiang, Yanshui Zhang, Sergey V Dubonos, Irina V Grigorieva, and Alexandr A Firsov. Electric field effect in atomically thin carbon films. *Science*, 306(5696):666–669, 2004.

[5] Sheneve Z Butler, Shawna M Hollen, Linyou Cao, Yi Cui, Jay A Gupta, Humberto R Gutiérrez, Tony F Heinz, Seung Sae Hong, Jiaxing Huang, Ariel F Ismach, et al. Progress, challenges, and opportunities in two-dimensional materials beyond graphene. *ACS nano*, 7(4):2898–2926, 2013.

[6] Mingsheng Xu, Tao Liang, Minmin Shi, and Hongzheng Chen. Graphene-like two-dimensional materials. *Chemical reviews*, 113(5):3766–3798, 2013.

[7] Cheng Gong and Xiang Zhang. Two-dimensional magnetic crystals and emergent heterostructure devices. *Science*, 363(6428):eaav4450, 2019.

[8] A. K. Geim and et al. Van der Waals heterostructures. *Nature*, 499:419, 2013.

[9] Jose Ángel Silva-Guillén, Pablo San-Jose, and Rafael Roldán. Electronic band structure of transition metal dichalcogenides from ab initio and slater–koster tight-binding model. *Applied Sciences*, 6(10):284, 2016.

[10] M. Zhang and et al. Two-Dimensional Molybdenum Tungsten Diselenide Alloys: Photoluminescence, Raman Scattering, and Electrical Transport. *ACS Nano*, 8:7130–7137, 2014.

[11] A. Splendiani and et al. Emerging Photoluminescence in Monolayer MoS_2. *Nano Letters*, 10:1271, 2010.

[12] Kin Fai Mak, Changgu Lee, James Hone, Jie Shan, and Tony F. Heinz. Atomically Thin MoS_2: A New Direct-Gap Semiconductor. *Phys. Rev. Lett.*, 105:136805, Sep 2010.

[13] Gui-Bin Liu, Wen-Yu Shan, Yugui Yao, Wang Yao, and Di Xiao. Three-band tight-binding model for monolayers of group-vib transition metal dichalcogenides. *Physical Review B*, 88(8):085433, 2013.

[14] Emilia Ridolfi, Duy Le, TS Rahman, ER Mucciolo, and CH Lewenkopf. A tight-binding model for MoS_2 monolayers. *Journal of Physics: Condensed Matter*, 27(36):365501, 2015.

[15] Mark Fox. *Optical properties of solids*. Oxford University Press, 2012.

[16] Gang Wang, Alexey Chernikov, Mikhail M. Glazov, Tony F. Heinz, Xavier Marie, Thierry Amand, and Bernhard Urbaszek. Colloquium: Excitons in atomically thin transition metal dichalcogenides. *Reviews of Modern Physics*, 90(2):21001, 2018.

[17] Alejandro Molina-Sánchez, Davide Sangalli, Kerstin Hummer, Andrea Marini, and Ludger Wirtz. Effect of spin-orbit interaction on the optical spectra of single-layer, double-layer, and bulk MoS $_2$. *Physical Review B*, 88(4):045412, 2013.

[18] Andor Kormányos, Guido Burkard, Martin Gmitra, Jaroslav Fabian, Viktor Zólyomi, Neil D Drummond, and Vladimir Fal'ko. k· p theory for two-dimensional transition metal dichalcogenide semiconductors. *2D Materials*, 2(2):022001, 2015.

[19] K Kośmider, Jhon W González, and Joaquın Fernández-Rossier. Large spin splitting in the conduction band of transition metal dichalcogenide monolayers. *Physical Review B*, 88(24):245436, 2013.

[20] Alexey Chernikov, Timothy C Berkelbach, Heather M Hill, Albert Rigosi, Yilei Li, Ozgur Burak Aslan, David R Reichman, Mark S Hybertsen, and Tony F Heinz. Exciton binding energy and nonhydrogenic Rydberg series in monolayer WS_2. *Physical review letters*, 113(7):076802, 2014.

[21] Diana Y Qiu, H Felipe, and Steven G Louie. Optical spectrum of MoS_2: Many-body effects and diversity of exciton states. *Physical review letters*, 111(21):216805, 2013.

[22] Miguel M Ugeda, Aaron J Bradley, Su-Fei Shi, Felipe H Da Jornada, Yi Zhang, Diana Y Qiu, Wei Ruan, Sung-Kwan Mo, Zahid Hussain, Zhi-Xun Shen, et al. Giant bandgap renormalization and excitonic effects in a monolayer transition metal dichalcogenide semiconductor. *Nature materials*, 13(12):1091–1095, 2014.

[23] Keliang He, Nardeep Kumar, Liang Zhao, Zefang Wang, Kin Fai Mak, Hui Zhao, and Jie Shan. Tightly bound excitons in monolayer WSe_2. *Physical review letters*, 113(2):026803, 2014.

[24] Jason S Ross, Sanfeng Wu, Hongyi Yu, Nirmal J Ghimire, Aaron M Jones, Grant Aivazian, Jiaqiang Yan, David G Mandrus, Di Xiao, Wang Yao, et al. Electrical control of neutral and charged excitons in a monolayer semiconductor. *Nature communications*, 4(1):1–6, 2013.

[25] Timothy C Berkelbach, Mark S Hybertsen, and David R Reichman. Theory of neutral and charged excitons in monolayer transition metal dichalcogenides. *Physical Review B*, 88(4):045318, 2013.

[26] Kin Fai Mak, Keliang He, Changgu Lee, Gwan Hyoung Lee, James Hone, Tony F Heinz, and Jie Shan. Tightly bound trions in monolayer MoS_2. *Nature materials*, 12(3):207–211, 2013.

[27] Meinrad Sidler, Patrick Back, Ovidiu Cotlet, Ajit Srivastava, Thomas Fink, Martin Kroner, Eugene Demler, and Atac Imamoglu. Fermi polaron-polaritons in charge-tunable atomically thin semiconductors. *Nature Physics*, 13(3):255–261, 2017.

[28] Dmitry K Efimkin and Allan H MacDonald. Many-body theory of trion absorption features in two-dimensional semiconductors. *Physical Review B*, 95(3):035417, 2017.

[29] T Smoleński, Ovidiu Cotlet, Alexander Popert, Patrick Back, Yuya Shimazaki, Patrick Knüppel, N Dietler, Takashi Taniguchi, Kenji Watanabe, Martin Kroner, et al. Interaction-induced shubnikov–de haas oscillations in optical conductivity of monolayer mose 2. *Physical Review Letters*, 123(9):097403, 2019.

[30] Ashish Arora, Karol Nogajewski, Maciej Molas, Maciej Koperski, and Marek Potemski. Exciton band structure in layered $MoSe_2$: from a monolayer to the bulk limit. *Nanoscale*, 7(48):20769–20775, 2015.

[31] Ashish Arora, Maciej Koperski, Karol Nogajewski, Jacques Marcus, Clément Faugeras, and Marek Potemski. Excitonic resonances in thin films of WSe_2: from monolayer to bulk material. *Nanoscale*, 7(23):10421–10429, 2015.

[32] Maciej Koperski, Maciej R Molas, Ashish Arora, Karol Nogajewski, Artur O Slobodeniuk, Clement Faugeras, and Marek Potemski. Optical properties of atomically thin transition metal dichalcogenides: observations and puzzles. *Nanophotonics*, 6(6):1289–1308, 2017.

[33] Xiaodong Xu, Wang Yao, Di Xiao, and Tony F Heinz. Spin and pseudospins in layered transition metal dichalcogenides. *Nature Physics*, 10(5):343–350, 2014.

[34] Grant Aivazian, Zhirui Gong, Aaron M Jones, Rui-Lin Chu, Jiaqiang Yan, David G Mandrus, Chuanwei Zhang, David Cobden, Wang Yao, and Xiaodong Xu. Magnetic control of valley pseudospin in monolayer WSe_2. *Nature Physics*, 11(2):148–152, 2015.

[35] Gang Wang, Louis Bouet, MM Glazov, Thierry Amand, EL Ivchenko, Etienne Palleau, Xavier Marie, and B Urbaszek. Magneto-optics in transition metal diselenide monolayers. *2D Materials*, 2(3):034002, 2015.

[36] Ajit Srivastava, Meinrad Sidler, Adrien V Allain, Dominik S Lembke, Andras Kis, and A Imamoğlu. Valley Zeeman effect in elementary optical excitations of monolayer WSe_2. *Nature Physics*, 11(2):141–147, 2015.

[37] F. Cadiz, E. Courtade, C. Robert, G. Wang, Y. Shen, H. Cai, T. Taniguchi, K. Watanabe, H. Carrere, D. Lagarde, M. Manca, T. Amand, P. Renucci, S. Tongay, X. Marie, and B. Urbaszek. Excitonic linewidth approaching the homogeneous limit in MoS_2-based van der Waals heterostructures. *Physical Review X*, 7(2):1–12, 2017.

[38] Obafunso A Ajayi, Jenny V Ardelean, Gabriella D Shepard, Jue Wang, Abhinandan Antony, Takeshi Taniguchi, Kenji Watanabe, Tony F Heinz, Stefan Strauf, XY Zhu, et al. Approaching the intrinsic photoluminescence linewidth in transition metal dichalcogenide monolayers. *2D Materials*, 4(3):031011, 2017.

[39] HH Fang, B Han, C Robert, MA Semina, D Lagarde, E Courtade, T Taniguchi, K Watanabe, T Amand, B Urbaszek, et al. Control of the exciton radiative lifetime in van der waals heterostructures. *Physical review letters*, 123(6):067401, 2019.

[40] Ke Xu, Yuanfeng Xu, Hao Zhang, Bo Peng, Hezhu Shao, Gang Ni, Jing Li, Mingyuan Yao, Hongliang Lu, Heyuan Zhu, et al. The role of Anderson's rule in determining electronic, optical and transport properties of transition metal dichalcogenide heterostructures. *Physical Chemistry Chemical Physics*, 20(48):30351–30364, 2018.

[41] Zhirui Gong, Gui Bin Liu, Hongyi Yu, Di Xiao, Xiaodong Cui, Xiaodong Xu, and Wang Yao. Magnetoelectric effects and valley-controlled spin quantum gates in transition metal dichalcogenide bilayers. *Nature Communications*, 4(May):1–6, 2013.

[42] J. Kang and et al. Band offsets and heterostructures of two-dimensional semiconductors. *Applied Physics Letters*, 102:22–25, 2013.

[43] Yuzheng Guo and John Robertson. Band engineering in transition metal dichalcogenides: Stacked versus lateral heterostructures. *Applied Physics Letters*, 108(23):233104, 2016.

[44] V Ongun Özçelik, Javad G Azadani, Ce Yang, Steven J Koester, and Tony Low. Band alignment of two-dimensional semiconductors for designing heterostructures with momentum space matching. *Physical Review B*, 94(3):035125, 2016.

[45] Chenxi Zhang, Cheng Gong, Yifan Nie, Kyung-Ah Min, Chaoping Liang, Young Jun Oh, Hengji Zhang, Weihua Wang, Suklyun Hong, Luigi Colombo, et al. Systematic study of electronic structure and band alignment of monolayer transition metal dichalcogenides in van der waals heterostructures. *2D Materials*, 4(1):015026, 2016.

[46] N. R. Wilson and et al. Determination of band offsets, hybridization, and exciton binding in 2D semiconductor heterostructures. *Science Advances*, 3:1–7, 2017.

[47] Chenjing Quan, Chunhui Lu, Chuan He, Xiang Xu, Yuanyuan Huang, Qiyi Zhao, and Xinlong Xu. Band alignment of $MoTe_2/MoS_2$ nanocomposite films for enhanced nonlinear optical performance. *Advanced Materials Interfaces*, 6(5):1801733, 2019.

[48] Ming-Hui Chiu, Chendong Zhang, Hung-Wei Shiu, Chih-Piao Chuu, Chang-Hsiao Chen, Chih-Yuan S Chang, Chia-Hao Chen, Mei-Yin Chou, Chih-Kang Shih, and Lain-Jong Li. Determination of band alignment in the single-layer MoS_2/WSe_2 heterojunction. *Nature communications*, 6(1):1–6, 2015.

[49] Nathan P. Wilson, Hongyi Yu, Pasqual Rivera, Wang Yao, Xiaodong Xu, and Kyle L. Seyler. Interlayer valley excitons in heterobilayers of transition metal dichalcogenides. *Nature Nanotechnology*, 13(11):1004–1015, 2018.

[50] P. Rivera and et al. Observation of long-lived interlayer excitons in monolayer $MoSe_2$-WSe_2 heterostructures. *Nature communications*, 6:6242, 2015.

[51] John R Schaibley, Pasqual Rivera, Hongyi Yu, Kyle L Seyler, Jiaqiang Yan, David G Mandrus, Takashi Taniguchi, Kenji Watanabe, Wang Yao, and Xiaodong Xu. Directional interlayer spin-valley transfer in two-dimensional heterostructures. *Nature communications*, 7(1):1–6, 2016.

[52] Bastian Miller, Alexander Steinhoff, Borja Pano, Julian Klein, Frank Jahnke, Alexander Holleitner, and Ursula Wurstbauer. Long-lived direct and indirect interlayer excitons in van der waals heterostructures. *Nano letters*, 17(9):5229–5237, 2017.

[53] Pramoda K Nayak, Yevhen Horbatenko, Seongjoon Ahn, Gwangwoo Kim, Jae-Ung Lee, Kyung Yeol Ma, A-Rang Jang, Hyunseob Lim, Dogyeong Kim, Sunmin Ryu, et al. Probing evolution of twist-angle-dependent interlayer excitons in mose2/wse2 van der waals heterostructures. *ACS nano*, 11(4):4041–4050, 2017.

[54] Jason S Ross, Pasqual Rivera, John Schaibley, Eric Lee-Wong, Hongyi Yu, Takashi Taniguchi, Kenji Watanabe, Jiaqiang Yan, David Mandrus, David Cobden, et al. Interlayer exciton optoelectronics in a 2d heterostructure p–n junction. *Nano letters*, 17(2):638–643, 2017.

[55] Hoseok Heo, Ji Ho Sung, Soonyoung Cha, Bo-Gyu Jang, Joo-Youn Kim, Gangtae Jin, Donghun Lee, Ji-Hoon Ahn, Myoung-Jae Lee, Ji Hoon Shim, et al. Interlayer orientation-dependent light absorption and emission in monolayer semiconductor stacks. *Nature communications*, 6(1):1–7, 2015.

[56] Yongji Gong, Junhao Lin, Xingli Wang, Gang Shi, Sidong Lei, Zhong Lin, Xiaolong Zou, Gonglan Ye, Robert Vajtai, Boris I Yakobson, et al. Vertical and in-plane heterostructures from ws2/mos2 monolayers. *Nature materials*, 13(12):1135–1142, 2014.

[57] E. M. Alexeev and et al. Imaging of interlayer coupling in van der Waals heterostructures using a bright-field optical microscope. *Nano Letters*, 17:5342–5349, 2017.

[58] Matthew Z Bellus, Frank Ceballos, Hsin-Ying Chiu, and Hui Zhao. Tightly bound trions in transition metal dichalcogenide heterostructures. *ACS nano*, 9(6):6459–6464, 2015.

[59] Hui Fang, Corsin Battaglia, Carlo Carraro, Slavomir Nemsak, Burak Ozdol, Jeong Seuk Kang, Hans A Bechtel, Sujay B Desai, Florian Kronast, Ahmet A Unal, et al. Strong interlayer coupling in van der waals heterostructures built from single-layer chalcogenides. *Proceedings of the National Academy of Sciences*, 111(17):6198–6202, 2014.

[60] Ming-Hui Chiu, Ming-Yang Li, Wengjing Zhang, Wei-Ting Hsu, Wen-Hao Chang, Mauricio Terrones, Humberto Terrones, and Lain-Jong Li. Spectroscopic signatures for interlayer coupling in MoS_2–WSe_2 van der Waals stacking. *ACS nano*, 8(9):9649–9656, 2014.

[61] Dinh Hoa Luong, Hyun Seok Lee, Guru Prakash Neupane, Shrawan Roy, Ganesh Ghimire, Jin Hee Lee, Quoc An Vu, and Young Hee Lee. Tunneling Photocurrent Assisted by Interlayer Excitons in Staggered van der Waals Hetero-Bilayers. *Advanced Materials*, 29(33):1701512, 2017.

[62] Shinichiro Mouri, Wenjing Zhang, Daichi Kozawa, Yuhei Miyauchi, Goki Eda, and Kazunari Matsuda. Thermal dissociation of inter-layer excitons in MoS_2/$MoSe_2$ hetero-bilayers. *Nanoscale*, 9(20):6674–6679, 2017.

[63] Kai Wang, Bing Huang, Mengkun Tian, Frank Ceballos, Ming-Wei Lin, Masoud Mahjouri-Samani, Abdelaziz Boulesbaa, Alexander A Puretzky, Christopher M Rouleau, Mina Yoon, et al. Interlayer coupling in twisted WSe_2/WS_2 bilayer heterostructures revealed by optical spectroscopy. *ACS nano*, 10(7):6612–6622, 2016.

[64] Daniel Erkensten, Samuel Brem, and Ermin Malic. Exciton-exciton interaction in transition metal dichalcogenide monolayers and van der waals heterostructures. *Phys. Rev. B*, 103:045426, Jan 2021.

[65] Zilong Wang, Patrick Altmann, Christoph Gadermaier, Yating Yang, Wei Li, Lavinia Ghirardini, Chiara Trovatello, Marco Finazzi, Lamberto Duò, Michele Celebrano, et al. Phonon-mediated interlayer charge separation and recombination in a $MoSe_2$/WSe_2 heterostructure. *Nano Letters*, 21(5):2165–2173, 2021.

[66] S Charbonneau, MLW Thewalt, Emil S Koteles, and B Elman. Transformation of spatially direct to spatially indirect excitons in coupled double quantum wells. *Physical Review B*, 38(9):6287, 1988.

[67] YJ Chen, Emil S Koteles, BS Elman, and CA Armiento. Effect of electric fields on excitons in a coupled double-quantum-well structure. *Physical Review B*, 36(8):4562, 1987.

[68] Monique Combescot, Roland Combescot, and François Dubin. Bose–einstein condensation and indirect excitons: a review. *Reports on Progress in Physics*, 80(6):066501, 2017.

[69] Zefang Wang, Yi-Hsin Chiu, Kevin Honz, Kin Fai Mak, and Jie Shan. Electrical tuning of interlayer exciton gases in wse2 bilayers. *Nano letters*, 18(1):137–143, 2018.

[70] Nadine Leisgang, Shivangi Shree, Ioannis Paradisanos, Lukas Sponfeldner, Cedric Robert, Delphine Lagarde, Andrea Balocchi, Kenji Watanabe, Takashi Taniguchi, Xavier Marie, et al. Giant Stark splitting of an exciton in bilayer MoS_2. *Nature Nanotechnology*, 15(11):901–907, 2020.

[71] Pasqual Rivera, John R Schaibley, Aaron M Jones, Jason S Ross, Sanfeng Wu, Grant Aivazian, Philip Klement, Kyle Seyler, Genevieve Clark, Nirmal J Ghimire, et al. Observation of long-lived interlayer excitons in monolayer $MoSe_2$–WSe_2 heterostructures. *Nature communications*, 6(1):1–6, 2015.

[72] Alessandro Catanzaro. *Fabrication and characterization of transition metal dichalcogenide alloys and their heterostructures*. Thesis, University of Sheffield, oct 2019.

[73] Emma C Regan, Danqing Wang, Eunice Y Paik, Yongxin Zeng, Long Zhang, Jihang Zhu, Allan H MacDonald, Hui Deng, and Feng Wang. Emerging exciton physics in transition metal dichalcogenide heterobilayers. *Nature Reviews Materials*, pages 1–18, 2022.

[74] Chendong Zhang, Chih-Piao Chuu, Xibiao Ren, Ming-Yang Li, Lain-Jong Li, Chuanhong Jin, Mei-Yin Chou, and Chih-Kang Shih. Interlayer couplings, Moiré patterns, and 2D electronic superlattices in MoS_2/WSe_2 hetero-bilayers. *Science advances*, 3(1):e1601459, 2017.

[75] Hongyi Yu, Gui-Bin Liu, Jianju Tang, Xiaodong Xu, and Wang Yao. Moiré excitons: From programmable quantum emitter arrays to spin-orbit–coupled artificial lattices. *Science advances*, 3(11):e1701696, 2017.

[76] Long Zhang, Rahul Gogna, G William Burg, Jason Horng, Eunice Paik, Yu-Hsun Chou, Kyounghwan Kim, Emanuel Tutuc, and Hui Deng. Highly valley-polarized singlet and triplet interlayer excitons in van der waals heterostructure. *Physical Review B*, 100(4):041402, 2019.

[77] Fengcheng Wu, Timothy Lovorn, and Allan H MacDonald. Topological exciton bands in moiré heterojunctions. *Physical review letters*, 118(14):147401, 2017.

[78] Fengcheng Wu, Timothy Lovorn, Emanuel Tutuc, and Allan H MacDonald. Hubbard model physics in transition metal dichalcogenide moiré bands. *Physical review letters*, 121(2):026402, 2018.

[79] Mit H Naik and Manish Jain. Ultraflatbands and shear solitons in moiré patterns of twisted bilayer transition metal dichalcogenides. *Physical review letters*, 121(26):266401, 2018.

[80] Sara Shabani, Dorri Halbertal, Wenjing Wu, Mingxing Chen, Song Liu, James Hone, Wang Yao, Dmitri N Basov, Xiaoyang Zhu, and Abhay N Pasupathy. Deep moiré potentials in twisted transition metal dichalcogenide bilayers. *Nature Physics*, 17(6):720–725, 2021.

[81] Mit H Naik, Sudipta Kundu, Indrajit Maity, and Manish Jain. Origin and evolution of ultraflat bands in twisted bilayer transition metal dichalcogenides: Realization of triangular quantum dots. *Physical Review B*, 102(7):075413, 2020.

[82] Mit H Naik, Indrajit Maity, Prabal K Maiti, and Manish Jain. Kolmogorov–crespi potential for multilayer transition-metal dichalcogenides: capturing structural transformations in moiré superlattices. *The Journal of Physical Chemistry C*, 123(15):9770–9778, 2019.

[83] Roland Gillen and Janina Maultzsch. Interlayer excitons in mose 2/wse 2 heterostructures from first principles. *Physical Review B*, 97(16):165306, 2018.

[84] Evgeny M Alexeev, David A Ruiz-Tijerina, Mark Danovich, Matthew J Hamer, Daniel J Terry, Pramoda K Nayak, Seongjoon Ahn, Sangyeon Pak, Juwon Lee, Jung Inn Sohn, et al. Resonantly hybridized excitons in moiré superlattices in van der waals heterostructures. *Nature*, 567(7746):81–86, 2019.

[85] Kha Tran, Galan Moody, Fengcheng Wu, Xiaobo Lu, Junho Choi, Kyounghwan Kim, Amritesh Rai, Daniel A Sanchez, Jiamin Quan, Akshay Singh, et al. Evidence for moiré excitons in van der waals heterostructures. *Nature*, page 1, 2019.

[86] SJ Magorrian, VV Enaldiev, V Zólyomi, Fábio Ferreira, Vladimir I Falko, and David A Ruiz-Tijerina. Multifaceted moiré superlattice physics in twisted WSe_2 bilayers. *Physical Review B*, 104(12):125440, 2021.

[87] Astrid Weston, Yichao Zou, Vladimir Enaldiev, Alex Summerfield, Nicholas Clark, Viktor Zólyomi, Abigail Graham, Celal Yelgel, Samuel Magorrian, Mingwei Zhou, et al. Atomic reconstruction in twisted bilayers of transition metal dichalcogenides. *Nature Nanotechnology*, 15(7):592–597, 2020.

[88] Jason Horng, Tineke Stroucken, Long Zhang, Eunice Y Paik, Hui Deng, and Stephan W Koch. Observation of interlayer excitons in MoSe $_2$ single crystals. *Physical Review B*, 97(24):241404, 2018.

[89] Iann C. Gerber, Emmanuel Courtade, Shivangi Shree, Cedric Robert, Takashi Taniguchi, Kenji Watanabe, Andrea Balocchi, Pierre Renucci, Delphine Lagarde, Xavier Marie, and Bernhard Urbaszek. Interlayer excitons in bilayer MoS_2 with strong oscillator strength up to room temperature. *Physical Review B*, 99(3):1–8, 2019.

[90] Eugene Hecht. Optics 4ed, 2002.

[91] A Kavokin, G Malpuech, and Bernard Gil. Semiconductor microcavities: towards polariton lasers. *Materials Research Society Internet Journal of Nitride Semiconductor Research*, 8, 2003.

[92] European Optical Society. *Journal of the European Optical Society: Quantum and semiclassical optics. Part B*, volume 7. Institute of Physics Pub., 1995.

[93] Paul M. Walker Maksym Sich and Gareth Jones. Semiconductor exciton polaritons.

[94] A Kavokin, JJ Baumberg, G Malpuech, and FP Laussy. Microcavities oxford university press inc. *New York*, 2007.

[95] J. J. Hopfield. Theory of the contribution of excitons to the complex dielectric constant of crystals. *Physical Review*, 112(5):1555–1567, 1958.

[96] Vladimir M Agranovich and AN Faidysh. Effect of reabsorption on the luminescence quantum yield of solid solutions of organic compounds. *Optika i Spektroskopiya*, 1(7):885–895, 1957.

[97] S.I. Pekar. Theory of electromagnetic waves in a crystal with excitons. *Journal of Physics and Chemistry of Solids*, 5(1-2):11–22, jan 1958.

[98] Christian Schneider, Mikhail M Glazov, Tobias Korn, Sven Höfling, and Bernhard Urbaszek. Two-dimensional semiconductors in the regime of strong light-matter coupling. *Nature communications*, 9(1):1–9, 2018.

[99] S. Dufferwiel, S. Schwarz, F. Withers, A. A.P. Trichet, F. Li, M. Sich, O. Del Pozo-Zamudio, C. Clark, A. Nalitov, D. D. Solnyshkov, G. Malpuech, K. S. Novoselov, J. M. Smith, M. S. Skolnick, D. N. Krizhanovskii, and A. I. Tartakovskii. Exciton-polaritons in van der Waals heterostructures embedded in tunable microcavities. *Nature Communications*, 6(May):1–7, 2015.

[100] Xiaoze Liu, Tal Galfsky, Zheng Sun, Fengnian Xia, Erh Chen Lin, Yi Hsien Lee, Stéphane Kéna-Cohen, and Vinod M. Menon. Strong light-matter coupling in two-dimensional atomic crystals. *Nature Photonics*, 9(1):30–34, 2014.

[101] Gang Wang, Etienne Palleau, Thierry Amand, Sefaattin Tongay, Xavier Marie, and Bernhard Urbaszek. Polarization and time-resolved photoluminescence spectroscopy of excitons in mose2 monolayers. *Applied Physics Letters*, 106(11):112101, 2015.

[102] S. Dufferwiel, T. P. Lyons, D. D. Solnyshkov, A. A.P. Trichet, F. Withers, S. Schwarz, G. Malpuech, J. M. Smith, K. S. Novoselov, M. S. Skolnick, D. N. Krizhanovskii, and A. I. Tartakovskii. Valley-addressable polaritons in atomically thin semiconductors. *Nature Photonics*, 11(8):497–501, 2017.

[103] Zheng Sun, Jie Gu, Areg Ghazaryan, Zav Shotan, Christopher R Considine, Michael Dollar, Biswanath Chakraborty, Xiaoze Liu, Pouyan Ghaemi, Stéphane Kéna-Cohen, et al. Optical control of room-temperature valley polaritons. *Nature Photonics*, 11(8):491–496, 2017.

[104] Yen-Jung Chen, Jeffrey D Cain, Teodor K Stanev, Vinayak P Dravid, and Nathaniel P Stern. Valley-polarized exciton–polaritons in a monolayer semiconductor. *Nature Photonics*, 11(7):431–435, 2017.

[105] N Lundt, S Stoll, P Nagler, A Nalitov, S Klembt, S Betzold, J Goddard, E Frieling, AV Kavokin, C Schüller, et al. Observation of macroscopic valley-polarized monolayer exciton-polaritons at room temperature. *Physical Review B*, 96(24):241403, 2017.

[106] Nils Lundt, Łukasz Dusanowski, Evgeny Sedov, Petr Stepanov, Mikhail M Glazov, Sebastian Klembt, Martin Klaas, Johannes Beierlein, Ying Qin, Sefaattin Tongay, et al. Optical valley hall effect for highly valley-coherent exciton-polaritons in an atomically thin semiconductor. *Nature nanotechnology*, 14(8):770–775, 2019.

[107] Yuan Huang, Eli Sutter, Norman N Shi, Jiabao Zheng, Tianzhong Yang, Dirk Englund, Hong-Jun Gao, and Peter Sutter. Reliable exfoliation of large-area high-quality flakes of graphene and other two-dimensional materials. *ACS nano*, 9(11):10612–10620, 2015.

[108] Andres Castellanos-Gomez, Michele Buscema, Rianda Molenaar, Vibhor Singh, Laurens Janssen, Herre SJ Van Der Zant, and Gary A Steele. Deterministic transfer of two-dimensional materials by all-dry viscoelastic stamping. *2D Materials*, 1(1):011002, 2014.

[109] PJ Zomer, MHD Guimarães, JC Brant, N Tombros, and BJ Van Wees. Fast pick up technique for high quality heterostructures of bilayer graphene and hexagonal boron nitride. *Applied Physics Letters*, 105(1):013101, 2014.

[110] Satoshi Toyoda, Teerayut Uwanno, Takashi Taniguchi, Kenji Watanabe, and Kosuke Nagashio. Pinpoint pick-up and bubble-free assembly of 2d materials using pdms/pmma polymers with lens shapes. *Applied Physics Express*, 12(5):055008, 2019.

[111] Thiti Taychatanapat, Kenji Watanabe, Takashi Taniguchi, and Pablo Jarillo-Herrero. Quantum Hall effect and Landau-level crossing of Dirac fermions in trilayer graphene. *Nature Physics*, 7(8):621–625, 2011.

[112] A. V. Kretinin, Y. Cao, J. S. Tu, G. L. Yu, R. Jalil, K. S. Novoselov, S. J. Haigh, A. Gholinia, A. Mishchenko, M. Lozada, T. Georgiou, C. R. Woods, F. Withers, P. Blake, G. Eda, A. Wirsig, C. Hucho, K. Watanabe, T. Taniguchi, A. K. Geim, and R. V. Gorbachev. Electronic properties of graphene encapsulated with different two-dimensional atomic crystals. *Nano Letters*, 14(6):3270–3276, 2014.

[113] L Wang. One-Dimensional Electrical Contact to. *Science (New York, N.Y.)432*, 342(November):614–617, 2013.

[114] Lene Gammelgaard, James Hone, Filippo Pizzocchero, Bjarke S. Jessen, Lei Wang, Timothy J. Booth, Peter Bøggild, and José M. Caridad. The hot pick-up technique for batch assembly of van der Waals heterostructures. *Nature Communications*, 7(1), 2016.

[115] Riccardo Frisenda, Efrén Navarro-Moratalla, Patricia Gant, David Pérez De Lara, Pablo Jarillo-Herrero, Roman V. Gorbachev, and Andres Castellanos-Gomez. Recent progress in the assembly of nanodevices and van der Waals heterostructures by deterministic placement of 2D materials. *Chemical Society Reviews*, 47(1):53–68, 2018.

[116] Jeffrey J. Schwartz, Hsun Jen Chuang, Matthew R. Rosenberger, Saujan V. Sivaram, Kathleen M. McCreary, Berend T. Jonker, and Andrea Centrone. Chemical Identification of Interlayer Contaminants within van der Waals Heterostructures. *ACS Applied Materials and Interfaces*, 11(28):25578–25585, 2019.

[117] S. Tongay and et al. Two-dimensional semiconductor alloys: Monolayer $Mo_{1-x}W_xSe_2$. *Applied Physics Letters*, 104:1–5, 2014.

[118] Kei Kinoshita, Rai Moriya, Momoko Onodera, Yusai Wakafuji, Satoru Masubuchi, Kenji Watanabe, Takashi Taniguchi, and Tomoki Machida. Dry release transfer of graphene and few-layer h-bn by utilizing thermoplasticity of polypropylene carbonate. *npj 2D Materials and Applications*, 3(1):1–8, 2019.

[119] Kirill Efimenko, William E Wallace, and Jan Genzer. Surface modification of sylgard-184 poly (dimethyl siloxane) networks by ultraviolet and ultraviolet/ozone treatment. *Journal of colloid and interface science*, 254(2):306–315, 2002.

[120] A. Evren Özçam, Kirill Efimenko, and Jan Genzer. Effect of ultraviolet/ozone treatment on the surface and bulk properties of poly(dimethyl siloxane) and poly(vinylmethyl siloxane) networks. *Polymer*, 55(14):3107–3119, 2014.

[121] Achint Jain, Palash Bharadwaj, Sebastian Heeg, Markus Parzefall, Takashi Taniguchi, Kenji Watanabe, and Lukas Novotny. Minimizing residues and strain in 2d materials transferred from pdms. *Nanotechnology*, 29(26):265203, 2018.

[122] Aidan P Rooney, Aleksey Kozikov, Alexander N Rudenko, Eric Prestat, Matthew J Hamer, Freddie Withers, Yang Cao, Kostya S Novoselov, Mikhail I Katsnelson, Roman Gorbachev, et al. Observing imperfection in atomic interfaces for van der waals heterostructures. *Nano letters*, 17(9):5222–5228, 2017.

[123] KS Novoselov, A Mishchenko, A Carvalho, and AH Castro Neto. 2d materials and van der waals heterostructures. *Science*, 353(6298):aac9439, 2016.

[124] Evgeny M Alexeev, David A Ruiz-Tijerina, Mark Danovich, Matthew J Hamer, Daniel J Terry, Pramoda K Nayak, Seongjoon Ahn, Sangyeon Pak, Juwon Lee, Jung Inn Sohn, et al. Resonantly hybridized excitons in moiré superlattices in van der waals heterostructures. *Nature*, 567(7746):81, 2019.

[125] Hyeonjun Baek, Mauro Brotons-Gisbert, Zhe Xian Koong, Aidan Campbell, Markus Rambach, Kenji Watanabe, Takashi Taniguchi, and Brian D Gerardot. Highly tunable quantum light from moir\'e trapped excitons. *arXiv preprint arXiv:2001.04305*, 2020.

[126] Sadao Adachi. *Properties of semiconductor alloys: group-IV, III-V and II-VI semiconductors*, volume 28. John Wiley & Sons, 2009.

[127] LM Xie. Two-dimensional transition metal dichalcogenide alloys: preparation, characterization and applications. *Nanoscale*, 7(44):18392–18401, 2015.

[128] G. Wang and et al. Spin-orbit engineering in transition metal dichalcogenide alloy monolayers. *Nature Communications*, 6:1–7, 2015.

[129] Lihui Li, Weihao Zheng, Chao Ma, Hepeng Zhao, Feng Jiang, Yu Ouyang, Biyuan Zheng, Xianwei Fu, Peng Fan, Min Zheng, et al. Wavelength tunable interlayer exciton emission at near-infrared region in van der waals semiconductor heterostructures. *Nano Letters*, 2020.

[130] X. Hong and et al. Ultrafast charge transfer in atomically thin MoS_2/WS_2 heterostructures. *Nature Nanotechnology*, 9:1–5, 2014.

[131] Dezheng Sun, Yi Rao, Georg A Reider, Gugang Chen, Yumeng You, Louis Brezin, Avetik R Harutyunyan, and Tony F Heinz. Observation of rapid exciton–exciton annihilation in monolayer molybdenum disulfide. *Nano letters*, 14(10):5625–5629, 2014.

[132] Pasqual Rivera, Hongyi Yu, Kyle L Seyler, Nathan P Wilson, Wang Yao, and Xiaodong Xu. Interlayer valley excitons in heterobilayers of transition metal dichalcogenides. *Nature nanotechnology*, page 1, 2018.

[133] Roland Gillen. Interlayer excitonic spectra of vertically stacked $Mose_2$/Wse_2 heterobilayers. *physica status solidi (b)*, 258(7):2000614, 2021.

[134] Aubrey T Hanbicki, Hsun-Jen Chuang, Matthew R Rosenberger, C Stephen Hellberg, Saujan V Sivaram, Kathleen M McCreary, Igor I Mazin, and Berend T Jonker. Double indirect interlayer exciton in a mose2/wse2 van der waals heterostructure. *ACS nano*, 12(5):4719–4726, 2018.

[135] Michael Förg, Anvar S Baimuratov, Stanislav Yu Kruchinin, Ilia A Vovk, Johannes Scherzer, Jonathan Förste, Victor Funk, Kenji Watanabe, Takashi Taniguchi, and Alexander Högele. Moiré excitons in $MoSe_2$-WSe_2 heterobilayers and heterotrilayers. *Nature communications*, 12(1):1–7, 2021.

[136] Alberto Ciarrocchi, Dmitrii Unuchek, Ahmet Avsar, Kenji Watanabe, Takashi Taniguchi, and Andras Kis. Polarization switching and electrical control of interlayer excitons in two-dimensional van der waals heterostructures. *Nature photonics*, 13(2):131–136, 2019.

[137] A Delhomme, D Vaclavkova, A Slobodeniuk, M Orlita, M Potemski, DM Basko, K Watanabe, T Taniguchi, Diego Mauro, Céline Barreteau, et al. Flipping exciton angular momentum with chiral phonons in $MoSe_2/WSe_2$ heterobilayers. *2D Materials*, 7(4):041002, 2020.

[138] Tianmeng Wang, Shengnan Miao, Zhipeng Li, Yuze Meng, Zhengguang Lu, Zhen Lian, Mark Blei, Takashi Taniguchi, Kenji Watanabe, Sefaattin Tongay, et al. Giant valley-Zeeman splitting from spin-singlet and spin-triplet interlayer excitons in $WSe_2/MoSe_2$ heterostructure. *Nano letters*, 20(1):694–700, 2019.

[139] EV Calman, LH Fowler-Gerace, DJ Choksy, LV Butov, DE Nikonov, IA Young, S Hu, A Mishchenko, and AK Geim. Indirect excitons and trions in $MoSe_2/WSe_2$ van der Waals heterostructures. *Nano Letters*, 20(3):1869–1875, 2020.

[140] Elyse Barré, Ouri Karni, Erfu Liu, Aidan L O'Beirne, Xueqi Chen, Henrique B Ribeiro, Leo Yu, Bumho Kim, Kenji Watanabe, Takashi Taniguchi, et al. Optical absorption of interlayer excitons in transition-metal dichalcogenide heterostructures. *Science*, 376(6591):406–410, 2022.

[141] Alan R Denton and Neil W Ashcroft. Vegard's law. *Physical review A*, 43(6):3161, 1991.

[142] L. Y. Gan and et al. Order-disorder phase transitions in the two-dimensional semiconducting transition metal dichalcogenide alloys $Mo_{1-x}W_xX_2$ (X = S, Se, and Te). *Scientific Reports*, 4:1–5, 2014.

[143] En Li, Jin-Xin Hu, Xuemeng Feng, Zishu Zhou, Liheng An, Kam Tuen Law, Ning Wang, and Nian Lin. Lattice reconstruction induced multiple ultra-flat bands in twisted bilayer WSe_2. *Nature communications*, 12(1):1–7, 2021.

[144] Etienne Lorchat, Malte Selig, Florian Katsch, Kentaro Yumigeta, Sefaattin Tongay, Andreas Knorr, Christian Schneider, and Sven Höfling. Excitons in Bilayer MoS_2 Displaying a Colossal Electric Field Splitting and Tunable Magnetic Response. *Physical Review Letters*, 126(3):037401, 2021.

[145] Namphung Peimyoo, Thorsten Deilmann, Freddie Withers, Janire Escolar, Darren Nutting, Takashi Taniguchi, Kenji Watanabe, Alireza Taghizadeh, Monica Felicia Craciun, Kristian Sommer Thygesen, and Saverio Russo. Electrical tuning of optically active interlayer excitons in bilayer MoS_2. *Nature Nanotechnology*, 16(8):888–893, 2021.

[146] Charalambos Louca, Armando Genco, Salvatore Chiavazzo, Thomas P Lyons, Sam Randerson, Chiara Trovatello, Peter Claronino, Rahul Jayaprakash, Kenji Watanabe, Takashi Taniguchi, et al. Nonlinear interactions of dipolar excitons and polaritons in MoS_2 bilayers. *arXiv preprint arXiv:2204.00485*, 2022.

[147] Jonas Gaël Roch, Guillaume Froehlicher, Nadine Leisgang, Peter Makk, Kenji Watanabe, Takashi Taniguchi, and Richard John Warburton. Spin-polarized electrons in monolayer MoS_2. *Nature Nanotechnology*, 14(5):432–436, 2019.

[148] Long Zhang, Fengcheng Wu, Shaocong Hou, Zhe Zhang, Yu-Hsun Chou, Kenji Watanabe, Takashi Taniguchi, Stephen R Forrest, and Hui Deng. Van der waals heterostructure polaritons with moiré-induced nonlinearity. *Nature*, 591(7848):61–65, 2021.

[149] V. Shahnazaryan, I. Iorsh, I. A. Shelykh, and O. Kyriienko. Exciton-exciton interaction in transition-metal dichalcogenide monolayers. *Phys. Rev. B*, 96:115409, Sep 2017.

[150] O. Kyriienko, E. B. Magnusson, and I. A. Shelykh. Spin dynamics of cold exciton condensates. *Phys. Rev. B*, 86:115324, Sep 2012.

[151] K. Kristinsson, O. Kyriienko, T. C. H. Liew, and I. A. Shelykh. Continuous terahertz emission from dipolaritons. *Phys. Rev. B*, 88:245303, Dec 2013.

[152] Monique Combescot, Odile Betbeder-Matibet, and François Dubin. The many-body physics of composite bosons. *Physics Reports*, 463(5):215–320, 2008.

[153] RPA Emmanuele, M Sich, O Kyriienko, V Shahnazaryan, F Withers, A Catanzaro, PM Walker, FA Benimetskiy, MS Skolnick, AI Tartakovskii, et al. Highly nonlinear trion-polaritons in a monolayer semiconductor. *Nature communications*, 11(1):1–7, 2020.

[154] N. Lundt, A. Maryński, E. Cherotchenko, A. Pant, X. Fan, S. Tongay, G. Sek, A. V. Kavokin, S. Höfling, and C. Schneider. Monolayered $MoSe_2$: A candidate for room temperature polaritonics. *2D Materials*, 4(1), 2017.

[155] Daniel J. Gillard, Armando Genco, Seongjoon Ahn, Thomas P. Lyons, Kyung Yeol Ma, A. Rang Jang, Toby Severs Millard, Aurélien A.P. Trichet, Rahul Jayaprakash, Kyriacos Georgiou, David G. Lidzey, Jason M. Smith, Hyeon Suk Shin, and Alexander I. Tartakovskii. Strong exciton-photon coupling in large area $MoSe_2$ and WSe_2 heterostructures fabricated from two-dimensional materials grown by chemical vapor deposition. *2D Materials*, 8(1), 2021.

[156] Jie Gu, Biswanath Chakraborty, Mandeep Khatoniar, and Vinod M Menon. A room-temperature polariton light-emitting diode based on monolayer WS_2. *Nature Nanotechnology*, 14(11):1024–1028, 2019.

[157] Jie Gu, Valentin Walther, Lutz Waldecker, Daniel Rhodes, Archana Raja, James C Hone, Tony F Heinz, Stéphane Kéna-Cohen, Thomas Pohl, and Vinod M Menon. Enhanced nonlinear interaction of polaritons via excitonic Rydberg states in monolayer WSe_2. *Nature Communications*, 12(1), 2021.

[158] Li Bing Tan, Ovidiu Cotlet, Andrea Bergschneider, Richard Schmidt, Patrick Back, Yuya Shimazaki, Martin Kroner, and Ataç İmamoğlu. Interacting polaron-polaritons. *Physical Review X*, 10(2):021011, 2020.

[159] T. P. Lyons, D. J. Gillard, C. Leblanc, J. Puebla, D. D. Solnyshkov, L. Klompmaker, I. A. Akimov, C. Louca, P. Muduli, A. Genco, M. Bayer, Y. Otani, G. Malpuech, and A. I. Tartakovskii. Giant effective Zeeman splitting in a monolayer semiconductor realized by spin-selective strong light-matter coupling. *Arxiv*, 2021.

[160] Hui Deng, Hartmut Haug, and Yoshihisa Yamamoto. Exciton-polariton Bose-Einstein condensation. *Reviews of Modern Physics*, 82(2):1489–1537, 2010.

[161] J. Kasprzak et al. Bose-Einstein condensation of exciton polaritons. *Nature*, 443(7110):409–414, 2006.

[162] S. Christopoulos et al. Room-temperature polariton lasing in semiconductor microcavities. *Physical Review Letters*, 98(12):126405, 2007.

[163] Pallab Bhattacharya et al. Room temperature electrically injected polariton laser. *Physical Review Letters*, 112(23):236802, 2014.

[164] A. Amo et al. Collective fluid dynamics of a polariton condensate in a semiconductor microcavity. *Nature*, 457(7227):291–295, 2009.

[165] AM Fox, DAB Miller, G Livescu, JE Cunningham, and WY Jan. Excitonic effects in coupled quantum wells. *Physical Review B*, 44(12):6231, 1991.

[166] Peter Cristofolini, Gabriel Christmann, Simeon I Tsintzos, George Deligeorgis, George Konstantinidis, Zacharias Hatzopoulos, Pavlos G Savvidis, and Jeremy J Baumberg. Coupling quantum tunneling with cavity photons. *Science*, 336(6082):704–707, 2012.

[167] Emre Togan, Hyang-Tag Lim, Stefan Faelt, Werner Wegscheider, and Atac Imamoglu. Enhanced Interactions between Dipolar Polaritons. *Phys. Rev. Lett.*, 121:227402, Nov 2018.

[168] Ioannis Paradisanos, Shivangi Shree, Antony George, Nadine Leisgang, Cedric Robert, Kenji Watanabe, Takashi Taniguchi, Richard J Warburton, Andrey Turchanin, Xavier Marie, et al. Controlling interlayer excitons in MoS_2 layers grown by chemical vapor deposition. *Nature communications*, 11(1):1–7, 2020.

[169] A Amo, D Sanvitto, FP Laussy, D Ballarini, E del Valle, MD Martin, A Lemaitre, J Bloch, DN Krizhanovskii, MS Skolnick, et al. Collective fluid dynamics of a polariton condensate in a semiconductor microcavity. *Nature*, 457(7227):291–295, 2009.

[170] Seong-Yeon Lee, Tae-Young Jeong, Suyong Jung, and Ki-Ju Yee. Refractive index dispersion of hexagonal boron nitride in the visible and near-infrared. *physica status solidi (b)*, 256(6):1800417, 2019.

[171] Ian H Malitson. Interspecimen comparison of the refractive index of fused silica. *Josa*, 55(10):1205–1209, 1965.

[172] T Begou, Christophe Hecquet, Fabien Lemarchand, and Michel Lequime. All dielectric broadband mirror for fabry-perot interferometer. In *Optical Interference Coatings*, pages PTE–6. Optica Publishing Group, 2013.

[173] Nina Sultanova, S Kasarova, and Ivan Nikolov. Dispersion proper ties of optical polymers. *Acta Physica Polonica-Series A General Physics*, 116(4):585, 2009.

[174] N Lundt et al. Room-temperature Tamm-plasmon exciton-polaritons with a WSe$_2$ monolayer. *Nature Communications*, 7:13328, 2016.

[175] Tao Hu, Yafeng Wang, Lin Wu, Long Zhang, Yuwei Shan, Jian Lu, Jun Wang, Song Luo, Zhe Zhang, Liming Liao, et al. Strong coupling between tamm plasmon polariton and two dimensional semiconductor excitons. *Applied Physics Letters*, 110(5):051101, 2017.

[176] V. Savona, L.C. Andreani, P. Schwendimann, and A. Quattropani. Quantum well excitons in semiconductor microcavities: Unified treatment of weak and strong coupling regimes. *Solid State Communications*, 93(9):733–739, 1995.

[177] A Armitage, TA Fisher, MS Skolnick, DM Whittaker, P Kinsler, and JS Roberts. Exciton polaritons in semiconductor quantum microcavities in a high magnetic field. *Physical Review B*, 55(24):16395, 1997.

[178] Natalia G Berloff, Matteo Silva, Kirill Kalinin, Alexis Askitopoulos, Julian D Töpfer, Pasquale Cilibrizzi, Wolfgang Langbein, and Pavlos G Lagoudakis. Realizing the classical xy hamiltonian in polariton simulators. *Nature materials*, 16(11):1120–1126, 2017.

[179] Aymeric Delteil, Thomas Fink, Anne Schade, Sven Höfling, Christian Schneider, and Ataç İmamoğlu. Towards polariton blockade of confined exciton–polaritons. *Nature materials*, 18(3):219–222, 2019.

[180] O Kyriienko, DN Krizhanovskii, and IA Shelykh. Nonlinear quantum optics with trion polaritons in 2d monolayers: conventional and unconventional photon blockade. *Physical Review Letters*, 125(19):197402, 2020.

[181] Matej Velicky, Gavin E Donnelly, William R Hendren, Stephen McFarland, Declan Scullion, William JI DeBenedetti, Gabriela Calinao Correa, Yimo Han, Andrew J Wain, Melissa A Hines, et al. Mechanism of gold-assisted exfoliation of centimeter-sized transition-metal dichalcogenide monolayers. *ACS nano*, 12(10):10463–10472, 2018.

[182] Yuan Huang, Yu-Hao Pan, Rong Yang, Li-Hong Bao, Lei Meng, Hai-Lan Luo, Yong-Qing Cai, Guo-Dong Liu, Wen-Juan Zhao, Zhang Zhou, et al. Universal mechanical exfoliation of large-area 2d crystals. *Nature communications*, 11(1):1–9, 2020.

[183] Satoru Masubuchi, Masataka Morimoto, Sei Morikawa, Momoko Onodera, Yuta Asakawa, Kenji Watanabe, Takashi Taniguchi, and Tomoki Machida. Autonomous robotic searching and assembly of two-dimensional crystals to build van der waals superlattices. *Nature communications*, 9(1):1–12, 2018.

[184] Ifan Hughes and Thomas Hase. *Measurements and their uncertainties: a practical guide to modern error analysis*. OUP Oxford, 2010.

[185] E. Cappelluti, R. Roldán, J. A. Silva-Guillén, P. Ordejón, and F. Guinea. Tight-binding model and direct-gap/indirect-gap transition in single-layer and multilayer MoS_2. *Phys. Rev. B*, 88:075409, 8 2013.

[186] Pierluigi Cudazzo, Ilya V. Tokatly, and Angel Rubio. Dielectric screening in two-dimensional insulators: Implications for excitonic and impurity states in graphane. *Phys. Rev. B*, 84:085406, 8 2011.

[187] Mark Danovich, David A Ruiz-Tijerina, Ryan J Hunt, Marcin Szyniszewski, Neil D Drummond, and Vladimir I Falko. Localized interlayer complexes in heterobilayer transition metal dichalcogenides. *Physical Review B*, 97(19):195452, 2018.

[188] EL Ivchenko, MA Kaliteevski, AV Kavokin, and AI Nesvizhskii. Reflection and absorption spectra from microcavities with resonant bragg quantum wells. *JOSA B*, 13(5):1061–1068, 1996.

[189] C Ciuti, V Savona, C Piermarocchi, A Quattropani, and P Schwendimann. Role of the exchange of carriers in elastic exciton-exciton scattering in quantum wells. *Physical Review B*, 58(12):7926, 1998.

[190] Christoph Schindler and Roland Zimmermann. Analysis of the exciton-exciton interaction in semiconductor quantum wells. *Physical Review B*, 78(4):045313, 2008.

[191] Roland Zimmermann and Christoph Schindler. Exciton–exciton interaction in coupled quantum wells. *Solid state communications*, 144(9):395–398, 2007.

APPENDIX A

ALLOY EXCITONS AND IX IN $MoxW1-xSe2/WSe2$

The data in this section are believed to support the findings of Chapter 4. My contribution to the data shown here is partial with other PhD students and postdocs being the main contributors.

A.1 $Mo_xW_{1-x}Se_2$ monolayers and bilayers

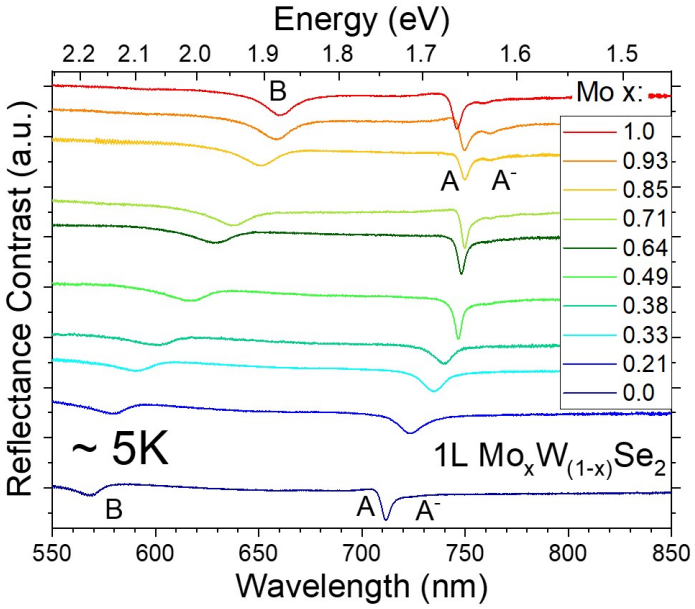

Fig. A.1 **A and B excitons in $Mo_xW_{(1-x)}Se_2$ monolayers.** Reflectance contrast (RC) spectra measured at low temperature of isolated $Mo_xW_{(1-x)}Se_2$ alloys monolayers with different Mo concentrations (x). The trends of A and B excitons as a function of x are clearly displayed. In some samples a small feature ascribed to the trion A- is also visible

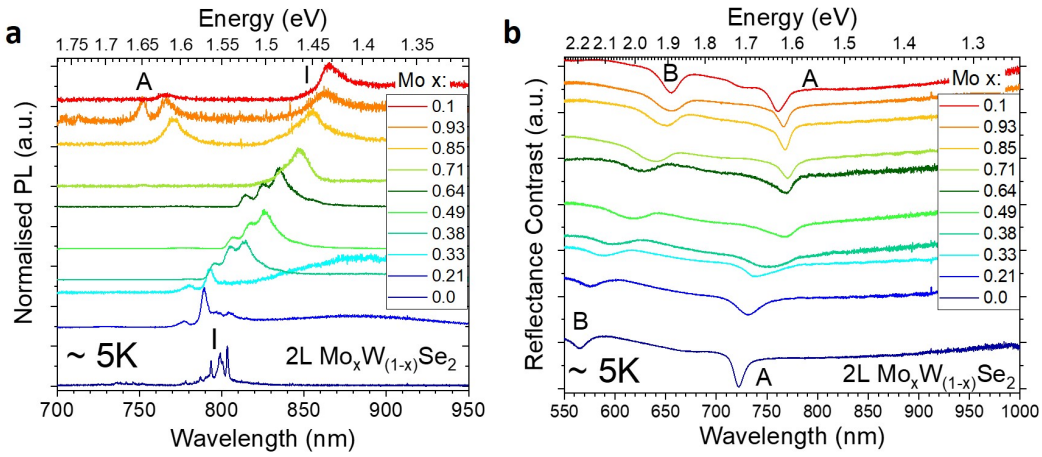

Fig. A.2 **Excitons transitions in $Mo_xW_{(1-x)}Se_2$ alloy bilayers.a,** PL spectra measured at low temperature of isolated $Mo_xW_{(1-x)}Se_2$ alloys bilayers with different Mo concentrations (x). The indirect transition (I) appears to be prominent compared to the direct one (A) in all the samples, as expected from generic TMD bilayers. **b,** RC spectra measured at low temperature of isolated $Mo_xW_{(1-x)}Se_2$ alloys bilayers with different Mo concentrations (x). A and B exciton energies as a function of x are displayed.

A.2 IX in $Mo_xW_{1-x}Se_2/WSe_2$ heterobilayers

A.2.1 IX energy tuning with concentration

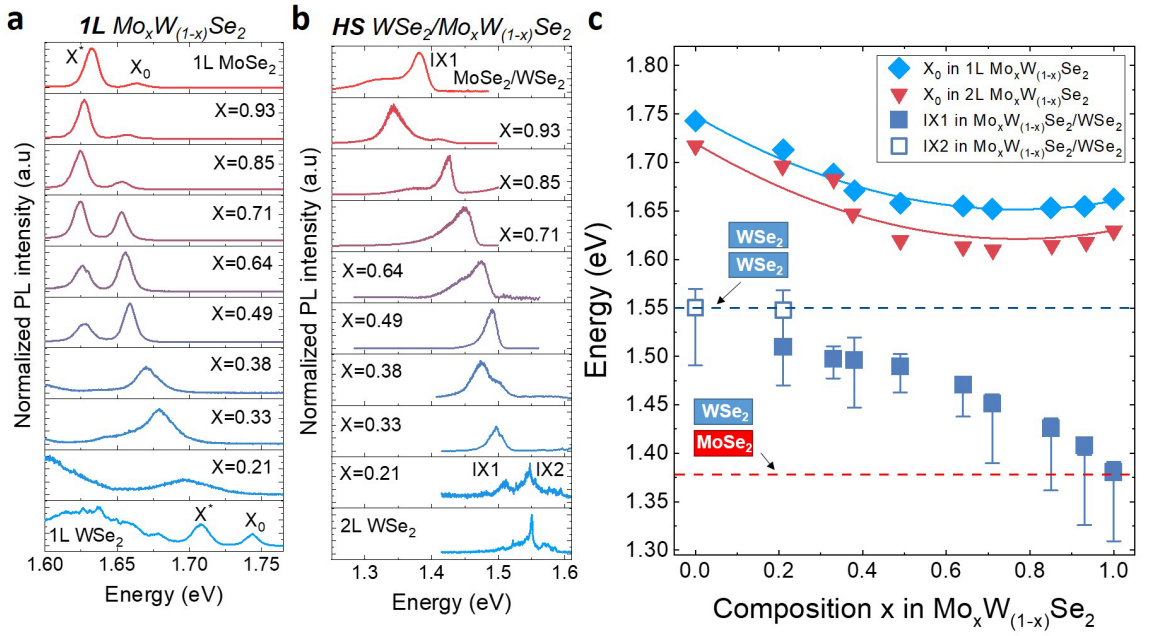

Fig. A.3 **Intra- and inter-layer excitons emission in alloys monolayers and heterostructures. a,** Normalized PL spectra measured at 10K of isolated $Mo_xW_{(1-x)}Se_2$ alloys monolayers with different Mo concentrations (x), showing the neutral exciton (X_0) and the trion (X^*) peaks. X_0 peak position follows a parabolic trend, as shown in **c**. **b,** Normalized PL spectra of the $Mo_xW_{(1-x)}Se_2/WSe_2$ HBLs measured at 10K for different alloys compositions x. The label IX1 (IX2) refers to interlayer (indirect) excitons. **c,** Peak position of the highest energy IX peak in the alloy/WSe_2 (blue squares) HBLs as a function of Mo composition x in the alloy layer, together with the neutral exciton peak position of the alloy monolayers (sky blue diamonds) and bilayers (red triangles). The error bars depict the spreading in energy of multiple indirect transitions peaks. Sky blue and orange solid lines are parabolic fits of the DX peak energy in isolated alloy monolayers and bilayer respectively. The dashed red (blue) horizontal line refers to the IX energy in $MoSe_2/WSe_2$ HBLs (WSe_2 homobilayers).

A.2.2 IX lifetimes with concentration

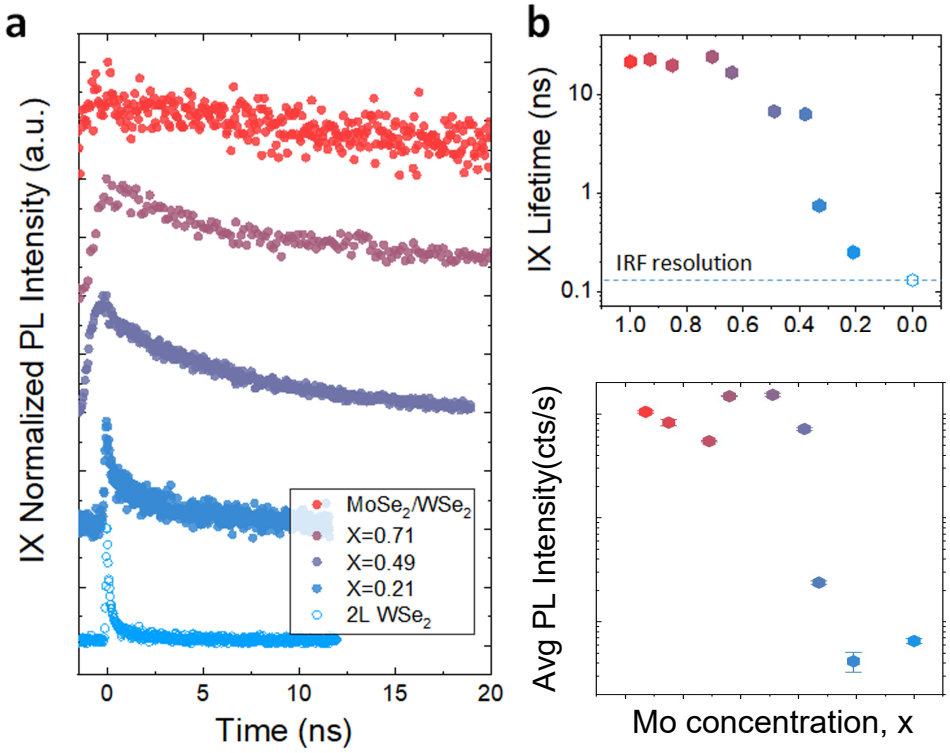

Fig. A.4 **Interlayer excitons temporal dynamics and emission a,** Transient PL traces of IX in different $Mo_xW_{(1-x)}Se_2/WSe_2$ HBLs measured at 10K. The Mo composition x in the alloy layer is indicated in the legend. **b,** (top)IX decay times as a function of the Mo composition in the alloys/WSe_2 HSs extracted from the PL temporal traces. The dashed line indicates the temporal resolution limit given by the instrument response function of the experimental setup (IRF).(bottom) The average PL intensity at each concentration. The sharp intensity decrease approaching the homobilayer suggests moving to a momentum indirect transition.

A.2.3 Conduction and valence bands offsets predictions

We can predict the energy band offsets in each alloy monolayer simply knowing the experimental direct exciton energies of WSe_2 and $MoSe_2$ (DX_{MoSe2} and DX_{WSe2}), the one in $Mo_xW_{(1-x)}Se_2$ at different Mo compositions (DX_{alloy}) and the interlayer exciton energy in the $WSe_2/MoSe2_2$ HS ($IX_{MoSe2/WSe2}$), then performing a linear interpolation. The contribution of the excitons binding energies has not been taken into account for this estimation. In the case of **WSe_2**/$Mo_xW_{(1-x)}Se_2$ HSs, the band offsets have been calculated relatively to

the CB energy of WSe_2 (at 0 energy in Figure A.5). For this reason the WSe_2 VB energy is equal to its DX energy, which can be extracted from the experiments . Hence, the conduction and valence bands offsets of $MoSe_2$ (ΔCB_{MoSe2} and ΔVB_{MoSe2} in Fig. A.5) are calculated according to:

$$\Delta CB_{MoSe2} = DX_{WSe2} - IX_{MoSe2/WSe2}$$

$$\Delta VB_{MoSe2} = \Delta CB_{MoSe2} + DX_{MoSe2} - DX_{WSe2}$$

The VB offset for each $Mo_xW_{(1-x)}Se_2$ alloy (ΔVB_{alloy} in Fig. A.5) can be interpolated assuming a linear variation of the valence band energy with the Mo content. As previously reported, the metal orbitals involved in the valence band edge composition for both WSe_2 and $MoSe_2$ are the same (d_{xy} and $d_{x^2-y^2}$), leading to a uniform shift of the VB energy varying the alloy composition. In contrast, the metal orbitals which contribute to the conduction band edges of the two materials are different, resulting in a non-linear energy shift.[142] The quadratic dependence of the experimental alloys exciton energies and the related bowing parameter are a direct consequence of this effect. From the interpolated VB_{alloy} offsets, ΔCB_{alloy} are then calculated for each different composition, applying the following formula:

$$\Delta CB_{alloy} = DX_{WSe2} + \Delta VB_{alloy} - DX_{alloy}$$

Regarding the **$MoSe_2$**/$Mo_xW_{(1-x)}Se_2$ HSs, the band offsets are easily calculated as a difference between the previously found values for $MoSe_2$ and alloys: $\Delta CB_{alloy/MoSe2} = \Delta CB_{MoSe2} - \Delta CB_{alloy/WSe2}$ and $\Delta VB_{alloy/MoSe2} = \Delta VB_{MoSe2} - \Delta VB_{alloy/WSe2}$.

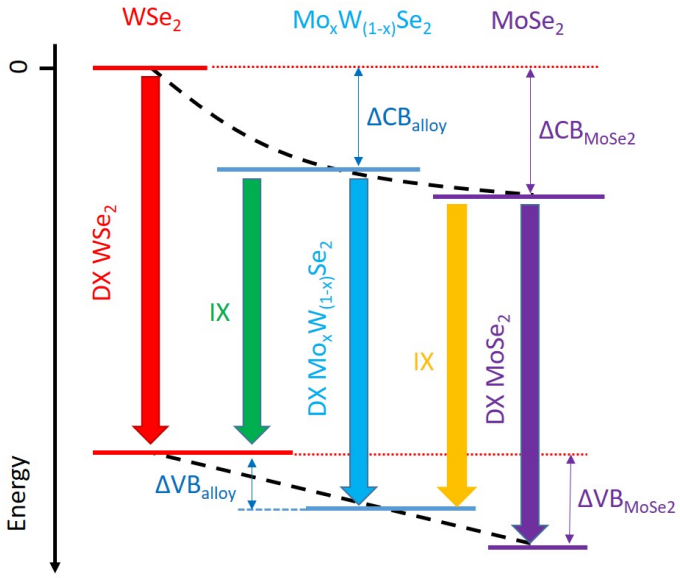

Fig. A.5 **Band offsets schematic diagram for WSe_2, $MoSe_2$ and $Mo_xW_{(1-x)}Se_2$ monolayers.**

APPENDIX B

MoS_2 BILAYER: DENSITY CALCULATIONS AND THEORETICAL MODELS

B.1 Exciton and Polariton density estimation

Exciton and polariton densities were calculated using an experimental approach considering a convolution of the laser profile and the Reflectance Contrast spectra, as in [148]. Reflectance contrast, A_{res}, represents with good approximation the absorption of the each excitonic/polaritonic resonance [148]. Power absorbed by each exciton/polariton, P_{res}, can be calculated as

$$P_{\text{res}} = \frac{P \int L(E) \text{A}_{\text{res}}(E) \text{d}E}{I_{\text{laser}}}, \tag{B.1}$$

where P is the experimentally measured power, $\int L(E) \text{A}_{\text{res}}(E) \text{d}E$ is the convolution of the laser spectrum profile, L(E), and the Reflectance Contrast spectrum in the range of energies of the resonant transition peak and $I_{\text{laser}} = \int L(E) \text{d}E$ is the laser spectrum integrated intensity.

The expression (B.1) can then be used to calculate the particle density, n_{res}, considering the laser repetition rate, R_{laser}, laser spot size, S_{laser}, and the excitation central energy, E_{res}. Explicitly, an estimate for the density reads

$$n_{\text{res}} = \frac{P_{\text{res}}}{R_{\text{laser}} E_{\text{res}} S_{\text{laser}}}. \tag{B.2}$$

We note that for the polariton density estimations, since A_{res} is dependent on the angle, P_{res} was calculated integrating all the spectral quantities in both the energy and angular range of LPB and UPB. As such, the densities calculated with this procedure are the total polariton densities, which consider both LPB and UPB.

For the values of polariton/exciton densities the error, $\varepsilon_{\mathrm{n}} = \sqrt{\left(\frac{\varepsilon_{\mathrm{Pres}}}{\mathrm{P_{res}}}\right)^2 + \left(\frac{\varepsilon_{\mathrm{Eres}}}{\mathrm{E_{res}}}\right)^2}$, is propagated with respect to standard error analysis rules [184]

The rest of this Appendix is a detailed theoretical microscopic model to support the experimental findings in Chapter 5,6 and is the work of collaborators Salvatore Chiavazzo and Dr Oleksandr Kyriienko from the Univeristy of Exeter

B.2 Theoretical estimate of exciton properties — energy and hybridisation

In this section, we describe details of theoretical description of MoS_2 homobilayers. Properties of excitons in a bilayer system have been discussed in the main text, and we support them by modelling. The optical response of the system is characterised by the response of three different species of quasi-particles, namely X_A, hIX and hX_B. Here we provide an intuitive picture of the homobilayer physics and estimate the system parameters. In particular, we estimate exciton Bohr radii and a hole tunnelling rate as relevant parameters when studying nonlinear properties.

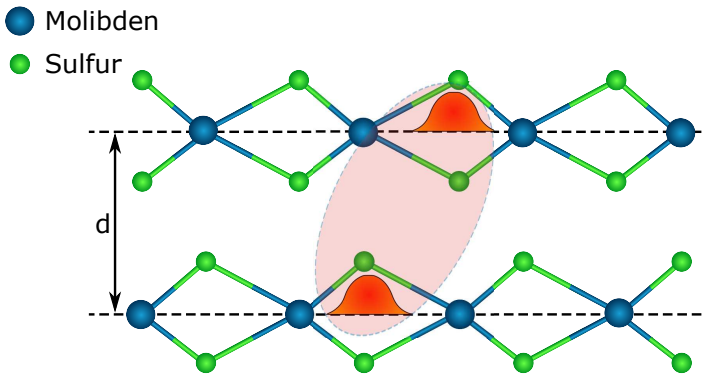

Fig. B.1 **Side view of 2H-stacked MoS_2 bilayer.** Blue spheres are Mo (molybdenum) atoms and green are S (sulphide) atoms. We picture a hole wave function in each layer, constructing a hybrid state through tunneling process (hole delocalisation). This allows for hybrid hX_B and hIX excitons. We define the distance between the layer as the distance between particle centres of charge. In absence of external fields, the centre of charge is located in between the S planes [185].

We consider a MoS_2 homobilayer system with 2H stacking (see Fig. B.1). This is comprised of two parallel layers of MoS_2, with centres located at a distance d from each other (charge separation distance). The physics of bilayers is defined by properties of

electrons and holes that interact through the Keldysh-Rytova potential [186, 25, 20], being different for in-plane and out-of-plane interaction [187]. Within the $k \cdot p$ framework, electrons and holes are treated as particles with effective mass provided by a band dispersion. In MoS_2 the typical values for effective masses are 0.46 m_e for conduction bands and 0.56 m_e for the valence bands (with m_e being the electron mass) [89, 18]. The attractive Kledysh-Rytova potential has a different form depending on the relative position between particles. We call $V_{\mathrm{KR}}^{\mathrm{intra}}$ the attractive potential of particles being in the same layer, and $V_{\mathrm{KR}}^{\mathrm{inter}}$ the attractive potential of particles being in separate layers. In momentum space the different potentials read as

$$V_{\mathrm{KR}}^{\mathrm{intra}}(\mathbf{q}) = -\frac{e^2}{4\pi\varepsilon\varepsilon_0}\frac{1+(r_0q/\varepsilon)(1-\exp(-2qd))}{(1+r_0q/\varepsilon)^2-(r_0q/\varepsilon)^2\exp(-2qd)}, \tag{B.3a}$$

$$V_{\mathrm{KR}}^{\mathrm{inter}}(\mathbf{q}) = -\frac{e^2}{4\pi\varepsilon\varepsilon_0}\frac{\exp(-qd)}{(1+r_0q/\varepsilon)^2-(r_0q/\varepsilon)^2\exp(-2qd)}, \tag{B.3b}$$

where e is the electron charge, ε_0 is the vacuum permittivity, ε in an average environment permittivity, r_0 is a screening length (defined as for monolayers), and $\mathbf{q}$ is an exchanged particle momentum [187]. We compute a binding energy of an exciton bound state by assuming the Keldysh-Rytova attractive potential and free particle dispersion defined by the effective masses. To provide a simple understanding of the system, we approach the problem using an ansatz wavefunction $\phi(\rho) = \sqrt{2/\pi\alpha^2}\exp(-\rho/\alpha)$, with ρ being the in-plane projection of electron-hole distance and α the exciton Bohr radius. This describes well an internal structure of an exciton, and gives the information about its shape, collected in the Bohr radius. In Fourier space, the function $\phi(q)$ reads

$$\phi(q) = \sqrt{\frac{2}{\pi}}\frac{\alpha}{(1+q^2\alpha^2)^{3/2}}. \tag{B.4}$$

With the given wave function [Eq. (B.4)], and the given potentials [Eq. (B.3)], we can find the binding energy and the Bohr radius of the excitons by minimizing the energy of the system. This procedure is performed in the range of possible interlayer separation d. Fig. B.2(a) shows the energy change with the separation. The blue curve corresponds to the hIX mode,

while orange and red curves correspond to X_A and hX_B, respectively. We considered a band-gap of 2.12 eV, and spin-orbit splitting of 13 meV for conduction band and 150 meV for valence band, as suggested by the ab initial calculations [18].

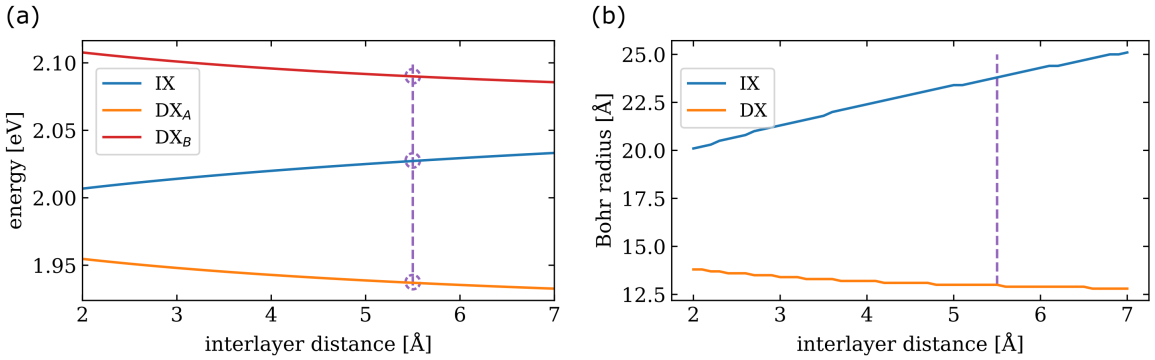

Fig. B.2 **Evolution of particle properties with interlayer distance. a)** Energy of quasiparticle modes with distance. The blue line is the hIX mode, and the orange and red respectively are X_A and hX_B. The redshift of direct modes with the increase of interlayer distance is due to reduced screening effects, as characteristic of Keldysh-Rytova potential in Eq. (B.3). On the contrary, the hIX mode sees a blueshift that is due to the lower attraction of particles located in separate layers. The purple dashed line is the distance to match with the experimental data. **b)** Dependence of Bohr radius with interlayer distance. Here we only report one direct exciton as both A and B excitons have the same behavior. The orange one is the evolution for direct excitons, and the blue line is for indirect excitons. Both plots (a) and (b) show similiar increase (or increase) with distance as the screening mechanism affects the considered parameters the same way. This analysis reveals the hIX Bohr radius to be roughly twice as much as the X one.

Here we estimate the interlayer distance d thanks to experimental knowledge of energy distance between exciton energy modes. Note the peak of X_A mode is not shifted by any tunneling, while X_B and IX are coupled through tunneling constant J [84]. That is, the theoretical energy distance Δ_0 between the two modes has to be fixed to match the experimental result $\Delta = 109$ meV. With considering two coupled harmonic oscillators, we find the corrected energy shift to be

$$\Delta = \sqrt{\Delta_0^2 + 4J^2}. \tag{B.5}$$

By matching with the experimental data for the energy distance between modes, we extract $d = 5.5$ Å and estimate the effective tunneling rate to be $J = 45$ meV. As a consequence, 21%

of X_B oscillator strength is transferred to IX mode, in agreement with previous observations [89]. Finally, Fig. B.2(b) shows the evolution of particle Bohr radii with the interlayer distance. We respectively call the Bohr radius of direct and indirect exciton α_D and α_I. The blue curve is the Bohr radius of hIX, while the orange one described the X modes. With X_A and hX_B being very similar, we describe both with one orange curve. The energy separation is provided only by the spin-orbit splitting. Typical values of α_D are approximately 1 nm, with α_I being approximately 2 nm. Note the opposite behavior of α_D and α_I with distance. hIX Bohr radius grows with distance due to the reduced attraction between particles in separate layers. On the contrary, by increasing the interlayer distance, we see the reduced screening for particles in the same layer, resulting in a decrease of the Bohr radius and consequent increase of the binding energy.

B.3 Theoretical discussion on interaction constants

In our work we observed several nonlinear effects with contributions that depend on excitation conditions. In the BB regime, we already discussed the presence of two main species (flavours) of particles, namely direct X and indirect hIX excitons, determining the features of the sample's optical response. This can be seen from the reflectance spectra in Fig. 6.4a,b. We observe both the energy shifts (discussed above), and additional bleaching of the peaks. This hints that the presence of conservative nonlinear processes (energy shifts) is accompanied by dissipative nonlinear processes. Below, we discuss various contributions, including the Coulomb-mediated scattering, optical saturation due to phase space filling, and nonlinear change of non-radiative decay and dephasing processes.

We stress that in general all the aforementioned processes contribute to the spectral signal we observed. The peak shape is due to the competing contribution of radiative and non-radiative decay processes. Both radiative Γ_R and non-radiative Γ_{NR} rates depend on the particle densities n_D and n_I, for direct and interlayer excitons respectively. Here we simply refer to some generic density n, without specifying the particle flavour involved, as similar consideration apply to both. We relate the exciton radiative decay rate and the Rabi

frequency Ω for polaritons, as they are both proportional to the particle oscillator strength $\Gamma_R, \Omega \propto f_{osc}$ [160]. More accurately, we know that $\Gamma_R \propto f_{osc}$, and $\Omega(n) \propto \sqrt{f_{osc}}$. With $\Omega(n) = \Omega_0\sqrt{1-\xi_{sat}n}$, we write the relation: $\Gamma_R(n) = \Gamma_0 - g_{sat}n$, with g_{sat} being a saturation constant to be determined ($g_{sat} \propto \xi_{sat}$). As consequence of geometrical properties of excitons, the saturation factor shape $\xi_{sat} \simeq 4\alpha^2$ [153], where α is the exciton Bohr radius.

In parallel to this process, non-radiative processes play a major role in bleaching. As there are many decay and dephasing channels, the full treatment of possible processes if formidable. Here, we address as the key effect the decay process due to Coulomb scattering [64]. As a result, the Coulomb scattering induced decay is proportional to the Coulomb scattering matrix

$$\Gamma_{NR} \propto \sum_{\mathbf{q}\neq 0} |V^{dir}(\mathbf{q}) - V^{exch}(\mathbf{q})|^2 \delta(E(\mathbf{q}) + E(-\mathbf{q}) - 2E(\mathbf{Q}\sim 0)), \tag{B.6}$$

where E is the energy of involved particles and $V^{dir,exch}(\mathbf{q})$ are direct and exchange particle scattering amplitudes, as discussed in Sec. S9. Note that in the main text for brevity we refer to the combined effect of different Coulomb-based processes using the combined interaction constant V_{Coul}. The discussed decay properties of generic particles combine into the final shape of spectral peak $\mathscr{L}(E)$, see Fig. 5.8 [188]:

$$\mathscr{L}(E) = \frac{1}{\pi}\frac{\Gamma_R(n)^2}{(E-E_0)^2 + [\Gamma_R(n) + \Gamma_{NR}(n)]^2}, \tag{B.7}$$

where E_0 is the position of the peak, Γ_R is the radiative decay rate and Γ_{NR} is the non-radiative rate. Analysing the experimental data with minimal square method, we estimate the non-radiative decay rate to be of the order of ~ 1 meV for direct excitons and ~ 10 meV for indirect excitons. The ratio between the two agrees well with the estimates for the interaction constants (see the discussion below). With combining both radiative and non-radiative bleaching, we find the experimental data are well described by the relation

$$\Omega(n) = \sqrt{\Omega_0^2(1-\xi_{sat}\alpha^2\, n)^2 - \Gamma_{NR}^2(1+\xi_{NR}\alpha^2\, n)^2}, \tag{B.8}$$

where the discussed experimental observation are well described by $\xi_{\mathrm{NR}} \sim 10$, and $\xi_{\mathrm{sat}} \sim 7$ describes the nonlinear saturation of the Rabi splitting. The origin of the saturation term comes from the interlayer exciton phase space filling, and is reminiscent to phase space filling effects discussed in Ref. [153].

Finally, let us consider the exciton-exciton Coulomb scattering. We provide here the estimates for interaction constants, with considering our gained knowledge of the effective interlayer distance d and particles Bohr radii $\alpha_{\mathrm{D,I}}$. We build the interaction by following the procedure in Refs. [150, 189]. As a signature of particle indistinguishability, we have to consider both direct scattering $V^{\mathrm{dir}}(\mathbf{q})$ and exchange scattering $V^{\mathrm{exch}}(\mathbf{q})$ amplitudes, with $\mathbf{q}$ being the exchanged momentum. We omitted particle momenta as we consider total momentum to be zero. Explicitly, the two contributions read

$$\begin{aligned} V^{\mathrm{dir}}(\mathbf{q}) = \int d^2 r_{\mathrm{e}}\, d^2 r_{\mathrm{h}}\, d^2 r_{\mathrm{e}'}\, d^2 r_{\mathrm{e}'}\, \phi^*(\mathbf{r}_{\mathrm{e}}, \mathbf{r}_{\mathrm{h}})\phi^*(\mathbf{r}_{\mathrm{e}'}, \mathbf{r}_{\mathrm{h}'}) \\ \Phi^{\mathrm{tot}}(\mathbf{r}_{\mathrm{e}}, \mathbf{r}_{\mathrm{h}}, \mathbf{r}_{e'}, \mathbf{r}_{\mathrm{h}'})\phi(\mathbf{r}_{\mathrm{e}}, \mathbf{r}_{\mathrm{h}})\phi(\mathbf{r}_{e'}, \mathbf{r}_{\mathrm{h}'}), \end{aligned} \tag{B.9}$$

and

$$\begin{aligned} V^{\mathrm{exch}}(\mathbf{q}) = \int d^2 r_{\mathrm{e}}\, d^2 r_{\mathrm{h}}\, d^2 r_{\mathrm{e}'}\, d^2 r_{\mathrm{e}'}\, \phi^*(\mathbf{r}_{\mathrm{e}}, \mathbf{r}_{\mathrm{h}})\phi^*(\mathbf{r}_{\mathrm{e}'}, \mathbf{r}_{\mathrm{h}'}) \\ \Phi^{\mathrm{tot}}(\mathbf{r}_{\mathrm{e}}, \mathbf{r}_{\mathrm{h}}, \mathbf{r}_{e'}, \mathbf{r}_{\mathrm{h}'})\phi(\mathbf{r}_{e'}, \mathbf{r}_{\mathrm{h}})\phi(\mathbf{r}_{\mathrm{e}}, \mathbf{r}_{\mathrm{h}'}), \end{aligned} \tag{B.10}$$

where we define $\Phi^{\mathrm{tot}}(\mathbf{r}_{\mathrm{e}}, \mathbf{r}_{\mathrm{h}}, \mathbf{r}_{e'}, \mathbf{r}_{\mathrm{h}'})$ as the sum of mutual particle interaction. For the scattering elements above, we shall consider two separate cases for direct and indirect excitons, as both wavefunctions and Coulomb terms differ.

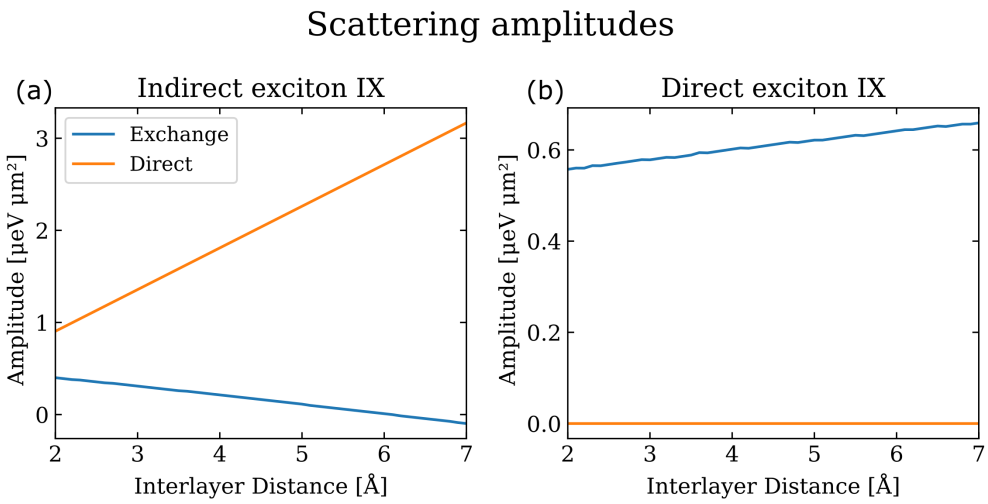

Fig. B.3 **Scattering amplitudes for exciton-exciton Coulomb interaction. (a,b)** We show the change of scattering amplitudes with the interlayer distance. In **(a)**, note the behavior of exchange scattering amplitude for indirect excitons, becoming negative past a threshold distance. Direct scattering amplitude grows linearly with distance. **(b)** We plot characteristic scattering amplitudes for direct excitons, where the direct process is zero at the negligible exchanged momentum (orange line), and the blue line corresponds to the exchange processes.

With direct excitons, we have $V^{\mathrm{dir}}_{\mathrm{X-X}}(\mathbf{q}=\mathbf{0})=0$, and

$$V^{\mathrm{exch}}_{\mathrm{X-X}}(\mathbf{q}=\mathbf{0}) = \left(\frac{2}{\pi}\right)^2 \frac{e^2}{4\pi\varepsilon\varepsilon_0}\alpha_D \int dx\,dy\,d\theta \frac{2\pi xy}{\delta(x,y,\theta)} \frac{1}{(1+r_0\delta(x,y,\theta)/\alpha_{\mathrm{D}})^2 - (\delta(x,y,\theta)r_0/\alpha_{\mathrm{D}})^2 e^{-2\delta(x,y,\theta)\frac{d}{\alpha_{\mathrm{D}}}}} \cdot \left(1+\frac{r_0}{\alpha_{\mathrm{D}}}\left(1-e^{-2\delta(x,y,\theta)\frac{d}{\alpha_{\mathrm{D}}}}\right)\right) \cdot \left(\frac{(-1)}{(1+x^2)^3}\frac{1}{(1+y^2)^3} + \frac{1}{(1+x^2)^3}\frac{e^{-\delta(x,y,\theta)\frac{d}{\alpha_{\mathrm{D}}}}}{(1+y^2)^{3/2}(1+x^2)^{3/2}}\right), \tag{B.11}$$

where $\delta(x,y,\theta)=\sqrt{x^2+y^2-2xy\cos\theta}$. With indirect excitons, the direct scattering amplitude recovers the capacitor formula $V^{\mathrm{dir}}_{\mathrm{I-I}}(\mathbf{q}=\mathbf{0})=e^2/(\varepsilon\varepsilon_0 A)d$, where A is the sample area.

Finally, the indirect exciton exchange potential has to be evaluated as

$$V_{\mathrm{I-I}}^{\mathrm{exch}}(\mathbf{q}=\mathbf{0}) = \left(\frac{2}{\pi}\right)^2 \frac{e^2}{4\pi\varepsilon\varepsilon_0}\alpha_D \int dx\,dy\,d\theta \frac{2\pi xy}{\delta(x,y,\theta)} \frac{1}{(1+r_0\delta(x,y,\theta)/\alpha_{\mathrm{I}})^2 - (\delta(x,y,\theta)r_0/\alpha_{\mathrm{I}})^2 e^{-2\delta(x,y,\theta)\frac{d}{\alpha_{\mathrm{I}}}}} \cdot \left[\frac{(-1)}{(1+x^2)^3}\frac{1}{(1+y^2)^3}\left(1+\frac{r_0}{\alpha_{\mathrm{I}}}\left(1-e^{-2\delta(x,y,\theta)\frac{d}{\alpha_{\mathrm{I}}}}\right)\right) + \frac{1}{(1+x^2)^3}\frac{e^{-\delta(x,y,\theta)\frac{d}{\alpha_{\mathrm{I}}}}}{(1+y^2)^{3/2}(1+x^2)^{3/2}}\right]. \tag{B.12}$$

Figs. B.3(a) and (b) show the dependence of scattering amplitudes on the interlayer distance. We note the behavior of exchange scattering amplitude for indirect excitons, becoming negative past threshold distance (see Fig. B.3(a)). Characteristically, for intralayer (i.e. direct) excitons we have a zero direct scattering amplitude, with non-zero contributions only due to the particle exchange process. With the estimated parameters, we find interlayer exciton-exciton interaction to have a scattering constant of $V_{\mathrm{I-I}}(\mathbf{q}=\mathbf{0}) \simeq 2.5\ \mu\mathrm{eV}\ \mu\mathrm{m}^2$, setting the scale for the Coulomb-based interactions.

B.4 Theory for energy shift

The out-of-cavity results (see Fig. 5.5, 5.6) reveal an opposite behavior of the sample response depending on the excitation regimes, where narrow bandwidth (NB) and the broad bandwidth (BB) regimes are considered. In the NB case, we observe a blueshift for the hIX peak, as already reported in literature for dipolar excitons [190, 191, 150], while in the BB regime we observe a redshifted signal. The latter is unexpected, as in the system with dipolar excitons and predominantly positive scattering matrix elements for exchange terms, the emergence of some effective attractive nonlinearities requires a new possible mechanism. Below, we motivate the emergence of such a mechanism unique to the bilayer system.

First, let us analyse the energy of system as the expectation value of the full Hamiltonian $\hat{\mathscr{H}}$. We consider electrons and holes distributed over bilayer as shown in Fig.5.3a. We call

$N_{\mathrm{I(D)}}$ the number of indirect (direct) excitons in the sample, and $n_{\mathrm{I(D)}}$ the particle density. The spin indices are omitted for brevity. The Hamiltonian of the system can be written as

$$\hat{\mathscr{H}} = \hat{\mathscr{H}}_{\mathrm{T}} + \hat{\mathscr{H}}_{\mathrm{sm}} + \hat{\mathscr{H}}_{\mathrm{df}}, \tag{B.13}$$

where $\hat{\mathscr{H}}_{\mathrm{T}}$ is the kinetic term, $\hat{\mathscr{H}}_{\mathrm{sm}}$ and $\hat{\mathscr{H}}_{\mathrm{df}}$ are the Coulomb interactions. With $\hat{\mathscr{H}}_{\mathrm{sm}}$ we refer to interacting particles belonging to a same band, and $\hat{\mathscr{H}}_{\mathrm{df}}$ corresponds to different dispersion bands. Explicitly, the kinetic energy reads

$$\hat{\mathscr{H}}_{\mathrm{T}} = \sum_{\mathbf{k}} \left[\varepsilon_c^t(\mathbf{k}) \hat{a}_{\mathbf{k}}^\dagger \hat{a}_{\mathbf{k}} + \varepsilon_v^t(\mathbf{k}) b_{\mathbf{k}}^\dagger b_{\mathbf{k}} + \varepsilon_c^b(\mathbf{k}) c_{\mathbf{k}}^\dagger c_{\mathbf{k}} \right], \tag{B.14}$$

where $\hat{a}_{\mathbf{k}}^\dagger$ and $\hat{b}_{\mathbf{k}}^\dagger$ are creation operators for conduction and valence bands of the top layer, respectively. $\hat{c}_{\mathbf{k}}^\dagger$ is an electron annihilation operator for the conduction band of the bottom layer. Each operator is labelled with a crystal momentum $\mathbf{k}$. $\varepsilon_{\mathrm{c(v)}}^{\mathrm{t(b)}}(\mathbf{k})$ are dispersions for conduction (valence) bands in the top (bottom) layer. The interactions are mediated through the Keldysh-Rytova potential. The corresponding interaction Hamiltonian reads

$$\hat{\mathscr{H}}_{\mathrm{sm}} = \frac{1}{2} \sum_{\mathbf{k},\mathbf{k}',\mathbf{q}} \left[V_{\mathrm{KR}}^{\mathrm{intra}}(\mathbf{q}) (a_{\mathbf{k}-\mathbf{q}}^\dagger \hat{a}_{\mathbf{k}'+\mathbf{q}}^\dagger \hat{a}_{\mathbf{k}'} \hat{a}_{\mathbf{k}} + \hat{b}_{\mathbf{k}-\mathbf{q}}^\dagger \hat{b}_{\mathbf{k}'+\mathbf{q}}^\dagger \hat{b}_{\mathbf{k}'} \hat{b}_{\mathbf{k}} + c_{\mathbf{k}-\mathbf{q}}^\dagger \hat{c}_{\mathbf{k}'+\mathbf{q}}^\dagger \hat{c}_{\mathbf{k}'} \hat{c}_{\mathbf{k}}) \right], \tag{B.15}$$

$$\hat{\mathscr{H}}_{\mathrm{df}} = \sum_{\mathbf{k},\mathbf{k}',\mathbf{q}} \left[V_{\mathrm{KR}}^{\mathrm{inter}}(\mathbf{q}) (\hat{a}_{\mathbf{k}-\mathbf{q}}^\dagger \hat{c}_{\mathbf{k}'+\mathbf{q}}^\dagger \hat{c}_{\mathbf{k}'} \hat{a}_{\mathbf{k}} + \hat{b}_{\mathbf{k}-\mathbf{q}}^\dagger \hat{c}_{\mathbf{k}'+\mathbf{q}}^\dagger \hat{c}_{\mathbf{k}'} \hat{b}_{\mathbf{k}}) + V_{\mathrm{KR}}^{\mathrm{intra}} \hat{a}_{\mathbf{k}-\mathbf{q}}^\dagger \hat{b}_{\mathbf{k}'+\mathbf{q}}^\dagger \hat{b}_{\mathbf{k}'} \hat{a}_{\mathbf{k}} \right]. \tag{B.16}$$

We define the exciton creation operators in the form

$$\hat{D}_\mu^\dagger(\mathbf{Q}) = \sum_{\mathbf{k}} \phi_{\mathrm{D}}^\mu(\mathbf{k}) \hat{a}_{\mathbf{k}+\gamma_{\mathrm{e}}\mathbf{Q}}^\dagger \hat{b}_{\mathbf{k}-\gamma_{\mathrm{h}}\mathbf{Q}}, \tag{B.17}$$

$$\hat{I}_\nu^\dagger(\mathbf{P}) = \sum_{\mathbf{k}} \phi_{\mathrm{I}}^\nu(\mathbf{k}) \hat{a}_{\mathbf{k}+\gamma_{\mathrm{e}}\mathbf{P}}^\dagger \hat{c}_{\mathbf{k}-\gamma_{\mathrm{h}}\mathbf{P}}, \tag{B.18}$$

with $\hat{D}_\mu^\dagger(\mathbf{Q})$ [$\hat{I}_\nu^\dagger(\mathbf{P})$] and $\phi_{\mathrm{D}}^\mu(\mathbf{k})$ [$\phi_{\mathrm{I}}^\nu(\mathbf{k})$] being the direct [indirect] exciton creation operator and wave function, respectfully. $\mathbf{Q}, \mathbf{P}$ are crystal momenta, and μ, ν are state indices. When we omit the μ and ν indices, and the total momentum, we refer the ground state at crystal momentum $\mathscr{Q} = 0$. To take into account for particle non-bosonicity and consequent nonlinear

behaviour, we consider the expectation value of a system over a multi-particle state created by exciting the vacuum state $|\Omega_0\rangle$. It includes N_D direct excitons and N_I indirect excitons. The expectation $\langle\Omega_0|\hat{D}^{N_\mathrm{D}}\hat{I}^{N_\mathrm{I}}\hat{\mathscr{H}}\hat{D}^{\dagger N_\mathrm{D}}\hat{I}^{\dagger N_\mathrm{I}}|\Omega_0\rangle$ then denotes the total energy of the many-body system. By following a procedure for accounting non-bosonic correction at increasing order [152], we first commute the Hamiltonian with the product of exciton operators $\hat{D}^{\dagger N_\mathrm{D}}$, leading to

$$\begin{aligned}[\mathscr{H},\hat{D}^{\dagger N_\mathrm{D}}] =& N_\mathrm{D}E_\mathrm{D}\hat{D}^{\dagger N_\mathrm{D}-1} + N_\mathrm{D}\hat{D}^{\dagger N_\mathrm{D}-1}\hat{V}_\mathrm{D} \\ &+ \frac{N_\mathrm{D}(N_\mathrm{D}-1)}{2}\hat{D}^{\dagger N_\mathrm{D}-2}\sum_{\mu,\nu,\mathrm{q}} V^{\mu,\nu}_{\mathrm{D-D}}(\mathbf{q})\hat{D}^\dagger_\nu(\mathbf{q})\hat{D}^\dagger_\mu(-\mathbf{q}),\end{aligned} \tag{B.19}$$

where $V^{\mu,\nu}_{\mathrm{D-D}}(\mathbf{q})$ is the scattering matrix element of two direct excitons exchanging a momentum of $\mathbf{q}$. $\hat{V}_\mathrm{D}$ is the scattering potential [152], which arises from the commutator $[\mathscr{H},\hat{D}^\dagger]$ and is a signature of the phase space filling. Similarly, for indirect excitons we get

$$\begin{aligned}[\mathscr{H},\hat{I}^{\dagger N_\mathrm{I}}] =& N_\mathrm{I}E_\mathrm{I}\hat{I}^{\dagger \mathrm{N}_I-1} + N_\mathrm{I}\hat{I}^{\dagger N_\mathrm{I}-1}\hat{V}_\mathrm{I} \\ &+ \frac{N_\mathrm{I}(N_\mathrm{I}-1)}{2}\hat{I}^{\dagger \mathrm{N}_\mathrm{I}-2}\sum_{\mu,\nu,\mathrm{q}} V^{\mu,\nu}_{\mathrm{I-I}}(\mathbf{q})\hat{I}^\dagger_\nu(\mathbf{q})\hat{I}^\dagger_\mu(-\mathbf{q}),\end{aligned} \tag{B.20}$$

with the notation being similar to Eq. (B.19). We note the property of the scattering potential such that $\hat{V}_{\mathrm{D,I}}|\Omega_0\rangle = 0$. With the given commutators, we can rewrite the total energy as

$$\begin{aligned}&\langle\Omega_0|\hat{D}^{N_\mathrm{D}}\hat{I}^{N_\mathrm{I}}\hat{\mathscr{H}}\hat{D}^{\dagger N_\mathrm{D}}\hat{I}^{\dagger N_\mathrm{I}}|\Omega_0\rangle = \\ &= N_\mathrm{I}E_\mathrm{I}\langle\Omega_0|\hat{D}^{N_\mathrm{D}}\hat{I}^{N_\mathrm{I}}\hat{D}^{\dagger N_\mathrm{D}}\hat{I}^{\dagger N_\mathrm{I}}|\Omega_0\rangle + N_\mathrm{D}E_\mathrm{D}\langle\Omega_0|\hat{I}^{N_\mathrm{I}}\hat{D}^{N_\mathrm{D}}\hat{D}^{\dagger N_\mathrm{D}}\hat{I}^{\dagger N_\mathrm{I}}|\Omega_0\rangle \\ &+ \frac{N_\mathrm{I}(N_\mathrm{I}-1)}{2}\hat{I}^{\dagger N_\mathrm{I}-2}\sum_{\mu,\nu,\mathrm{q}} V^{\mu,\nu}_{\mathrm{I-I}}(\mathbf{q})\langle\Omega_0|\hat{D}^{N_\mathrm{D}}\hat{I}^{N_\mathrm{I}}\hat{D}^{\dagger N_\mathrm{D}}\hat{I}^{\dagger N_\mathrm{I}-2}\hat{I}^\dagger_\nu(\mathbf{q})\hat{I}^\dagger_\mu(-\mathbf{q})|\Omega_0\rangle \\ &+ \frac{N_\mathrm{D}(N_\mathrm{D}-1)}{2}\hat{D}^{\dagger N_\mathrm{D}-2}\sum_{\mu,\nu,\mathrm{q}} V^{\mu,\nu}_{\mathrm{D-D}}(\mathbf{q})\langle\Omega_0|\hat{D}^{N_\mathrm{D}}\hat{I}^{N_\mathrm{I}}\hat{D}^{\dagger N_\mathrm{D}-2}\hat{D}^\dagger_\nu(\mathbf{q})\hat{D}^\dagger_\mu(-\mathbf{q})\hat{I}^{\dagger N_\mathrm{I}}|\Omega_0\rangle \\ &+ N_\mathrm{D}N_\mathrm{I}\sum_{\mu,\nu,\mathbf{q}} V^{\mu,\nu}_{\mathrm{D-I}}(\mathbf{q})\langle\Omega_0|\hat{D}^{N_\mathrm{D}}\hat{I}^{N_\mathrm{I}}\hat{D}^{\dagger N_\mathrm{D}-1}\hat{D}^\dagger_\mu(\mathbf{q})\hat{I}^\dagger_\nu(-\mathbf{q})\hat{I}^{\dagger N_\mathrm{I}-1}|\Omega_0\rangle.\end{aligned} \tag{B.21}$$

Eq. (B.21) describes various energy contributions (linear and nonlinear) that are present in the system. We note that each term is proportional to the expectation value $\langle\Omega_0|\hat{D}^{N_\mathrm{D}}\hat{I}^{N_\mathrm{I}}\hat{D}^{\dagger N_\mathrm{D}}\hat{I}^{\dagger N_\mathrm{I}}|\Omega_0\rangle$,

which deviates from 1 due to the non-bosonicity of composite excitons. This reveals three possible creation potentials $\hat{V}^{\mu,\nu}_{\mathrm{D-D}}, \hat{V}^{\mu,\nu}_{\mathrm{I-I}}$, and $\hat{V}^{\mu,\nu}_{\mathrm{D-I}}$, which noticeably generate cross-flavour interaction. The presence of creation potentials, as well as quadratic scaling of these terms in the total energy, is the signature of nonlinear behaviour. Terms in lines 2 and 3 of Eq. (B.21) are the energy shifts for direct and indirect excitons due to phase space filling within the same exciton flavour. The last term in line 4 is the cross interaction of direct and indirect excitons, allowing for extra energy shifts in modes that are not statistically independent. Namely, the corresponding operators for intralayer and interlayer excitons do not commute as they share a hole, but formed by different electrons in conduction bands. This leads to the negative valued commutator, and here we identify the origin of unusual redshift, as observed in the work. We refer to this effect as hole crowding, where hole population being shared between the two different particles (hIX and $\mathrm{X_A}$). This is different from statistical deviation of same excitons, where both carriers are exchanged, which we simply refer as interlayer exciton phase space filling, in analogy to the monolayer case. The effect of intra-flavour terms has already been discussed in Ref. [153], and leads to positive energy shifts. However, the cross-flavour terms only emerge in bilayers, and to date remained unexplored. We evaluate the considered term in $\mathbf{q} \simeq 0$, as it gives the dominant contribution observed in experiments, and we consider particles being in the ground state as a main occupation at low temperatures. With this, we rewrite the mutual energy shift $\Delta E_{\mathrm{I}} = \sum_{\mu,\nu,\mathbf{q}} V^{\mu,\nu}_{\mathrm{D-I}}(\mathbf{q}) \langle \Omega_0 | \hat{D}^{N_{\mathrm{D}}} \hat{I}^{N_{\mathrm{I}}} \hat{D}^{\dagger N_{\mathrm{D}}-1} \hat{D}^{\dagger}_{\mu}(\mathbf{q}) \hat{I}^{\dagger}_{\nu}(-\mathbf{q}) \hat{I}^{\dagger N_{\mathrm{I}}-1} | \Omega_0 \rangle$ as

$$\Delta E_{\mathrm{I}} = -\xi \frac{e^2}{4\pi\varepsilon\varepsilon_0 A} \mathscr{I}\alpha, \tag{B.22}$$

with A being the sample area, and parameter ξ of the order of unity, $\xi \sim 1$, is tuned to match with experimental data setting an effective area. Here, $\alpha = (\alpha_{\mathrm{D}}^{-1} + \alpha_{\mathrm{I}}^{-1})^{-1}$ is the reduced

particle Bohr radius. The dimensionless exchange integral $\mathscr{I}$ has the form

$$\begin{aligned}\mathscr{I} = &\int d^2x d^2y \tilde{V}_{\mathrm{KR}}^{\mathrm{intra}}(|\mathbf{x}-\mathbf{y}|)\frac{1}{(1+\alpha_1^2x^2)^{3/2}}\frac{1}{(1+\alpha_2^2y^2)^3}\cdot\\ &\cdot\left(\frac{1}{(1+\alpha_1^2x^2)^{3/2}}-\frac{1}{(1+\alpha_2^2y^2)^{3/2}}\right)\\ &+\tilde{V}_{\mathrm{KR}}^{\mathrm{inter}}(|\mathbf{x}-\mathbf{y}|)\frac{1}{(1+\alpha_2^2y^2)^{3/2}}\frac{1}{(1+\alpha_1^2y^2)^{3/2}}\frac{1}{(1+\alpha_2^2x^2)^{3/2}}\cdot\\ &\cdot\left(\frac{1}{(1+\alpha_1^2x^2)^{3/2}}-\frac{1}{(1+\alpha_1^2y^2)^{3/2}}\right),\end{aligned} \tag{B.23}$$

where $\tilde{V}_{\mathrm{KR}}^{\mathrm{inter}}(|\mathbf{x}-\mathbf{y}|)$ is Keldysh-Rytova potential in dimensionless form, α_1 and α_2 are respectfully equal to $\alpha_{\mathrm{D}}/\alpha$ and $\alpha_{\mathrm{I}}/\alpha$. By estimating the exciton density as proportional to oscillator strength, we find $n_{\mathrm{I}} \simeq n_{\mathrm{D}}/4$. Numerically, we estimate the shift with $\varepsilon = 4$, $\alpha \simeq 6.7$ Å. The resulting shift can be estimated as $\Delta E_{\mathrm{I}} = -0.24\xi\ \mu\mathrm{eV}\ \mu\mathrm{m}^2\sqrt{n_{\mathrm{D}}n_{\mathrm{I}}}$.